Dottorato di Ricerca in Scienze Agrarie, Alimentari e Forestali

Dipartimento di Scienze Agrarie, Alimentari e Forestali (SAAF)

Settore Scientifico Disciplinare AGR/09

Remote and Proximal Sensing in Precision Oliviculture

IL DOTTORE
Eliseo Roma

IL COORDINATORE
Prof. Vincenzo Bagarello

IL TUTOR
Prof. Pietro Catania

IL CO-TUTOR
Prof.ssa Mariangela Vallone

CICLO XXXV
ANNO 2022

Index

1. INTRODUCTION

1.1. Precision Farming

Precision agriculture represents one of the most important opportunities that can be implemented by companies in order to ensure quantitatively and qualitatively satisfactory productions (Fountas et al., 2015; Schrijver et al., 2016). Recently, the International Society of Precision Agriculture (ISPA) released this definition:

"Precision Agriculture is a management strategy that gathers, processes and analyses temporal, spatial and individual data and combines it with other information to support management decisions according to estimated variability for improved resource use efficiency, productivity, quality, profitability and sustainability of agricultural production."

Precision farming (PF) is a management method that aims to investigate the spatial and temporal variability of an agroecosystem in order to carry out site-specific treatments, applying different technologies and methodologies. The intra- and inter-crop variability that occurs within the crop is determined by the spatial and temporal variability of the soil, the crop species, and the climate (Lal, 2015). The main advantages of this practice include: savings on the quantity of inputs used (López-Granados et al., 2004; Noori and Panda, 2016), lower environmental impact (Van Evert et al., 2017), higher crop productivity, and product quality. Its application is widely carried out in herbaceous crops and, to a lesser extent, in tree crops, where PF is mainly applied in viticulture, as it succeeds in achieving the best combination of production quality, environmental impact, and costs (Santesteban, 2019).

Smart agriculture is developing beyond the modern concept of precision agriculture, which uses data from global navigation satellite systems (GNSS) and different geographic information system (GIS) programs (European Agriculture Machinery Association, 2017). However, this new form of agriculture is based on the concepts of precision farming, but is enhanced by contextual awareness and is triggered by real-time events, improving its performance. Smart farming incorporates intelligent services for the application and management of information and communication technologies (ICT) and enables cross integration along the entire agri-food chain with regard to food safety and traceability (Sundmaeker et al., 2016; Vieri et al., 2012). This complete interconnection of services and technologies can be done in different ways: Among them, IoT represents the most efficient (Villa-Henriksen et al., 2020). The application of IoT called AIoT (Zou and Quan, 2017), Ag-IoT (Zhai et al., 2017), or IoF, meaning Internet of farming (Alahmadi et al., 2018) or Internet of food and farm (Sundmaeker et al., 2016), has received more interest in the scientific community.

Certainly, the possibility of interconnecting multiple technologies available today such as UAVs, WSNs, and IoT, makes precision agriculture more efficient and could bring about a momentous change in the concept of agriculture, as happened in the past during the so-called green revolution (Patel, 2013; Popescu et al., 2020). To manage and analyse that all information is possible use the Machine Learning (ML; Virnodkar et al., 2020). This technology is a branch of artificial intelligence and allows the automation of decision-making processes and the development of a farm-specific management system in real time, simplifying farmers' work. Indeed, ML provides an effective approach to build a model for regression and classification of a multivariate, non-linear system, due to machine learning models. Different machine learning algorithms, such as decision trees (DTs), support vector machines (SVMs), artificial neural networks (ANNs), genetic algorithms (GAs), and ensemble learning, have been used effectively on remotely sensed information (Mountrakis et al., 2011). Recently, the use of machine learning techniques combined with remote sensing data has reshaped precision agriculture in many ways, such as crop identification, yield prediction, and crop water stress assessment, with better accuracy than conventional remote-sensing methods. ML can be used to improve data from any platform. Makhloufi et al., (2021), using this technology, were able to more accurately estimate the biophysical data and phenological stages of the olive tree from remote platforms. One problem in implementing ML algorithms is the high computing power required. However, advances in ML algorithms reduce the computational time for data processing.

These new emerging technologies, such as geospatial technologies, Internet of things (IoT), big data analytics, and artificial intelligence (AI) (Jha et al., 2019), despite posing new technological and cognitive challenges to be overcome, could be used to make informed management decisions in order to further improve the agri-food sector.

1.2. Precision Oliviculture

The world population and its food consumption are growing rapidly, while the effects of climate change complicate the possibility of ensuring food security in a sustainable way (Godfray et al., 2010; Tilman et al., 2011). Therefore, new methods of cultivation and farm management are being sought that ensure the proper supply of food to the population and a low incidence of environmental impact. In recent years, there has been an increase in the agricultural area devoted to olive growing and in the consumption of extra virgin olive oil (EVOO) (FAOSTAT, n.d.). Precision olive growing today represents a method of farm management that certainly brings undeniable benefits to the sector from all points of view: productive (Álamo et al., 2012), qualitative, and environmental (Van Evert et al., 2017). Indeed, precision olive growing involves the application of

different technologies in order to optimize the use of different agricultural inputs (Rosati et al., 2015). In addition, a continuous change in cultivation techniques has been observed, which poses new challenges to ensure the environmental and economic sustainability of olive farms (De Gennaro et al., 2012). Today, the olive tree is cultivated in about 40 countries and occupies a global area of about 10.5 million hectares (FAOSTAT, n.d.). Its cultivation is almost entirely (over 98%) in countries bordering the Mediterranean Sea, where olive growing has always been a traditional practice and a descriptive element of many landscapes in rural and peri-urban areas (Baldoni and Belaj, 2009). However, it is also continuously expanding in other continents, such as Australia and South America (FAOSTAT, n.d.). The world olive system is divided into three forms of cultivation: traditional olive cultivation (OT), intensive (HI) or high intensity (HD) olive cultivation, and superintensive (SHI) or very high density (SHD) olive cultivation (Rallo, 2006; Tous et al., 2007). These three major classes are profoundly different in cultivation techniques and require appropriate agronomic choices for a successful crop.

These techniques are able to modify the vegetative and productive activity of the olive tree and require appropriate choices depending on the agro-climatic context. These include phytosanitary management, irrigation, soil management, pruning, fertilization, etc. However, the most important agronomic practices that need to be different depending on the type of cropping system in which precision farming can allow a clear improvement are fertilization and irrigation.

Fertilization can directly and indirectly influence the vegetative-productive activity of plants and the whole agrosystem. Such application proves to be beneficial in terms of productivity and quality (size, oil content, etc.) when the foliar nutrient concentration is below the threshold (Bouhafa et al., 2014; Fernández-Escobar and Marín, 1997; Rosati et al., 2015). However, this practice is often carried out without considering the real needs of the crop, the real availability, and the soil characteristics (Fernández-Escobar, 2011). In fact, excessive doses are used with a consequent increase in vegetative activity to the detriment of productivity (to this condition the olive tree is very sensitive, manifesting itself with a clear alternation of production), increased management costs, pollution (Fernández-Escobar and Marín, 1997), etc. Furthermore, the use of massive doses of fertilizer leads to a deterioration in oil quality (Dag et al., 2009; Fernández-Escobar et al., 2006; Tognetti et al., 2008), due to a reduction in polyphenol content (Fernández-Escobar et al., 2002) without any increase in oil yield.

Irrigation, more than any other agronomic practice, is capable of modifying the quality and quantity of the fruit (Fernández et al., 2018); unfortunately, it is difficult to reach the right compromise. In fact, there can be negative effects on fruit quality such as a reduction of the phenolic component (excessive doses) and on productivity (lower doses). On the other hand, the positive effects are linked to an increase in production and a reduction in production alternation. The olive tree is a species that has always been recognized as resistant–tolerant to water

stress with an average water requirement of 1500–2500 m^3 ha^{-1}. For this reason, in traditional systems it is grown without the aid of irrigation (Tognetti et al., 2009). Unfortunately, the new SHD farming systems, characterized by higher productivity, cannot be managed without the use of this agronomic practice. Moreover, the water resource is decreasing due to its continuous exploitation. Therefore, it is evident that it is necessary to use techniques and agronomic choices able to maximize crop water efficiency (WUE). This objective can be pursued in different ways: acting on the quantity of water supplied, acting differently on the different phenological moments, acting on the methods of irrigation distribution (micro-flow, sprinkling, etc.), and/or through the right agronomic choices (pruning, fertilization, etc.). However, in order to achieve this, the water status of the crops must be measured accurately and reliably in order to provide a predetermined stress level. In this perspective, precision irrigation can provide excellent results on the identification of water stress variability in the field (Fernández et al., 2018).

In short, the profound differences between farming systems and the different repercussions that agronomic practices can have on them pose new challenges and problems in successfully transferring and applying precision agriculture to this agronomic system. The aim of this work was to provide state of the art studies carried out on the application of precision farming to olive growing, in its different forms (OT, HD, and SHD), and to illustrate its potential applications. The research was done thoroughly by examining the existing literature work done in the context.

1.2.1. *Remote Sensing Sensors for Spatial Variability Detection*

The first step in precision agriculture is the investigation of spatial variability, using different types of sensors capable of acquiring raster or vector information (Zhang et al., 2002). As reported by Zhang et al. (2002) (Zhang et al., 2002), the variability affecting agricultural production can be classified into six groups: yield variability; field variability; soil variability; crop variability; variability related to abnormal factors; and management variability. The sensors used for this purpose are capable of acquiring information of different kinds and cover a more or less wide area. In order to be able to apply them in the best possible way, it is necessary to know the variable to be investigated and the acquisition platform on which they will be placed. In fact, the same sensor, such as a multispectral camera, can be used on remote or proximal sensing platforms and give very different information. In this article, we focus on the sensors that are the most used in remote sensing of olive trees as they are the most used in precision farming. Generally, these sensors are cameras capable of acquiring images (raster information) in different multispectral bands. Their use differs according to the spatial, spectral, radiometric, and temporal resolution they offer. The spatial resolution of a sensor is defined by the size of the pixel representing the investigated area. Spectral

resolution is indicated by the width of the spectral bands of the acquired electromagnetic spectrum. Radiometric resolution represents the number of different signal intensities that the sensor is able to acquire; the measurement scale is expressed in bits and generally ranges from 8 to 16. Temporal resolution is associated with the platform hosting the sensor rather than the sensor itself and represents the time between one acquisition and the next of the same object (Deng et al., 2018). There are many classifications of sensors that can be used remotely, as they can be distinguished based on their operation, type of acquisition, number of acquisition bands (multispectral and hyperspectral), and more. In remote sensing, RGB, hyperspectral, and multispectral images are generally present as sources of spectral information. However, these provide different information, so it is necessary to understand their actual potential. In precision olive growing, multispectral images represent the most widely used spectral information. In this article, the classification was made on the basis of the main crop characteristics (nutritional, water, and canopy structural status) that can be investigated by remote sensors on olive trees in the literature.

1.2.2. *Sensors and Technologies for Identifying the Physiological State of the Olive Tree*

For the identification of nutritional deficiencies, canopy structural information, water status of olive trees, and more generally plant health conditions, sensors capable of detecting the electromagnetic energy reflected or emitted by plants are used in precision agriculture (Rubio-Delgado et al., 2021). This is because leaf reflectance is influenced by several factors (presence or absence of particular molecules, environmental factors, etc.) in specific regions of the electromagnetic spectrum, such as: in the visible wavelengths by photosynthetic pigments such as chlorophyll a, chlorophyll b, and carotenoids; in the near-infrared by leaf structure (size and distribution of air and water inside the canopy), and the presence of water and biochemical substances such as lignin, cellulose, starch, proteins, and nitrogen (Liang, 2005). Therefore, this optical technique is based on measuring the reflectance of incident electromagnetic radiation at different wavelengths in the range from 350 to approximately 25,000 nm. This range includes the frequency bands most commonly used in precision farming, such as: visible (VIS), near-infrared (NIR), shortwave infrared (SWIR), and thermal infrared (TIR). The set of spectral responses of a crop at high spectral resolution (narrow bands) allows its spectral signature to be identified. The spectral signature is typical for each crop and each stress situation (Figure 1).
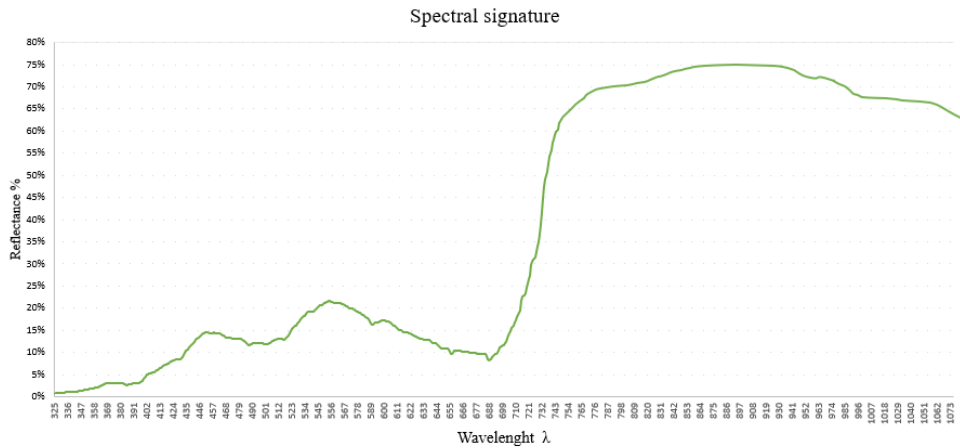
Figure 1. Spectral signature of the olive tree.

The reflectance curves of olive tree leaves show the same spectral pattern typical of the main agricultural crops (Liang, 2005) for all measured wavelengths, although the magnitude and amplitude varied especially in the NIR region (750–1100 nm) due to different crop characteristics such as canopy structure, water content, etc. In the study by Rubio–Delgado et al. (2021) (Rubio-Delgado et al., 2021) the reflection curves showed different reflection peaks and absorption sinks. In the VIS region, one reflection peak was centered at 554 nm (green region) and two absorption sinks were centered at 390 and 680 nm (blue and red regions, respectively). The NIR region had a higher reflection than the VIS region. In the SWIR region (1100–2300 nm), three absorption wells were identified as: 1200, 1450, and 1720 nm, and three reflection peaks centered at 1280, 1650, and 2200 nm (Rubio-Delgado et al., 2021). Thus, the most suitable electromagnetic spectrum regions for characterizing the absorption spectrum of olive trees are between 350–1350, 1421–1800, and 1961–2300 nm. The first two represent the electromagnetic regions of greatest interest as they are used to investigate the nitrogen and chlorophyll content and some structural properties of the canopy. The absorption regions of the band are caused by the presence of water and have a high presence of noise, resulting in a low signal-to-noise ratio (Tanriverdi, 2006). Therefore, alterations in photosynthetic activity are related to the nutritional status, health, and vigor of plants, and can be easily detected with multispectral and hyperspectral sensors (Lee et al., 2010).
Since the 1980s, the first vegetation indices (VI) have been created to examine growing conditions (Table 1).

Table 1. Shows the main VI used on olive trees.

VI	Acronym	Equation	Author of index
Chlorophyll Absorption in Reflectance Index	*CARI*	CAR * (ρ700/ρ670)	Kim et al., 1994
Double-peak Canopy Nitrogen Index	*DCNI*	$[(\rho720 - \rho700) / (\rho700 - \rho670)] / (\rho720 - \rho670+0.03)$	Chen et al., 2010
Green Index	*GI*	ρ550/680	Chamard et al. 1991
Green Normalized Difference Vegetation Index	*GNDVI*	(ρ800−ρ550)/(ρ800+ρ550)	Gitelson and Merzlyak, 1994
Modifed Chlorophyll Absorption in Reflectance Index I1510	*MCARI*	$[(\rho700 - \rho1510) - 0.2(\rho700 -\rho550)] / (\rho700/\rho151)$	Daughtry et al., 2000
Moisture Stress Index	*MSI*	ρ858/ρ1240	Hunt & Rock, 1989
Normalized Difference Greenness Vegetation Index	*NDGVI*	(ρ550−ρ680) / (ρ550+ρ680)	Chamard et al. 1991
Normalized Difference Red-Edge Index	*NDRE*	(ρNir−ρRedEge) / (ρNir+ρRedEdge)	Maccioni et al., 2001
Normalized Difference Vegetation Index	*NDVI*	(ρ800−ρ680)/(ρ800+ρ680)	Rouse, Haas, Deering, & Sehell, 1974
Normalized Difference Water Index	*NDWI*	(ρ858−ρ1240) / (ρ858+ρ1240)	Gao, 1996
Optimized Soil-Adjusted Vegetation Index	*OSAVI*	(ρNIR - ρR) /(ρNIR+ ρR+0.16)	Rondeaux et al., 1996
Soil Adjusted Vegetation Index	*SAVI*	(ρNir-ρRed) * (ρNir+ρRed+L) * (1+L)	Huete et al., 1988
Simple Ratio 550,670	*SR*	ρ550/ρ670	
Simple Ratio 780,550	*SR*	ρ780/ρ550	
Simple Ratio 780,670	*SR*	ρ780/ρ670	
Simple Ratio Water Index	*SRWI*	ρ680/ρ1240	Zarco-Tejada, Rueda, & Ustin, 2003
Transformed Chlorophyll Absorption Ratio Index1510	*TCARI*	$3[(\rho700 -\rho1510) - 0.2(\rho700 - \rho550)(\rho700/\rho1510)]$	Haboudane et al., 2002
Water Index	*WI*	ρ680/ρ858	Peñuelas et al., (1993)

These are calculated from the individual reflectance value wavelengths acquired. These are classified into two large families: slope-based and distance-based (Xue and Su, 2017). In addition to their simple use, several processing techniques have also been experimented with in order to obtain greater precision and information of vegetation indices such as smooting (SM), partial least squares regression (PLSR) techniques, etc. Using PLSR techniques, it is possible to extrapolate spectral information of the crop from the entire reflectance spectrum (350–2500 nm) (Hansen and Schjoerring, 2003). In olive trees, the most widely used VI are probably the normalized difference vegetation index (NDVI) and the soil-adjusted vegetation index (SAVI). However, there have not yet been exhaustive studies in the field that have determined their real potential for use in stress discrimination. Given the high sensitivity of Vis to variations in chlorophyll content, nitrogen, and plant nutritional status, their application has focused on precision fertilization techniques (Ali et al., 2017; Barranco-Navero et al., 2017; Rotundo et al., 2003) and precision irrigation (Fernández et al., 2018).

Regarding the ability and aptitude of the different IAs to discriminate and investigate the nutritional status of the olive tree, there are not many studies; moreover, they seem to be in slight contrast. Gómez-Casero et al., (2007) showed that N and K deficiencies can be discriminated using about 26 different wavelengths, and the best indices were: NIR/G, G/R, and NDVI. In general, the best wavelengths for the calculation of VI were between 830 and 890 nm (mainly in the NIR region) for both nutrients. Noguera et al., (2020) viewed the reflectance curve, in the VIS-NIR region, of olive trees under different treatments of nitrogen, phosphorus, and potassium. Their results showed that potassium and phosphorus had a similar pattern with peaks evident at 550 and 700 nm and to a lesser extent at 670 nm; in the case of N, they were not significant. Furthermore, using different methods of data analysis they found that non-parametric analysis (ANN, neural network analysis) generated the best prediction of leaf element concentration.

The study by (Rubio-Delgado et al., 2021) contributed significantly to the evaluation of the spectral characteristics of olive leaves with the aim of estimating the nutritional status of this crop. All the wavelengths used gave a low predictive capacity for leaf nitrogen content. The best results of the VI used in Rubio-Delgado et al., (2021) were provided by the indices: double-peak canopy nitrogen index (DCNI, $r^2 = 0.72$), modified chlorophyll absorption in reflectance index (MCARI, $r^2 = 0.53$), and transformed chlorophyll absorption ratio index (TCARI, $r^2 = 0.64$). The best vegetation index was DCNI, with a correlation of 0.72, combining the following wavelengths: 395, (blue); 652 (red), and 1275 nm (SWIR). No index combining wavelengths from the NIR region presented a high coefficient of determination, underlining those combinations using blue, red, and SWIR wavelengths are the most suitable for estimating leaf nitrogen concentration (LNC) in olive trees using hyperspectral data. Furthermore, Rubio-Delgado et al., (2021) processed the raw data with different methodologies in order to verify which one is the best for determining the LNC. The results showed that the raw data resulted in an increase in the correlation between VI and LNC,

especially when second derivative and smoothing (SM) and/or standard normal variate (SNV) were used as a pre-processing method. The PLSR models produced very good accuracy compared to VI, although the uncertainties associated with noise in the hyperspectral data were higher. Similar results were obtained by Rotbart et al., (2013) and Zarco-Tejada et al., (2004). Rotbart et al., (2013) estimated the LNC using the same methodology (albeit in the laboratory) over a reduced reflection spectrum (SWIR was not considered). They conclude the work by stating that due to several confounding factors such as leaf orientation, water content, etc., it was not possible to build a robust model to be applied in the field. Precision irrigation is currently more and more successful, also due to the high technology push and the gradual reduction of the cost of the necessary equipment in the last years (Noguera et al., 2020). However, it still remains a well implemented practice for different crops (Cohen et al., 2005). In precision oliviculture, this practice is under continuous experimentation, since the spatially variable application of water is advantageous for environmental, economic, and management sustainability (cost reduction, better balance between production and vegetation, and higher quality of the final product). Several techniques can be used to directly or indirectly determine the water status of the crop. The most widely used in precision oliviculture to investigate the entire variability of the field are thermography and/or the use of Vis closely linked to the crop's water content.

The main advantage of using Vis for the identification of plant water conditions lies in the possibility of exploiting the wavelengths that are recorded with multispectral or better hyperspectral chambers, which are usually used for the identification of the correct nutritional and health status of crops. These Vis are based on reflectance spectroscopy in the electromagnetic regions of the visible (VIS), near infrared (NIR), and shortwave infrared (SWIR) and can be applied for indirect assessments of the water status of olive trees, as water content can greatly influence crop spectral signatures (Agam et al., 2014; Elsayed et al., 2011; Jorge et al., 2019; Sims and Gamon, 2002). Recently, a specific database containing several indices related to "vegetation water" applications has been created and published online by the Institute of Crop Science and Resource Conservation (INRES, www.indexdatabase.de; 1 February 2022) of the University of Bonn. Unfortunately, the proposed indices are not related to any specific crop or physical variable.

Rallo et al., (2014) described the accuracy of several VIs and the use of partial least squares regression (PLSR) to determine leaf water potential (LWP). The best prediction was found using the moisture stress index (MSI) (RMSE = 0.72 and r^2 = 0.45) and the normalized difference water index (NDWI, RMSE = 0.75 and r^2 = 0.45). Using the PLSR technique, a good prediction of LWP was obtained at both tree canopy and leaf levels. However, this technique requires the availability of complete high-resolution spectra, which can only be obtained with portable spectroradiometers or hyperspectral remote sensors. Although the use of VI seems to have good applications in crop water stress management, high correlations are

not always observed. This is because water stress is a condition that determines the change of the leaf structure and its spectral response but not always in the short term, and it is also linked to many other stress conditions such as nutrition and the management of the olive grove itself.

Even today, methodologies or techniques are proposed that use leaf temperature alone (in the case of olive trees, the range of stress variability is between 28–37 °C), to distinguish different levels of stress. Unfortunately, this poses numerous limitations due to the high influence of environmental conditions. For this reason, they are less used today, and it is preferred to use some normalized indices (Idso et al., 1981; Jackson et al., 1981; Möller et al., 2007). The main index that allows the evaluation of the water status of olive trees is the crop water stress index (CWSI). This index was invented by Jackson et al., (1981) and Idso et al., (1981) and can have a value ranging from 0 to 1, indicating stress and good irrigation conditions, respectively. It is determined from the temperature of the object (in this case the leaf temperature) at a given time (T_0). This temperature is closely correlated with water stress, since the physical principle behind the temperature change depends on transpiration. In fact, the stomatal closure that occurs due to water stress causes less leaf transpiration (loss of water vapor), which in turn causes an increase in leaf temperature.

From the different studies that have been found in the bibliography, we can state that CSWI has proven to be a good indicator of the crop's water status as it presents very good correlations with canopy temperature and the different stress indices (Ben-Gal et al., 2009, p.; Cohen et al., 2005; Egea et al., 2017; Sepulcre-Cantó et al., 2005). Egea et al., (2017) correlated CSWI and the main water stress indicator parameters such as: stem water potential (Ψ_{st}), leaf water potential (Ψ_l), leaf transpiration rate (Em), and stomatal conductance (gsm), obtaining significant linear regressions (Figure 2).
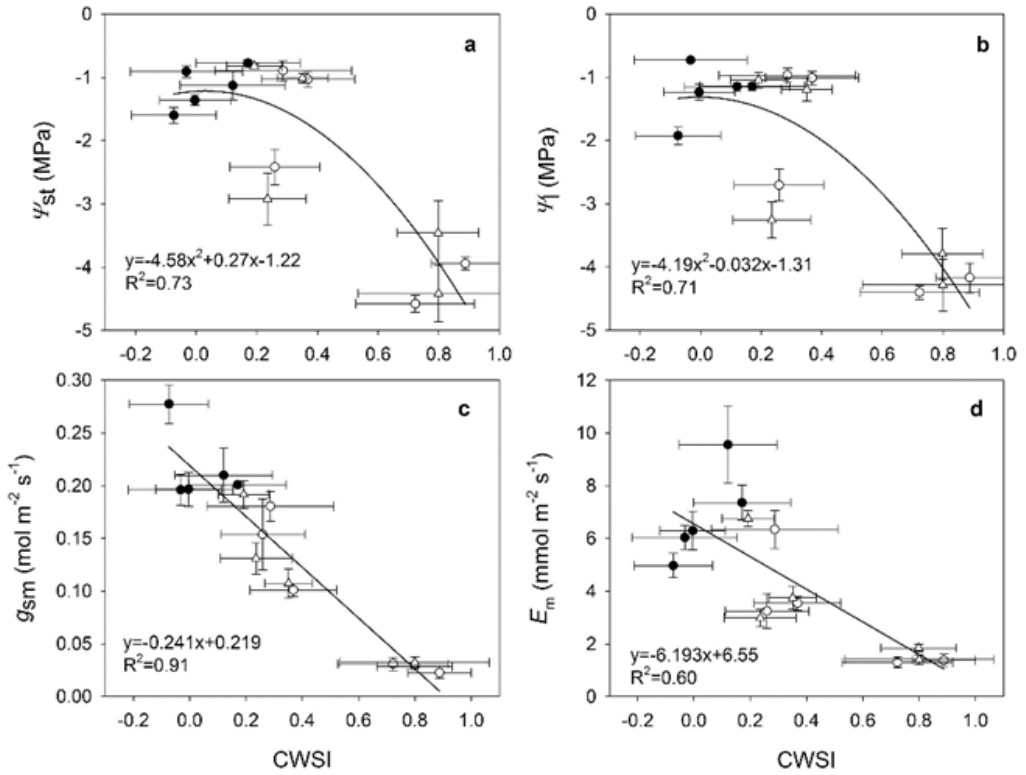
Figure 2. Relationship between CWSI determined from aerial thermal imaging and (**a**) midday stem water potential (Ψst), (**b**) midday leaf water potential (Ψl), (**c**) stomatal conductance (gsm), and (**d**) leaf transpiration rate (Em) for FI, 45RDICC, and 45RDITP treatments. The straight lines represent the fitted regression lines to the data. Data from (Egea et al., 2017).

The CWSI can be calculated from images acquired at wavelengths (λ) between 7–14 nm. The original formula that was proposed is as follows:

$$CSWI = \frac{dT - dTll}{dTul - dTll} \qquad (1)$$

where dT is given by (Tc−Ta), i.e., the difference between the canopy temperature (Tc) and the air temperature (Ta); dT_{ll} is the No-Water Stressed Baseline (NWSB) of fully irrigated crops; and dT_{ul} is the upper baseline. The dT_{ll} and dT_{ul} are the temperature values of fully irrigated and water stressed crops respectively. The dT_{ll} and dT_{ul} are both a function of the atmospheric vapor pressure deficit (VPD) (Idso et al., 1981; Veysi et al., 2017). Both upper and lower limits are species-specific and can be derived. Unfortunately, the different published NWSB equations for olive are site-dependent, as the VPD normalization procedure used to obtain *CWSI* does not take into account differences in net radiation and drag that are known to influence this index. Furthermore, as shown by Egea et al.,

(2017) the intercept and equation of the NWSB varies with season and time of day.

In response to this, Berni et al. (2009) proposed to calculate the NWSB empirically using the Tc-Ta values of trees from the full irrigation (FI) treatment near solar noon (12:30 GMT), using hourly mean values from clear days from April to September. Thus calculated, the NWSB (Tc-Ta = −0.35 − VPD + 2.08, $r^2 = 0.67$) shows differences in Tc-Ta varying less than 1.5 K even with large variations in VPD. This difference is very small when compared to NWSB for herbaceous crops but also for some tree species such as pistachio and peach (Bellvert et al., 2016; Tognetti et al., 2006) as well as the slope of the same, probably due to the high transpiration regulation capacity of olive trees (Bellvert et al., 2016; J. A. Berni et al., 2009; Egea et al., 2017).

Given the laboriousness, in olive trees, other calculation methods have also been identified for their determination. To eliminate the problem of knowing the NWSB, Jones, (1999) modified the *CWSI* and defined a new normalized *CWSI*, which is described as follows.

$$CWSI = \frac{T_{canopy} - T_{wet}}{T_{dry} - T_{wet}} \tag{1}$$

where T_{canopy} is actual canopy temperature obtained from the thermal image and T_{wet} and T_{dry} are the lower and upper boundary temperatures representing a fully transpiring leaf with open stomata and a non-transpiring leaf with closed stomata, respectively. Note that T_{wet} and T_{dry} are equivalent to dT_{ll} e dT_{ul} in the original formulation of *CWSI* by Idso et al., (1981). However, normalizing CWSI is a more complex process with changing atmospheric conditions than using VPD alone. Indeed, varying atmospheric conditions complicate the normalization of CWSI. In this regard, T_{dry} and T_{wet} can be calculated using an empirical approach.

In the empirical approach, T_{dry} can be determined by adding 5 °C to the air temperature (Irmak et al., 2000), while T_{wet} can be determined by two methods. One of these involves the spraying part of the canopy with water some 20 s prior to thermal image acquisition (Möller et al., 2007) or by measuring the temperature of a wet artificial reference surface (WARS). As detailed by Cohen et al., (2005) and Meron et al., (2003), the WARS is a permanently wet surface of reproducible radiometric and physical properties, such a wet object, which can also take the form of an artificial wet cloth (Meron et al., 2003), with a typical size of 30 × 40 cm. Three main drawbacks limit the applicability of CWSI$_E$ for high spatiotemporal monitoring of stress (Agam et al., 2013; Ben-Gal et al., 2009). The first is the empirical value of 5 °C. While it had indeed been proven to represent the maximum leaf temperature under several conditions (Cohen et al., 2005; Irmak et al., 2000; Möller et al., 2007), the CWSI$_E$ is quite sensitive to the value assigned to T_{dry}, and a significant uncertainty is induced to the index's value when use of this empirical formulation is adopted. The second drawback is that it must

necessarily be placed inside each thermal image acquired and the third required high-spatial resolution (to detect a significant number of pixels within the reference, while avoiding mixed pixels) (Ben-Gal et al., 2009). For these reason, one analytical method can be used to calculate T_{dry} and T_{wet}. It is quite expensive in terms of calculation. This method is based on the energy balance equation (Jackson et al., 1988; Jones, 1999a) and requires the measurement of incoming solar radiation, air temperature, relative humidity, drag, and wind speed (Möller et al., 2007). These measurements are available from any meteorological station and can be representative of very large areas, but may have a degree of uncertainty that affects their accuracy. For the analytical calculation, an energy balance is performed to derive the net solar radiation (W m^2), using the sum of incoming and outgoing radiation. The analytical form is proposed by Jones (CWSI$_A$, (Jones, 1999a)). This form has been used extensively in several studies in olive groves (Ben-Gal et al., 2009; J. Berni et al., 2009). Berni et al., (2009) developed an approach suitable for monitoring areas in the order of hundreds of hectares using an unmanned aircraft that could provide frequent visits and short lead times to detect water stress for irrigation scheduling. The methodology presented does not require the use of reference areas and relies on physical models to estimate all input variables of the energy balance equations. Berni et al., (2009) calculated firstly the resistance of the canopy to heat transport (rc). The model used to calculate the CWSI considers not only the vapor pressure deficit but also Rn and wind speed, parameters known to influence temperature differences between air and tree canopy. Once the rc is known and the potential canopy resistance for a well-watered crop (rcp) is estimated (Moriana et al., 2002; Testi et al., 2006), one can proceed with the calculation of the *CWSI* with a purely analytical solution, as reported below:

$$\text{CWSI} = \frac{\gamma(\text{rc} - \frac{\text{rcp}}{\text{ra}})}{\Delta + \gamma \left(1 + \left(\frac{\text{rcp}}{\text{ra}}\right)\right)} \tag{2}$$

According to Ben-Gal et al., (2009), a comparison of the two methodologies was carried out. The best of the two methods (analytical and empirical) turns out to be the CWSI$_A$, although there are not clear differences. On the other hand, Agam et al., (2013) obtained contrasting results with Ben-Gal et al., (2009) as they showed that the use of CWSI$_E$ for the identification of the water status of olive trees during stress and recovery phase is better than the analytical one. Furthermore, Agam et al., (2013) observed a poor applicability of CWSI$_A$ indices throughout the day, in contrast to CWSI$_E$, which proved to be better able to differentiate well-watered trees from stressed trees and better represented the evapotranspirative trend of the crop. Agam et al., (2013) proposed that the CWSI$_A$ can be used not so much for the estimation of the water status of the olive tree, but for an indirect estimation of the stomatal conductance, with which it is closely related.

Agam et al., (2013) proposed the application of a new *CSWI* that is intermediate between the empirical and the analytical method, assuming that T_{wet} is calculated analytically (Jones method), and thus overcoming one of the application limitations of CWSI$_E$. Since T_{wet}, calculated according to Jones (1999), has been shown to produce good CWSI values, it is therefore proposed to combine CWSI$_A$ with CWSI$_E$ to form a CWSI$_{AE}$. In the latter method, T_{dry} is determined empirically, while T_{wet} is calculated analytically, using meteorological measurements in the field.

There is also another methodology to calculate *CSWI* that is used for satellite imagery (Guadalupe Sepulcre-Cantó et al., 2006a). This methodology turns out to be very similar to the use of CSWI$_E$ in that the image is calibrated based on the two references, hot and cold, present in the image. Veysi et al., (2017), using this methodology, were able to determine the *CWSI* using only remote sensing satellite data, using the following equation:

$$CWSI = \frac{T_s - T_{cold}}{T_{hot} - T_{cold}} \qquad (3)$$

where T_s is the land surface temperature (LST) derived from a satellite image providing the canopy temperature, T_{cold} is the temperature of the cold pixels, and T_{hot} is the temperature of the hot pixels. Cold pixels are those covered by fully irrigated crops and hot pixels represent crops under water stress. Bastiaanssen et al., (1998) described the correct procedure for selecting hot and cold pixels while Veysi et al., (2017) made some modifications for selecting hot pixels. Hot pixels are selected from the area with maximum water stress while LST is calculated using thermal images. The LST calculation requires an image with no cloud cover or atmospheric correction of it, radiometric calibration, and knowledge of the emissivity of the considered surface. These are challenging tasks; moreover, existing terrestrial observations (EO) do not provide TIR images with detailed temporal and spatial resolution, and do not appear to be able to adequately distinguish individual canopies (G Sepulcre-Cantó et al., 2006; Guadalupe Sepulcre-Cantó et al., 2006a; Sepulcre-Cantó et al., 2007). Fuentes-Peñailillo et al., (2018) also proposed an intermediate methodology to be applied on remote stellar platforms to the Shuttleworth and Wallace model (Shuttleworth and Wallace, 1985). This methodology foresaw the use of terrestrial meteorological data (to determine the intra-plot variability of an olive grove) and satellite images (Landsat 7), obtaining results with reliable values but still with little applicative possibilities. Unfortunately, given the average size of olive farms and the implementation of new acquisition platforms with higher spatial resolution, the use of satellite platforms and CWSI calculation methods from these platforms have not been widely applied to olive growing. For this reason, applications of new thermal sensors on board unmanned aerial platforms (UAV) are gaining interest in water status investigation. They provide a spatial resolution of less than one square meter, allowing the retrieval of the real canopy temperature, thus

minimizing ground thermal effects compared to images from satellite platforms; despite the uncertainty caused by the high signal-to-noise ratio due to the high resolution. In addition, atmospheric effects and atmospheric transmittance should also be considered for low-altitude platforms aimed at keeping temperature measurement errors below 1 K. In conclusion, it can be stated that the *CSWI*, although reliable enough to predict crop water stress conditions, needs further studies in order to outline a standard protocol applicable in all soil and climate contexts.

1.2.3. *Sensors and Technologies for Olive Canopy Characterization*

Characterization of the canopy provides us with data on the amount of biomass, growth activity, productivity, water consumption (Caruso et al., 2019), health status, etc. Thus, canopy characteristics provide valuable information for specific tree management to reduce production costs and environmental pollution. There is a whole range of key cultivation operations, such as pesticide treatments (Gil et al., 2014), irrigation (Rufat et al., 2018; Sola-Guirado et al., 2017), and fertilization that depend largely on the structural and geometric properties of the trees. When talking about geometric variables, we refer to tree height, volume, area, and width, while structural variables mainly concern leaf area index (LAI), canopy penetrability, and canopy porosity. These can be determined in different ways and in a more or less empirical manner. Of these, the leaf area index (LAI) is the most important parameter. The LAI is a dimensionless variable and was initially defined as the total unilateral area of photosynthetic tissue per unit area of soil (Jonckheere et al., 2004; Villalobos et al., 2006).

The structural and geometrical parameters of trees, such as volume and vegetation area, are generally derived from manual measurements of height and width. However, as this methodology is slow and expensive, alternative methods have been used in the last 10 years. The measurement and structural characterization of plants can be carried out remotely using different sensing principles. The main technologies that can be used for geometric characterization of crops include: ultrasound-based systems (Zaman and Schumann, 2005), digital photographs (Hernández-Clemente et al., 2014), laser sensors (Rosell et al., 2009; Sola-Guirado et al., 2018), stereoscopic images (Rovira-Más et al., 2005), light sensors (Castillo-Ruiz et al., 2016; Giuliani et al., 2000), high-resolution radar images (Bongers, 2001), or high-resolution X-ray computed tomography (Stuppy et al., 2003). Among these, light detection and ranging (LiDAR) and stereoscopic vision systems are probably the most promising techniques to obtain 3D images and maps of plants and canopies (Rosell and Sanz, 2012). It must be stressed that not all the previously mentioned technologies have been able to best describe the 3D structure of trees, due to the actual field conditions.

For the manual characterization of the olive tree canopy, several methods can be used. Among the main ones we find the projected vertical crown area (VCPA)

method, ellipsoid volume (VE) method, and tree silhouette volume (VTS) method (Miranda-Fuentes et al., 2015). The main disadvantage of these methods concerns their high laboriousness without any possibility of being able to investigate the whole spatial variability of the plot. The methods of detecting biophysical parameters of olive trees remotely can be estimated from satellite area platforms with high spatial resolution (Gómez et al., 2011), on UAV (Caruso et al., 2019; Torres-Sánchez et al., 2015a; Zarco-Tejada et al., 2014a), from sensors mounted on unmanned aerial vehicle (UGV) or on tractors (Gamarra-Diezma et al., 2015; Martínez-Casasnovas et al., 2017; Miranda-Fuentes et al., 2015).

A technology that arouses interest especially for canopy qualification in order to better define the direction and quantity of plant protection product is the use of ultrasound (Gamarra-Diezma et al., 2015). Ultrasonic sensors turn out to be cheap, robust, simple to use, and have shown reasonable accuracy under field conditions, sufficient for most cases (Rosell and Sanz, 2012; Tumbo et al., 2002). On the other hand, their main disadvantage is the error produced by some factors, mainly the shape and distance from the target, interference with the signal coming from the sensors, atmospheric conditions, and a low spatial resolution (requiring the use of a larger number of sensors).

Among the most applied methodologies for the quantification of biophysical parameters of olive trees, there are applications using stereoscopic vision techniques, namely structure from motion (SfM) and image matching algorithms, which allow the automatic reproduction of high-resolution topographic scenes from multiple overlapping photographs (Jay et al., 2015). In order to orientate a set of overlapping images, it is necessary to identify a sufficient number of homologous points (called 'tie points') that connect the various survey images. SfM technology is applied using unsupervised algorithms that enable the identification of image tie points in a fully automated form. The identification of tie points begins with the extraction of feature points (or 'keypoints') from each image using feature detection algorithms (Manzo, 2020). Using specific algorithms, point feature descriptor information is obtained for each extracted feature, which are numerical vectors describing the gradient trend in the neighbourhood of the point. The next step is featuring matching (Bianco et al., 2018). Usually, software is based on Euclidean distance calculation, which determines the similarity between two descriptors and classifies them, during this process a percentage of outliers can be found that is often not irrelevant, so it is necessary to identify geometrically consistent matching points by removing outliers using specific algorithms such as RANSAC (RANdom Sample Consenso) (Ghahremani et al., 2021). After this stage, the process involves performing Triangulation and Bundle Adjustment operations that iteratively add new points to the reconstruction. Subsequently, using specific algorithms, such as Multi-View Stereo (MVS) (Hui et al., 2018), which considers all the characteristic points of the scene, the dense point cloud is obtained, which allows the 3D geometry of the canopy to be constructed.

This technique involves the use of consumer RBG chambers (with or without an infrared filter), which allow 3D image reconstruction (Figure 3). The advantage of these technologies lies in the simple and reliable applicability of the system and its low cost (Anifantis et al., 2019; Caruso et al., 2019; Díaz-Varela et al., 2015; Küng et al., 2011; Zarco-Tejada et al., 2014b). Anifantis et al., (2019), using a low-cost drone and a simple RGB camera, managed to obtain very good estimates of canopy structure and morphology compared to conventional classical methods. For the application of the SfM technique, the workflow after image acquisition involves orthomosaicking, reconstruction of the digital surface model (DSM) using structure from motion (SfM) image reconstruction, and finally GIS analysis to calculate the height and diameter of the canopy. A DSM is a digital representation of a topographical surface that represents the height of the top surface of the ground and objects on it, which can be used to obtain information on tree height. A digital terrain model (DTM) represents the topographic surface by including only the height of the ground surface, thus excluding the height of objects on it (Caruso et al., 2019).

Based on the different spatial resolutions, very good results are obtained at plant and individual tree level. Of course, this technology can be tested and used on any type of planting (traditional and intensive) (Díaz-Varela et al., 2015). Caruso et al. (2019) (Caruso et al., 2019), with the same methodology, managed to obtain excellent correlations between biophysical and trunk section area (TCSA) parameters, underlining how vegetative activity and spectral response are closely related to the intensity of agronomic practices. Torres-Sánchez et al., (2015a), in order to fully exploit this technology, implemented more robust and automatic image analysis procedures (Figure 3), using a technique based on the methodology called geographic object-based image analysis (GEOBIA). GEOBIA overcomes some limitations of pixel-based methods by grouping adjacent pixels with homogeneous spectral values after a segmentation process and using the created 'objects' as the basic elements of the analysis (Blaschke et al., 2014; Karydas et al., 2017). GEOBIA, or OBIA, combines spectral, topological, and contextual information of these objects to address complicated classification problems. Karydas et al., (2017), starting from RGB and multispectral images with high spectral resolution, have obtained good results from the application of OBIA methodology. Stateras and Kalivas, (2020) have effectively applied OBIA technology on olive grove, managing to formulate a predictive model of yield based on canopy structural parameters and NDVI.

<div align="center">(a)   (b)</div>

Figure 3. 3D representation of a traditional plantation generated with a multispectral sensor (**a**) and a row plantation generated with a visible light camera (**b**). Data from (Torres-Sánchez et al., 2015a).

Finally, the use of LiDAR is presented as a method of quantification and characterization of the canopy. This technology is becoming more and more successful in fruit growing, as it allows precise, objective, and fast determination of morphological parameters. Such systems can be mounted on any type of platform, even on the same tractor, so that normal cultivation operations can be used to identify and determine the entire olive grove. In the olive field, its use lays the foundations to immense application possibilities, especially in the case of SHD olive groves that need adequate conditioning of vegetative and productive activity to optimize production (Boussadia et al., 2010; Caruso et al., 2014; Tognetti et al., 2006). There are different types of LiDAR sensors on the market, with different modes of operation, and with a significantly lower cost than other technologies. LiDAR laser technology is a non-destructive remote sensing technique for measuring distances, providing a relatively new tool for generating a complete description of tree structure. The distance between the sensor and the target can be measured by two methods: by measuring the time a laser pulse takes to travel between the sensor and the target (LIDAR time-of-flight) or by measuring the phase difference between the incident and reflected laser beams (LIDAR phase shift measurement). In agricultural applications, 2D terrestrial LIDAR sensors can be used, which are much cheaper to use than 3D LiDAR sensors (Sola-Guirado et al., 2018). 2D LIDAR sensors obtain a point cloud corresponding to a plane or section of the object of interest. The fact that these sensors only scan in one plane does not necessarily limit their scope to 2D perception. Sola-Guirado et al., (2018), using a 2D LiDAR sensor, easily managed to obtain on-the-go measurements that could be used for canopy quantification for different crop operations.

This technology, compared to the previously presented technologies, has the advantage of achieving much higher levels of resolution. Martínez-Casasnovas et

al., (2017) obtained correlations around 91%, compared to estimates made manually, with a high saving in time. Furthermore, they managed to identify the behaviour of sunlight within the canopy with an r^2 of 0.97. Indeed, they observed that in the first section, sunlight could easily penetrate the canopy up to a distance of about 0.8 m. The comparison of sunlight extinction coefficients within the canopy can be used to evaluate the effect of different cultivation techniques, such as different pruning systems (Jiménez-Brenes et al., 2017) or different irrigation schemes. The possibility of investigating canopy structure with this technology offers more application possibilities than other methodologies (Castillo-Ruiz et al., 2016). Moorthy et al., (2011) managed to excellently characterize the olive tree canopy and related structural parameters using an intelligent laser ranging and imaging system (ILRIS-3D). They developed robust methodologies to characterize diagnostic architectural parameters, such as tree height ($r^2 = 0.97$, rmse = 0.21 m), crown width ($r^2 = 0.97$, rmse = 0.13 m), crown height ($r^2 = 0.86$, rmse = 0.14 m), crown volume ($r^2 = 0.99$, rmse = 2.6 m^3), and plant area index (PAI) ($r^2 = 0.76$, rmse = 0.26 m^2). The algorithm used to process the LiDAR-3D data was the one developed and tested in the laboratory and proposed by (Moorthy et al., 2008). The disadvantage of this technology is related to its cost and the complexity of calculations, which are not yet standardized.

1.3. Monitoring Technologies

The primary objective of the monitoring process is to acquire the maximum amount of georeferenced information within the olive grove. A wide range of sensors can be used to monitor the different parameters that characterize the plant growth environment. The three agronomic variables that must be monitored in order to apply precision farming correctly are soil, climate, and crop. In the literature, very few works carried out in the olive grove have allowed the investigation of the spatial variability of the soil and climate characteristics, also considering what their influence on the cultivation activity might be. The main scientific progress has been made in the interpretation of data from biophysical parameters, production data, and spectral responses from the crop. The use of vegetation indices or punctual data closely linked to the productivity of the olive grove (such as the production map) are the main methods of analysis and management of the vegetative-productive variability found.
Senay et al., (1998) distinguish three ways of measuring spatial variability in the field: continuously, discretely (e.g., point sampling of soil or plant properties), and remotely (e.g., through aerial photographs). Discrete sampling is generally characterized by a high precision of the investigated variable but cannot describe the complete variability in the field. When adopting this technique, proper geostatistical techniques must be applied, which allow the measurement of the variable to be transformed from discrete to continuous (Fountas et al., 2011). As far as continuous surveying methods are concerned, its progressive use is being

observed in precision olive growing, especially for the creation of particular maps, such as the production map. Finally there is remote sensing: This determines the creation of continuous measurements in space but acquired from platforms more or less distant from the object (Matese and Di Gennaro, 2015). It represents the most interesting and scientifically focused mode of data acquisition, as it allows a more precise, less laborious and often cheaper investigation than point sampling. The problem with remote/proximal sensing techniques is that generally an indirect estimate of the variable to be investigated is obtained and the correlation cannot always be generalized to other locations. For example, if we obtain an NDVI map in an olive grove, we can predict the amount of production that will be obtained, but this correlation is not always equally applicable. The literature often distinguishes the remote sensing technique into two large families based on the distance between the sensor making the measurement and the variable, in this case we speak of remote sensing and proximal sensing. Their differentiation is based on the distance between the sensor and the object of investigation. Generally, proximal sensing is based on the use of ground moving vehicles carrying various types of sensors, handheld sensors, and systems placed directly in the soil (ground sensing) or on the crop (Matese and Di Gennaro, 2015), while remote sensing identifies more distant and generally mobile platforms such as satellites, aircraft, and UAVs. These two categories are extremely different from each other and in precision oliviculture, the most used type of acquisition is remote sensing. However, proximal sensing in view of technological developments such as LiDAR, unmanned ground vehicle, etc., make this acquisition mode very interesting.

1.3.1. Remote Sensing

The application of remote sensing technologies for precision olive growing has increased rapidly in the last decades. The unprecedented availability of high-resolution (spatial, spectral, and temporal) satellite imagery has promoted the use of remote sensing in many PA applications, including crop monitoring, irrigation management, nutrient management, disease management, pest management, and yield forecasting (Sishodia et al., 2020).

The technologies available for the remote investigation of olive trees are very varied and allow increasingly precise monitoring. These are remote image acquisitions with different resolution scales, capable of describing the olive grove by detecting and recording reflected sunlight or wavelengths emitted from the surface of objects. Remote sensing techniques quickly provide a description of the shape, size, vigor, water status, nutritional status, stress state of the olive tree, and allow the assessment of variability within the olive grove. The three platforms mainly used in remote sensing are satellites, aircraft, and unmanned aerial vehicles or remotely-piloted aerial systems (UAV or RPAS). There are substantial differences between the different acquisition platforms depending on the

acquisition distance and the technical characteristics of the platforms themselves. In the case of precision oliviculture, it is possible to adopt satellite or airborne remote sensing techniques and obtain acceptable results (Apan et al., 2004; Noori and Panda, 2016). Such techniques can be used mainly at territorial level, for olive groves of large extents and with very large planting distances or even by public administrations and control bodies (Cruz-Ramírez et al., 2012). However, as today's olive cultivation is also characterized by promiscuous forms of cultivation, with very small areas, this type of acquisition does not lend itself very well to precise monitoring in all forms of cultivation and to the correct application of variable rate technologies. On the other hand, when UAV platforms are adopted, plant investigation can be carried out with greater accuracy and precision of data (Figure 4), and even spatial resolutions of the order of a few centimeters can be achieved (J. Berni et al., 2009; Jurado et al., 2020). However, there are studies that emphasize the potential of remote sensing from satellite for the acquisition of multispectral images, especially when dealing with large areas (Ferwerda and Skidmore, 2007; Peña-Barragán et al., 2004; Solano et al., 2019).
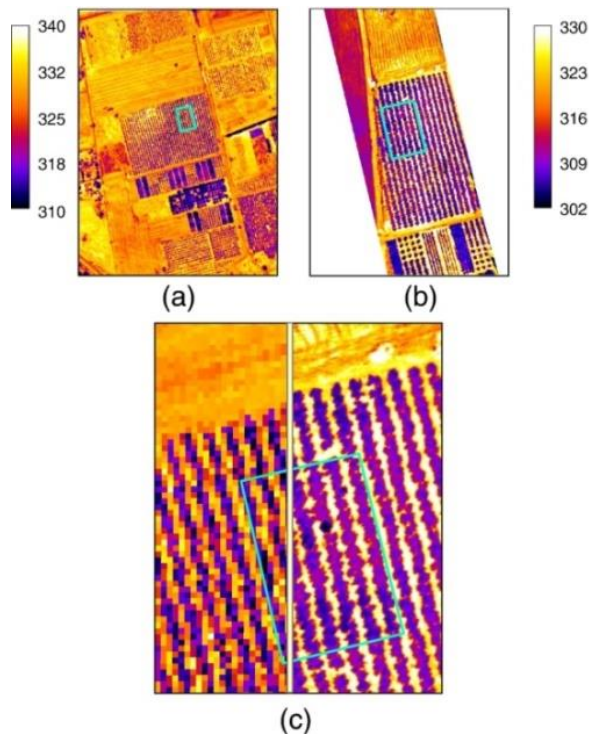

Figure 4. Airborne thermal imagery acquired over the study site: a) AHS image collected at 12:30GMT on 16 July 2005; b) UAV image collected at 13:30 GMT on 23 August 2007; c) image detail showing the spatial resolution differences of AHS (2 m) against the UAV (40 cm). The spatial resolution of the UAV imagery shows individual tree crown, enabling pure crown temperature extraction. Data from (J. Berni et al., 2009).

All of the above platforms can be used to obtain information on soil, climate, and, above all, crops. Naturally, crop information is of greater interest as it allows the direct investigation of the health status of the olive tree (Zipori et al., 2020), in order to make the correct site-specific applications. The method involves the acquisition of different types of images such as multispectral, hyperspectral, and thermal images. From their processing, using GIS and photogrammetry software, it is possible to obtain the different information. Generally, there is also the need to carry out direct measurements in the field in order to better calibrate the final information by making it quantitative. In this way, it is possible to obtain thematic maps that are used to construct the prescription maps that represent the basis for carrying out site-specific management (Fountas et al., 2011; López-Granados et al., 2004; Peña-Barragán et al., 2004). How the different platforms have been applied in precision oliviculture is discussed below.

1.3.2. Satellite

Satellites have been used in agriculture since the early 1970s when the Landsat 1 platform (in orbit since 1972), equipped with a multispectral sensor, became operational. However, the first applications in olive cultivation have been carried out since the 2000s for the identification of different optical and reflectance properties of the crop. Today, several satellite platforms are available and are constantly evolving due to the launch of new satellites by government space agencies and private companies. Indeed, the availability of images has increased over the years and is now very wide. Thus, the range of sensors available on the different platforms has also increased, ranging from multispectral sensors to hyperspectral and thermal sensors. Therefore, given the high availability and types of images that are acquired by satellite, these platforms are increasingly used for different precision farming applications. Unfortunately, images may be available for a fee or free of charge, and often a high image cost is associated with a high spatial resolution.

Satellites are classified according to their spatial resolution capability (Giovos et al., 2021) (Table 2), high definition ones include RapidEye, which acquires images in 5 multispectral bands, with a resolution of 5 metres, first launched into orbit in 1996 and developed by a European project, since it has been active it has been used in many agriculture and forestry studies (Stoll et al., 2012). Another satellite with medium to high spatial resolution is Landsat 8 OLI (Operational Land Imager) which has provided excellent results, it consists of nine spectral bands with a spatial resolution of 30 m for the bands operating on visible light, it also consists of bands operating in the shortwave infrared. While a band has been implemented that reduces the disturbance caused by clouds. With the Landsat system, progress was made in terms of image resolution, however, high-resolution satellite systems such as IKONOS and Quickbird were later devised, the former providing panchromatic (PAN) images with a resolution of 0.80 m, the latter

launched in October 2001 provided images with a higher resolution than IKONOS (Yang, 2018). Another satellite is Planet, which provides a high-resolution, continuous, and comprehensive view of agronomic field conditions (Cheng et al., 2020). GeoEye-1 launched in 2008 and WorldView-3 launched in 2014, are very high-resolution commercial satellites, for example WorldView-3 has 29 spectral bands and an average revisit time of less than 1 day. The MODIS satellite acquires data in 36 spectral bands with wavelengths from 0.4 μm to 14.4 μm and varying spatial resolutions, two bands at 250 m, five bands at 500 m and 29 bands at 1 km.

Table. 2 Representation of satellites used for monitoring.

Satellite	Temporal Cover Age	Spectral Bands	Ground Sample Distance (GSD)	Global revisit time
RapidEye AG	1996 - 2020	VIS-NIR	6.5 m	5.5 days
IKONOS	1999–2015	PAN-VIS-NIR	0.8 m PAN 3.6 m multispectral	3 days MS 12 days PAN
Terra satellite (EOS AM-1): (MODIS)	1999 –present	VIS-NIR	250–500 m	2 days
Terra satellite (EOS AM-1): (ASTER)	1999 –present	VIS-NIR	15 m	4–16 days
Quickbird	2001–2015	PAN-VIS-NIR	0.6 m PAN 2.5 m multispectral	3 days
TerraSAR-X	2007–present	X-band SAR	3 m	3 days
WorldView-2	2009–present	PAN-VIS-NIR	0.46 m PAN 1.84 m multispectral	1 day
Planet	2009 - present	VIS-NIR	3.7 m	1 day
WorldView-3	2014–present	PAN-VIS-NIR	0.31 m PAN 1.24 m multispectral	1 day
Sentinel-2	2015–present	VIS-NIR	10 – 30 m	5 days

The satellite provides large scale global dynamics measurements of the entire earth's surface, minimising the effect of cloud disturbance. One of the most widely used satellites in PA is the Sentinel-2 this satellite is capable of sampling 13 spectral bands up to a resolution of 10m. The main advantage of Sentinel-2 over other satellites is that the data are open-source (Varghese et al., 2021). The use of data derived from satellite platforms is very wide, examples include studies to identify vineyards growing in large regions or areas (Zhao et al., 2019), monitor olive variability. Landsat and MODIS satellites are often used to monitor evapotranspiration processes and in general are useful for detecting water status. Another satellite that is being used to conduct vineyard water stress prediction surveys is the Advanced Spaceborne Thermal Emission and Reflection Radiometer (ASTER) satellite (Alkassem et al., 2022). Consisting of 15 bands with 15 m resolution, it is suitable for measuring soil properties, soil temperatures (Silvero et al., 2020). Another satellite system used to evaluate soil moisture content is TerraSAR-X, which is equipped with a synthetic aperture radar (SAR)

24

antenna that provides high-quality radar images (Tang et al., 2020)). Finally, the use of satellite systems is also important for monitoring soil erosion phenomena (Baiamonte et al., 2019). The use of satellite information is increasingly in demand, to date, petabyte-scale remote sensing data archives can be accessed free of charge through government agencies (NASA; NOAA; Copernicus) (Loveland and Dwyer, 2012), which provide geospatial data processing tools.

The main limitation of these technologies relates to spatial resolution and the need to obtain images with good radiometric correction to obtain more accurate data. In general, thermal images have low spatial resolutions. For example, Landsat 7 and 8 have spatial resolutions in the order of 60 and 100 m, respectively.

Satellite remote sensing techniques can be used for different purposes. In precision oliviculture, they can be used with the aim of better managing the main cultivation techniques such as: precision irrigation, description of biophysical parameters (Gómez et al., 2011; Solano et al., 2019) and for precision fertilization. High-resolution images are needed for the identification and description of biophysical and structural parameters of olive trees. Indeed, the results obtained from satellite platforms have resolutions that are hardly comparable to those obtained from proximal acquisition platforms or UAVs (Zhang and Kovacs, 2012). In the study by Gómez et al., (2011), using images from the CASI satellite with a spatial resolution of 1 m and an algorithm developed by (Pouliot et al., 2002), the authors managed to obtain correlations of 0.82 and 0.87 with very high significance and an RMSE of 4.8 m^2 and 8.4 m^3, for canopy size (m^2) and volume (m^3), respectively. However, using other satellite platforms, such as QuickBird, no acceptable results were obtained.

Precision irrigation of olive trees using satellite imagery can be skilfully applied through the calculation of water-sensitive VIs and thermography. The main limitation of thermography is the possibility to obtain images with high spatial resolution, which are able to derive the pure temperature of the canopy, minimizing the effect of the soil (Fernández, 2017; Ha et al., 2013).

From satellite, given the wide availability of multispectral sensors with the main VIS, NIR, and SWIR bands, it is possible to calculate the different vegetation indices in order to carry out precision fertilization. Unfortunately, in the literature there were not many studies highlighting the application of this practice on the olive grove. Yet, fertilization represents an extremely important practice for the determination and maximization of production quality and quantity (Fernández-Escobar et al., 2006; Tognetti et al., 2006). Precision fertilization is carried out on the basis of satellite, soil, climate, and crop data. It allows the differentiated distribution of different fertilizers (variable rate application, VRA) according to actual needs. An application study concerning precision fertilization in the olive grove using satellite information was conducted by (Noori and Panda, 2016). Using images from the ALOS-Avnir-2 satellite of the Japanese Aerospace Exploration Agency (JAXA), they managed to obtain several correlation algorithms that could be used for the creation of variable rate fertilization (VRF) maps. Unfortunately, these algorithms need to be tested for complete reliability

before they can be applied in other areas. In this study, in addition to multispectral data, information on soil, structural, and cultural properties was acquired. The multispectral data were acquired with the classic acquisition bands such as B, G, R, and IR, in order to calculate the three most widely used vegetation indices in the literature: normalized difference vegetation index (NDVI) and the soil adjusted vegetation index (SAVI).

1.3.3. Aircraft

Airborne missions for classical precision farming applications have not been very successful, as they are overpriced and often linked to private agencies. However, they have a better resolution of the final image than satellite platforms and can cover large areas. In precision oliviculture, the applications coming from this type of acquisition have been little used and concern only precision irrigation. In fact, good results have been obtained from airborne campaigns with high spatial resolution regarding the investigation of water status (J. Berni et al., 2009; Sepulcre-Cantó et al., 2005; Guadalupe Sepulcre-Cantó et al., 2006a; Sepulcre-Cantó et al., 2007). In Sepulcre-Cantó et al., (2005), the aerial campaign was conducted with the airborne hyperspectral scanner (AHS) (Daedalus Enterprise Inc., USA). The AHS has a sensor that allows it to acquire 80 spectral bands between 430 and 12,500 nm. In this work, they were able to achieve a spatial resolution of 2.5 m. Three different flights were also carried out at different times of the day. Using this platform, they were able to faithfully describe the variability of the water status of olive trees. The relationships found for individual trees between the estimated and calculated temperature on the ground resulted in the following correlation indices: $r^2 = 0.81$; $r^2 = 0.52$, and $r^2 = 0.56$, respectively, for the three flights performed. Sepulcre-Cantó et al., (2006) also demonstrated that high spatial resolution AHS images enabled the study of spatial and temporal thermal effects caused by water stress. In Sepulcre-Cantó et al., (2007), using the same sensor, they were able to monitor yield and fruit quality parameters. This time, the spatial resolution obtained was 2 m with the same bands. In this study, the quality parameter was related to the water content of the olive with respect to the different water conditions of the plants under different irrigation strategies. These results suggest that high-resolution thermal remote sensing is a potential indicator of yield and some fruit quality parameters under different irrigation regimes. Indeed, Tc-Ta maps could be used to assess the level of water deficits in orchards and to predict its impact on yield and fruit quality.

Unfortunately, no article has been found in the literature attempting to apply spectral data from such a platform in order to apply other variable rate cultivation practices such as fertilization. However, the good results that have been found in the previously mentioned works on precision irrigation give hope for an implementation of the use of this acquisition platform.

1.3.4. Unmanned Aerial Vehicles (UAV)

In the last decade, to overcome some limitations related to the use of satellites and aircraft such as low versatility and reduced spatial resolution also called UAVs (Unmanned Aerial Vehicle) or UAS (Unmanned Aerial System) or more commonly Drones. These platforms have numerous advantages thanks to the wide operational flexibility. In fact, they can be equipped with different types of sensors making these platforms suitable for a multitude of surveys. Their most evident benefits are associated with the speed of data acquisition, the ability to fly below 120 m which allows to obtain a high geometric resolution and consequently very detailed information. The recent innovations of these platforms have significantly reduced the costs of purchase and use. Furthermore, the temporal resolution allows the surveys to be carried out at certain times linked to the agronomic conditions, however this advantage can be thwarted by the meteorological conditions. UAVs face some technical limitations, such as battery efficiency, communication distance and payload. There are different models on the market that can be classified according to the flight mode adopted (Figure5).
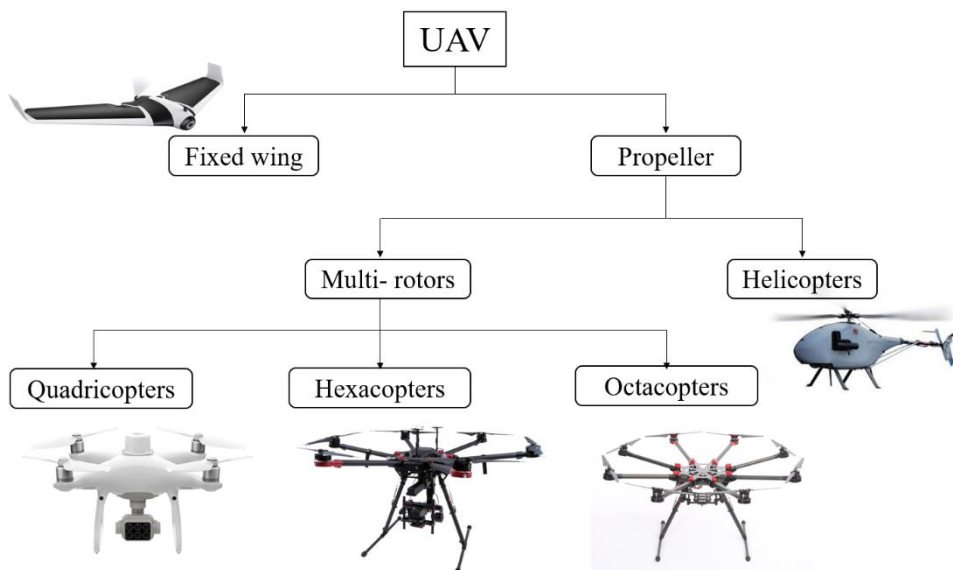

Figure 5. Classification of the several UAVs used in agriculture.

In this case we distinguish two macro categories, namely fixed wing and propeller. Fixed-wing UAVs take advantage of aerodynamic thrust and lift and are mainly used for spraying and photography over a wide range in a homogeneous orographically area. The macro category of rotary wing UAVs can be divided into helicopters and multirotors. The helicopter type features a large propeller on top of the aircraft. While, multirotor models are characterized by multiple rotors that allow them to move. Depending on the different number of

rotors, they are divided into: quadricopters, hexacopters and octacopters. These categories of drones are mostly used in Italy due to their versatility of use in fragmented areas and with irregular orography. This is due to a vertical take-off and landing mode and a facilitated altitude variation according to the terrain profile.

Regardless of the type of drone, it is necessary to know how the different flight variables can influence the final acquisition of the data and the entire processing process. The flight variables that can be modified by the operator include: flight altitude, forward speed, type of flight (manual or automatic), flight direction, gimbal inclination, frontal and lateral overlay of images, the aperture and closure of the lens, and the focal length. While the most important environmental variables include: wind speed and light conditions.

UAV platforms are the most successful spatial data acquisition platform in precision olive growing. They can be controlled from a visual distance by a pilot on the ground or fly autonomously to a user-defined set of waypoints, using a complex system of flight control sensors (gyroscopes, magnetic compass, GPS, pressure sensor, and triaxial accelerometers) controlled by a microprocessor. UAVs can be equipped with a variety of sensors, allowing a wide range of monitoring tasks to be performed. The particularity of the UAV application in remote sensing is its high spatial resolution (centimetres) and timeliness, due to reduced planning times. These features make it ideal in SHI or OT olive cultivation characterized by highly fragmented and heterogeneous areas. In fact, by adopting a common UAV it is possible to use different types of chambers and obtain very detailed information of the field conditions. For this reason, most of the scientific articles related to biomass quantification and characterization of olive tree canopy architecture have focused on the use of UAVs, also in view of future implementations of olive tree growth models that need high spatial resolution information (Moriondo et al., 2019; Stateras and Kalivas, 2020). Furthermore, such platforms can be used in some countries for direct field distribution of some inputs, such as plant protection products (Martinez-Guanter et al., 2020).

The use of UAV platforms in precision oliviculture has focused on the possibility of acquiring spectral reflectance images, thermal images, and RGB images for photogrammetric processing. The high spatial resolution of the images obtained can be attributed solely to the lower flight height compared to other platforms (Jurado et al., 2020). This high resolution makes it possible to better discriminate between different disturbing elements, such as bare soil, and to obtain pure crop pixels. The main applications of UAV in olive cultivation concern photogrammetry for the spatial reconstruction of the canopy (Díaz-Varela et al., 2015; Zarco-Tejada et al., 2014b) and its use in thermography to serve irrigation (Ben-Gal et al., 2009; J. Berni et al., 2009). The limitations of this technology are related to cost, technical training and weather conditions. UAV has been widely used recently for 3D reconstruction of olive tree structure, mainly using SfM techniques (Anifantis et al., 2019; Caruso et al., 2019; Díaz-Varela et al., 2015;

Küng et al., 2011; Zarco-Tejada et al., 2014b). An aspect of primary importance in the use of UAVs concerns the possibility of being able to find the right compromise between surface to be investigated, final resolution, and processing procedure (Torres-Sánchez et al., 2015a; Zarco-Tejada et al., 2014b). Zarco-Tejada et al., (2014b) obtained an $r^2 = 0.83$ and an overall root mean square error (RMSE) of approximately 35 cm among the canopy structural parameters measured using SfM, highlighting the importance of maintaining a pixel spatial resolution of at least 30 cm at the time of acquisition. Furthermore, compared to other platforms, it is possible to associate the geometric characteristics of the canopy with spectral information.

In addition to canopy investigation, literature has focused on the use of drones to collect thermographic information to serve precision irrigation (Ben-Gal et al., 2009; J. Berni et al., 2009; Egea et al., 2017; Rallo et al., 2014). While on other crops the possibility of acquiring multispectral images to carry out precision fertilization is a well-established practice, in the olive tree, there are not many studies about it. In fact, the application of drones in precision oliviculture in order to obtain spectral information and to carry out variable rate fertilization has not been investigated. However, much research points out that precision fertilization in the olive grove can also be conducted by the creation of prescription maps starting from soil element content measurements and obtain savings of up to 30% of fertilizer (Fountas et al., 2011; López-Granados et al., 2004; Van Evert et al., 2017).

1.3.5. Proximal sensing

Proximal sensing is a data acquisition system that exploits different technologies that are in proximity to or directly in contact with the target surface (land surface or plant). The main feature of proximal sensing is the high accuracy of the data compared to remote sensing but generally lower than in the laboratory. Another important feature of this system is that the sensors can be used either on-line or off-line. In-line sensors are generally used to directly perform operations in the field while off-line sensors need to be processed in order to be used (Pallottino et al., 2019). The advantages of proximal sensors advantages are their high-resolution imagery; their independence from external parameters; their suitability for small fields; and their simple application (i.e., mounting the sensor on the tractor). A very important factor to consider is the different sources of information that can be generated compared to remote sensing due to the different sensor-object position. The limitations of proximal sensing are due to its high cost and its low capacity to acquire data that are able to describe the entire variability present in the plot. In fact, they are often point data, which have to be spatialized in order to refer to the whole area (Zhang et al., 2002). The ground platforms used for proximal sensing can be grouped into three categories: portable, self-supporting in the field, and mounted on tractors or agricultural machinery or

UGVs (Sishodia et al., 2020). The development of UGVs is likely to greatly simplify crop operations that are carried out manually such as weed control, harvesting, etc. Regarding the use of UGVs in precision oliviculture, there have been no scientific applications in the literature yet, although the progress made in other sectors bodes well for their future application in olive cultivation (Saiz-Rubio et al., 2021).

Among the most interesting applications of proximal sensing with a direct effect on precision olive growing are LiDAR (Martínez-Casasnovas et al., 2017; Miranda-Fuentes et al., 2015) and ultrasonic sensors (Gamarra-Diezma et al., 2015). The latter have found practical use on the distribution of plant protection products. Solanelles and Planas, (2005) created an ultrasonic prototype that allowed the automatic calibration of plant protection products, based on the architecture of the canopy.

Among the proximal sensors are those involved in monitoring olive yield. (Alcalá Jiménez and Álamo Romero, 1998) initiated precision farming applied to olive groves, through the simple application of GPS sensors to map the production of olive trees. In fact, the production map represents one of the main sources of information for the creation of the correct fertilization map (Agüera-Vega et al., 2013; Castillo-Ruiz et al., 2015). Álamo et al., (2012) was able to determine area production (20–30 trees per area) simply by weighing production. In other fields, such as precision viticulture, several on-the-go methods already exist that can map plant production. The idea would be to be able to transfer this type of technology to precision olive growing as well, in order to obtain data on the productivity of individual trees, as this is one of the most important pieces of basic information. There are also other portable instruments that allow, for example, the calculation of chlorophyll content or the spectral response of the olive tree, directly in the field. However, they have not been well investigated for use in precision oliviculture.

Overall, precision olive cultivation has good possibilities to be developed under different climatic and agronomic conditions. As can be seen from this introduction, the main technologies used to investigate olive trees have been remote platforms equipped with different types of sensors. However, proximal platforms are also becoming more interesting from a scientific point of view and for various practical applications.

However, what has been illustrated so far in this section has focused on the application of different technologies or methodologies that can be applied without considering different factors. In fact, soil, climate and plants are interconnected and the management of each can change the behaviour of the others.

AIM OF THE RESEARCH

The main objective of this PhD thesis was the application of precision agriculture (PA) and smart farming (SF) in a typical orchard agroecosystem in the Mediterranean environment such as the olive tree (*Olea europea* var. *europea*). The experiment provided an agronomic decision support system (DSS) for the management of inter- and intra-plot variability. For this purpose, acquisition technologies and also data analysis methodologies were evaluated. Specifically, this thesis evaluated the proximal and remote sensing technologies equipped with RGB, multispectral, hyperspectral and thermal sensors. The main remote sensing applications focused on the study of UAV platforms, while proximal platforms involved the use of spectroradiometers and a handheld system. The UAV platform was used to understand the effect of the altitudes and flight paths in the final photogrammetric reconstruction in dense or sparse canopy conditions. Moreover, the multispectral images, the Orthomosaic and the Digital Elevation Model were processed to develop a GEOBIA (Geographic Object-Based Image Analysis) methodology to determine the vegetative, biometric and spectral crops condition in several GIS (Geographic Information System) software and scales of detail. The spectroradiometer was used to evaluate the spectral survey of the canopy from different viewpoints. During the research period abroad, an intelligent handheld system was evaluated in an olive orchard with different irrigation schedules. The accuracy of the GNSS positioning system, the different NDVI conditions of the canopy and the water stress conditions were evaluated. The water stress conditions were evaluated by calculating the CWSI empirically and analytically.

2. MATERIALS AND METHODS

2.1. Study area

The study area is located in Calatafimi Segesta (Trapani, Italy) with coordinates in the centroid of Lat 37°51'48.21 "N; Long 12°57'15.17 "E (Figure 6).
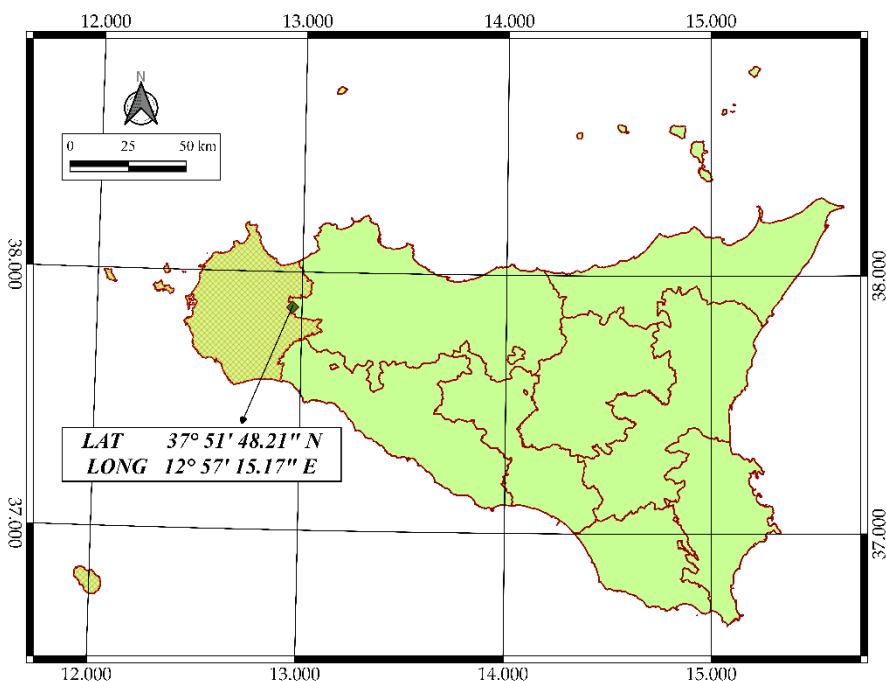

Figure 6. Experimental site location on a scale of 1: 1,500,000. Maps Data: Google ©2021, QGIS.

According to the Koppen–Geiger's classification, the climate of the area is classified as Mediterranean hot summer climates (Kottek et al., 2006). Climatic data was recorded from 2020 to 2022 in a weather station of the Sicilian Agrometeorological Information Service (SIAS) daily. The data collected were: average temperature, minimum temperature, maximum temperature, rain, potential evapotranspiration, average relative humidity.

The soil moisture regime is xeric, bordering with aridic, and the temperature regime is thermic. According to the United States Department of Agriculture (USDA) classification, the soil belongs to the Sandy-Clay-Loam granulometric class (Figure 7). The field has a perimeter of 344m and the surface area covers 5860 m^2, with a flat surface topography. The soil presents a low percentage of coarse fragments on most of the surface.
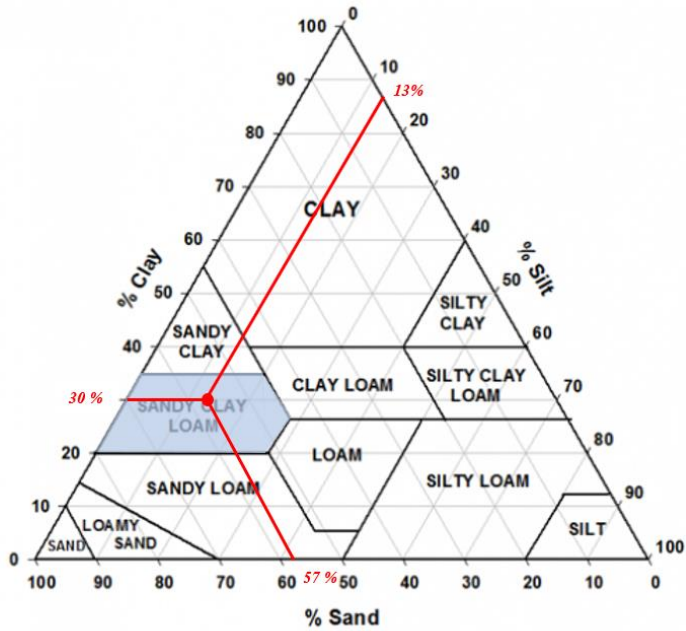
Figure 7. Granulometric class of the experimentation area.

The experiment was conducted between 2020 and 2022 in a 20-year-old olive grove cultivated according to ordinary management practices without irrigation system. The olive trees were planted in 2002 with single cultivar typical of the area, the cv. Cerasuola. During the experimentation period, the olive orchard was in full productivity. The olive orchard is cultivated with a traditional training system and a plant layout is 5 x 5,5 m; the direction of the rows is NE-SW at an angle of 60° to the North (Figure 8). The total number of trees considered in the tests was 211 however 24 of which were used for some particular multispectral and hyperspectral acquisition data.

Figure 8. Training system and plant layout.

2.2. Sampling and Surveys

In 2020, the first surveys were carried out, aimed at exploring the variability present in the field from a cultural and pedological point of view. Plot perimeter and plants were georeferenced on DOY (day of years) 161 using the instrument Stonex S7-G (S7-G, Stonex, New York USA) with differential RTK (Real Time Kinematic) correction. On DOY 163 the trunk cross section area (TCSA) at 0.50 m from the ground trying to exclude any hyperplasic nodes typical of the olive tree was measured (Noori and Panda, 2016). Field samplings were carried out in order to investigate soil and crop nutritional status variability using a regular 15m x 11m grid in both cases. The sampling point was identified at the intersection point (node) of the sampling grid, excluding the external part of the field. A total number of 36 points was sampled (Figure 9).
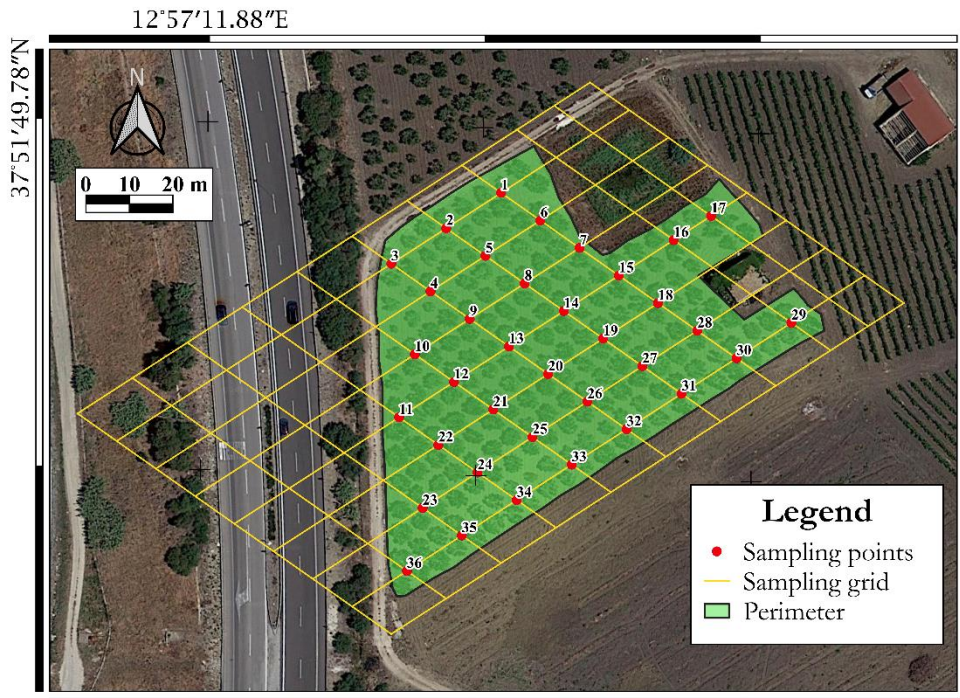
Figure 9: Sampling grid and sampling points used for characterization of the nutritional and soil condition.

Soil samples were taken at each intersection point of the grid; thus, the leaf sampling was represented by an experimental unit of four adjacent olive trees (Figure 10). Soil sampling was carried out on DOY 168 at a depth of 10-30 cm using an Edelman auger. Leaf sampling was carried out on DOY 205 (López-Granados et al., 2004). Each leaf sample consisted of four sub-samples of 25 healthy, fully expanded and mature leaves collected from the central portion of current season branches not shaded approximately 1.5 m above the soil surface, at the four cardinal points from each olive tree (Figure 10).
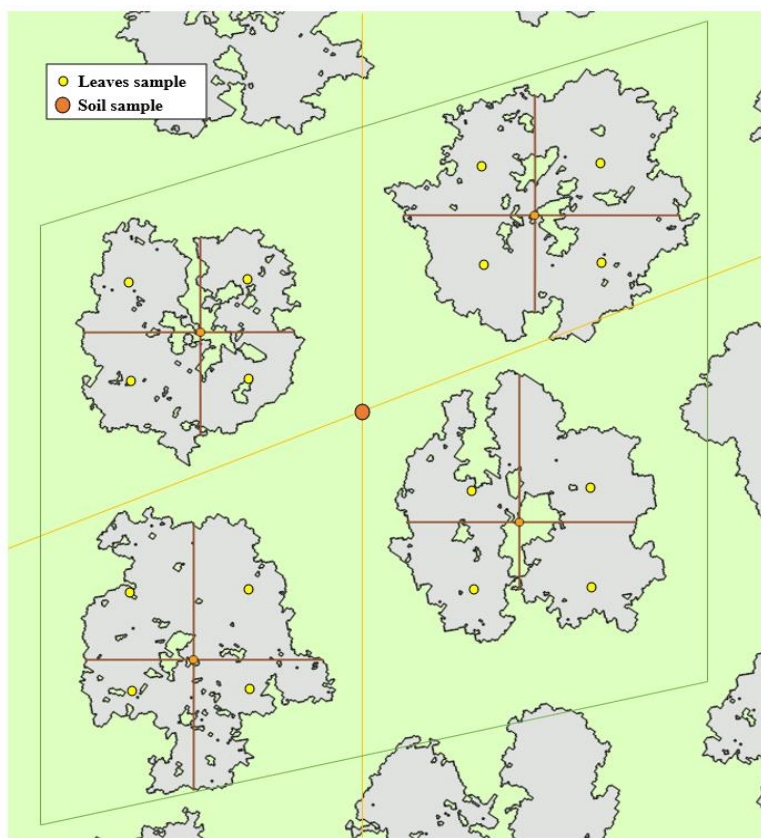
Figure 10. Leaves sample location in each single tree.

To determine the production map per plant in the year 2020, individual productions were quantified (Figure 11ab). In contrast, in the year 2021, no production was recorded as a result of intensive pruning. In the year 2022, production was only quantified for 20 selected plants in the two canopy portions facing north and south. In both season the olives were harvested when their maturity index was equal to 2.38 determined according to (Furferi et al., 2010) on DsOY 303-306 and 342 respectively. A team of four operators was employed to harvest the olives. Two of them used the hand-held electric harvester model OLIVION P230 (Pellenc, France).

(a)   (b)
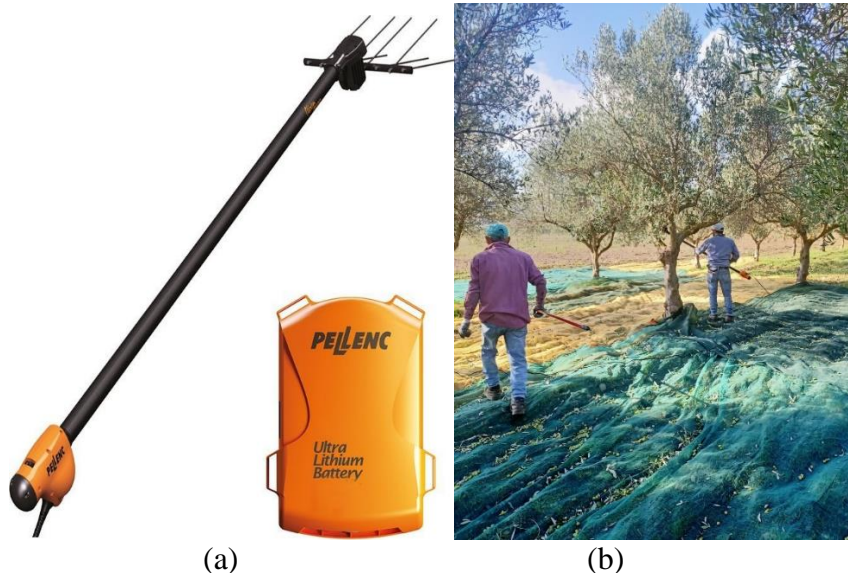
Figure 11. (**a**) hand-held electric harvester model OLIVION P230; (**b**) harvest team organization

The other two operators had the task of laying and wrapping the nets under each plant and quantify the harvested fruits for each plant and the average mass of the drupes in the field using two digital balances (Shimadzu ATY324R, Milan, Italy; Figure 12ab).
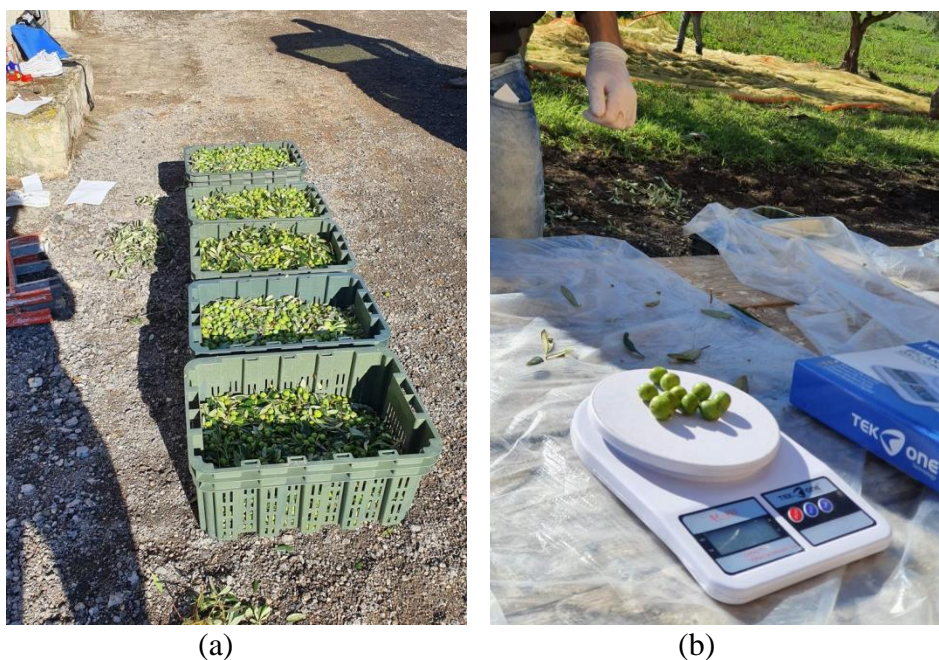

(a)   (b)

Figure 12. (**a**) Olives after harvest; (**b**) weighing the ten drupes for tree.

For each tree was countified the average weight of ten drupes. Furthermore, one hundred healthy drupes (25 drupes per tree) were sampled from four trees used to collect leaf samples.

2.3. Laboratory Analysis

Laboratory analyses were carried out at the Soil Chemistry laboratory of the Department of Agricultural, Food and Forest Sciences of the University of Palermo. After sampling, the leaves were dried at 70°C for 24 hours and milled to pass through a 0.25 mm mesh (Figure 13) thus the soil samples were ground and sieved at < 2 mm after the air drying.

Figure 13. Leaves dry process in stove.

2.3.1. Soil analysis

Soil samples were analyzed to determine texture, reaction, electrical conductivity (EC), total carbonates (TC), organic carbon (TOC) and total N (TN). Soil texture (sand, 2–0.02 mm; silt, 0.02–0.002 mm; clay, <0.002 mm) was determined by the standard methodology (Gee and Or, 2002, Figure 14ab).

(a)   (b)
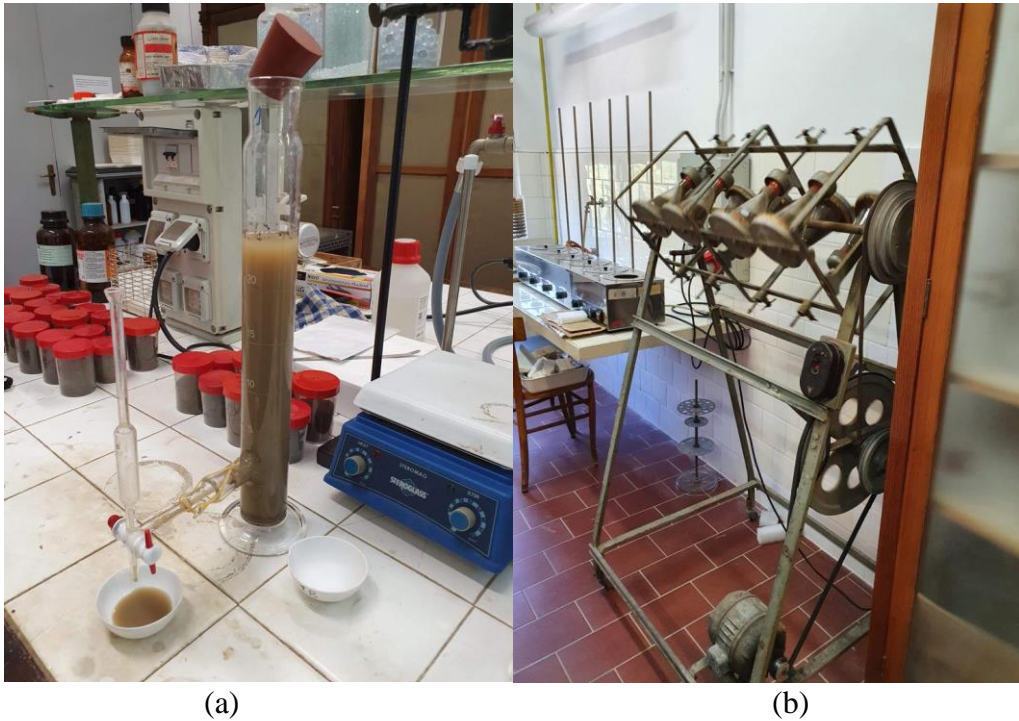
Figure 14. Texture analysis process: (**a**) sedimentation step; (**b**) shake step.

The methodology was as follows: 10g of sample was weighed and put into 300ml Erlenmeyer flasks. Then the flasks were filled with H20d until a volume of 200ml was reached. Using the double-stroke pipette, 10ml of clay dispersant was put in. At this point, the samples were shaken for 2 hours with a solution containing sodium hexametaphosphate and sodium carbonate. Once the shaking was complete, the contents of the flasks were poured into the sedimenters with a three-way tap. Naturally, the flasks were well cleaned with H2O$_d$. The sedimenters were brought to a volume of 500ml, shaken for 60 sec and left to stand with the cap open for 20 hours. The following day, after weighing the capsules, the first sample was taken. The second sampling was carried out after the settler had been shaken again for 60 sec and left for a further 12 minutes. Samples were taken by placing the withdrawn liquid into small bowls previously weighed with an electronic balance to four decimal places. The small bowls were placed in a water bath and then in an oven at 105°C and finally in a desiccator so that the samples could be weighed. Once the different samples were weighed, the percentages of the three particle size classes; clay, silt and sand, were determined by weight difference as represented in the follow equations 5, 6 and 7:

$$\% \ Clay = \frac{(W_c - 0.01) * 500ml}{10 * 10} * 100 \qquad (5)$$

$$\% \ Silt = \frac{(W_{c+s} - W_c) * 500ml}{10 * 10} * 100 \qquad (6)$$

$$\% \, Sand = 1 - (\% \, clay + \% \, slit) \qquad (7)$$

Where W_c is the weight of clay portion weighted from the capsules; W_{s+c} is the weight of clay plus slit portion weighted from the capsules.

Soil reaction was measured in distilled water using a soil/solution ratio of 1:2.5 (w/v) and a glass membrane electrode, whereas soil EC was measured in distilled water using a soil/distilled water ratio of 1:5 (w/v). The various steps were carried out with the same sample preparation. In fact, 20g of sample was taken and diluted 1:2.5 or 1:5, with 100ml of H20d then shaken for 2 hours in a horizontal position, respectively for pH and EC. At the end of shaking, the samples were filtered through funnels with Vatnan Filter Paper. The filtrate was accumulated in 300ml falcons. Any samples that showed a slight sediment were centrifuged at 1000 rpm for 5 minutes. Once the filtrate was obtained, it was used for the determination of pH and C.E. The pH measurement was done using the Metter Toledo, rinsing the probe with H2Od between the samples. The C.E. measurement was carried out with the HANNA (in $\mu S*cm{-}1$), again washing the probe with H20d between the samples.

Soil Total Organic Carbon and TN were determined on pulverised soil samples by the Walkley-Black dichromate oxidation method and the Kjeldahl method, respectively. The determination of TOC was carried out by performing two different desiccations. 5g of soil was taken and dried for 24 hours at 105°C in order to remove all residual moisture present. They were then cooled and weighed. Finally, they were further dried in a muffle furnace at 400°C for 16 hours. After cooling in the desiccator, they were weighed. The second drying process determined the complete degradation of the organic substances, as a result, the average organic matter (OM) content of the different samples was determined by a simple weight ratio. (Equation 8) Finally, the TOC was determined from the OM using the follow equation 9.

$$Organic \, Matter \, (OM) = \frac{W_{105°} - W_{400°}}{W_{105°}} * 100 \qquad (8)$$

$$TOC = OM * 0.58 \qquad (9)$$

Where $W_{105°}$ is the weight of the soil after the dry at 105°C; $W_{400°}$ is the weight of the soil after the dry at 400°C.

The determination of the N concentration in the soil (Total Nitrogen, TN) was carried out using the Kjeldahl method according to the equation 10. This, was carried out by taking 2g of soil, 10ml of sulphuric acid (H2SO4) and 0.5g of copper oxide (CuO) and placed to mineralise. Next, distillation was carried out and finally, titration with sodium oxide (NaOH).

$$TN \ (g * kg^{-1}) = \frac{H_2SO_4 * 0.1 * 14.007}{W_{sa}} \qquad (10)$$

Where W_{sa} is the weight of the samples; H_2SO_4 (ml); normality of H_2SO_4; 14.007 is the molecular weight of N.

Finally, the content of TC was determined by the gas-volumetric method using the Dietrich–Fruehling calcimeter (Williams, 1949) and according to the equation 11.

$$TC \ (\%) = \frac{Vol \ CO_{2 \ (soil)} * 0.3}{Vol \ CO_{2 \ (CaCO_3)}} \qquad (11)$$

Precisely, 1 g sample and 0.3 g pure CaCO3 were weighed for the determination of the percentage content of calcium carbonate. A 1:1 mixture of HCl with H20d was prepared. By adding 300ml of H_2Od and then the same amount of HCl (37% concentration). Once the samples were weighed and prepared, 10ml of the HCl solution was taken and poured into the bottle containing the sample. Based on the reaction between acid and HCl, a volume of CO_2 was obtained based on the amount of calcium carbonate reacting with the acid. A simple equation was used to derive the percentage concentration of CaCO3 for the different samples.

2.3.2. *Fogliar and Drupes analysis*

Foliar analysis of the main macro- and micro-elements was carried out to determine the nutritional and health conditions of the plants. Leaf samples were analysed to determine the total content of the following elements: N, K, Ca, Fe, Mn, Mg, B, Zn, Na, Cu. All elements, except for N, were determined by microwave plasma atomic emission spectrometer (MP-AES 4210, Agilent Technologies, California, United States) after leaf digestion with concentrated nitric acid and hydrogen peroxide. Nitrogen content in leaf and drupes samples was determined by the Kjeldahl method. To determine the concentrations of the aforementioned metals, approximately 0.250g was weighed in the electronic balance to four decimal places, then placed in Teflon tubes with 3ml of supra-grade nitric acid and 2ml of hydrogen peroxide (H_2O_2). The resulting sample was placed in a microwave oven for 50 minutes at 210°C and then left to cool. The mineralisation was recovered with millipor water in the falcon and brought to a level of 10ml. Finally, they were diluted 1:100 and analysed in ICP-MS.

The Kjeldahl method was performed by weighing 0.500g of leaf samples in the electronic balance to four decimal places. Mineralisation of the samples is carried out for about 3 hours by inputting 15 ml sulphuric acid (H_2SO_4) and 0.5g copper oxide (CuO). Once the compound is mineralised, distillation is carried out. Finally, by a simple titration with soda ash (NaOH), the N concentrations were obtained.

In order to determine the amount of nitrogen removed from the harvest, it was necessary to quantify the dry matter present in the drupes and its nitrogen content. After taking a random sample from the production, the fruits were washed and subsequently, dried at 80° C for 48 hours and finally weighed. Nitrogen determination was carried out using the previously described Kjeldahl method.

2.4   Nitrogen balance and prescription map realization

During the year 2020, foliar sampling was carried out for the detection of nutritional deficiencies. Subsequently it was possible to create a fertilization map using two different methods as described below. The general nutritional status of the trees was evaluated by determining the nutrient concentration of the leaves. The threshold method of leaf nutrient concentration was used to determine the percentage of the plot area showing deficiency of a given nutrient. The threshold value represents the concentration limit of a nutrient that defines the correct nutritional status of the olive tree. In our study, among the different nutrients, only N had a concentration below the threshold, therefore we focused only on N to draw up the fertilization plan. The threshold value used was N≥1.2% as reported in Fernández-Escobar et al., (2012). In addition, using the above threshold to determine the area in need of fertilization, another method was used for the constitution of the prescription map. This method involved dividing the area that needed fertilization into different sub-areas. The sub-areas were identified starting from the soil, production data, spectral and the vegetative parameters of the crop. These parameters, through kriging and co-kriging algorithms, were processed to determine the areas MZ. The vegetative, productive and spectral parameters were crossed by carrying out the multivariate analysis for the determination of the MZ zones. Specifically, NDVI, production, CA, CV and Hc were used. Once the different MZs had been determined, it was possible to trace the quantity of fertilizer to be distributed per area by means of a simple relationship between the maximum and minimum doses used in the area. The minimum dose was distributed in the less productive areas while the maximum dose was distributed in the more productive areas. In this way, it was possible to improve the prescription map obtained with the sole use of the threshold.

The balance of N (NB) created by (Fernández-Escobar et al., (2012) makes it possible to consider all the contributions and losses that may exist in a specific olive grove, to determine the correct quantity to apply. In this balance, in addition to the natural or external contributions that arrive through agronomic practices, there are various output parameters. Among these outputs we find the nitrogen losses that occur due to pruning and harvesting. The budget also includes other parameters such as possible losses to be entered such as: N lost by leaching; lost by ammonia volatilization; immobilized into organic matter; lost by erosion; lost by denitrification and fixed in clays. By applying the equation 12 it is possible to quantify the actual quantities removed by these two operations. Therefore, the

calculation of the amount of nitrogen removed in the third year was set taking into account the amount of nitrogen removed from fruit (Nf) and pruning (Nv).

$$N_r = [(Y * N_f) + (P * N_v)] \qquad (12)$$

where Nr is the amount of Nitrogen removed per plant (g plant[-1]), Y is the yield (kg plant[-1]), Nf is the nitrogen concentration in the fresh drupes (g kg^{-1}), P is the pruning biomass to each plant (kg plant-1), Nv is the amount of nitrogen removed by pruning residues per kg (g kg^{-1}).

N removal due to olive cultivation is the sum of N removed by drupes harvesting and pruning. N removed by drupes was obtained by multiplying the amount of N content of the drupes per amount of the olive harvested. The N removed by drupes was originated from the amount of product and its nitrogen concentration. This concentration was derived from the average amount of N contained in the fresh fruits, and was found to be 2.65 g kg-1 of N. This value was similar to that reported by other studies, such as in (Fernández-Escobar et al., 2015, 2012). The production per plant was determined from the yield map (Blackmore, 2003). The yield map was obtained in the third years using a multivariate analysis using the main vegetation parameters such as CA, CV, Hc, NDVI and the production data for the 20 selected plants. The quantity P * Nv was calculated starting from the values of volumes removed by pruning. From the processing of the UAV images, it was possible to calculate the volumes removed per plant. Subsequently, the weight of these volumes was calculated considering their density. The density was obtained from the 20 selected plants. Furthermore, since there were slightly different pruning densities between the vigor classes, as shown in the results, the respective coefficients were applied according to the vigor classes. However, an average value taken from the bibliography was used as the Nv value, equal to 0.51 g per kg of pruning.

2.5 Surveys equipment

2.5.1   GNSS receiver

Georeferencing of GNSS and some agronomic variables was carried out using the receiver Stonex S7-G (named S7, Milan, Italy) used in other studies and was shown to be accurate and precise (Catania et al., 2020, 2019; Figure15). It is able to receive L1 (1575.42 MHz) and L2 (1227.60 MHz) signals from the main constellation as GPS, GLONASS, BeiDou and SBAS (e.g., EGNOS) satellites; it has 120 channels, a maximum position update rate of 5 Hz (5 positions s[−1]), a size of $234 \times 99 \times 56$ mm and a weight (without battery) less than 900 g, and it is also powered by a battery of 11.1 V and 2500 mA.

Figure 15. Stonex S7 receiver and external antenna.

The internal antenna has a choke ring which can suppress multipath satellite signals. This receiver is equipped with a Cortex-A8-AM33X processor with a frequency of 1 GHz, internal memory of 8 GB, external memory of 8 GB on SD board and RAM of 512 MB, as well as working with a Windows Mobile 6.5 Professional operating system. The receiver S7-G is also equipped with a slot for a SIM card and a GSM/GPRS/EDGE modem, which allows a quick and effective Internet connection, in order to obtain differential correction data in real time from the network of RTK ground stations (CORS). This receiver is equipped with Wi-Fi and Bluetooth connections, as well as a high brightness colour TFT display Blanview 480×640 VGA, allowing an interface with the measured or previously logged data, by providing the user with excellent visibility of the field work. This instrument is also equipped with a camera with a resolution of 5 MPixel and autofocus. The horizontal (2D, longitude and latitude) accuracy specified by the manufacturer is 5 mm + 1 ppm rms (root mean square, i.e., 63–68% of measurements) in static (stand-alone) mode, 0.6 m rms by using SBAS satellites, 0.4 m rms in differential mode (only code), 20 mm + 1 ppm in RTK mode with internal antenna, 10 mm + 1 ppm in RTK mode with external antenna.

2.5.2. *Unmanned Aerial Vehicles (UAV)*

Multispectral data acquisition was performed using a Phantom4 Multispectral drone (DJI, Shenzhen, China), a high-precision drone with a fully integrated multispectral imaging system (Figure 16). This equipment represents a solution

created specifically for precision agriculture applications. Using the classification presented in the Figure 5, this UAV is a rotary wing and multirotor UAV.
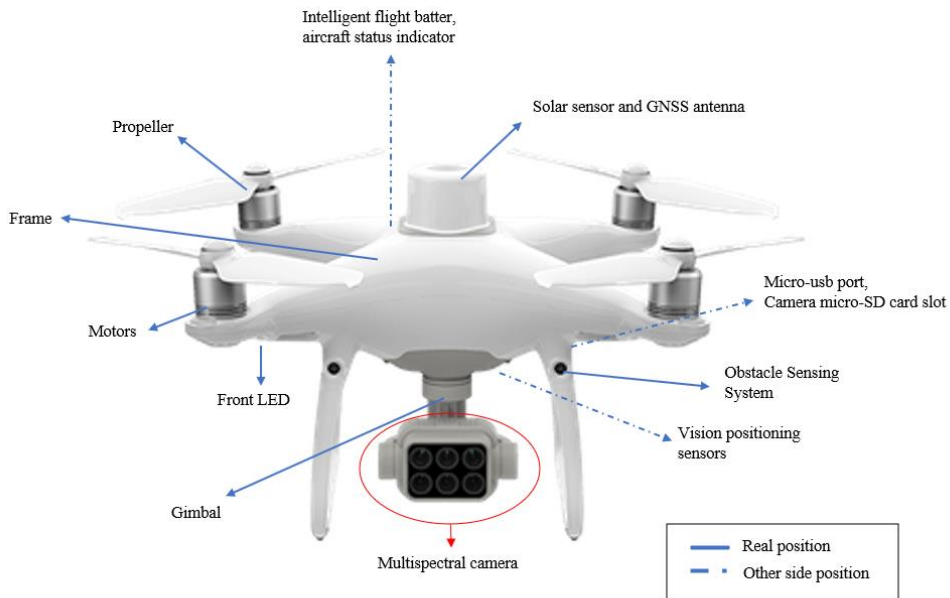

Figure 16. Phantom 4 multispectral components.

Precisely, it is equipped with four rotors (quadcopter) capable of autonomously flying over the predetermined route by the waypoints. It has a solar irradiance sensor on the top, which allows pre-calibrated images to be obtained. The positioning system consists of a multi-frequency Global Navigation Satellite System (GNSS) capable of receiving and decoding signals from the satellites constellation NAVSTAR (GPS), GLONASS, BeiDou and Galileo respectively in the bands L1/L2, L1/L2, B1/B2 and E1/E5, with possibility of RTK correction. Using the RTK correction, the precision of the position is 1.5 cm ±1ppm (RMS) and 1 cm ±1ppm (RMS) in vertical and horizontal direction respectively. The flight speed can be modified during the flight and depending on flight mode. The max speed is 50 km/h during the flight, thus in ascending and descending 6 m/s and 3 m/s respectively. The speed precision is 0.03 m/s.

The Phantom 4 is equipped with an Obstacle Sensing System that constantly scans for obstacles in front of it, allowing it to avoid collisions by going around, over or hovering. The DJI Vision Positioning System uses ultrasound and image data to help the aircraft maintain its current position. With the help of Vision Positioning, the Phantom 4 can hover in place more precisely and fly indoors or in other environments where a GPS signal is not available. The main components of the Vision Positioning System are located on the bottom; they include two ultrasonic sensors and four monocular sensors. Flight data is automatically recorded on the internal storage of the aircraft. This includes flight telemetry,

aircraft status information, and other parameters. To access these data, connect the aircraft to the PC through the Micro-USB port and launch the DJI GO app. The DJI Intelligent Flight Battery has a capacity of 5870 mAh, a voltage of 15.2 V, and a smart charge/ discharge functionality. It should only be charged using an appropriate charger and is capable of a flight time of approximately 27 minutes. Always calibrate the compass in every new flight location. The compass is very sensitive to electromagnetic interference, which can produce abnormal compass data and lead to poor flight performance or flight failure. Regular calibration is required for optimal performance.

The Phantom 4 remote controller is a multi-function wireless communication device that integrates the video downlink system and aircraft remote control system. The video downlink and aircraft remote control system operate at 2.4 GHz or 5.8 GHz with a maximum distance of transmission of 7 km. The controller battery is a LiPo 2s type of 6000 mAh and a voltage of 7.4 V. The remote controller features a number of camera control functions, such as taking and previewing photos and videos, as well as controlling gimbal motion. The battery level is displayed via LED indicators on the front panel of the remote controller.

2.5.3. *Multispectral camera*

The acquisitions of the multi-spectral images are carried out using a DJI multispectral camera implemented as payload in the UAV above described (Figure 17). The multispectral camera has six 1/2.9" CMOS sensors, such as an RGB sensor for visible light imaging and a multi-imager system formed of five narrow monochrome sensors for multispectral imaging with a final resolution of 2.08 MP pixels. The camera is not a multispectral camera properly speaking, because in the strict sense the sensor has a slightly distance offset. However, the camera is also able to compensate for image position and zero parallax error, as the relative positions of the CMOS sensor centres of the six cameras and the phase centre of the on-board D-RTK antenna are stored in the EXIF information of each image.The possibility of obtaining the same geometric resolution in the different bands is a very important condition as it allows us to obtain perfectly superimposed final images.
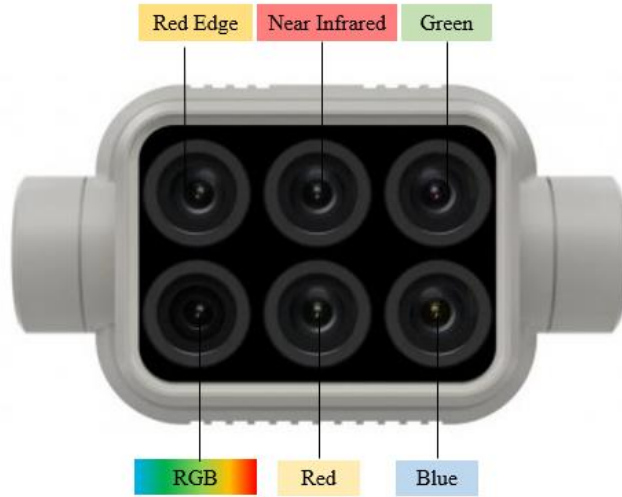
Figure 17. Multispectral camera diagram.

The lens has a FOV (field of view) of 62.7°, a focal length of 5.74 mm and an aperture of f/2.2. The maximum final image size is generally 1600 × 1300 (4; 3.25). The spectral characteristics of the monochromatic sensors are summarised in Table 3.

Table 3. Multispectral camera characteristics bands specification

Bands	Center of band wavelength [nm]	Spectral Resolution [nm]
Blue	450	±16
Green	560	±16
Red	650	±16
Red Edge	730	±16
NIR	840	±26

The sensors acquire the image as a global shutter (all pixels are acquired in the same time) and save the data in .jpeg and .tiff format in float at 32 bit (FP32). The geometric resolution was calculated using the equation 13 represented below (Yuan et al., 2021):

$$Ground\ Surface\ Distance\ (GSD) = \frac{H*Sw*100}{imW*Fr} \qquad (13)$$

Where Fr is the focal length (mm), Sw is the sensor width (mm), H is the flight height (m), imW is the image width (pixel) and 100 is a factor of conversion.

47

2.5.4. *Spectroradiometer*

The FieldSpec® HandHeld 2™ Spectroradiometer (HHS) was used to acquire hyperspectral data (Figure 18). The HHS is a handheld spectroradiometer that makes fast, accurate, non-destructive, non-contact measurements, operating in the spectral range from 325 to 1075 nm, with ±1 nm accuracy and a spectral resolution < 3 nm at 700 nm and a radiometric resolution at 16 bit. The geometric resolution of the acquisition area is determined by a square section and 25°FOV. It acquires high signal-to-noise ratio spectra in less than one second using a low light dispersion grating, an integrated shutter, DriftLock dark current compensation and second-order filtering. In addition, the HHS has a colour LCD display, built-in computing capability, large internal data memory (2,000 measurements), laser pointer and GPS (NMEA) input compatibility.

Figure 18. Proximal data acquisition with the hyperspectral sensor.

2.6. Multispectral data workflow

The workflow that was applied for the achievement of the experiment included three main phases (Figure 19): UAV data planning and acquisition; pre-processing (photogrammetric reconstruction, orthorectification and mosaicking, spectral calibration of the images, image georeferencing, topographic derivation); image processing and analysis (object-based image segmentation, vegetation index derivation, image classification, olive canopy extraction, extraction of pure canopy biometric and spectral data). The different steps are described in detail below.
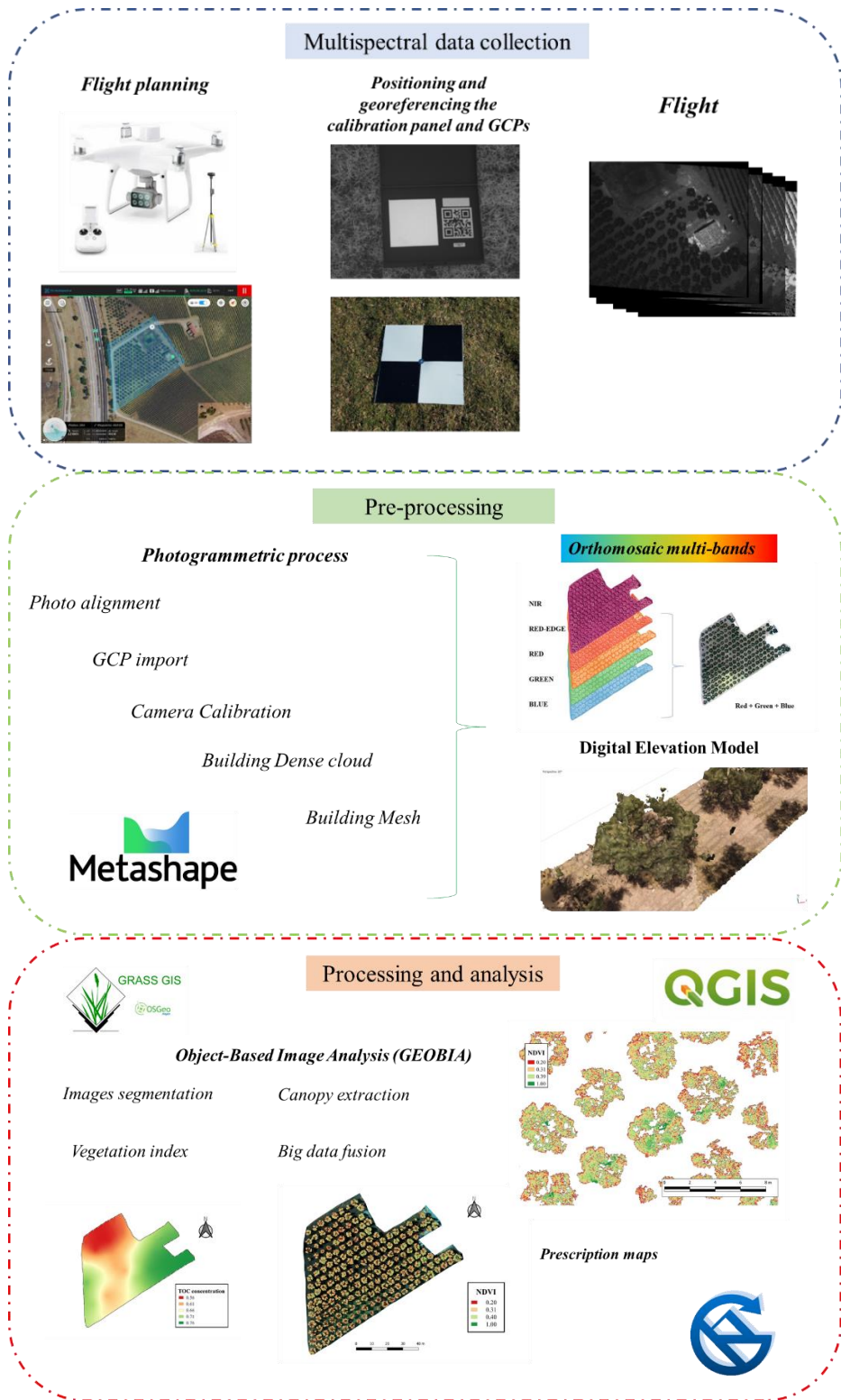
Figure 19. Synthetic operation workflow to manage the multispectral data.

2.6.3. *Multispectral data collection*

Before the multispectral data collection, the flights have been planned using the specific and official DJI software, which is only available on the IOS system (Figure 20).
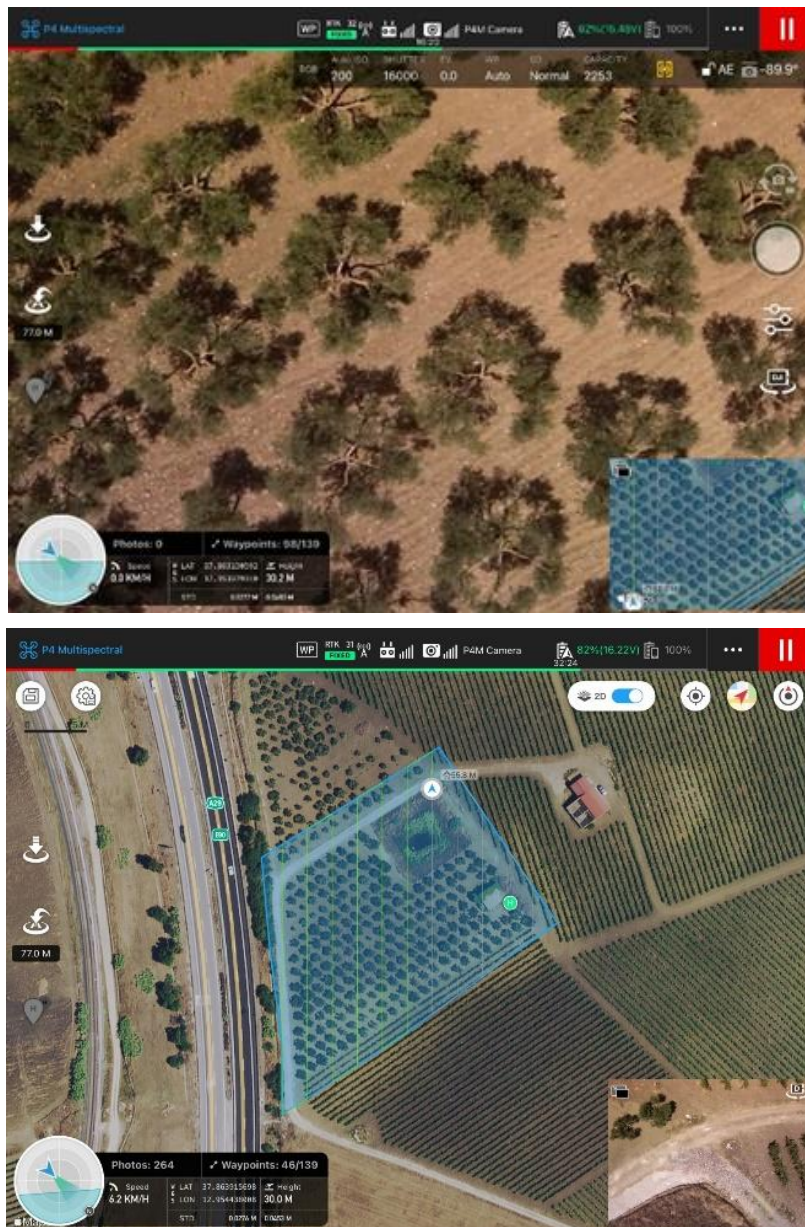

Figure 20. (Image above) Drone view; (Image below) flight plan.

In particular the following was set: flight altitude, the ground surface distance (GSD), investigation surface, speed, path, camera setting, gimbal orientation, time of the flight, side overlap and the forward overlap. Before the flights, a harrowing was made and some Ground Control Points (GCPs) and the reflectance calibration panel were positioned. The harrowing was planned in some flights in order to remove the vegetation underneath, which could have created problems in locating the pure canopies. The GCP and calibration panel were positioned to make the geometric and the radiometric calibration in the photogrammetric process. Six GCP were placed evenly at the edges and centre of the plot on a solid platform (Figure 21). The GCPs were georeferenced using a GNSS instrument, specifically the Stonex S7-Gwith external antenna and RTK correction.
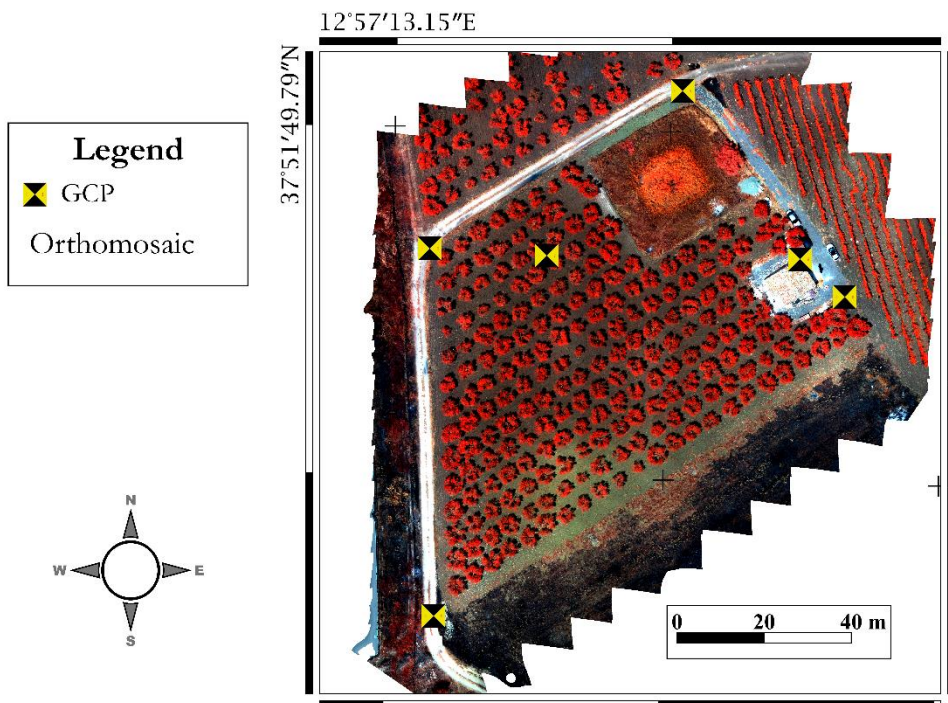
Figure 21. Ground Control Points (GCP) in the experimental plot.

Four and Five flight days were carried out during the 2021 and 2022 years respectively. All flights were performed in excellent weather conditions with high light intensity and low wind speed at 12 noon to minimise shadowing. Whole flights were carried out with the automatic flight configuration following the routes and waypoints predetermine.

Whole flights, image acquisition was carried out at an average speed of 10 m*s^{-1} with the stop-and-go mode, in order to minimise speed-related distortions. The image overlap ratio, front overlap ratio and side overlap ratio was 70% while the gimbal pitch was set at 90° (Downwards); in order to obtain more detailed and less distorted images. The schedule of the flights is summarised in Table 4.

Table 4. Flight schedule

Years	ID Flight	DOY	Flight Height	Surveyed area in the single photo	Duration	GSD	Course lenght	Photo
--	--	--	[m]	[m²]	[s]	[cm]	[m]	[n]
2021	1	102	70	2695.68	8'.18"	3.6	1051	97
	2	176	70	2695.68	8'.18"	3.6	1051	97
	3a	189	30	532.48	26'.33"	1.6	2102	489
	3b		50	1406.08	12'.50"	2.6	1364	186
	3c		70	2695.68	8'.18"	3.6	1051	97
	4a	217	30	532.48	26'.33"	1.6	2102	489
	4b		50	1406.08	12'.50"	2.6	1364	186
	4c		70	2695.68	8'.18"	3.6	1051	97
2022	5	152	70	2695.68	8'.18"	3.6	1051	97
	6a	210	70	2695.68	7'.09"	3.6	887	87
	6b	210		2695.68	8'.17"	3.6	1039	98
	6c	210		2695.68	8'.37"	3.6	1124	97
	7a	278	30	532.48	26'.33"	1.6	2102	489
	7b	278	70	2695.68	8'.18"	3.6	1051	97
	8	339	70	2695.68	8'.18"	3.6	1051	97
	9	364	70	2695.68	8'.18"	3.6	1051	97

Precisely, during the year 2021, four flight days were carried out for a total of eight flights in order to make various tests.

1. ID Flight 1 was carried out to determine the spectral and indirectly vegetative state of the 211 plants in order to compare it with the ground truth of vigour (measured as TCSA), nutritional status and production taken during the previous season (2020).
2. ID Flight 2 was carried out to verify the growth of the plants during the new season.
3. ID Flight 3 days were carried out with 3 flights at three different flight heights to evaluate their influence in the reconstruction of the spectral and vegetative parameters. The heights that were used were: 30m, 50m and 70m a.g.l. (3a, 3b, 3c); obtaining a ground sample distance (GSD) of 1.6cm, 2.6 and 3.6cm respectively.
4. ID Flight 4 was performed to compare the hyperspectral data acquired laterally to the canopy with a spectroradiometer and flight 4b in order to

verify if the two points of view of the plants and the two types of spectral data provide different results. These surveys were conducted simultaneously. The three heights were also performed using the same methodology used in flight 3 to evaluate in-season plant change and the ability of flight height to detect it.

During the year 2022 a total of eight flights, in five days, were carried out.

5. ID Flight 5 was performed to determine the spectral and vegetative state of the 211 plants beginning of the new growing season of the olive grove following the site-specific management carried out in the first year.
6. ID Flight 6 was carried out to evaluate the effect of three different flight paths of the UAV on multispectral and biometric canopy reconstruction (Figure 22). Three different flight angles were used depending on the layout of the plants. Precisely, test 6a (diagonal test) had an angle to the north of 32°, test 6b (north-south test) had flight directions coinciding with the north-south direction (angle of 0°), and finally test 6c (east-west test) had an east-west flight direction with an angle of 90° to the north (Figure 22).
7. ID Flight 7 were carried out with two flights at different flight altitude to evaluate their influence in the reconstruction of the spectral and vegetative parameters in dense canopy condition. The heights that were used were: 30m and 70m a.g.l. (7a and 7b); obtaining a ground sample distance (GSD) of 1.6cm and 3.6cm respectively.

8 – 9. The last two flights were carried out to compare the impact of the pruning operation in the vegetative and biometric condition of each plant. Furthermore, 20 plants were selected to quantify the biomass amount and the real canopy size.
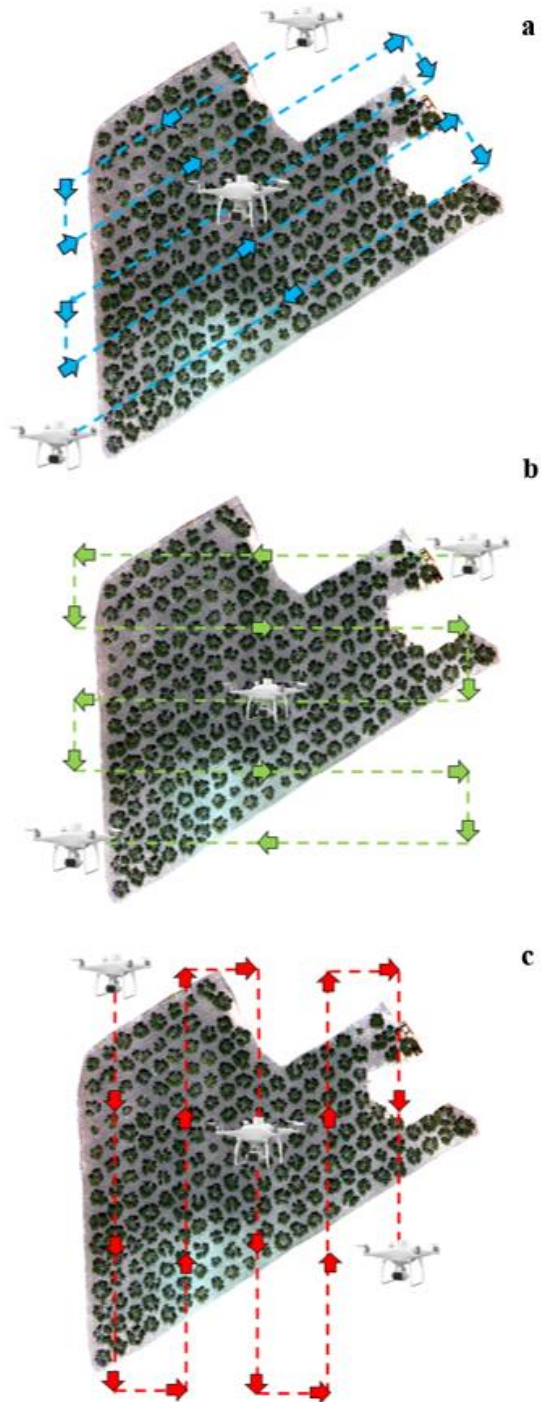
Figure 22. Schematic representation of flight paths. (a) Diagonal flight path; (b) East-West flight path; (c) North-South flight path.

2.6.4. Pre-processing of the images

Once the multispectral and RGB images were acquired, they were pre-processed in order to obtain the multi-bands orthomosaic, Digital Elevation Model (DEM) and the Digital Terrain Model (DTM). The photogrammetric process employed is the classic scheme. Precisely, the different band image has been downloaded and uploaded in the software. The next steps were the alignments, the GCP upload, the calibration in reflectance. Once the preparation was complete, we proceeded with the construction of the dens cloud, the Mesh to obtain the final products. Data processing was done using a photogrammetric software able to apply the Structure for Motion (SFM) algorithms. Specifically, Agisoft Metashape Professional (version 1.7.3) software was used. This software enables photogrammetric processing of digital images and generates 3D and 2D spatial data for use in GIS applications. The photogrammetric process of the different images was performed following the main steps summarised in the workflow below (Figure 23).
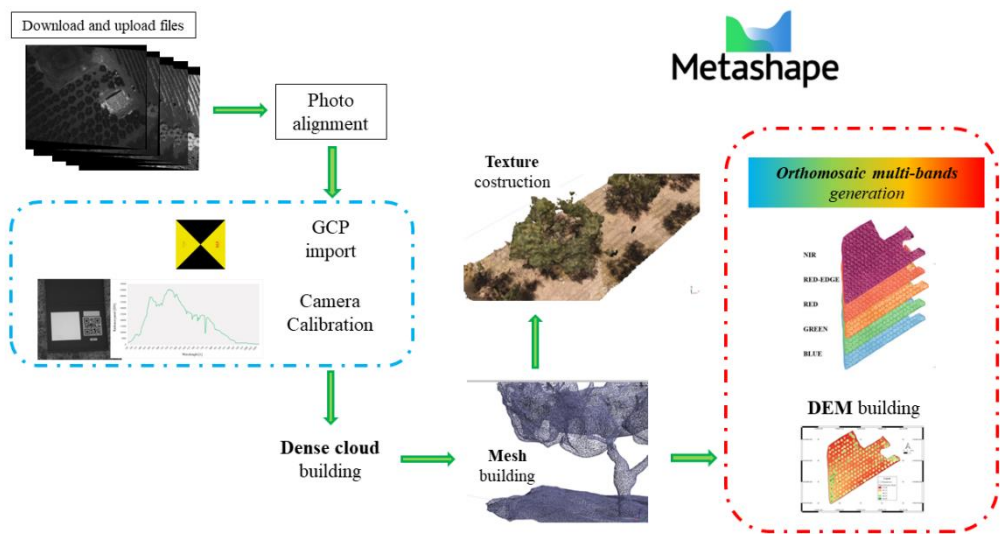
Figure 23. Work flow of photogrammetry data processing

The images detected by the sensor are digital images in which the detected scene is represented by a matrix of pixels, each of which is characterised by a number, the DN (Digital Number), which corresponds to the average radiance of the area covered by each pixel and is usually represented in greyscale. The number of shades available depends on the memory of each pixel, expressed in bits, which corresponds to the radiometric resolution of the observation system. Each pixel constituting the image is characterised by three values: the two spatial variables x and y, which identify the position of the pixel within the image and the DN, related

to the intensity of the radiance on the ground, which indicates the value of the colour shade, or grey, assumed by each individual pixel.

DNs are positive integer values obtained from a quantisation of the original electrical signal, through a signal conversion process, which translates them into levels of grey or light intensity. Each spectral band recorded by the sensor has a characteristic response function to perform the analogue-to-digital conversion of the electrical signal. The radiometric response function for a band is generally represented by a linear-type conversion function expressed by (equation 14):

$$DN = G * L_\lambda + B \tag{14}$$

This equation is typical for every sensor and when we make the reflectance calibration, the software uses this from the metadata of constructor. Image alignment was performed using the software and setting high accuracy, generic preselection, reference preselection and the sequential method. The number of key and tie point limits were left as default. Once the alignment had been carried out, the GCPs were inserted using the WGS84 geographical coordinate system (EPSG: 4326). Then, the identification of the GCPs on the different photos was done. After this, the most accurate topographic transformation can be carried out, depending on the number of GCPs present. The calibration of the images was made by the software using the brightness data recorded by the brightness sensor on the drone with follow equation 15:

$$\rho\lambda\% = \frac{\Phi r\lambda}{\Phi i\lambda} * 100 \tag{15}$$

Where ρ is the reflectance for each wavelength (λ); Φr is the power that reaches the sensor from the reflectance surface, Φi is the power incident on the reflectance surface.

In addition, to improve the calibration, a white panel was placed on the ground before the flight to complete the radiometric calibration. The reflectance calibration was achieved by putting the panel reflectance measure in the field with the spectroradiometer.

The construction of the Dense Cloud was carried out with a very high accuracy; then, it was possible to construct the Mesh and generate the texture between the multispectral and RGB images. Finally, the Digital Elevation Model (DEM) and the multiband orthomosaic was obtained through a process of orthorectification and mosaicking, (Figure 24).
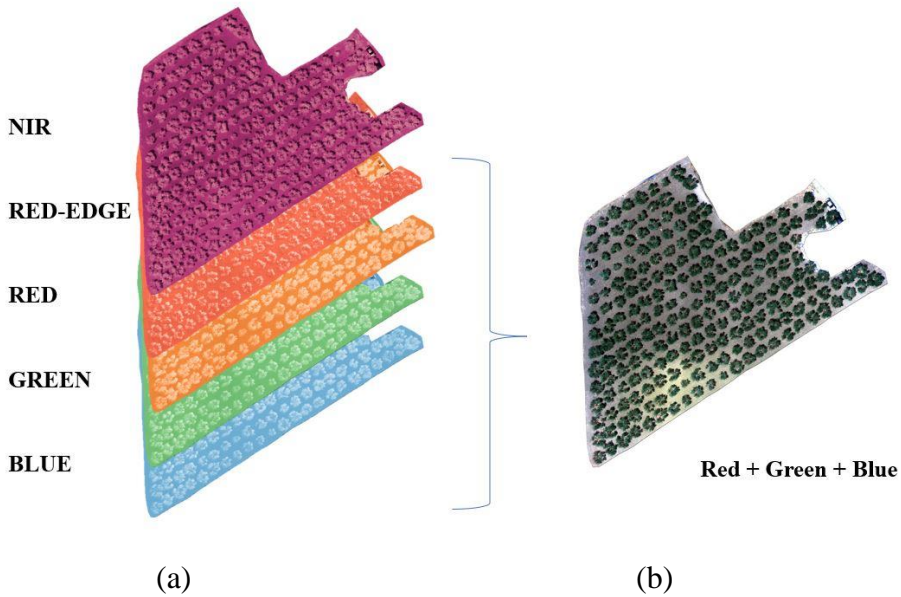
(a)	(b)

Figure 24. (**a**) Multispectral bands; (**b**) orthomosaic in RGB representation.

2.6.5. *Multispectral images processing and analysis*

Starting from the last products, orthomosaic, DEM, DSM and DTM, were processed and analyzed through the new GIS software. In this case, we used an important open-source software QGIS ver. 3.16.6 Hannover (QGIS.org, 2022). Moreover, the Saga and Grass tools already interconnected and implemented in QGIS were used. The best details of the image analysis in QGIS software are presented in the 2.7 section.

2.7. Hyperspectral data workflow and processing

The Hyperspectral data workflow that was applied for the achievement of the experiment included the acquisition, pre-processing and the analysis of the dataset (Figure 25).
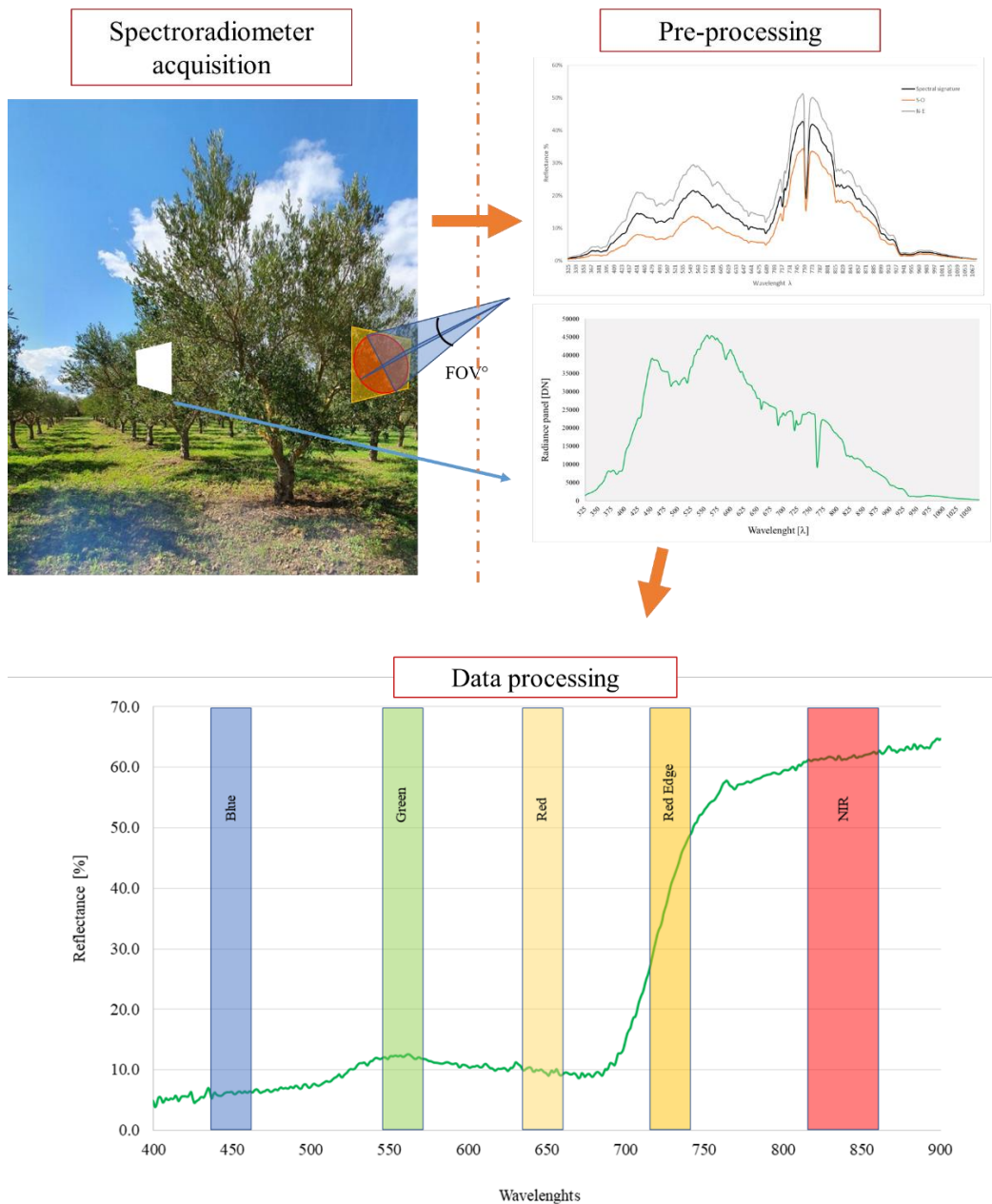
Figure 25. Hyperspectral data workflow.

Hyperspectral acquisitions with the spectroradiometer were carried out in the years 2021 and 2022. In the year 2021, four out of 24 randomly selected plants were flown at the same time. The measurements were carried out from 01:00 pm in the four exposures with the following sequence: South, West, North and East. In the year 2022, another 20 plants were selected to carry out hyperspectral measurements only in the north and south exposures of the canopy at 12:00pm.

Three outcomes were obtained for each exposure and the radiometric reflectance calibration was performed using a calibrated spectral on white reference with known reflectance characteristics. For both experiments, the acquisitions were carried out in the lateral portions of the plants directly in the field, placing the instrument at about one meter from the canopy (Figure 26).

Figure 26. Hyperspectral data acquisition process in the four-canopy exposure, DOY 217.

In this way, it was possible to examine the hyperspectral information of an entire portion of the canopy without any soil influence, for the four exposures. The acquired data were downloaded and processed by means of the software associated with the instrument (HH2 Sync and ViewSpec Pro). In this way, it was possible to calculate the spectral signature of each plant using the equations 14 and 15.

Obtained the spectral signature, using the position recorded on the instrument the data were transported to the QGIS software. This information has been joined to the corresponding canopy portion. For the first experiments, each canopy tree was divided into four parts to the exposure to the four cardinal directions. Considering that 0° is located at the centre of the North portion and turning clockwise: the North sector goes from 315° to 45°, East from 45° to 135°, South from 135° to 225° and West from 225° to 315° (Figure 27). In the 2nd experiment carried out in 2022 the canopy portion was divided in two sections, North and South to associate the corresponding data.
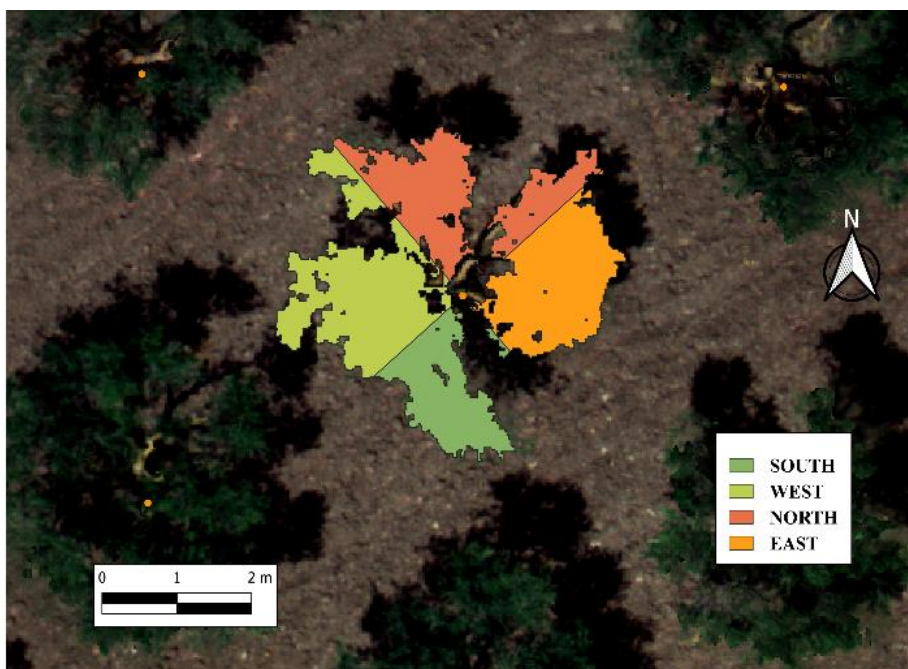
Figure 27. Detail of a plant sampled for hyperspectral measurements and the canopy divided into four portions (North, South, East, West).

2.8. GIS analysis

Starting from different datasets, we analyzed the data with the QGIS program. For the vector data, the main geostatistical methods were used to spatialize the data and create other maps, while the GEOBIA (Geographic Object Based Image Analysis) technique was used to analyze and process the raster data. Afterwards, all information was merged, combined and processed to create different layouts that were in turn used to produce intermediate maps and prescription maps (final product). In addition, the layouts were statistically analyzed to obtain the static characterization. In this way it was possible to extract several pieces of information such as canopy area, canopy volume, spectral characteristics as well as other information.

2.8.1. *Vector data and Geostatistical analysis*

The geostatistical analysis was applied in all point data that needed their spatialization in order to create continuous maps. In particular, it affected the leaf nutrient analysis, the several soil parameters and the different measurements of tree vigor. The leaf nutrient maps achieved by kriging were used to estimate the percentage of field surface affected by nutritional deficiencies to be fertilized. Based on a semi-variogram and a cross-validation analysis, appropriate models were fitted, and the input parameter employed the ordinary kriging interpolate.

This method can express the spatial variation of a specific variable by minimizing the distribution error of the predicted values.

Kriging interpolation assumes that the estimate at an arbitrary point in a specific zone of the field is expressed with a linear weighting of all observations. To provide the best linear estimation, semi-variograms are calculated, which consider the spatial structure (Chiles and Delfiner, 2009; Webster and Oliver, 2007a). In this case, the semi-variogram was calculated for each variable as follows.

$$y(h) = \frac{1}{2N\ (h)} \sum_{i=1}^{N(h)} [\ Z(xi + h) - Z(xi)]^2 \qquad (16)$$

where N(h) represents the number of pairs of observations separated by a value (h), which in turn corresponds to the distance deviation expressed in meters. The parameter Z(xi) is the value of the variable Z at the sampled location xi.

Kriging of geo-statistics is an optimum interpolation technique for making unbiased estimates of regionalized variables at unsampled locations in which the structural properties of the semi-variogram and the initial set of samples are used (Huang et al., 2006; Khan et al., 2021). The spatial prediction of the values of a soil variable Z at an unsampled point v0 is estimated as a weighted average followed by the equation 17:

$$Z\ (x_0) = \sum_{i=0}^{n} \lambda i\ z(xi) \qquad (17)$$

where $Z(x_0)$ is the value to be estimated at the location x_0, z(xi) is the known value at the sampling site xi, n is the number of neighbouring samples and λi is the weight.

The semi-variogram, therefore, allows modelling functions to be developed for many infinitely large environmental variables. Therefore, the selection of a semi-variogram is critical for geostatistics analysis techniques, as it allows the parameters needed to perform Kriging interpolation to be defined. The selection of the suitable semi-variogram was done by calculating the semi-variances at different distance intervals (h), fitting specific theoretical models. The experimental semi-variogram was adapted through the application of some appropriate theoretical models (Cressie, 2015): the spherical (18) and the exponential ones (19).

$$y(h) = C_0 + C\left[1.5\frac{h}{a} - 0.5\left(\frac{h}{a}\right)^3\right] \qquad (18)$$

$$y(h) = C_0 + C\left[1 - exp\left(-\frac{h}{a}\right)\right] \qquad (19)$$

In these mathematical models, the input parameters are the sill variance (C_0+C), the range indicated by (a), and nugget variance (C_0), these inputs were calibrated to identify the spatial variability of vineyard vigour. The sill variance concerns the amount of spatial structural variance in the data set. The range represents the distance in which the semi-variogram lies around a limit value. The nugget defines the variability of a sampling interval or analysis error.

Spherical, exponential and pure nugget models were fitted to the empirical semi-variograms. The parameters of the model: nugget semi-variance, range, and sill or total semi-variance, were determined. Nugget semivariance is the variance at zero distance; sill is the lag distance between measurements at which one value for a leaf nutrient does not influence neighbouring values; and range is the distance at which values of leaf nutrient become spatially independent of the neighbouring values. The ratio between nugget semi-variance and total semivariance or sill was used to define different classes of spatial dependence for leaf nutrients (López-Granados et al., 2004). The ratio between nugget semi-variance and total semi-variance or sill was used to define different classes of spatial dependence for leaf nutrients (Gargouri et al., 2006; López-Granados et al., 2004). If ratio was ≤25%, the leaf nutrient was considered to be strongly spatially dependent, or strongly distributed in patches; if ratio was between 26 and 75%, the leaf nutrient was considered to be moderately spatially dependent; if ratio was greater than 75%, the leaf nutrient was considered weakly spatially dependent; if the ratio was 100%, or the slope of the semi-variogram was close to zero, the leaf nutrient was considered as not being spatially correlated (pure nugget).

In cross-validation, the values estimated from ordinary kriging were compared with the values observed at the sampling points. Kriging calculation was carried out using several tools of QGIS software. A multivariate geostatistical approach, based on principal component analysis (PCA) and called factorial co-kriging (Webster and Oliver, 2007b), uses the information from spatial relationships among variables to subdivide an agricultural field into smaller, more homogeneous units (Buttafuoco et al., 2017). Moreover, most soil physical and chemical properties are likely to vary over a short-range (meters), whereas others vary at longer (thousand meters) distances. Therefore, soil properties are expected to be correlated among them in a way that is scale-dependent.

2.8.2.   Geographic object-based image analysis (GEOBIA)

OBIA or GEOBIA is an alternative to a pixel-based method with basic analysis unit as image objects instead of individual pixels grouping a number of pixels into shapes with a meaningful representation of the objects (Blaschke, 2010). The aim of OBIA is to address more complex classes that are defined by spatial and hierarchical relationships within and during the classification process (Lang, 2008). OBIA is usually composed of two main phases: (1) image segmentation,

and (2) feature extraction and classification. The most basic and critical step is image segmentation and the accuracy of following object based feature extraction and classification mainly depends on the quality of image segmentation (Cheng et al., 2001; Hossain and Chen, 2019). Image segmentation was performed in order to obtain a classification into homogeneous regions and different non-overlapping zones starting from the VI map realized with different vegetation indices (VI; Caruso et al., 2019; Roma and Catania, 2022), summarized in the Table 1.

In particular, the three main vegetation indices were used (Roma and Catania, 2022) to determine the spectral variability, such as: NDVI (Rouse et al., 1974), MSAVI (Qi et al., 1994) and NDRE (Maccioni et al., 2001).

$$\text{NDVI} = \frac{\rho_{nir} - \rho_{red}}{\rho_{nir} + \rho_{red}} \tag{20}$$

$$\text{NDRE} = \frac{\rho_{nir} - \rho_{red\ edge}}{\rho_{nir} + \rho_{red\ edge}} \tag{21}$$

$$\text{MSAVI} = \frac{\{2\rho Nir + 1 - \sqrt{[(2\rho Nir+1)2 - 8\ (\rho Nir - \rho Red)]}\}}{2} \tag{22}$$

Several algorithms for the image classification were applied. In particular, was applied a classification supervised and a classification unsupervised. The most widely used algorithm was the K-means algorithm. K-means is one of the simplest unsupervised learning algorithms that solve the well-known clustering problem. The procedure follows a simple and easy way to classify a given data set through a certain number of clusters (assume k clusters) fixed before.

$$J = \sum_{i=1}^{m} \sum_{k=1}^{K} w_{ik}\ \left\| x^i - \mu_{k\mu} \right\|^2 \tag{23}$$

where $w_{ik}=1$ for data point x_i if it belongs to cluster *k*; otherwise, $w_{ik}=0$. Also, μ_k is the centroid of x_i's cluster. The main idea is to define k centres, one for each cluster. These centres should be placed in a cunning way because of different location causes different result. K-means algorithm was applied to the VI map, which allowed to obtain a binary clustering of the image. This methodology was preferred over threshold clustering because any non-pure pixels (especially close to the canopy) that could be erroneously classified as soil. This clustering algorithm was in Saga's Images analysis library.

The images classified allowed the comparison and analysis of variability found in the olive orchard. Through several process of rasterization and vectorialization it was possible to extract different information from the tree (Caruso et al., 2019), such as biometric information while the spectral information concerned in the calculation of VI (Figure 28). The spectral information was obtained from the

ortho mosaic using Raster calculator a tool of QGIS. The NDVI map from the flight with a big difference in soil pixel and vegetation pixel was used to extract the CA.
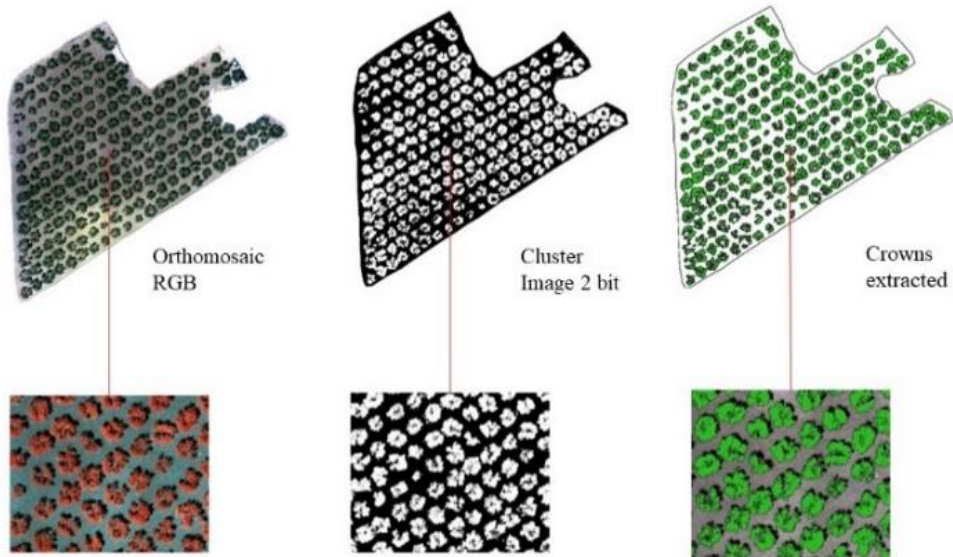

Figure 28. Canopy extrapolation sequence for plant.

However, in the flight performed during the season when there was weed above the canopy, the previous method cannot used. In this case, the elaboration method was performed starting from elevation maps. Precisely, the elevation maps were the DSM and the DTM. The DSM was extracted directly from the photogrammetric processing while the DTM was derived from some terrain point randomly selected and spatialized using a geo statistical method (Figure 29). After calculating DTM and DSM, it was possible to determine the CV using the following Equation 24. as defined in (Caruso et al., 2019):

$$CV = (DSM - DTM) - TrH \qquad (24)$$

where DSM is the Digital Surface Model; DTM is the Digital Terrain Model; TrH is the trunk height (mean value of the 50 selected plants).

2.9. Biometric Data validation

The aptitude of the ortho mosaic and their DSMs to build the tree structures and to retrieve their geometric features was evaluated. These parameters are namely the projected area of the canopy (CA) and crown volume (CV); they were evaluated by comparing the UAV-estimated values and the on-ground values

observed in the validation fields. For this purpose, twenty olive trees were randomly selected in the field and their shape was outlined manually using the orthomosaic image to be used as an observation measure. The results of the GEOBIA (geographic object-based image analysis) analysis on the estimation of the CA and CV were compared to the observed measurements to calculate the area of coincidence for each olive tree and calculate the overall accuracy. In the same olive trees selected for CA, the CV quantification and validation were applied. CV* was estimated starting from the manual measurement, assuming an ellipsoid form and applying a validated method (Equation 25) for olive tree geometric measurements using the parameters measured (Pastor Muñoz-Cobo, 2005; Torres-Sánchez et al., 2015b).

$$CV^* = \frac{\pi}{6} * \left(\frac{C_l * C_w}{2}\right)^2 * \frac{Th}{2} \qquad (25)$$

where Cl is the Canopy length (m); Cw is the Canopy width (m); Th is the tree canopy height (m). The effectiveness of the entire procedure to measure volume and area of the canopy of the fifty selected trees was evaluated by calculating the root mean square error (RMSE) and correlation coefficient derived from the regression fit.
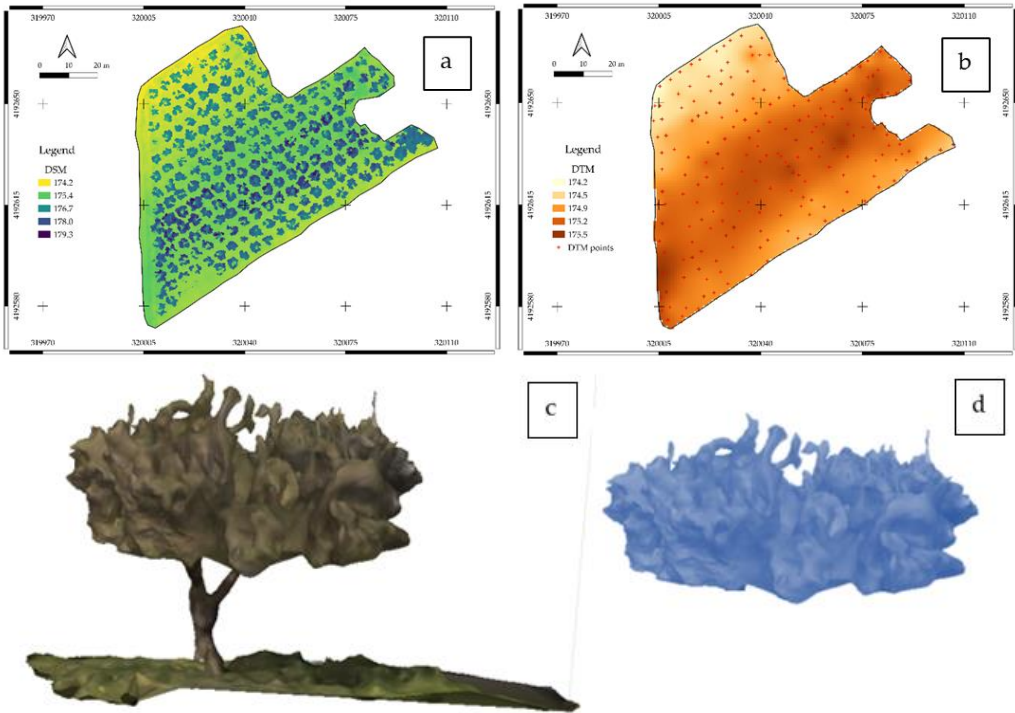
Figure 29. Data processing steps to obtain Crown Volume (CV). (a) Digital Surface Model (DSM); (b) Digital Terrain Model (DTM); (c) representation of the tree; (d) CV obtained using equation (1).

2.10. Statistical Analysis

Descriptive statistical analysis was carried out first to determine the mean, maximum, minimum, standard deviation, and coefficients of variation (CV) of the variables of the data.

The data obtained from the sampling, the survey from the ground, proximal and remote sensing platform were processed and analysed statistically.

To check the accuracy of the calculated predicted values the coefficient of determination (R^2; equation 26), the root means square error (RMSE; equation 27) and mean absolute percentage error (MAPE; equation 28) index was calculated as follows:

$$R^2 = 1 - \frac{\sum_{i=1}^{n}\{y(xi) - y^*(xi)\}^2}{\sum_{i=1}^{n}\{y(xi) - \bar{y}(xi)\}^2} \tag{26}$$

$$RMSE = \sqrt{\frac{\sum_{i=1}^{n}\{y(xi) - y^*(xi)\}^2}{N}} \tag{27}$$

$$MAPE \ \frac{100\%}{N}\sum_{i=1}^{n}\left|\frac{y(xi) - y*(xi)}{y(xi)}\right| \tag{28}$$

where *n* is the number of points, y(*xi*) is the measured value, and y *(xi)* is the predicted value, $\bar{y}(xi)$ is the mean value of the observed data, N is the total number of fitted points. The best prediction model was obtained when the RMSE and MAPE had the lowest value.

The analysis was made applying the base statistic to characterize the dataset. The main analysis performed were the variance analysis model (ANOVA), Tukey's multiple comparison tests. Relationships between the parameters were tested using regression analysis and Pearson's correlation coefficient. Furthermore, the principal component analysis (PCA) has been used to discriminate how the several parameters have influenced the results. All the statistical procedures were performed using R software (RStudio Team., 2015). and Microsoft Excel.

3. RESULTS

This section will focus on the results that have been obtained from the various tests conducted during the different years of the experiment. For a better understanding, this section has been divided into the three parts of the agroecosystem (soil, climate and plant) and finally into a sub-section showing their interactions for specific agronomic practices.

3.1. Weather conditions

Weather conditions showed a different seasonal trend in accordance with the mediterranea area. It was characterized by a mean annual air temperature of 17.50 ranging from 13.07 to 17.50 °C and a mean annual precipitation of 745 mm. The precipitation in all years was concentrated from September to March (Fig 30, 31 and 32), while the highest potential evapotraspiration was during the summer season (Fig 33). The distribution of monthly average temperatures shows that the warmest temperatures are concentrated during the spring-summer period. During the summer, average daily maximum temperatures exceeding 30 °C are observed in all three years. While the lowest temperatures occur during the autumn-winter period.
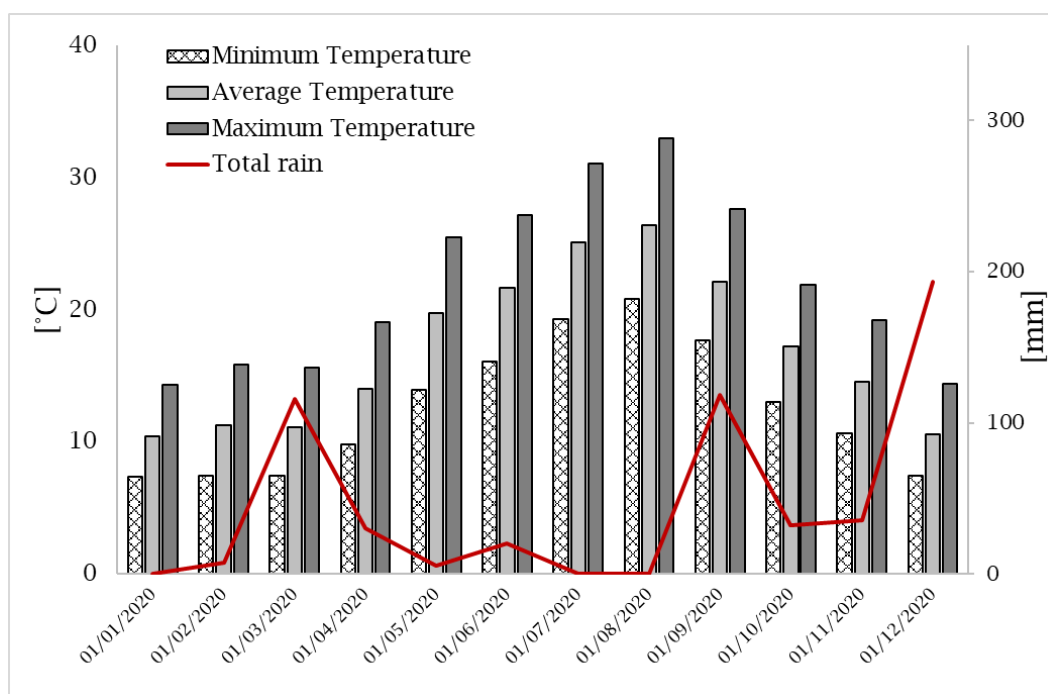
Figure 30. Monthly distribution of mean temperature, minimum temperature, maximum temperature and rainfall in the year 2020. Source data: weather station located in Calatafimi Long: 12°52'47.76"E Lat: 37°51'16.42"N.
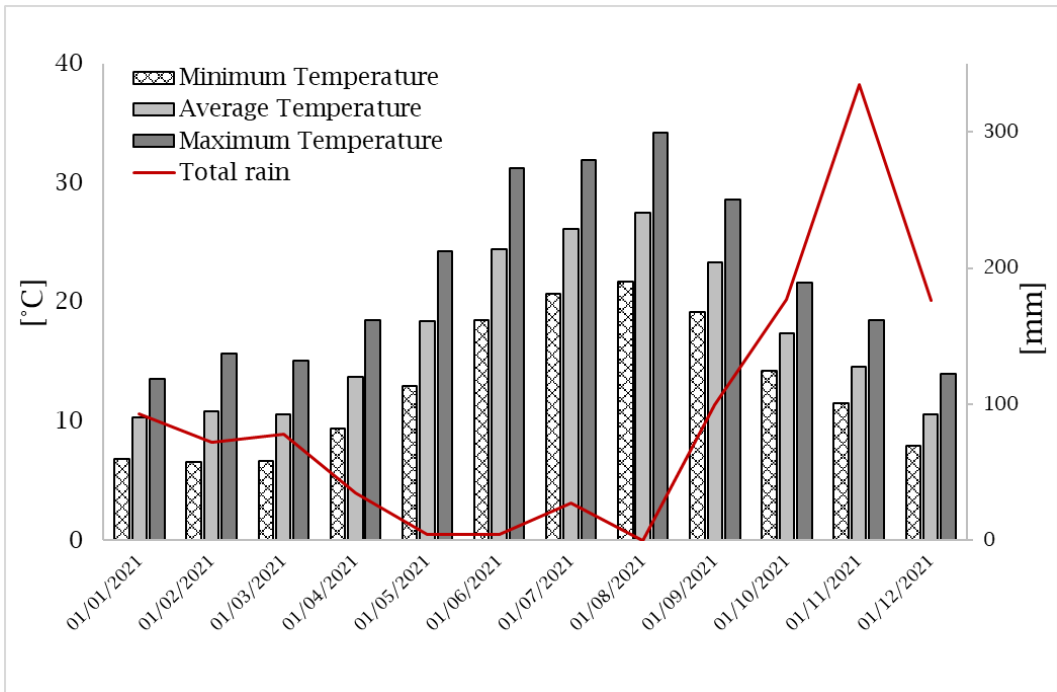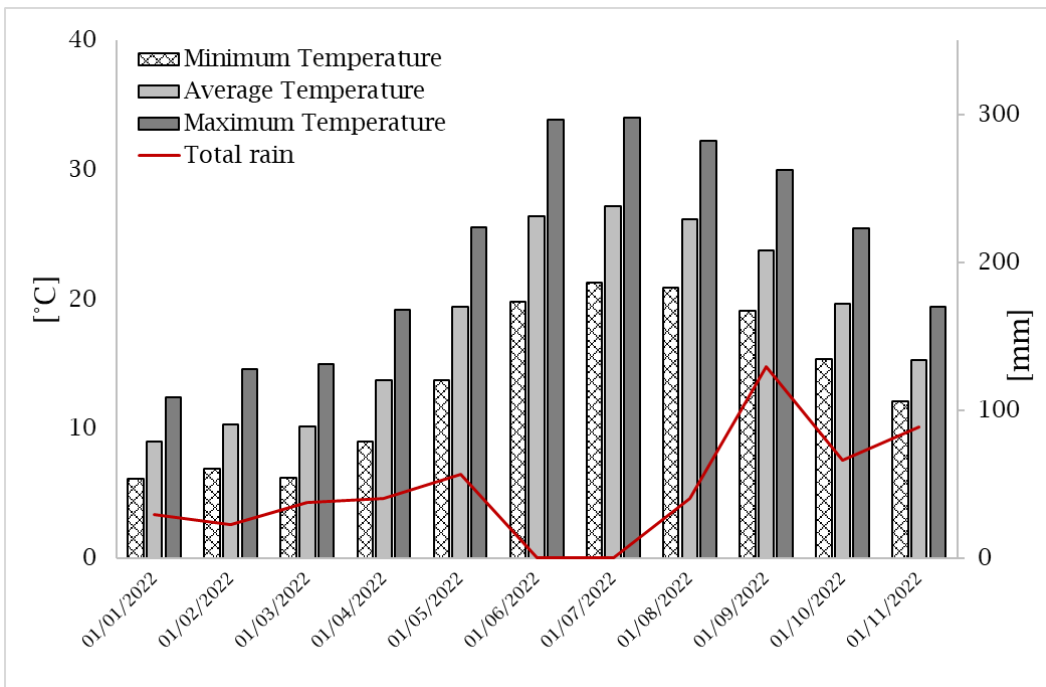
Figure 31. monthly distribution of mean temperature, minimum temperature, maximum temperature and rainfall in the year 2021. Source data: weather station located in Calatafimi Long: 12°52'47.76"E Lat: 37°51'16.42"N.

Figure 32. monthly distribution of mean temperature, minimum temperature, maximum temperature and rainfall in the year 2022. Source data: weather station located in Calatafimi Long: 12°52'47.76"E Lat: 37°51'16.42"N.
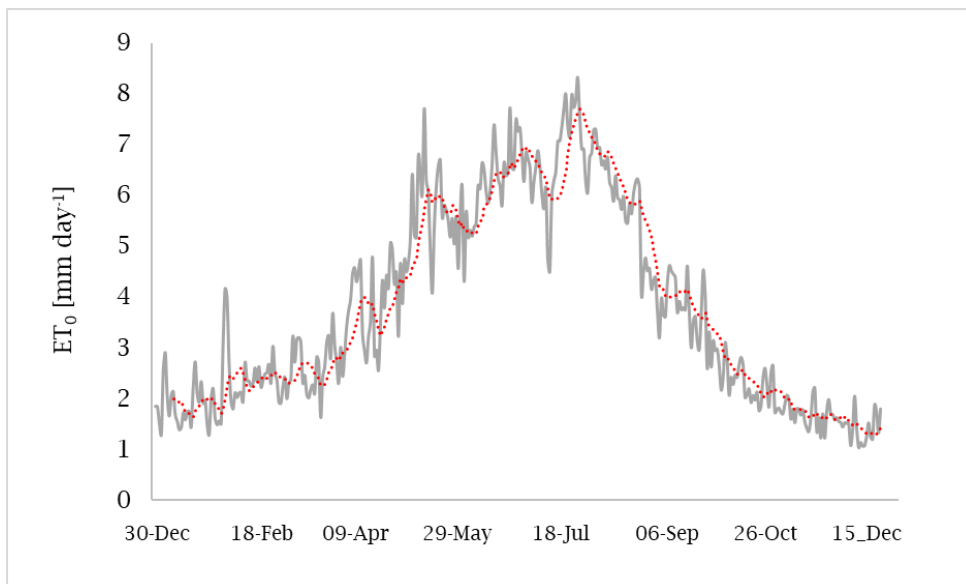
Figure 33. Trend of average daily potential evapotranspiration (ET$_0$) over the three experimental years (gray line). Moving average of the last ten ET$_0$ days (red line).

The year 2022 was the warmest on average compared to previous years (Fig 34) with an average annual temperature of 18.28 °C, while the year with the highest rainfall was the year 2021 (Figure 35) with an average annual rainfall of 1100 mm concentrated almost 72% between September and December.
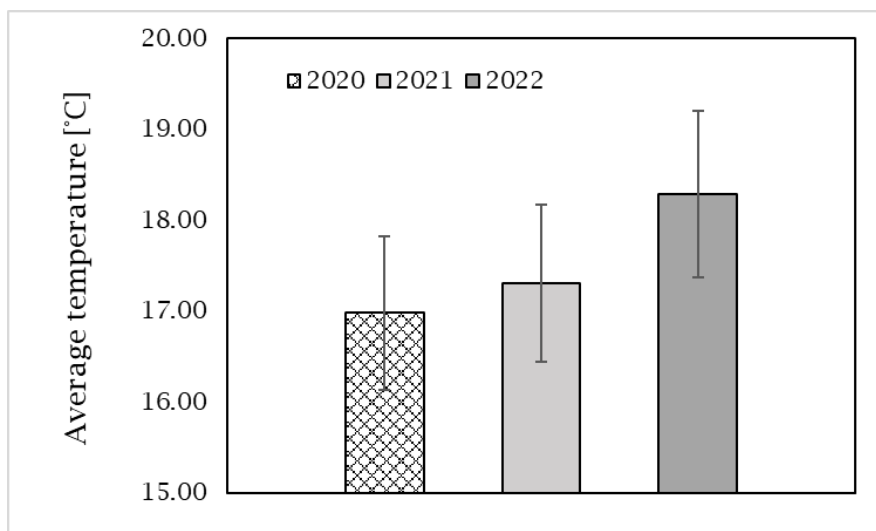
Figure 34. Average temperature annual trend over the three experimental years.
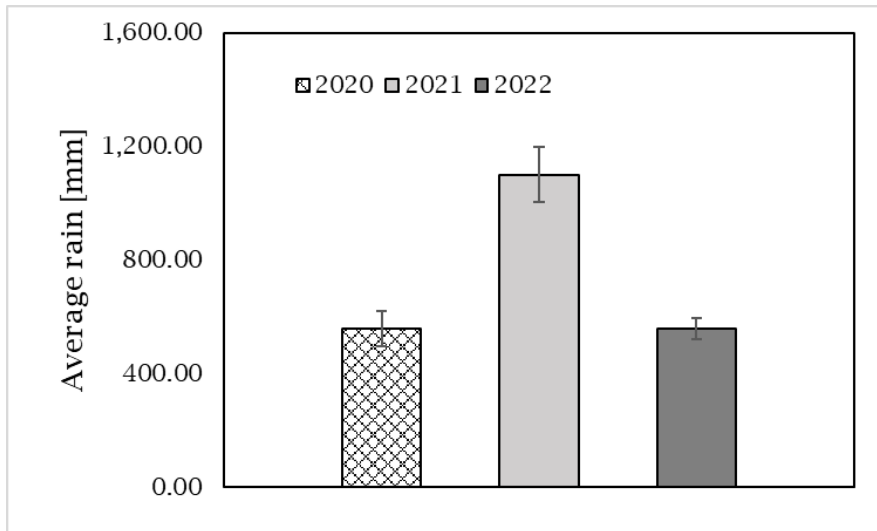
Figure 35. Average rain annual trend over the three experimental years.

3.2. Soil Variability

The Digital Terrain Model was obtained from surveys carried out on the 2020 (Figure 36). It allowed for the observation of whether there were any relationships between the soil variables and the terrain orography, even if the plot is typically flat.
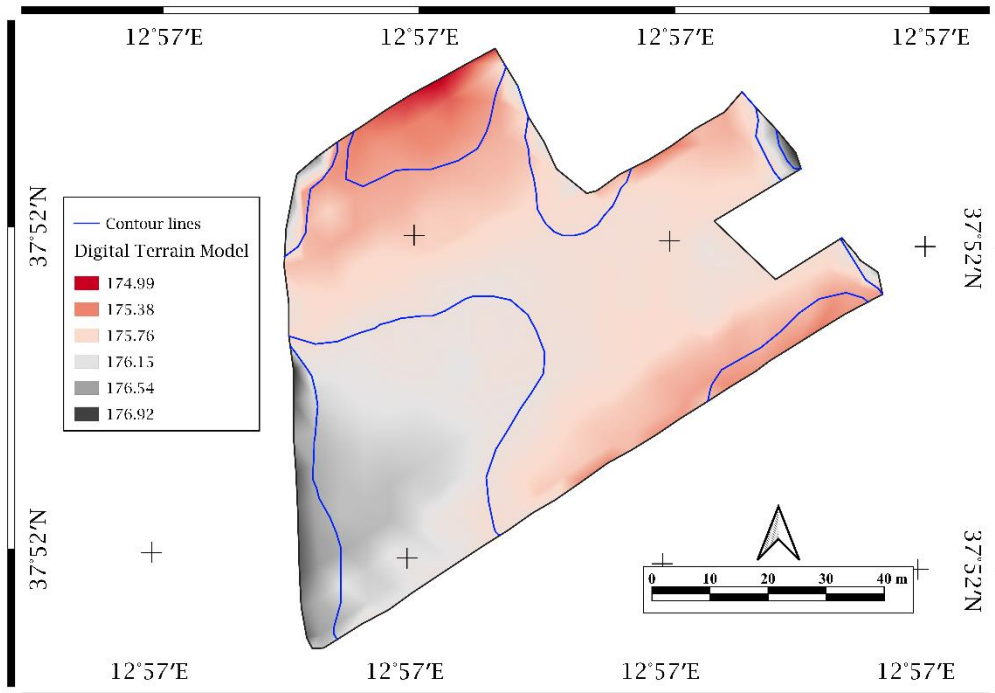
Figure 36. Digital Terrain Model of the experimentation area.

The main characteristics of the soil of the studied area are reported in table 5. According to the ISSS (International Society of Soil Science) classification system of soil particles, soil texture was sandy clay loam (Hillel, 2013). Soil reaction was neutral whereas both total carbonates and electrical conductivity (EC) showed low values. Total organic carbon and nitrogen concentration were also low.

Table 5. Characteristics of the soil of the studied area.

Parameter	Mean	SD	CV (%)
Clay (%)	30	3.30	11
Silt (%)	13	1.92	15
Sand (%)	57	4.01	7
Total organic carbon (%)	0.67	0.10	14
Total nitrogen (%)	0.15	0.03	20
Total carbonates (%)	5.09	3.23	64
pH	7.24	0.18	2
Electrical conductivity (dS m^{-1})	0.16	0.03	17

According to the ISSS the soil texture was homogenius in the whole plot with only a slight difference as showed in Figure 37.
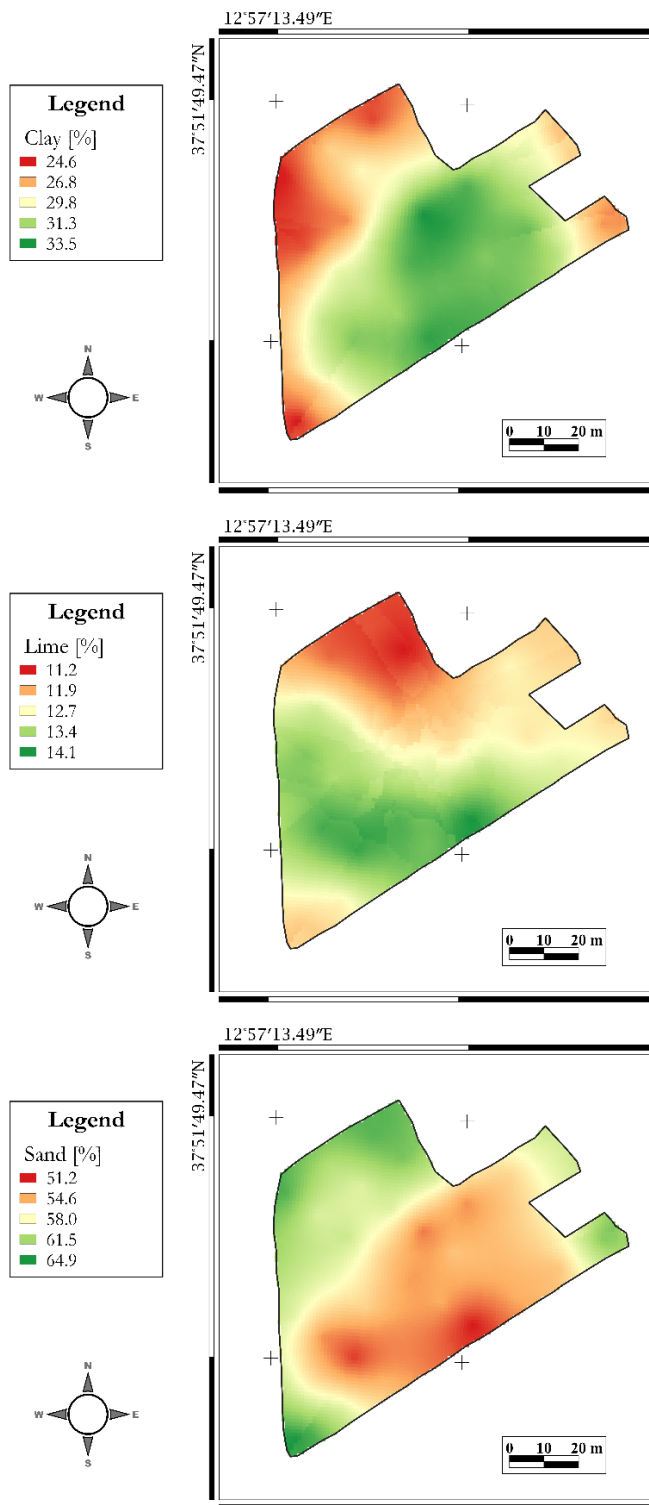
Figure 37. Caly, Lime and Sand maps created using the ordinary kriging method on the 36 soil samples.

Total N ranged from 0.10% to 0.25% and was positively related with TOC (r = 0.74***). The TOC ranged from 0.56% to 0.76%, being an average of 0.68%. The map describing soil TOC and TN spatial variability was provided through the interpolation with geostatic methods (Figure 38).
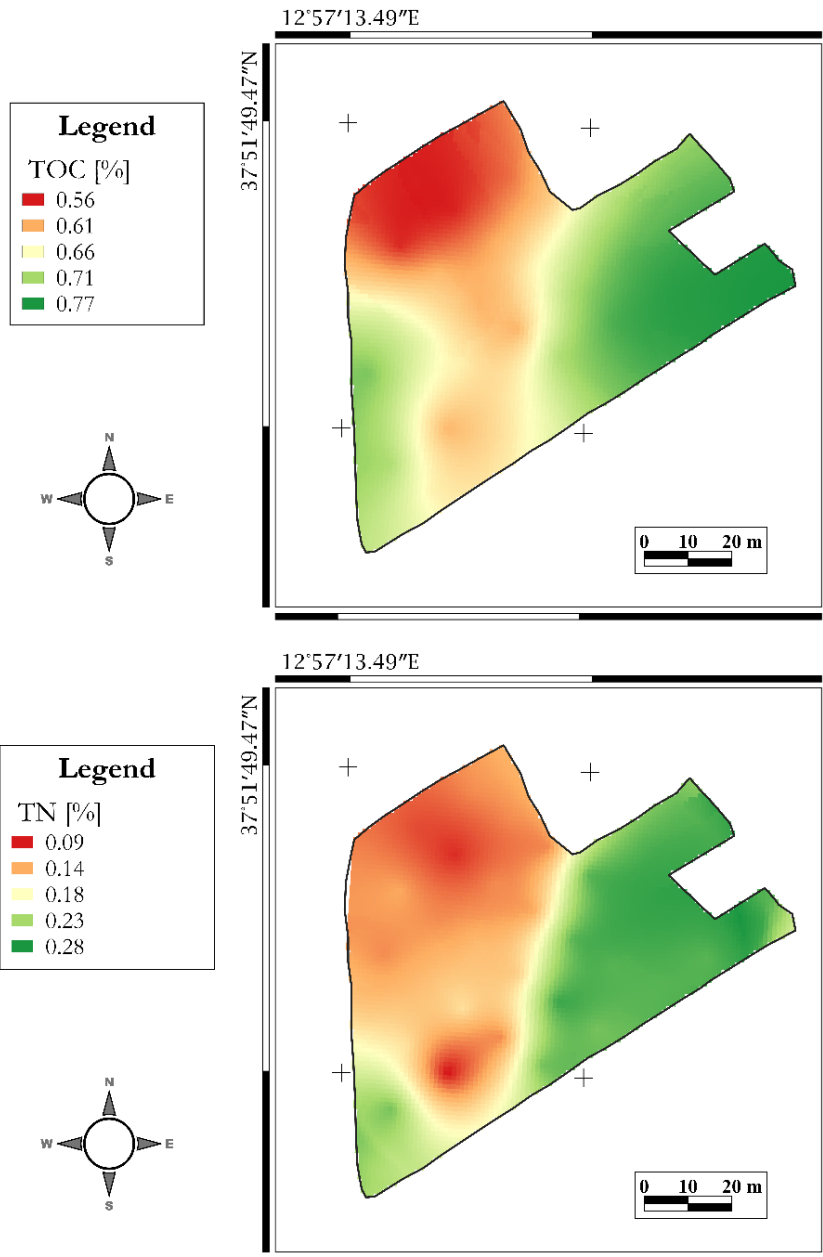

Figure 38. TOC (%) and TN (%) maps of the study area created using the ordinary kriging method on the 36 soil samples.

Other parameters such as EC, TC and soil reaction are well known in the literature to be good indicators of soil variability. In our experiment, soil reaction did not show enough variability to create differences on the map, which is why it is not represented (Table 4). In fact, this parameter varied by only 0.2 on the pH scale, from 7.15 to 7.33. Slight differences were observed in the EC (Table 4 and Figure 39). This seems to follow a similar trend to that found for the parameters TN and to a lesser extent TOC. Indeed there was strong statistical correlation with the TOC (r =0.32*) and TN (r =0.45**).
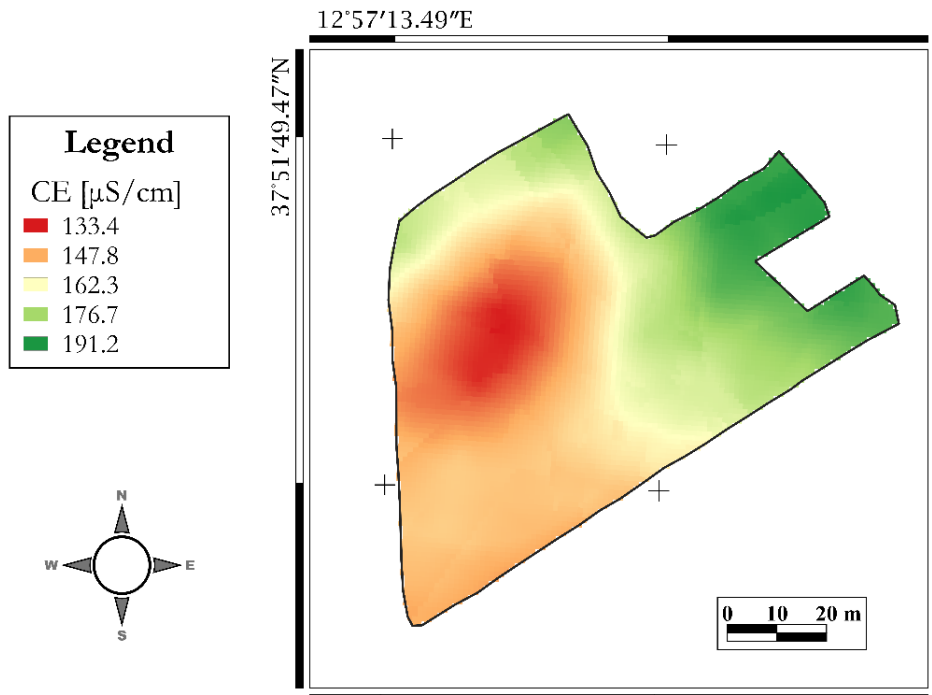
Figure 39. EC map created using the ordinary kriging method on the 36 soil samples.

The TC was slighly correlated only with the TN (r= 0.3*) as represented in the following table 6.

Table 6. Correlation matrix among the main soil parameters. Soil reaction (pH); Electrical conductivity (EC, dS m^{-1}); Total carbonates (TC, %); Clay (%); Lime (%); Sandy (%); Total Organic Carbon (TOC, %); Total Nitrogen (TN, %). *p_{value}<0.05; ** p_{value} <0.01; *** p_{value} <0.001.

	pH	E.C.	TC	Clay	Lime	Sandy	TOC	
E.C.	-0.20							1
TC	0.07	0.06						
Clay	0.10	-0.09	0.02					
Lime	0.13	-0.02	-0.07	0.12				
Sandy	-0.14	0.08	0.02	-0.88***	-0.58**			
TOC	-0.19	0.32*	0.10	0.12	0.03	-0.11		-1
TN	-0.10	0.45**	0.30*	0.02	-0.08	0.02	0.74***	

Using the co-kriging analysis it was possible to determine the three MZ using the texture, TOC, CE and TN parameters (Figure 40).
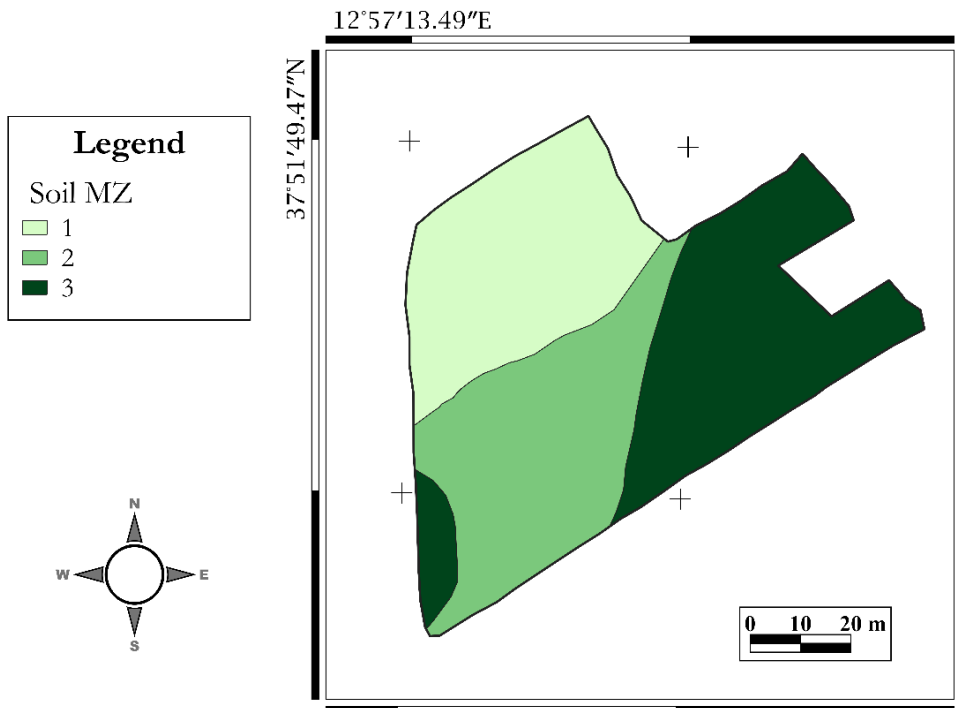

Figure 40. Different MZ from the co-kriging analysis among the main soil parameters.

In the soil MZ 3 a statistically higher concentration of TC, TOC and CE was observed compared to the other two classes. TC, TOC and CE had values of 1.01%, 0.75% and 172 dS m^{-1} respectively.

3.3. Crop variability

This section will show the results of crop investigations into the vegetative, nutritional and spectral conditions of plants. The vegetative features were expressed as biometric characteristics and the spectral condition.

3.3.1. Nutrition condition and Productivity

With regard to the crop nutritional status, of the nine elements determined on leaf samples to assess nutrient deficiencies (Table 7), only nitrogen had a concentration below the threshold (Akdemir et al., 2018; Barranco-Navero et al., 2017; Maran and Fernandez-Escobar, 1996).

Table 7. Leaf elements concentration and corresponding threshold.

Element	Mean value ± st.dev.	Threshold
N [%]	**0.92 ± 0.23**	**≥ 1.2**
K [%]	1.00 ± 0.57	≥ 0.8
Ca [%]	0.66 ± 0.24	≥ 0.5
Fe [%]	0.45 ± 0.28	≥ 0.1
Mg [%]	0.52 ± 0.38	≥ 0.1
Mn [ppm]	0.12 ± 0.02	≥ 0.06
Zn [ppm]	0.11 ± 0.02	≥ 0.06
Cu [ppm]	0.09± 0.02	≥ 0.06

TN concentration of plant leaves ranged from 0.40% to 1.46%, being on average 0.92% as reported in the figure below (Fugure 41).
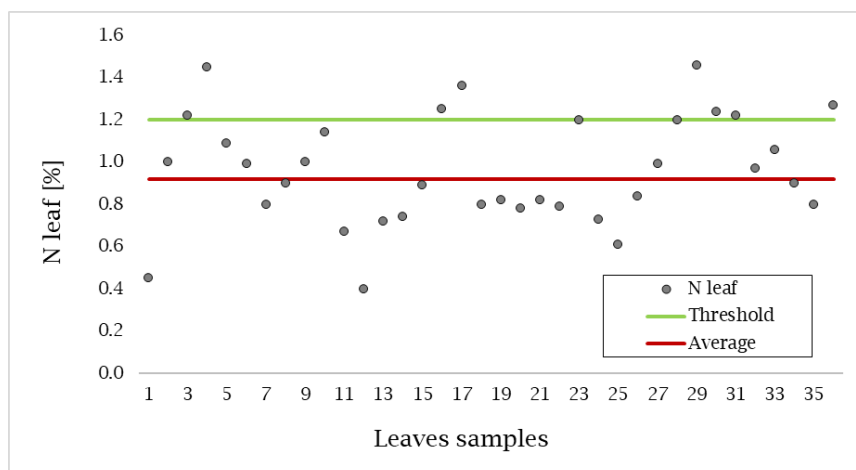

Figure 41. Distribiution of the leaf nitrogen concentration. The red line represents the average of the whole samples, while the green line represents the threshold.

The spatial distribution of the TN concentration showed a great area where it is very low. Only the right side field area showed a concentration slightly above the threshold (Figure 42).
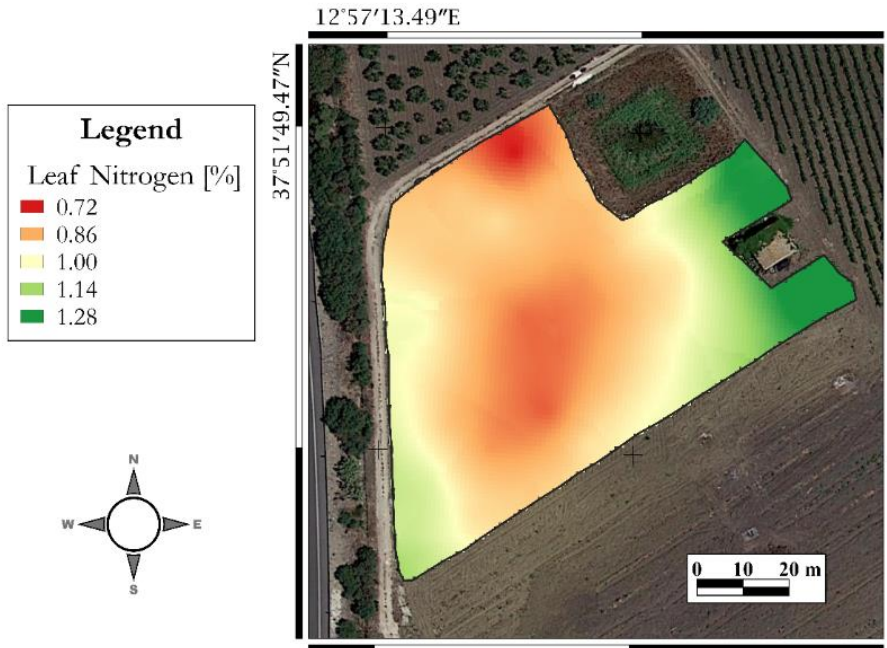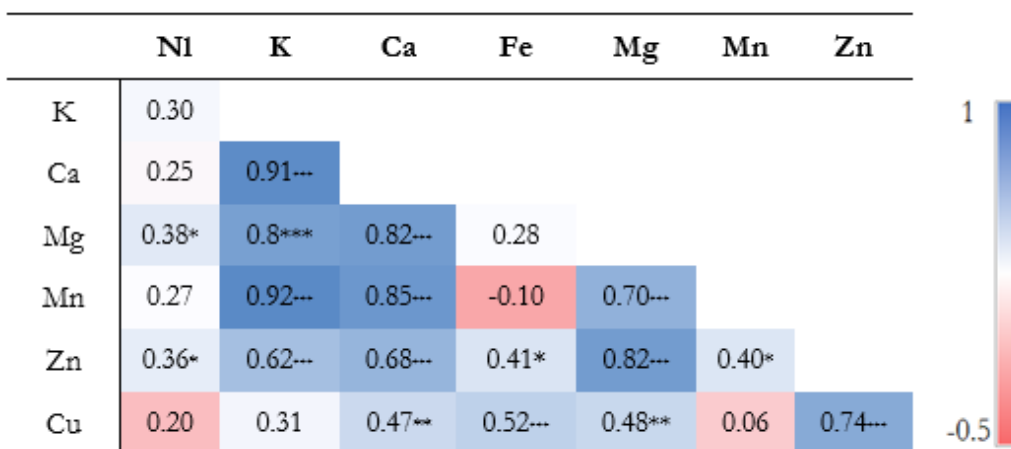

Figure 42. Nitrogen concentration Map determined from 36 leaves samples and kriging algorithm.

The different metal elements such as Ca, K, Fe, Mg, Mn, Zn and Cu showed statistically significant relationships among their leaf contents, as shown in table 8.

Table 8. Correlation matrix among the main leaf elements. Leaf Nitrogen (Nl, %); Leaf Potassium (K, %); Leaf Calcium (Ca, %); Leaf Iron (Fe, %), Leaf Magnesium (Mg, %); Leaf Manganese (Mn, ppm); Leaf Zinc (Zn, ppm); Leaf Copper (Cu, ppm); Yield (kg); TCSA (m^2); NDVI; Canopy area (m^2). *p_{value}<0.05; ** p_{value} <0.01; *** p_{value} <0.001.

	Nl	K	Ca	Fe	Mg	Mn	Zn
K	0.30						
Ca	0.25	0.91···					
Mg	0.38*	0.8***	0.82···	0.28			
Mn	0.27	0.92···	0.85···	-0.10	0.70···		
Zn	0.36*	0.62···	0.68···	0.41*	0.82···	0.40*	
Cu	0.20	0.31	0.47**	0.52···	0.48**	0.06	0.74···

Yield mapping can be considered an effective way to verify the actual response of a crop to within-field variation of soil and growth properties.

During the first experimentation year (2020) the production of each plant was determined and used to create the yield map. Total olive yield during the study year was 2.8 t, corresponding to 4.8 t ha^{-1} (12.8 kg plant^{-1}). While the second year, following intensive pruning, the plants did not produce. In the last year of the experiment (2022), there was a slightly lower average productivity than in the first year. However, the productivity of only a few sample plants were collected and quantified rather than all of them. By carrying out a multivariate analysis of the vegetative parameters most connected with production, it was possible to trace the production of each single tree. In this case, the estimated production was equal to 2.7 t ha^{-1}, while the total quantity actually produced was equal to 2.3 t ha^{-1}. Therefore, the estimated difference is around 15%.

Figure 43 shows the spatial distribution of the quantities produced by each plant in the 2020 season. It can be seen that in the lower part of the test area, there is a concentrated area of red colouring that shows almost zero production. While the greatest production is almost entirely accounted for by the border plants, a blue-coloured zone. From direct observations in the field, this zone shows a high presence of skeleton compared to the remaining part of the olive orchard.
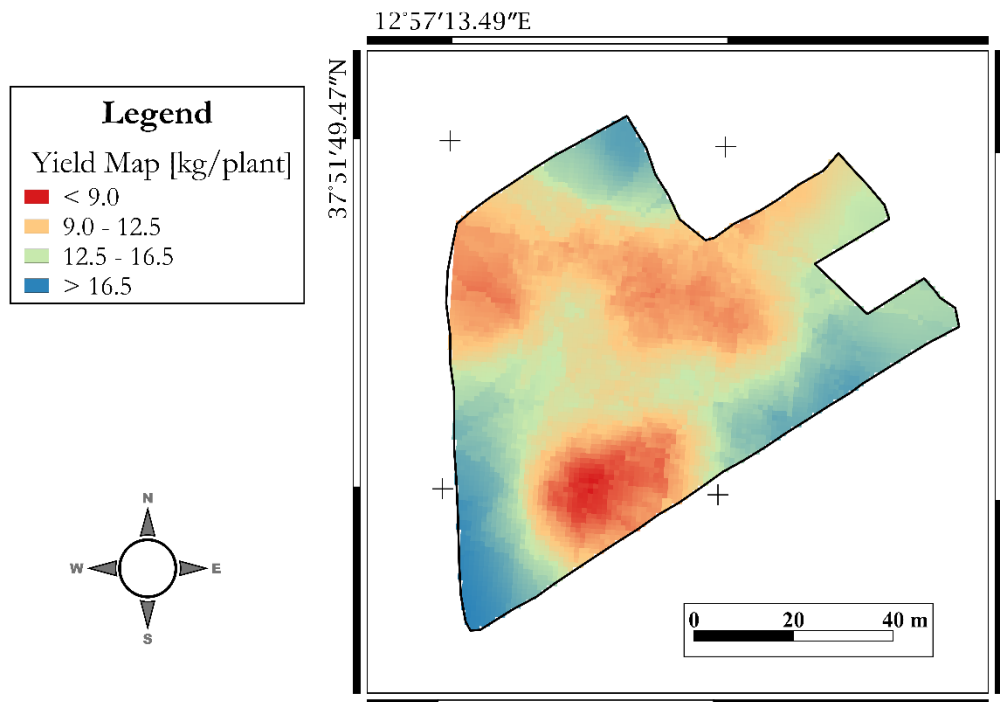
Figure 43. Yield map of the first experiemetation year in kg plant^{-1}.

The last aim of the precision olive culture is the management of the variability detected, to be able to modify the agronomic practice using the site-specific technologies. The agronomic practice investigated in the literature include management of irrigation, fertilization and pesticide spraying in the olive orchard. In our experiment, we created a nitrogen fertilisation prescription map taking into account the leaf nitrogen variability and the pedological condition assessed during the first year (Figure 44). In this case was applied 150 kg ha^{-1} only for the zone where the fertilization was required (yellow zone). It represents the 76% of the total area.
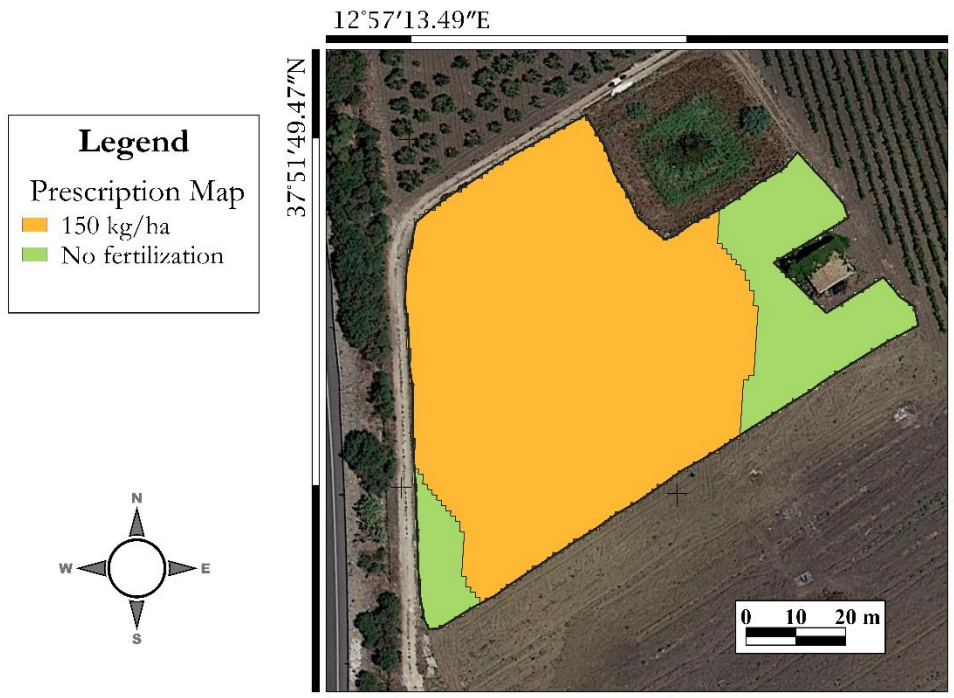
Figure 44. Prescription map according the leaf nitrogen deficit and pedological conditions.

According to the soil classes, with the main soil, vegetative, spectral variables and the production map, it was possible to obtain a greater spatial detail of the area that needed fertilization (Figure 45). In this case, the surface to be fertilized was always the same as in figure 44, but other areas with different nitrogen needs were identified. The three classes were identified by co-kriging while the quantity to be distributed was calculated by linear interpolation between the maximum and minimum dose that is generally applied in the area. The total quantity to be distributed per hectare in this case was equal to 50kg ha^{-1} This quantity was obtained by multiplying the quantity to be distributed per MZ by the relative surface area.
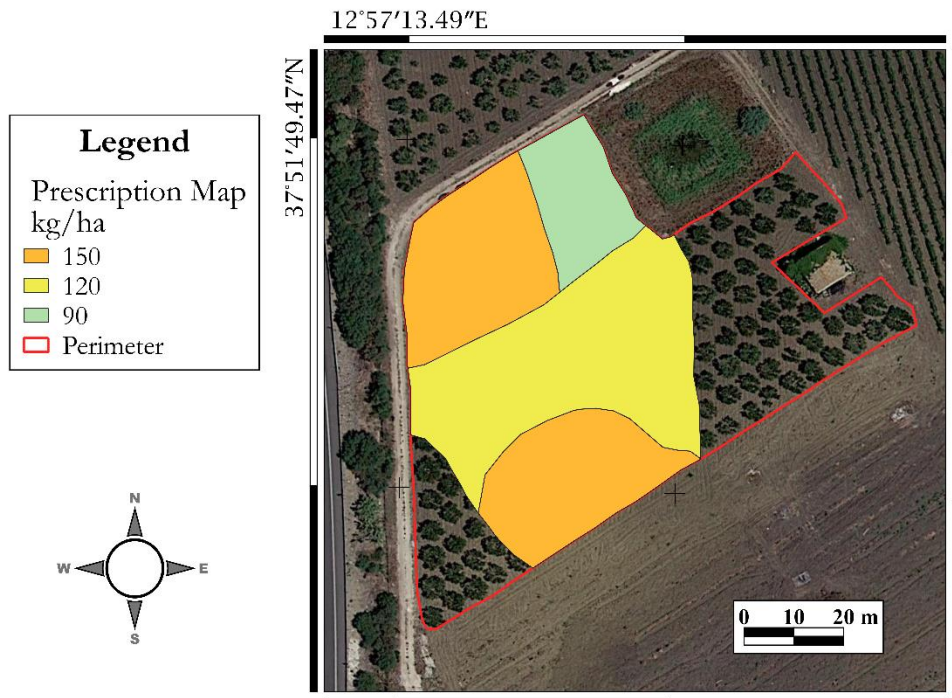
Figure 45. Prescription map according to the vegetative, spectral and productivity conditions merged with co-kriging method, calculated only for the nitrogen deficit zone

3.3.2. Biometric analysis

The biometric conditions of each plant can be expressed in several ways and represents their real vigour status. The olive orchard's vigour conditions can have a great influence on its optimal management. Therefore, their proper evaluation is an essential element of site-specific management. In this experiment, the biometric conditions has been expressed as: TCSA, HC, CA, and CV. TCSA showed a certain heterogeneity among the plants in the field, its values ranging in whole plot from 50 cm^2 to 600 cm^2 with a mean of 297.3 cm^2 ± 109.6. These differences were reflected in growth and production activity as showed also in Noori and Panda (2016). Indeed, the TCSA values were statistically significant correlated with different variables expressing plant vigour such as canopy area extracted from the multispectral image. During the 2021 the correlation was of r = 0.78*** while in the 2022 was sligtly lowest (r = 0.65***; Figure 46).

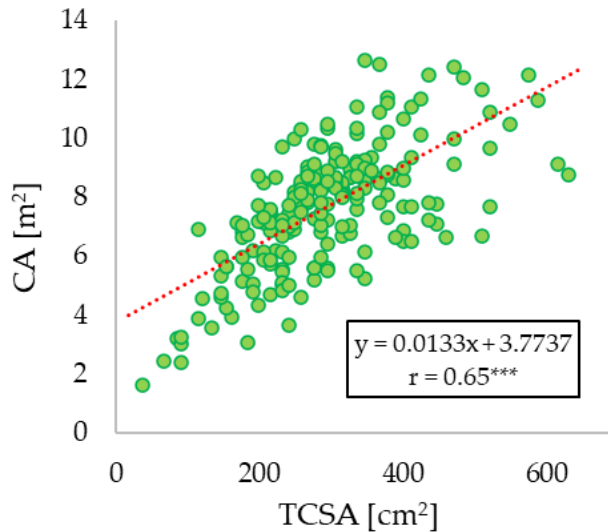**Figure 46.** Correlations between TCSA and CA. $p_{value} < 0.001(***)$.

Crown height is another of those parameters that is often used to quantify plant vigour. However, depending on the breeding form, this can be very variable and is not always a good indicator of vigour. From a remote platform, such as a UAV, it has been possible to derive this parameter, albeit with results that are not always satisfactory. However, this parameter was also able to describe the variability present in the olive orchard and in the third year, before pruning, had an average of 3.57m and 2.91 after pruning. This parameter shows an average of 4.25m, 3.57m and 3.1m from the lowest to the highest level of vigour. Thus, after the pruning the HC decreased for all vigour levels of 3.05m, 2.91m and 2.71m for LV, MV and HV respectively.

ANOVA was performed to evaluate the influence of the different flight path in the Hc reconstruction. It is observed that the NS flight path overestimated the Hc compared to the D and EO directions, which showed no statistically significant differences (Figure 47). Furthermore, the D flight path showed the highest correlation with the ground measurements (R^2 0.89***) compared to the other two directions, while the lowest value was given by the EO direction (R^2 0.57***).
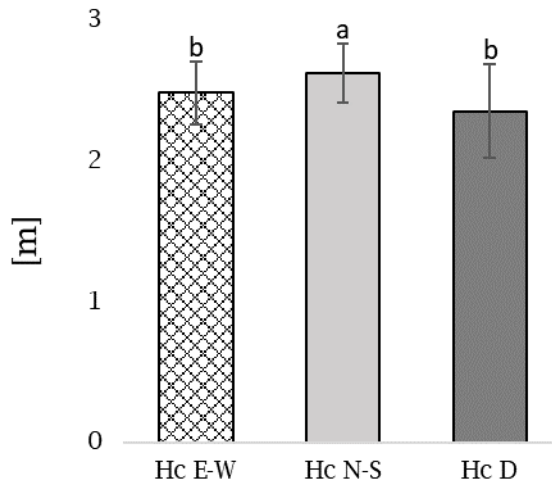
Figure 47. Influence of the different flight path (E-W, N-S, D) on the HC reconstruction. Results from ANOVA test ($p_{value} > 0.05$) and Tukey test.

The canopy area was extracted from the NDVI map or from the 3D model reconstruction such as explained in the previous paragraph. CA was the vigour parameter that correlated best with production, spectral conditions and other vigour characteristics. This showed a variable trend depending on the year and plant growth. However, the estimated CA in 2021 and that in 2022 with flights 3 and 7 at 70m showed a close correlation equal to $r = 0.81^{***}$. The pruning and the flight path have an important impact in its change and evaluation (Figure 48 and 49). In fact, using the flights 8 and 9 a reduction in CA is observed.
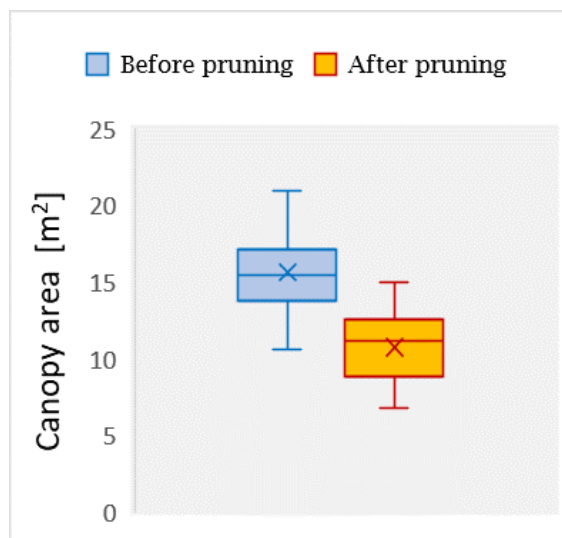

Figure 48. Boxplot of the CA before and after the pruning operation.

The CA before pruning had an average area of 15.62 m^2 and was reduced to 10.75 m^2 after pruning, showing a reduction of 31.17%. This percentage seems to be slightly different for the three vigour levels. The CA before pruning was on average 16.54m^2 and after pruning it was reduced to 10.43m^2 for the high vigour group; thus there was a reduction of 37%. The CA before pruning was on average 12.56 m^2 and after pruning it was reduced to 9.8m^2 for the medium vigour group; thus there was a reduction of 0.22%. Finally, the CA decreased from a value of 10.61m^2 to 7.23m^2 for the high vigour group; thus there was a reduction of 0.32%.
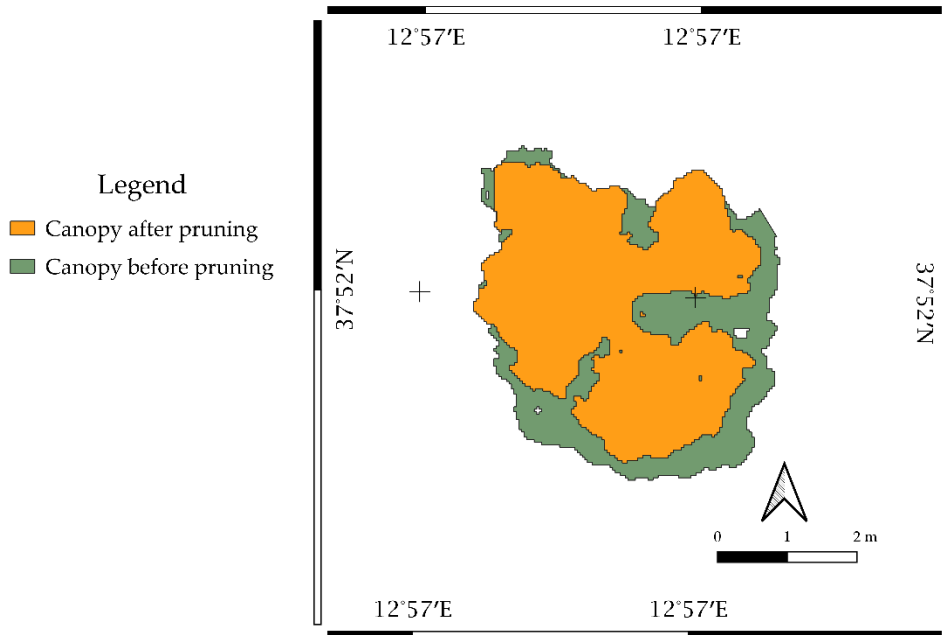

Figure 49. Comparison between the canopy area before and after pruning operation.

From the ANOVA analysis of the influence of the different flight directions, it is observed that the diagonal flight direction underestimated the canopy area compared to the NS and EO directions, which showed no statistically significant differences (Figure 50). Furthermore, the CA from the diagonal flight showed the lowest correlation with the ground measurements (R^2 0.76***) compared to the other two directions, while the highest value was given by the NS direction (R^2 0.99***).
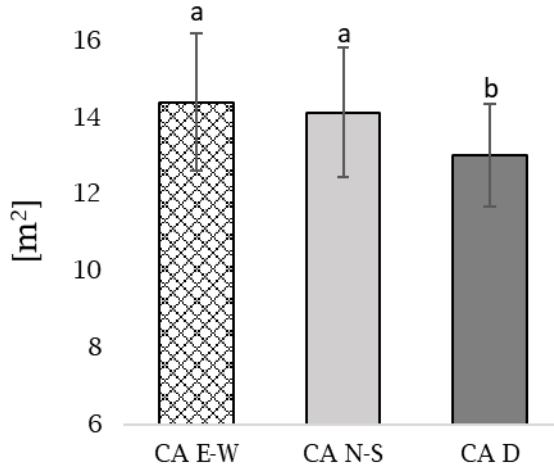
Figure 50. Influence of the different flight paths (E-W, N-S, D) on the CA reconstruction. Results from ANOVA test ($p_{value} > 0.05$) and Tukey test.

Comparing flights 3, 4 and 7 was evaluated the differences determined by the flight height on the geometric reconstruction and the canopy area estimation (Fig. 51 and 52). Multi-way ANOVA analysis showed that there were no statistically significant differences and interaction between the heights performed in flight 1 and 2 and the period. However, for flight 7 the plants were more developed and the ANOVA analysis showed statistically significant differences between the flight height of 30m and 70m. The greatest values were found in the flight at 70m.
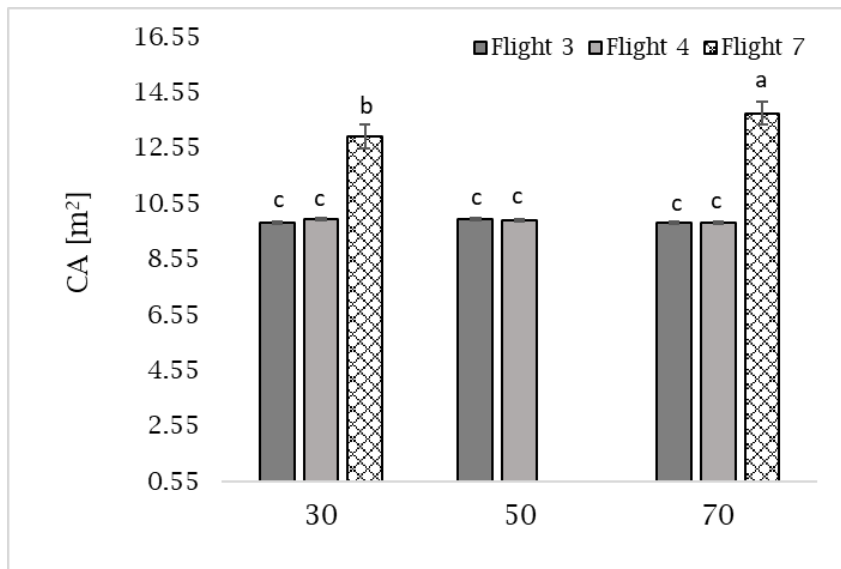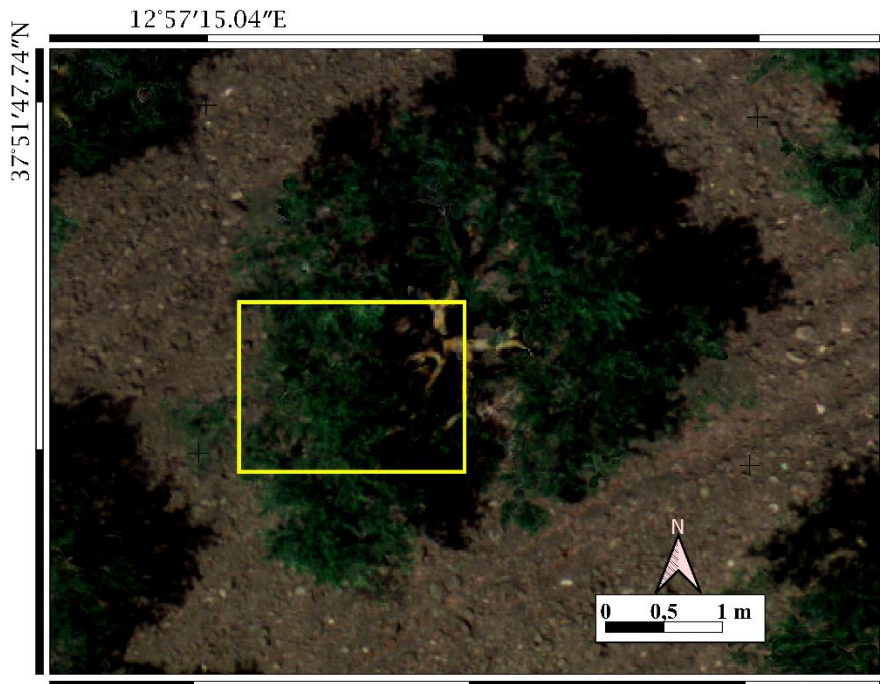

Figure 51. Influence of the different flight altitude on the CA reconstruction. Results from ANOVA test ($p_{value} > 0.05$) and Tukey test.

Flight alt: 70m   50m   30m
GSD: 3.68cm   2.63cm   1.58cm

Figure 52. Different geometric resolutions from the flights 3c, 3b and 3a.

Starting from the CA calculated using the Qgis software and the ground measure, it was possible to carry out data validation. In fact, the accuracy assessment between the observed and estimated values for CA resulted in RMSE equal to 0.54 and a statistically significant close linear relationship with $R^2 = 0.98$*** (Figure 53).
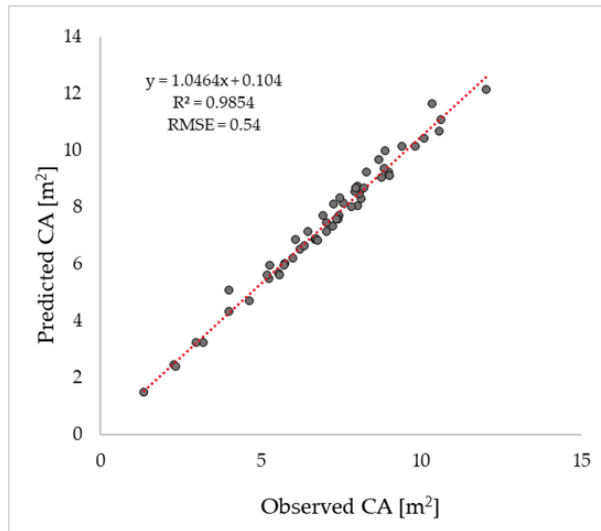
Figure 53. Comparison between ground measured and UAV-estimated CA.

CA data estimated using flight7 allowed the correlation between the flight made at 30m and the flight made at 70m to be identified. Their correlation showed a statically significant R^2 value of $0.87***$. Instead, the two datasets didn't show any difference applying the ANOVA test.

A particular parameter valuated using the flight 3 and 4 was the perimeter of the canopy. This parameter, when the tree had a canopy that was not very dense showed several differences. Indeed, from the ANOVA test showed differences statically significance between the flight altitude and period of flight (Figure 54).
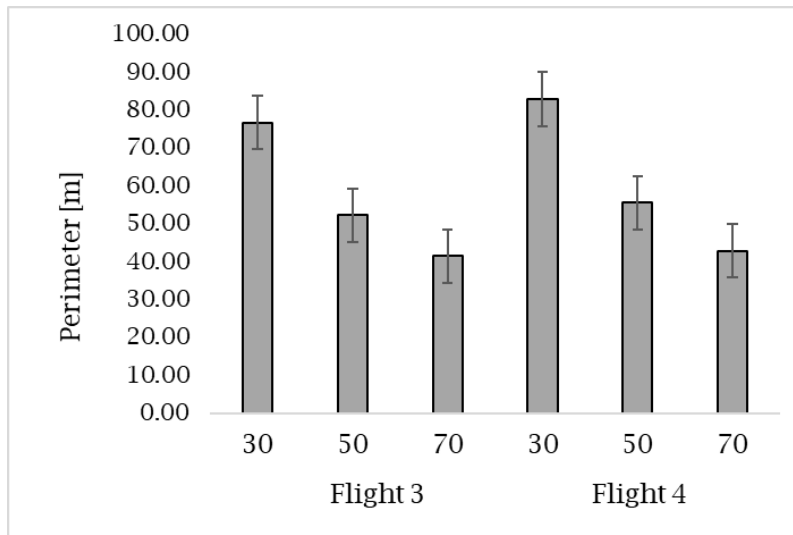

Figure 54. Influence of the different flight altitude on the canopy perimeter estimation. Result from ANOVA test ($p_{value} > 0.05$) and Tukey test.

The influence of the perimeter of the inner holes with respect to the outer perimeter was found to be different depending on the height of flight. However, the most interesting finding concerns the influence of the area of the holes compared to the air deprived of the holes (Figure 55)
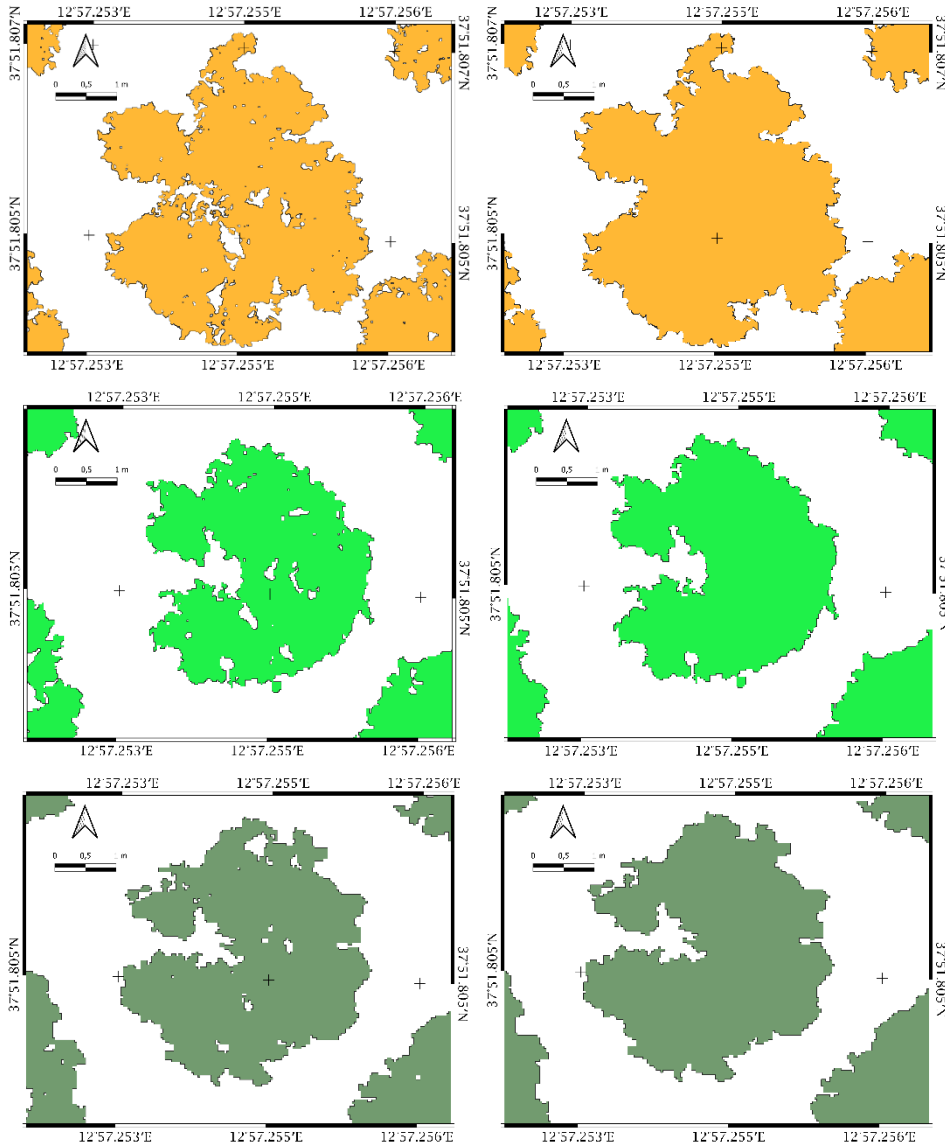

Figure 55. Difference between the CA with (sx) and without (dx) holes form the flights at 30m, 50m and 70m in above, medium and below images respectively.

These differences were statically different using the ANOVA test. They were 34%, 22% and 12% for flight heights 30, 50 and 70 respectively (Figure 56).
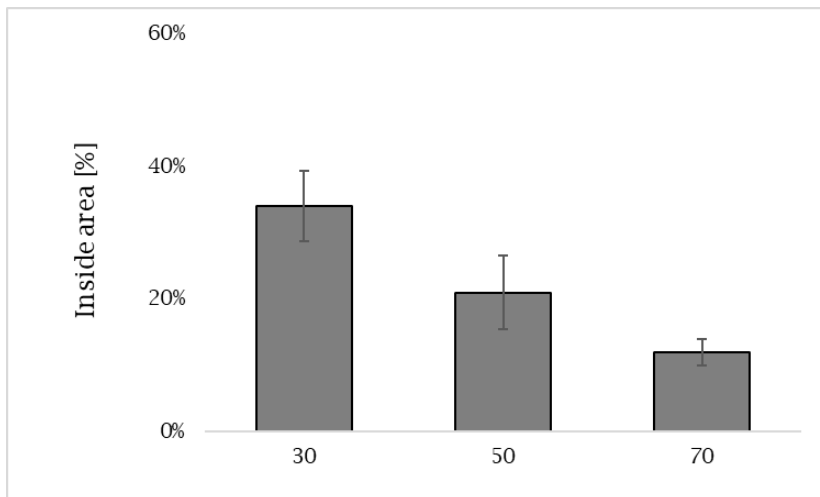
Figure 56. Percentage hole area respect to the entire CA without holes.

Figure 57 shows the 3-D representation generated in two fields with single-tree. Each flight camping generated images composed of two products: the ortho-mosaic and its associated DSM. The plants were modelled in 3-D with high accuracy, showing the irregular shape of the trees including typical crown gaps and branch distribution, which allowed computing tree volume regarding the real crown shape. The orthomosaic were successfully created in all the studied scenarios. The application of image reconstruction using SfM techniques allowed the generation of detailed DSM, as shown in Figure 57, CV showed a good ability in reconstructing the geometry for each individual tree in the whole plot. Indeed, it showed a strong relationship with the other vigour parameters and the production capacity of the plants ($r = 0.74$***).

Figure 57. 3D reconstruction of the whole study area and zoom of one tree.

CV was validated using the ground truth measured the same day as the flight. CV showed an underestimation of the final volume when compared to field measurements. In this case, the coefficient of determination was $R^2 = 0.67^{***}$ with RMSE equal to 9.5 m^3 (Figure 58).
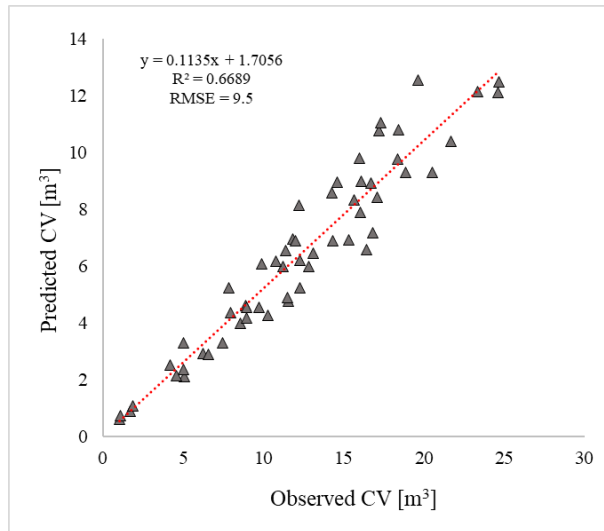
Figure 58. Comparison between ground measured and UAV-estimated CV.

Volume differences between the observed and estimated values do not denote real errors of the UAV-based measurements because the ground-based values were derived by applying the geometric equation that considers trees as full, ellipsoid shapes producing inaccurate estimates (Torres-Sánchez et al., 2015b; West, 2009). In contrast, the three-dimensional products derived from the 3D reconstruction, reproduce the irregular shape of the canopy, yielding better estimates of tree volume as showed in Figure 59.

Figure 59. Comparison between geometric (red shape) and SFM reconstruction of the tree.

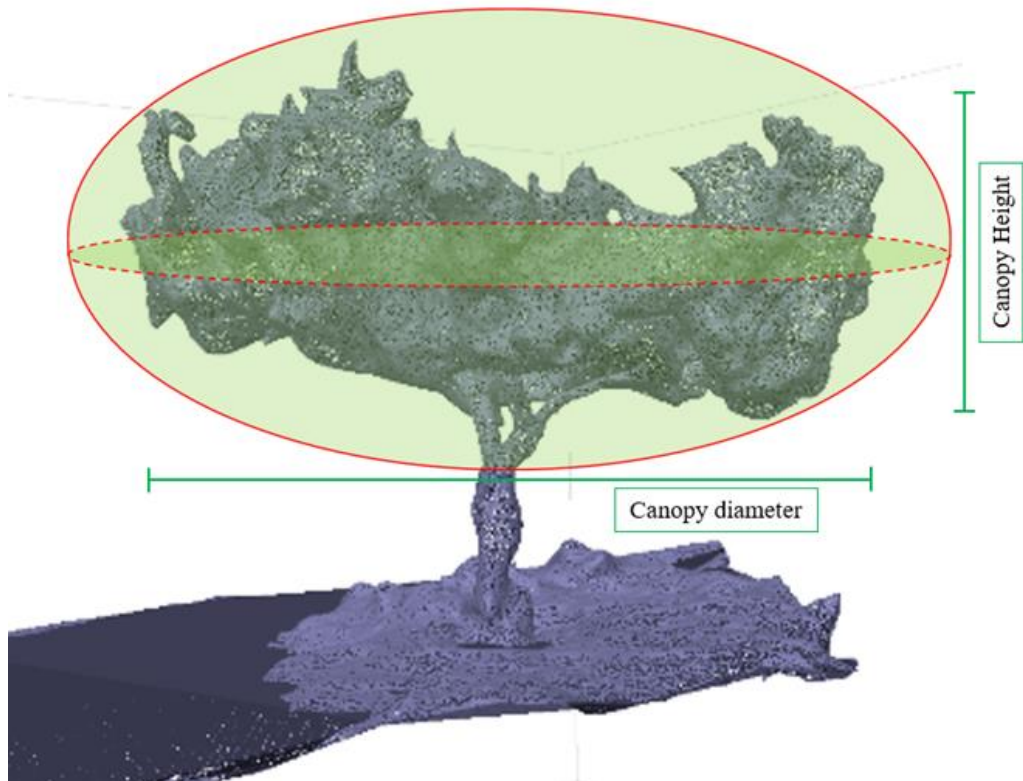The pruning operation had a determined impact on the CV variation (Figure 60ab). In fact, using the flights 8 and 9 a reduction in CV is observed. The CV before pruning had an average area of 43 m^3 and was reduced to 26 m^3 after pruning, showing a reduction of 39.2% in whole plot.
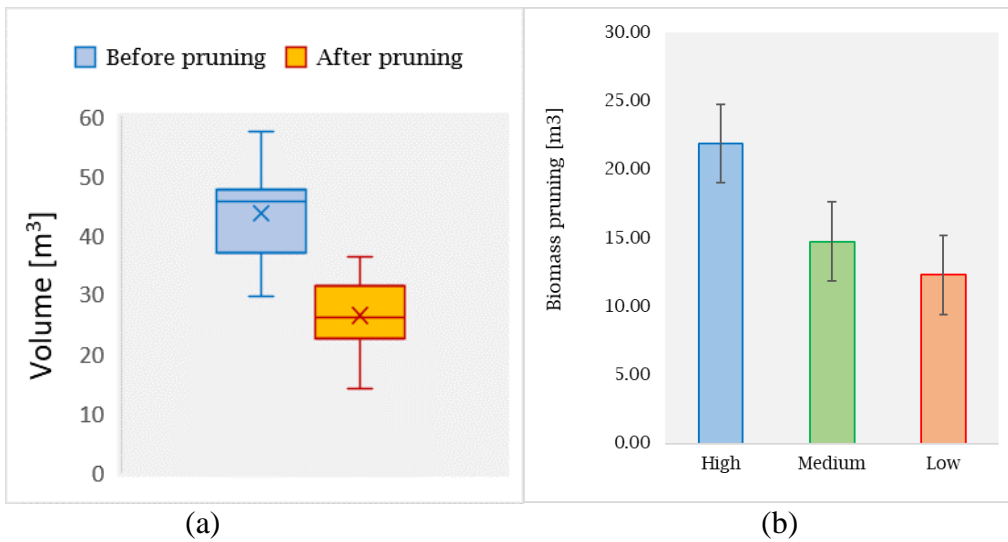
Figure 60. (**a**) Boxplot of the CV before and after the pruning operation; (**b**) Bar-plot of the biomass amount removed with the pruning operation in the three vigour levels.

This percentage seems to be slightly different for the three vigour levels. Indeed, the low vigour group showed a reduction of 41%, while the medium and high vigour group showed a reduction of 34% and 47%, respectively. However, the biomass amount pruning removed from the pruning operation was good correlated ($R^2 = 0.63$) in whole plot (Figure 61).
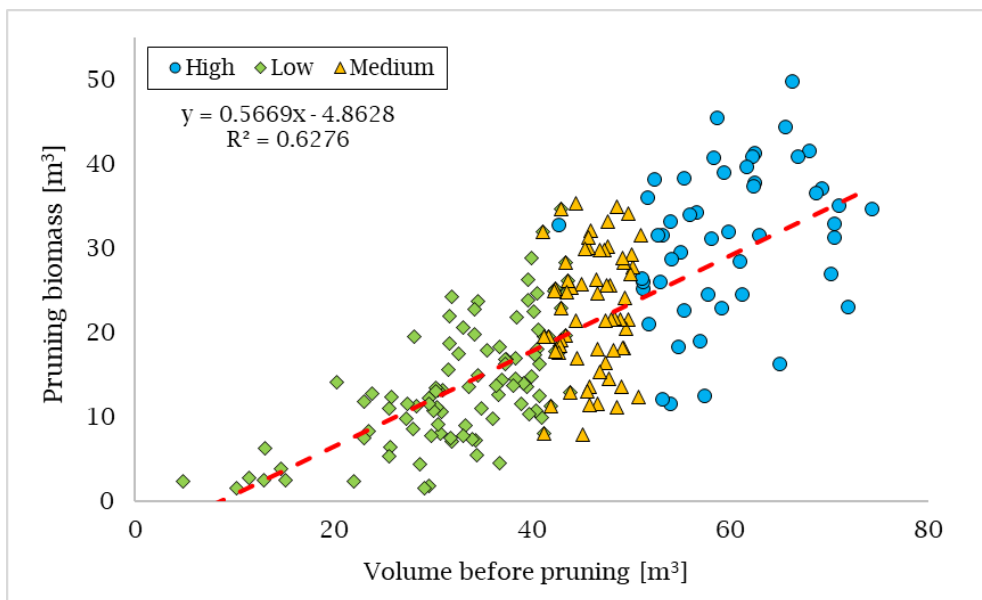
Figure 61. Correlation between the biomass quantity and the volume before the pruning separated for the three vigour levels.

Taking selected plants in which, a more balanced pruning was carried out, the correlation between the amount of biomass removed and the initial plant volume was higher (R^2 =0.76 ***, Figure 62 upper). The correlation between the difference of CV with the pruning weight showed a good linear correlation (R^2 =0.65***) in the plant selected with the same vigour level (Figure 62 below).
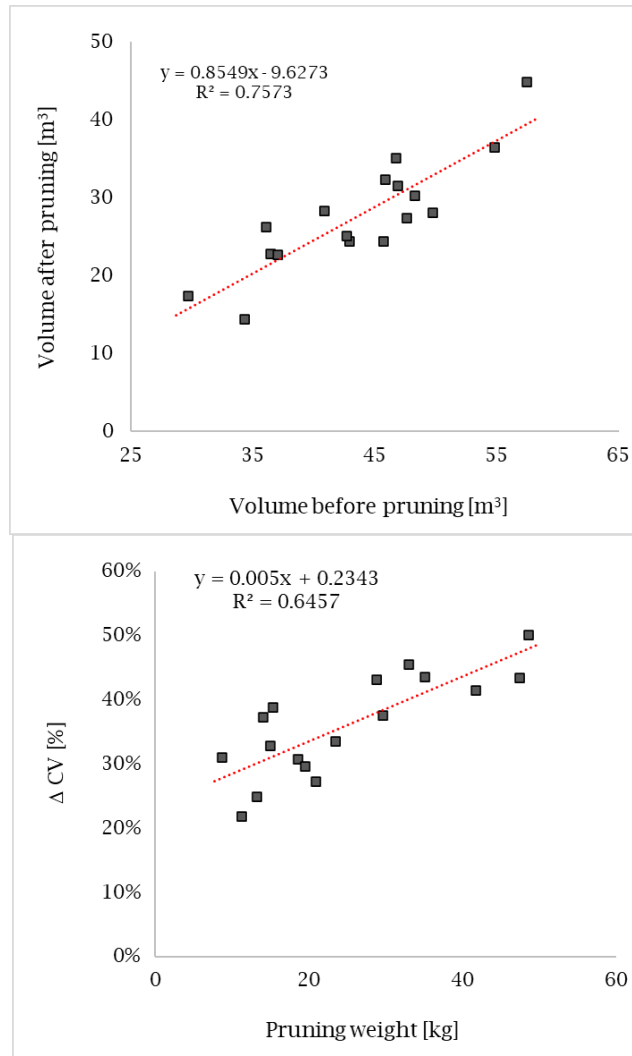
Figure 62. (above) Correlation between the biomass quantity and the volume before the pruning separated for the selected plants. (below) Correlation between the ΔCV and pruning weight.

Using the pruning weight data for the 30 selected plants, it was observed that the weight of the removed biomass was not proportional to the volume of the biomass. In fact, the pruning density (kg/m^3) was calculated and it was found that per vigour class there was a high homogeneity of the removed material (Figure 63). ANOVA analysis showed that there were statistically significant differences

between the high vigour group and the low vigour group, while the medium vigour group performed intermediately.
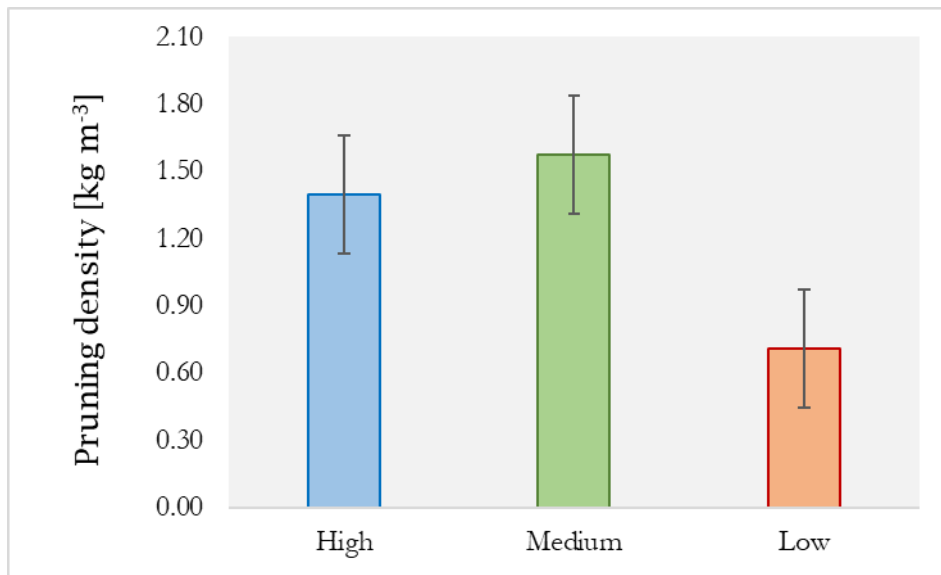
Figure 63. Bar-plot of the biomass pruning density removed with the pruning operation in the three vigour levels.

ANOVA was performed to evaluate the influence of the different flight path in the CV reconstruction. It is observed that the diagonal flight path overestimated the CV compared to the NS and EO directions, which showed no statistically significant differences (Figure 64). Furthermore, the CV from the diagonal flight showed the lowest correlation with the ground measurements (R^2 0.77***) compared to the other two directions, while the highest value was given by the NS direction (R^2 0.93***).

Figure 64. Influence of the different flight path ion the CV reconstruction. Result from ANOVA test ($p_{value} > 0.05$) and Tukey test.

Finally, in the Table 9 below is represent an overview of which were the best correlations results obtained between HC, CA and CV values found from the different flight directions and ground measurements.

Hc E-O

Ground Hc

$y = 0.8588x + 1.3413$
$R^2 = 0.5678$

Hc N-S

$y = 1.0452x + 0.6591$
$R^2 = 0.8705$

Hc Diagonal

$y = 1.0128x + 1.1128$
$R^2 = 0.8859$

CA E-O

Ground CA

$y = 0.7858x + 2.692$
$R^2 = 0.8165$

CA N-S

$y = 1.0864x - 0.7426$
$R^2 = 0.9852$

CA Diagonal

$y = 1.2902x - 2.4652$
$R^2 = 0.755$

CV E-O

Ground CV

$y = 1.0474x + 16.226$
$R^2 = 0.8327$

CV N-S

$y = 1.279x + 9.0594$
$R^2 = 0.9333$

CV Diagonal

$y = 1.0714x - 0.4741$
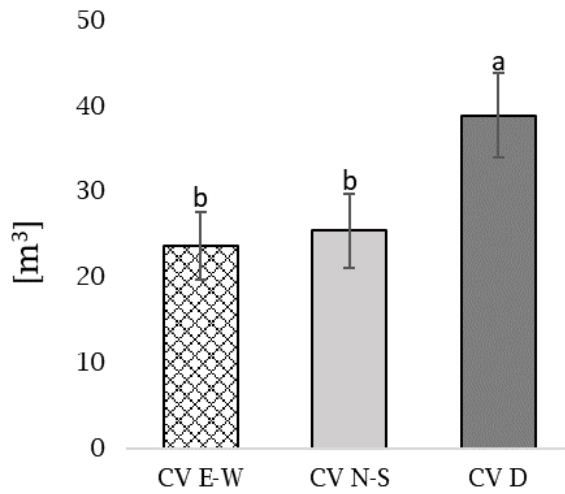$R^2 = 0.7664$
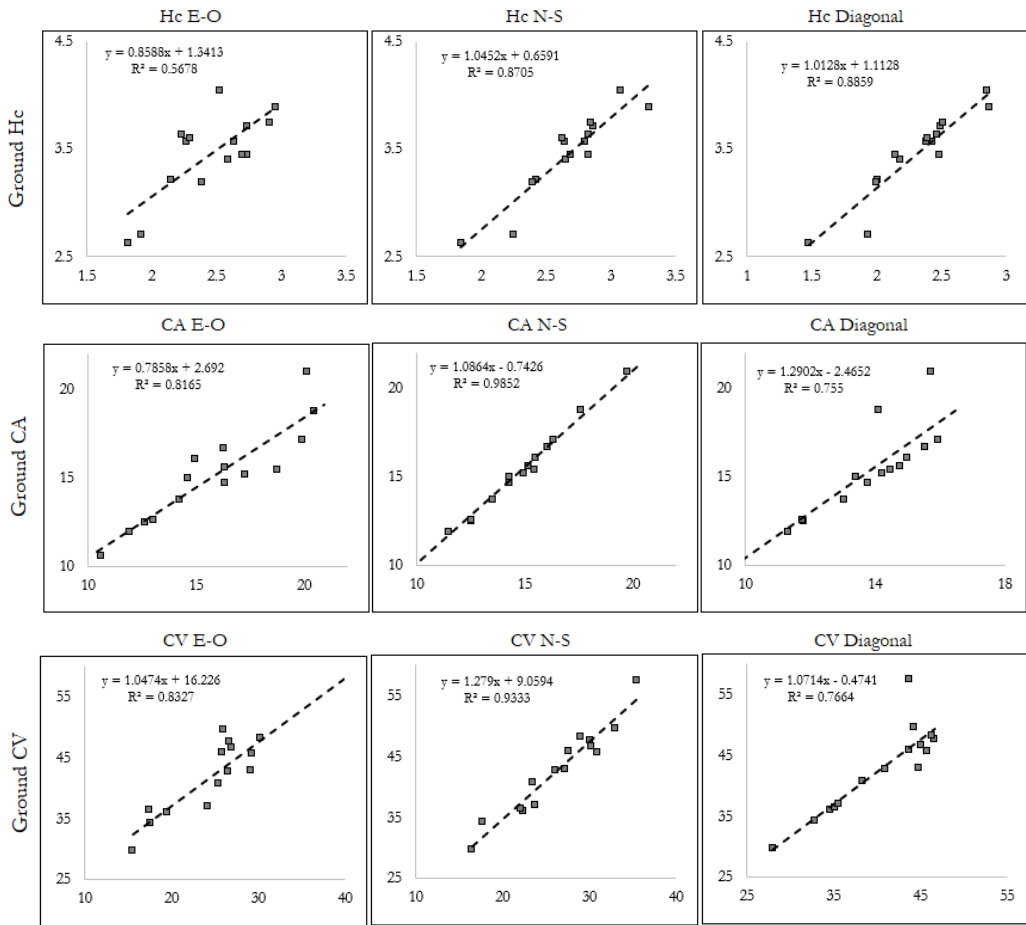
Table 9. Correlation among some vegetative parameters and their ground truth.

The correlation matrix results among Hc, Ca and CV calculated from different flight paths are summarized in table 10.

	CA E-O	CA N-S	CA D	Hc E-O	Hc N-S	Hc D	CV E-O	CV N-S	
CA E-O	1								1
CA N-S	0.903	1							
CA D	0.861	0.911	1						
Hc E-O	0.450	0.515	0.516	1					
Hc N-S	0.537	0.601	0.552	0.866	1				
Hc D	0.319	0.378	0.310	0.578	0.639	1			
CV E-O	0.853	0.828	0.775	0.775	0.730	0.451	1		
CV N-S	0.826	0.929	0.829	0.694	0.786	0.489	0.894	1	
CV D	0.837	0.909	0.949	0.684	0.733	0.437	0.871	0.934	0

Table 10. Correlation matrix among vegetative parameters: Hc, CA and CV estimated from the flight paths.

CV data estimated using ID Flight 7 allowed the correlation between the flight made at 30m and the flight made at 70m to be identified. Their correlation showed a statically significant R^2 value of 0.69 (Figure 65).
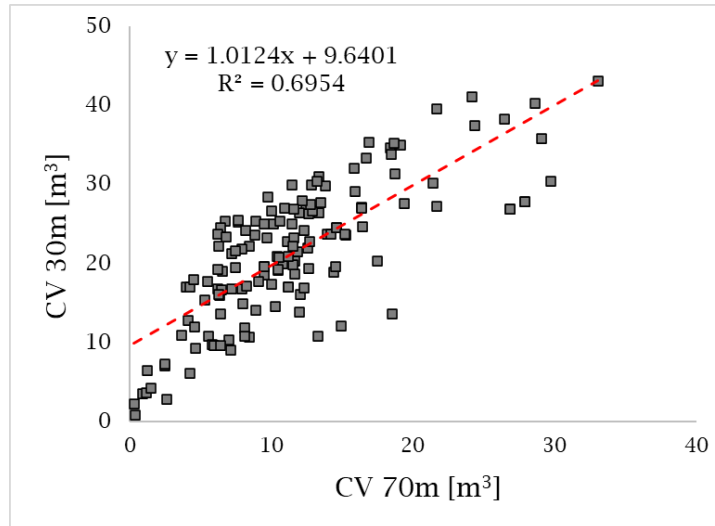
Figure 65. Comparison of CV values estimated from ID Flights 7a and 7b.

The highest values were present in the values estimated at 30m. The ANOVA analysis of variance shows that the two datasets were statically different. Another interesting finding that was not shown is that the best DSM reconstruction was performed using the RGB image processing compared to the multi-spectral images in the flight 7a. Instead, flight 7b showed a better estimation of the DSM from multispectral data processing. Either way, the best DSM elaboration was performed reconstructing it from the dense cloud. Instead, the Mesh product was not able to differentiate well the soil from the canopy.

By crossing all the vegetative variables such as TCSA, CA, CV and HC detected at the beginning of 2021, it was possible to define the MZ zones using the co-kriging method (Figure 66). These zones have allowed for the construction of a more accurate prescription map as shown later.
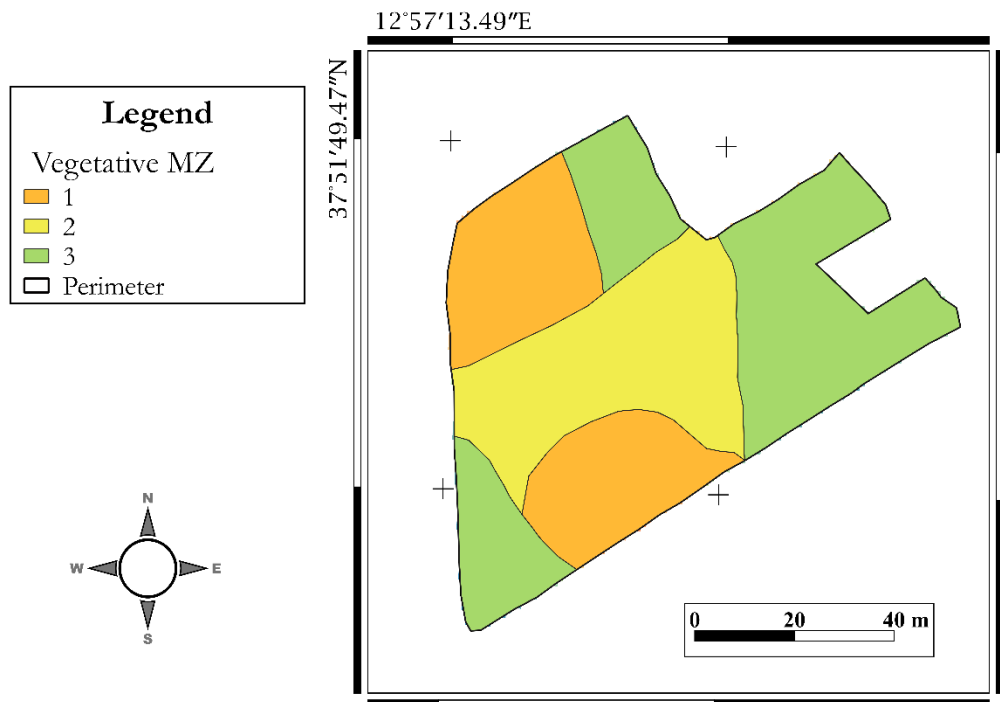
Figure 66. Different vegetative MZ from the co-kriging analysis among the main parameters.

3.3.3. Spectral analysis

The investigation of the spatial variability of crop spectral characteristics makes it possible to determine the actual growing conditions of each plant. These data can be expressed in different ways, but the use of the vegetation index is a simple and smart method to understand the spectral conditions of crops. In our study, we measured spectral conditions using two major platforms and sensors applied in precision olive growing. The platforms were a UAV and a spectroradiometer as described in materials and methods. Continuous monitoring of the vegetation during the years 2021 and 2022 made it possible to observe plant growth in spectral terms as well (Figure 67). The NDVI showed an increasing trend during the main growing season from April to September. This trend was observed for the three vigour levels determined by clustering. A characteristic peak is observed in the May period for both seasons and with minor effect for all three vigour levels. In general, the NDVI had an average value of 0.67 and 0.78 during the 2021 and 2022 seasons respectively.

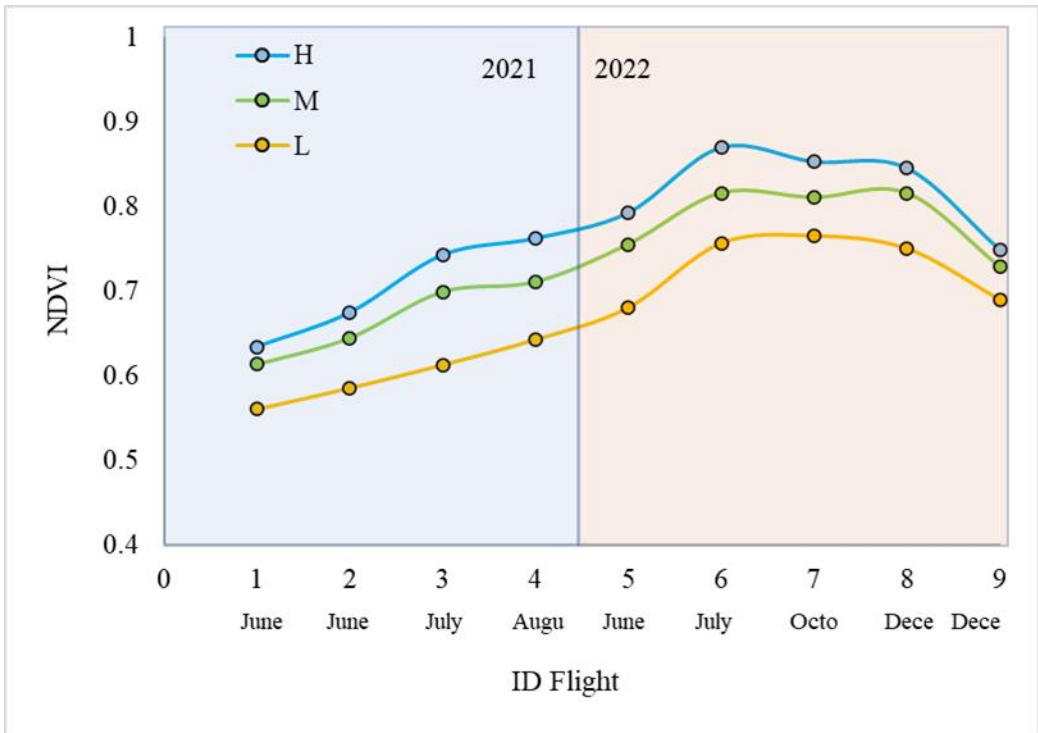**Figure 67**. Average NDVI trend of the total plants for the three vigour levels (H, M, L).

Sentinel 2 was used to observe the NDVI trend during the 2020, 2021 and 2022 years (Figure 68). It showed an increasing trend during the rainy season. However, an increasing trend can also be observed during the season from May to September, even with less intensity.
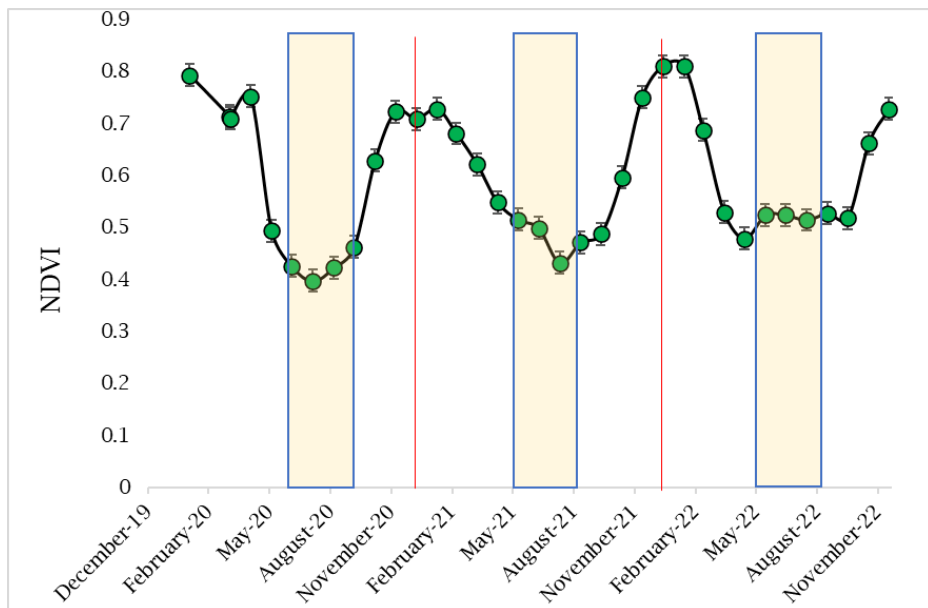
Figure 68. Average NDVI trend of the whole plot calculated with Sentinel2 images according to the equation 20 for the years 2020, 2021 and 2022. The bars highlight the growing season of the olive tree, while the red line splits the different years.

The multispectral informations were obtained for each individual tree canopy and for the different exposures using the UAV images. From the multispectral data, the mean values of the three vegetation indices recorded in the 24 selected plants were: 0.62 ± 0.03, 0.53 ± 0.03 and 0.71 ± 0.03 for NDVI, NDRE and MSAVI respectively. ANOVA analysis shows that the mean values of the three vegetation indices are statistically different ($p_{value} < 0.005$) from each other for each exposure. No statistically significant differences were found among the mean values of the four exposures for each index (Figure 69).
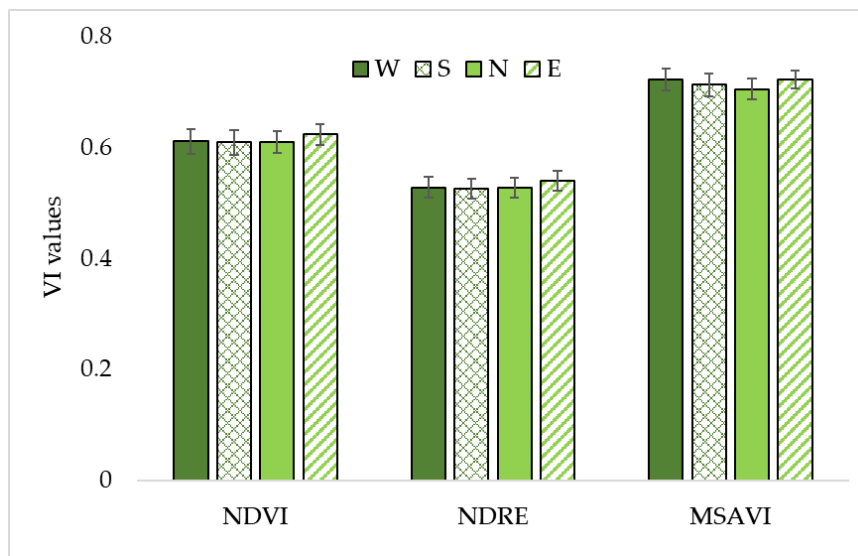
Figure 69. NDVI, NDRE and MSAVI mean values of the individual canopies (n = 24), divided into the four exposures.

The NDVI calculated from drone images, having a very low ground resolution (around 3cm), allowed for a good investigation of the spectral conditions of the canopy. As can be seen in the figure 70 it was possible to quantify which parts of the canopy are in a better vegetative state.
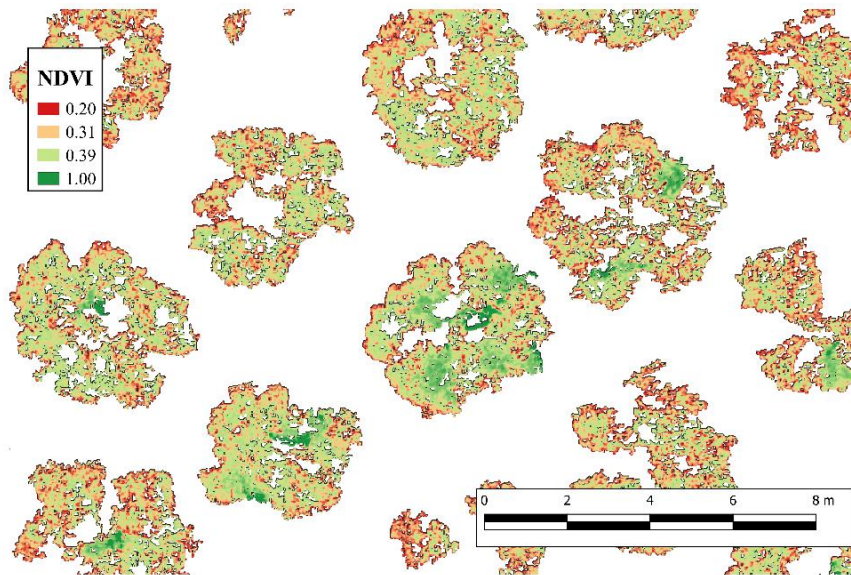
Figure 70. NDVI representation for each canopy in a portion of the plot.

NDVI correlates closely with plant vigour conditions, so any agronomic practices that are able to change them can influence the spectral response. Using the processed data from flights 8 and 9, it was also possible to see what the reduction in NDVI was between the vigour levels (Figure 71).
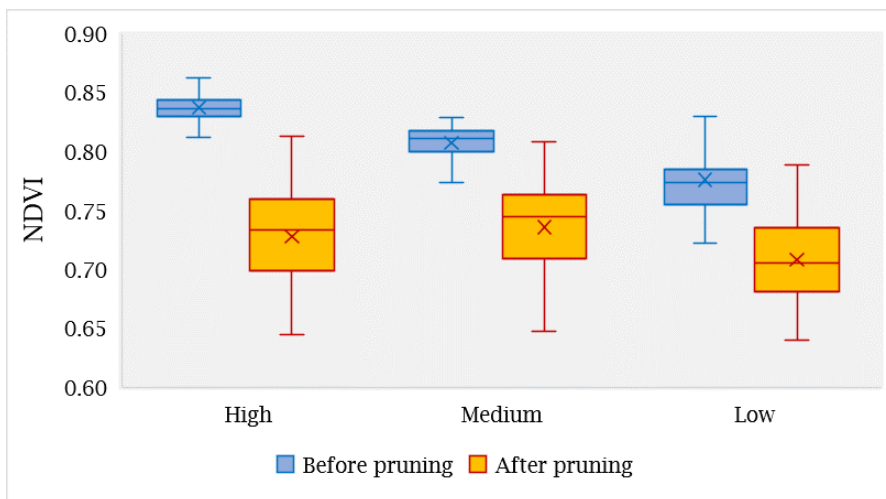
Figure 71. Different NDVI values before and after the pruning operation for the three vigour classes.

Vigour maps obtained from kriging interpolation on NDVI values before and after pruning showed a decrease in the HV and MV groups and an increase in the LV group (Figure 72).
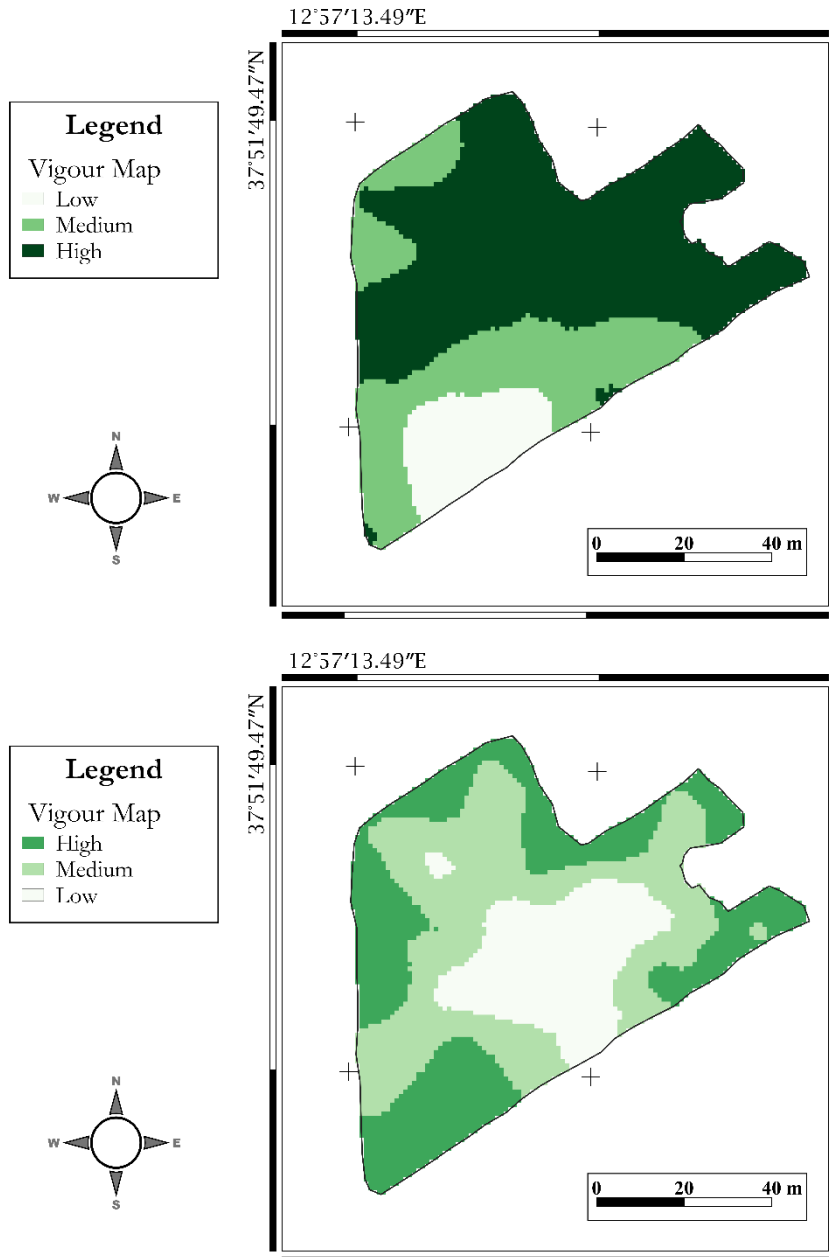
Figure 72. Vigour map before (above) and after (below) the pruning operation, obtained from the NDVI kriging interpolation.

ANOVA was performed to evaluate the influence of the different flight paths in the NDVIvalues. Unlike what was observed for CV, CA and Hc, the flight paths did not lead to statically significant differences (Figure 73).
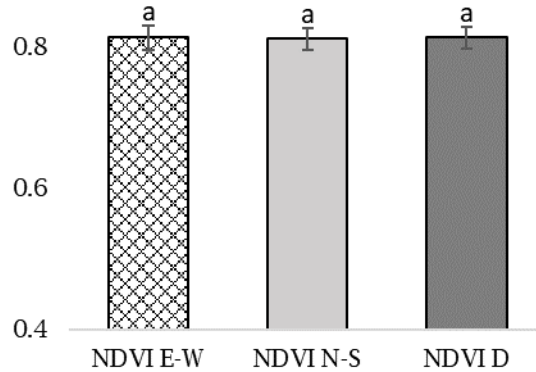
Figure 73. Influence of the different flight paths on the CV reconstruction. Results from ANOVA test ($p_{value} > 0.05$) and Tukey test.

Comparing flights 3, 4 and 7 was evaluated the differences determined by the flight height on the geometric reconstruction and the canopy area estimation (Figure 74). Multi-way ANOVA analysis showed that there were no statistically significant differences and interaction between the heights performed in flight 1 and 2 and the period. However, for flight 7 the plants were more developed and the ANOVA analysis showed statistically significant differences between the flight height of 30m and 70m. The greatest values were found in the flight at 30m.
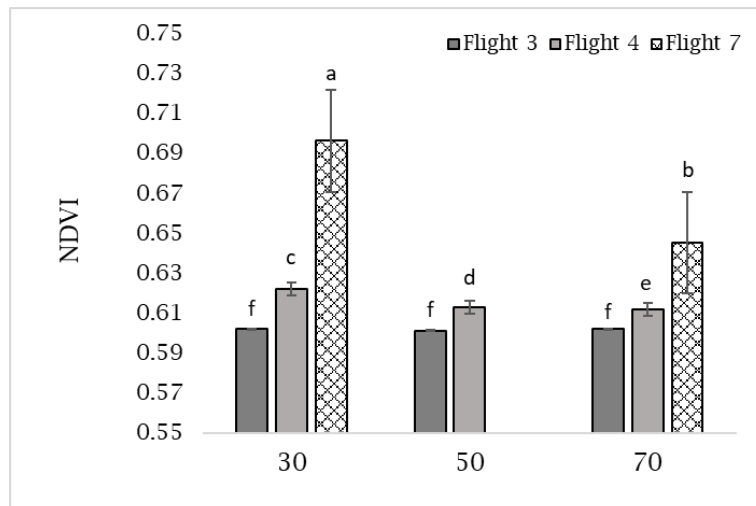
Figure 74. Influence of the different flight altitude on the NDVI estimation. Results from ANOVA test (p value > 0.05) and Tukey test.

The regression analysis shows that, in all the VIs, the values obtained from the four exposures are statistically correlated ($p_{value} < 0.001$) to the mean value

obtained per plant, with a very high coefficient of determination. In this case, the southern exposure gave the best results. In fact, the R^2 values found by comparing NDVI, NDRE and MSAVI of southern exposures with the relative mean values per plant were respectively: 0.754, 0.775 and 0.772 (Figure 75).
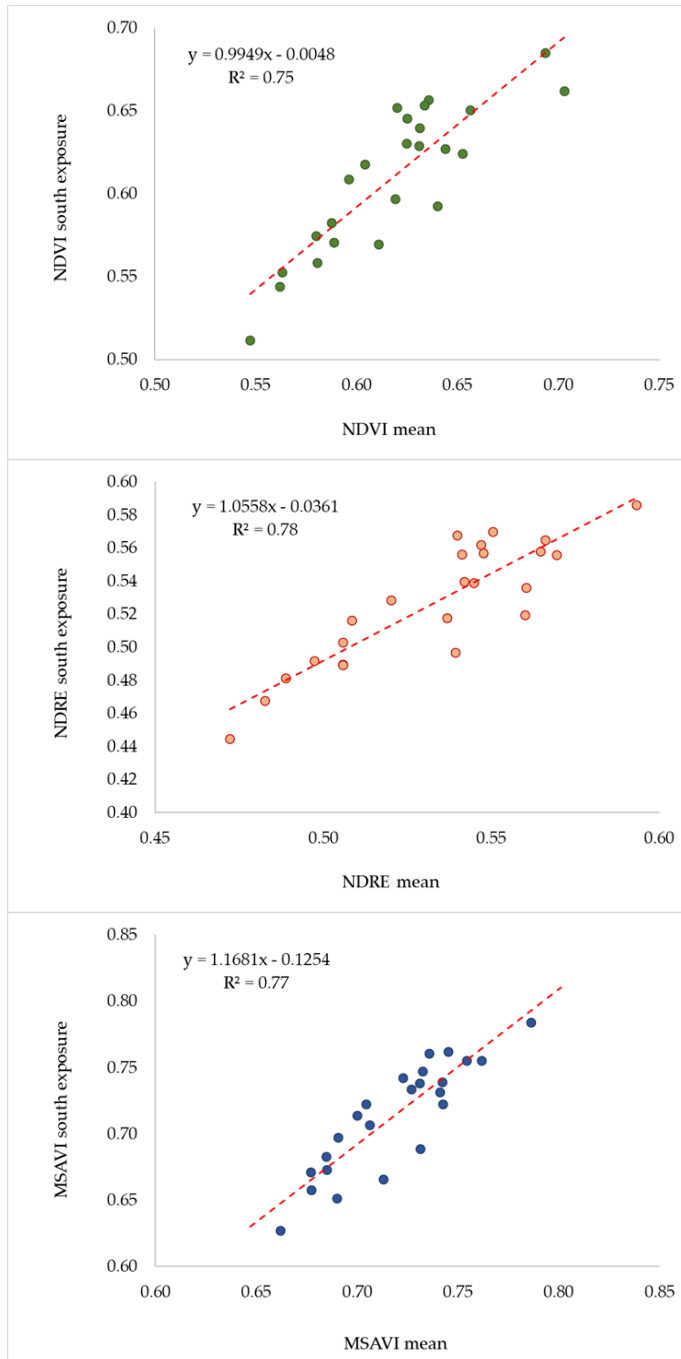
Figure 75. (Image above) Correlation between NDVI values of the south-facing portion of the canopy and the mean NDVI value of the canopy. (Medium image) Correlation

between NDRE values of the south-facing portion of the canopy and the mean NDRE value of the canopy. (Image below) Correlation between the MSAVI index of the south-facing portion of the canopy and the mean MSAVI of the canopy.

The hyperspectral data acquired with the spectroradiometer allowed us to see the spectral signatures of the 24 selected plants and the reflectance of the four parts exposed at the cardinal directions (Figure 76). The average spectral signature, for most of the reflectance spectra, showed the typical trend of agricultural crops, with a higher reflectance in the near-infrared (NIR) bands than in the visible (VIS) region. More specifically, peaks of reflectance were observed approximately at 555 nm in the green band and 770 nm in the NIR, while reflectance pits were recorded at around 690 nm. A different behaviour based on acquisition exposure was observed.
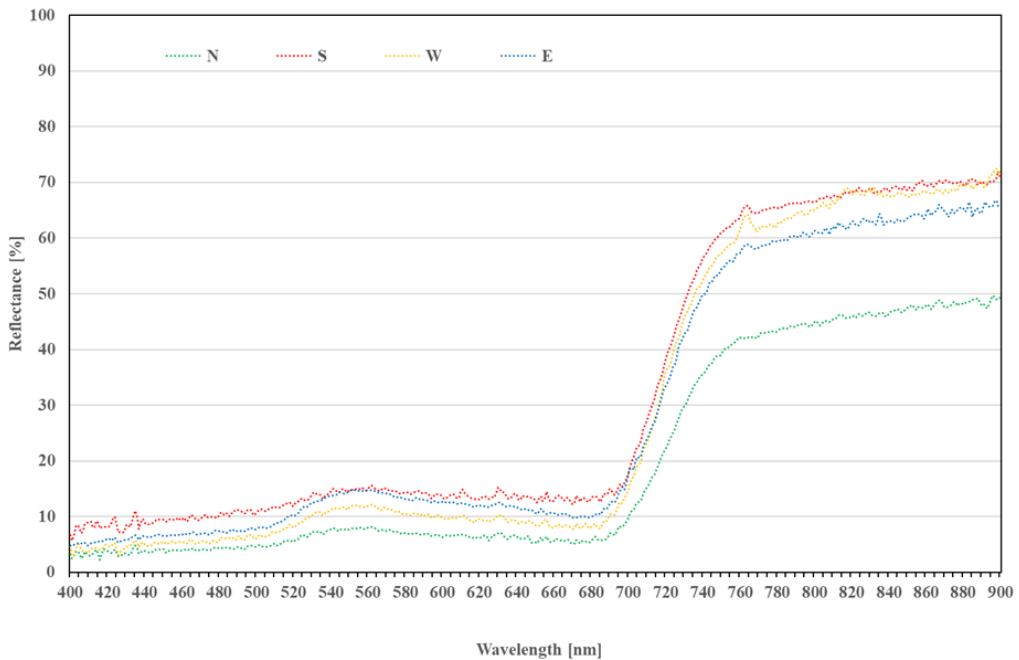
Figure 76. Representation of the reflectance of the four parts of the plants exposed at the cardinal directions (each line is the mean of 24 spectra).

The average reflectance that characterized the sampled plants were 6.2% in the blue band, 12.3% in the green, 9.8% in the red, 41.0% in the rededge, 61.7% in the NIR, respectively. It was observed a difference between the reflectance values acquired in the different cardinal directions, while maintaining the same trend along the curve.
The reflectance in the South exposure was always higher than the other three while the North exposure showed the lowest values (p value < 0.001). East and West exposures gave similar values; in particular, in the region between 400 and 680 nm, the West exposure shows values lower than those observed in the East

exposures, whereas in the NIR region the West exposure has on average significantly higher spectral reflectance values than East (p value < 0.001).

The hyperspectral data provided in the 2022 by the two sides of the selected plants confirmed the results found during the 2021. As can be seen in the figure below (Figure 77), the two reflectance curves show the same trend, which is typical for crops. The curve exposed to the south was found to be higher in both the visible and infrared regions. The NDVI calculated from them was found to be higher in the southern exposure with statically significant differences.
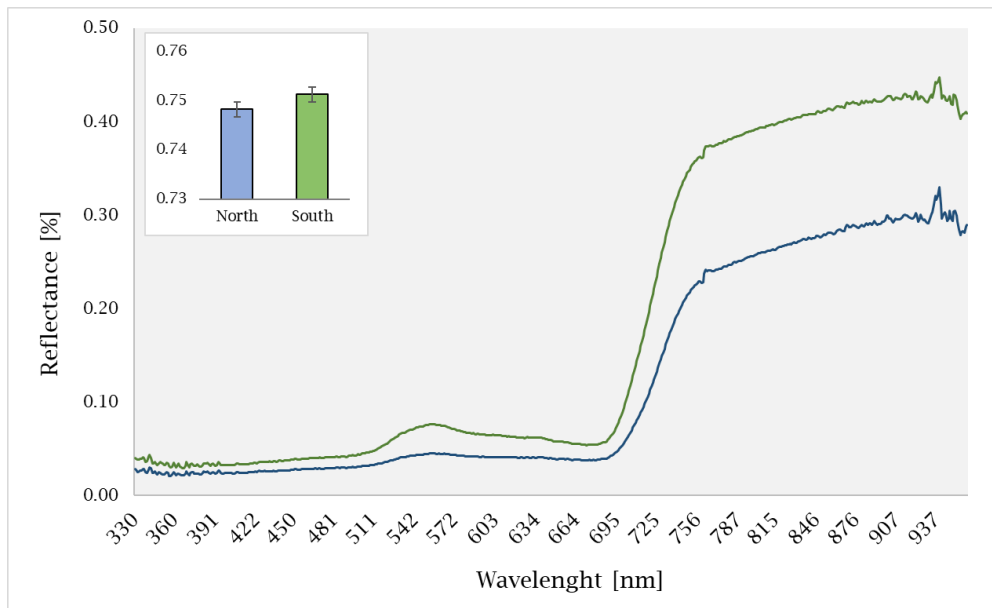
Figure 77. Representation of the average reflectance of the two-canopy sides of the plants (each line is the mean of 20 spectra).

As was well explained in Materials and Methods, the reflectance of the north side was corrected according to the formula 15. In fact, there was a marked increase in it, exceeding the value of 1 in the infrared zone.

PPFD measurements taken at the same time as the hyperspectral measurements showed a different amount of solar radiation in different areas of the plant (Figure 78).
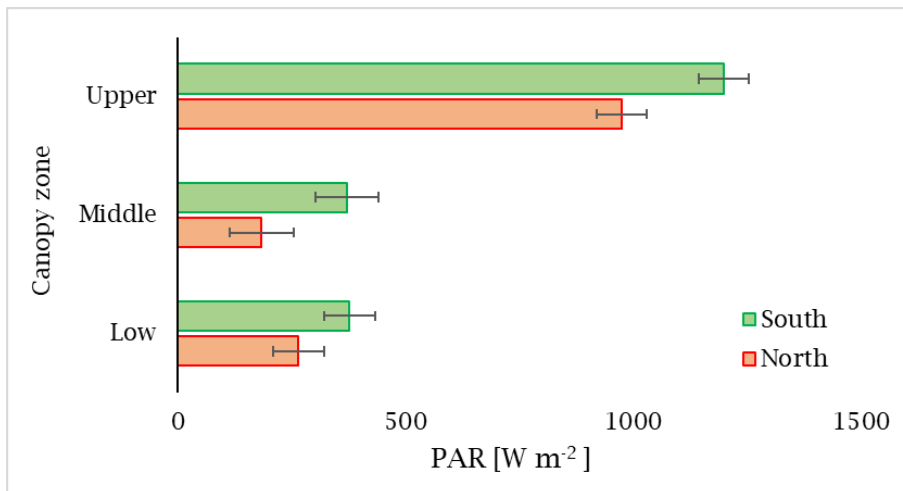
Figure 78. Distribution of PPF in the two exposures, North and South, in the three different zones of the canopy.

However, the areas exposed to the south always had statistically higher values than those exposed to the north. For both exposures, the highest values were observed in the upper canopy area. On the north side, the lowest values statistically were recorded in the middle zone. In the southern exposure, there were no statistically significant differences between the middle and low zones.

Three vegetation indices were calculated: NDVI, NDRE and MSAVI using the same range as the multispectral camera. Within each index, statistically significant differences were observed among the different exposures (Table 11). In particular, the South and West exposures gave for the three indices higher and significant values. Northern and Eastern exposures caused a greater dispersion of the data especially in NDVI and MSAVI. Statistically significant differences among the indices were also observed. MSAVI gave the highest average value with a mean of 0.718 ±0.14 followed by NDVI with a value of 0.574 ±0.13 and then NDRE with 0.156 ± 0.03.

Table 11. NDVI, NDRE and MSAVI from hyperspectral data. Values are mean ± st.dev. of the 24 selected plants. Different letters in the column indicate statistically significant differences at a significance level of $p_{value} < 0.05$.

Exposure	NDVI	NDRE	MSAVI
S	0.647 ± 0.05 a	0.170 ± 0.02 a	0.785 ± 0.04 a
W	0.643 ± 0.05 a	0.167 ± 0.02 a	0.781 ± 0.04 a
N	0.497 ± 0.15 b	0.139 ± 0.04 b	0.644 ± 0.20 b
E	0.508 ± 0.14 b	0.147 ± 0.03 ab	0.661 ± 0.13 b
Average	0.574 ± 0.13	0.156 ± 0.03	0.718 ± 0.14

The regression analysis between the indices used for the hyperspectral characterization of the plants showed statistically significant values ($p_{value} < 0.001$) and high R^2 values. NDVI had R^2 value of 0.80 and 0.97 with NDRE and MSAVI respectively. NDRE showed R^2 of 0.79 with the MSAVI value. Therefore, the coefficient of determination values between the indices were very high, with statistically significant differences; the R^2 highest value was observed between MSAVI and NDVI (Figure 79).
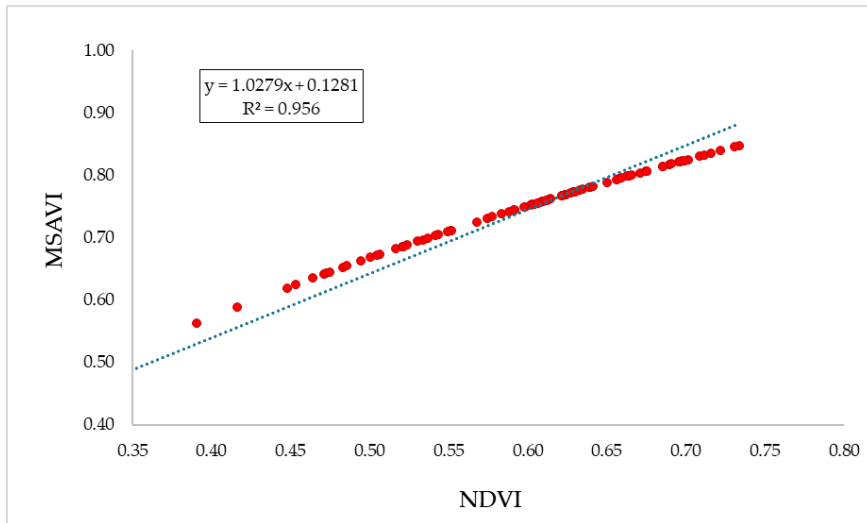
Figure 79. Linear correlation between NDVI and MSAVI.

Important results were found out from the ANOVA test used to compare multispectral and hyperspectral data obtained by the two sensors. The test was performed using the responses of the three different vegetation indices on each expousure (Figure 80). The effect of exposure was statical significant and more pronounced in the hyperspectral data than in the multispectral ones. West and South exposures gave the most consistent results with the multispectral images and the least scatter in the data for all indices used. In general, the effect of exposure had no impact on the multispectral data unlike the hyperspectral ones. Specifically, in the South and West exposures, NDVI and MSAVI values were statistically higher than those obtained from multispectral images (p value <0.05). In the North and East exposures, the values were always lower than the ones obtained from the multispectral data for all the VIs but the high dispersion determines no difference.
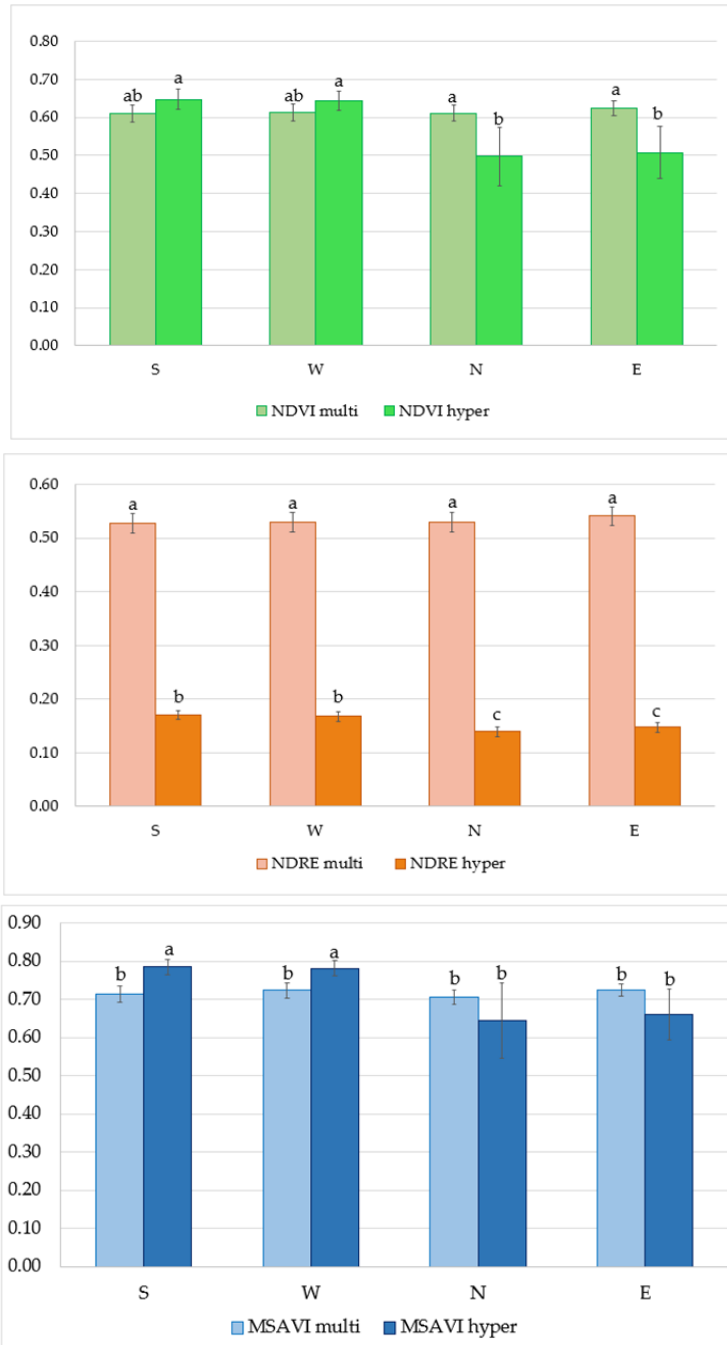
Figure 80. NDVI, NDRE and MSAVI data calculated from multispectral and hyperspectral images for the different portions of the canopy.

The best correlation between the indices calculated from the two different datasets was obtained in the southern and western exposures, for all three indices. In particular, NDVI in the West exposure showed r = 0.69** between multispectral and hyperspectral data, while for MSAVI the best correlation was r = 0.63** in

the same exposure. For NDRE, the correlation between multispectral and hyperspectral data showed r = 0.74** in the South exposure.

3.4 Variability and management

Precision agriculture is an important tool that can be deployed to determine spatial and temporal variability in order to manage it efficiently. In the previous sub-section, the results given from the soil, climate and crop variability were shown. The previous results gave a clear idea of the capabilities of the platforms and sensors used to extract different types of information from the olive orchard. In this sub-paragraph we compare the results obtained to understanding their interconnection and as can be used to create prescription maps that allow an efficiently site-specific management.

The geostatic processing carried out on the soil parameters investigated in the experiment allowed obtaining base maps for understanding the spatial variability and the correlation with the vegetative parameters. The soil parameters were able to influence the growth conditions of the plants and their production. The nutritional status of the leaves was strongly influenced by the availability of elements in the soil (Table 12).

Table 12. Correlation among the main soil, vegetative and production parameters. Electrical conductivity (EC, dS m^{-1}); Total carbonates (TC, %); Sandy (%); Total Organic Carbon (TOC, %); Total Nitrogen (Ns, %); Leaf Nitrogen (Nl, %); Leaf Potassium (K, %); Leaf Calcium (Ca, %); Leaf Iron (Fe, %), Leaf Magnesium (Mg, %); Leaf Manganese (Mn, ppm); Leaf Zinc (Zn, ppm); Leaf Copper (Cu, ppm); Yield (kg); TCSA (m^2); NDVI; Canopy area (m^2). $p_{value} < 0.05*$; $p_{value} < 0.01**$; $p_{value} < 0.001***$.

	pH	E.C.	TC	Clay	Lime	Sandy	TOC	TN
Nf	-0.03	0.30*	0.08	-0.33	-0.02	0.28*	0.62***	0.79***
K	-0.06	-0.13	0.43**	-0.14	0.04	0.10	-0.24	0.34*
Ca	-0.08	-0.03	0.41**	-0.03	0.00	0.03	-0.12	0.38*
Fe	-0.03	-0.02	-0.24	0.14	0.04	-0.13	-0.05	-0.08
Mg	0.00	-0.13	0.27	-0.03	0.05	0.00	-0.23	0.10
Mn	-0.08	-0.04	0.63***	-0.02	0.04	0.00	-0.02	0.43**
Zn	-0.04	-0.04	0.00	-0.07	0.08	0.02	-0.32	0.00
Cu	0.18	-0.08	-0.16	0.05	0.07	-0.07	-0.37	0.05

Most of the metals present in the leaves as: K, Ca and Mn were in a statistically significant close relationship with some soil variables. Sandy, Tc, TOC and Tn were well correlated with several leaf parameters. In particular, TN and TOC were

strongly correlated (p-value < 0.01) with leaf nitrogen (Nf) with an r of 0.79 and 062 respectively.

Sand, electrical conductivity, organic matter and total N values were positively correlated with some crop variables such as TCSA, yield, NDVI and canopy area (Table 13) thus suggesting the importance of soil fertility and nitrogen for olive orchard growth. Strong correlations were obtained, in particular, between Sand and yield, but also good correlation was found with TN and TOC. The spectral condition of the plants also showed good correlation with the main soil parameter such as E.C. (r = 0.30*), sand (r =0.33**) and TOC (r =0.42**).

Table 13. Correlation among main soil, vegetative, spectral and production parameters. Electrical conductivity (EC, dS m^{-1}); Sandy (%); Total Organic Carbon (TOC, %); Soil Nitrogen (Ns, %); pvalue<0.05*; pvalue <0.01**; pvalue <0.001***.

	E.C.	Sand	TOC	TN
TCSA	0.35**	0.20	0.24	0.12
Yield	0.20	0.49***	0.34*	0.42**
NDVI	0.30*	0.33*	0.42**	0.12
CA	0.21	0.37**	0.32*	0.13

The vegetative parameters TCSA, CA and CV during the different experimental seasons always correlated well with the crop's spectral response. TCSA were statistically significant correlated with NDVI during the different years. In the 2021 the correlation was of r = 0.73*** while in the 2022 was sligtly lowest (r = 0.58***; Figure 81). While lowest correlation was found with the productivity values (r = 0.42***).
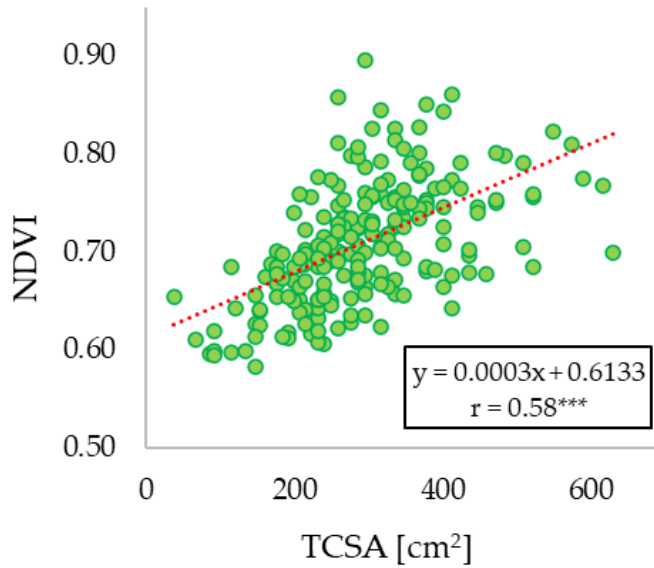
Figure 81. Correlations between TCSA and NDVI calculated as the average of all pixels within the CA of each tree. pvalue < 0.001(***).

NDVI, CA and CV have been calculated using the drone's multispectral image and GIS processing; therefore, they made it possible to quickly and easily investigate the variability of the field. NDVI, CA and CV had respectively an average value of 0.71 ± 0.06, 7.7 ± 2.09 m^2 and 18.02 ± 2.2m^3. Crossing all vigour parameters such as CA, CV, and TCSA, the plants were clustered in three vigour groups (C1, C2, C3) using K-means as cluster algorithm. These cluster groups represent the three-vigour classes (Figure 82): High (HV), Medium (MV) and Low Vigour (LV).
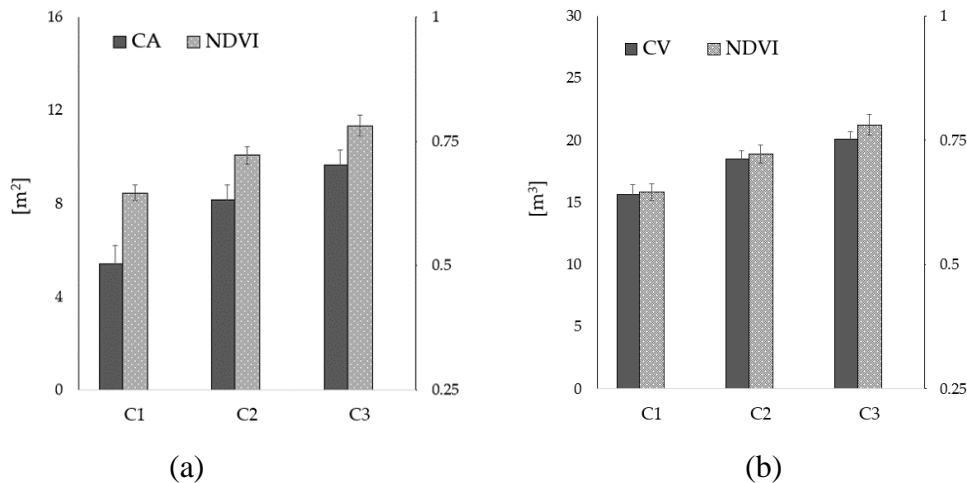
Figure 82. (**a**) CA and NDVI values (±st. dev) for the three clusters; (**b**) CV and NDVI values (±st. dev) for the three clusters.

The three vigour groups showed clear differences in terms of vigour (Figure 82). The three parameters showed an increasing data trend for the three vigor groups. CA showed values of 5.4 $m^2 \pm 0.8$, 8.15 $m^2 \pm 0.6$ and 9.6 $m^2 \pm 0.65$ for the three-vigour levels, respectively; NDVI showed values of 0.64 ± 0.02, 0.72 ± 0.02 and 0.78 ± 0.02 going from C1 to C3; CV showed values of 15.6 $m^3 \pm 0.84$, 18.5 $m^3 \pm 0.73$ and 20.1 $m^3 \pm 0.80$ for the three-vigour levels. From the statistical analysis, it appears that the NDVI of each individual tree was able to describe the variability of the field especially in terms of vigour characteristics. In fact, NDVI was strong statistically significant correlated with the values of canopy area during the 2021 r = 0.90***) and 2022 (r = 0.87***, Figure 83).
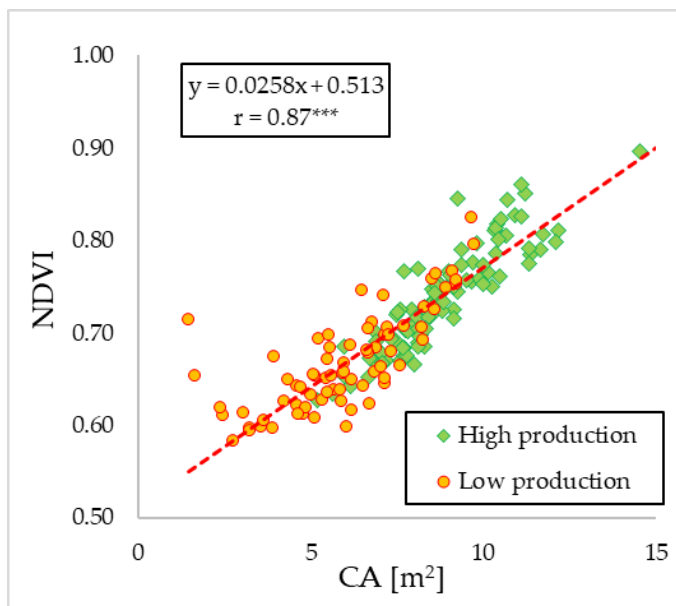
Figure 83. Correlation value between NDVI and Canopy area (m^2). $p_{value} < 0.001(***)$.

All the vegetative parameters estimated in the 2021 before the new growth season showed an important correlation with the previus yield, especially NDVI (r = 0.70***) and canopy area (r =0.76***). Also in the 2022 the NDVI of the selected plants showed a good relationship with production activity (r = 0.63***, Figure 84).
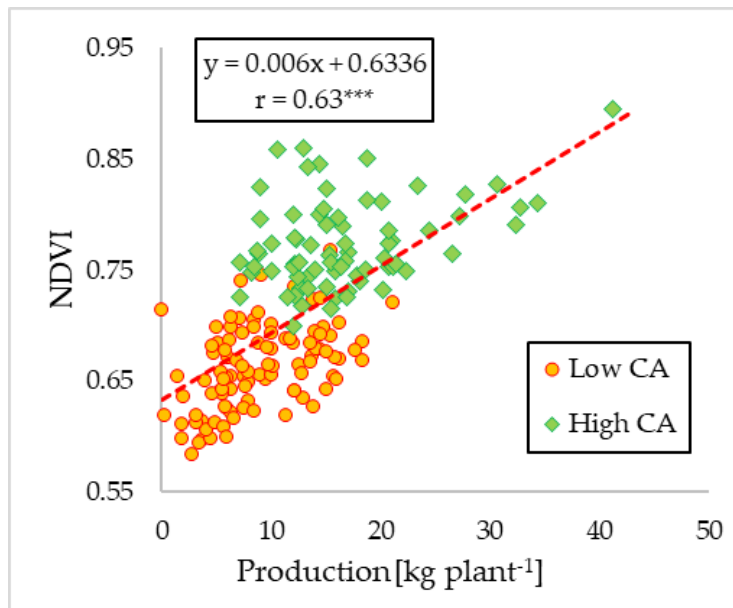
Figure 84. Correlation value between NDVI and Production (kg plant^{-1}). $p_{value} < 0.001(***)$.

The hyperspectral data provided by the two sides of the selected plants showed important correlations with the production of the same side (Figure 85). The NDVI calculated from them was found to be higher in the southern exposure with statically significant differences. The yield per side gave the same results as the NDVI; confirming the NDVI as a good index for predicting yield ($R^2 = 0.68***$).
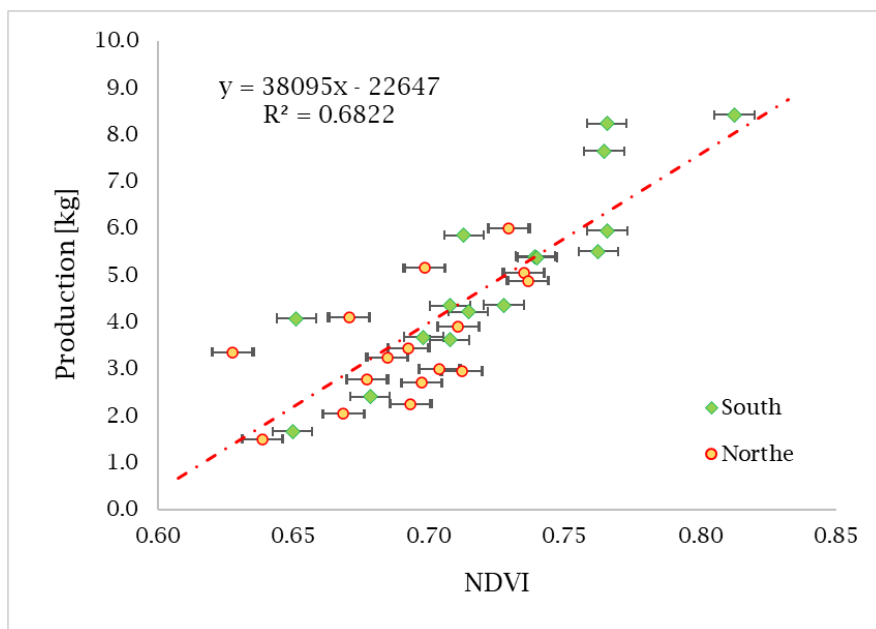
Figure 85. Correlation between NDVI and production for North and South canopy exposure.

Also, CA had a good influence on the productivity of the olive grove. Indeed, it was observed that productivity depends on the canopy area of the single plants (r = 0.75***, Figure 86). This result is supported by PCA analysis, where it was possible identify as the trees with high and low vigour were clustered with high and low production respectively (Figure 87). The average production and CA of all plants were used as a threshold to distinguish high and low production and canopy area.
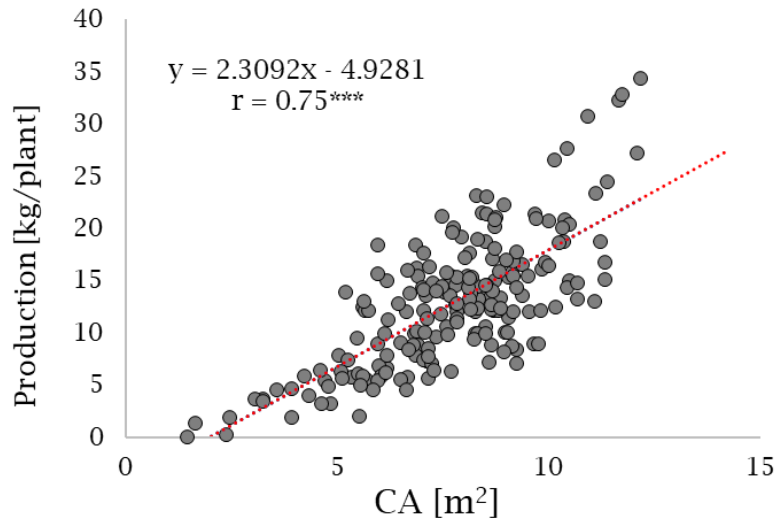
Figure 86. Correlation between CA and Production. $p_{value} < 0.001(***)$.
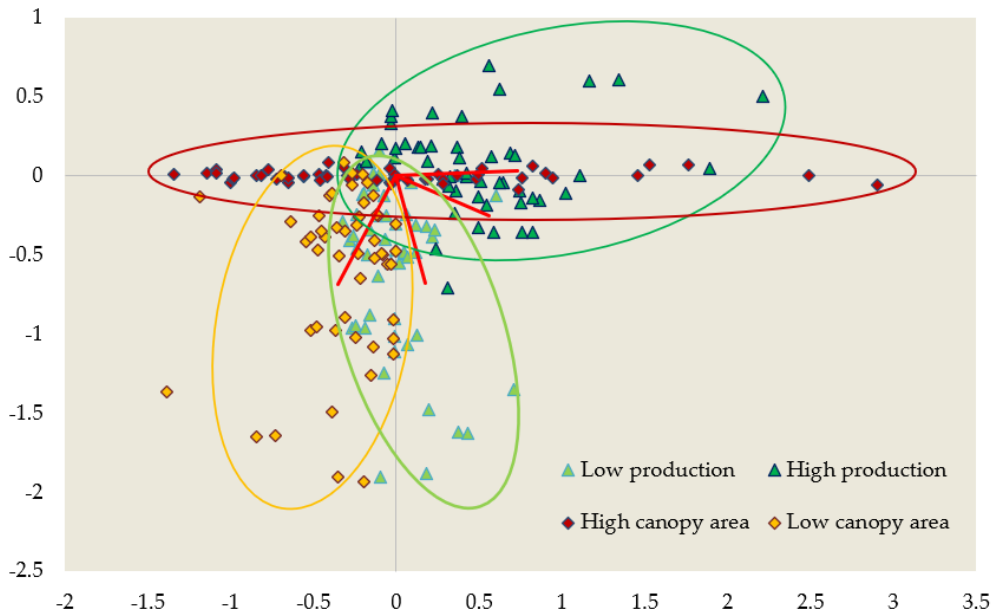
Figure 87. Principal Component Analysis (PCA) of high and low CA and production.

CV showed similar correlation results of the CA. CV had a good influence on the productivity of the olive grove showing a r= 0.74*** (Figure 88).
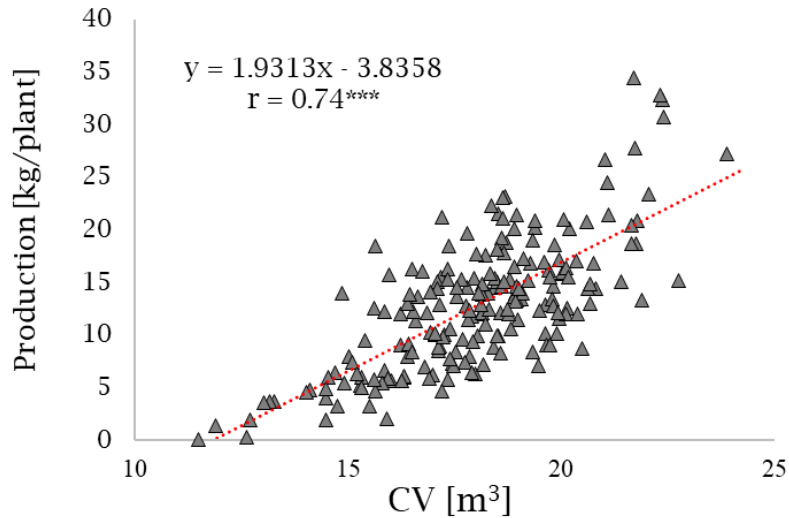
Figure 88. Correlation between CV and Production. $p_{value} < 0.001$(***).

Using the GEOBIA method, it was possible to analyse all information from soil, nutrient and vigour conditions together to understand how this influenced the final productivity of the plants. Cluster analysis enabled three groups of plants to be statistically differentiated on the basis of all the variables examined so far (Figure 89). Using the three groups of clusters and plotting their score of nitrogen concentration and canopy area, it was observed that the whole plot showed clear heterogeneities. These clusters were statistically different *p* (<0.001) in terms of productivity by ANOVA analysis (Figure 89). Moreover, the ANOVA test showed that CA has a greater effect than nitrogen concentration.
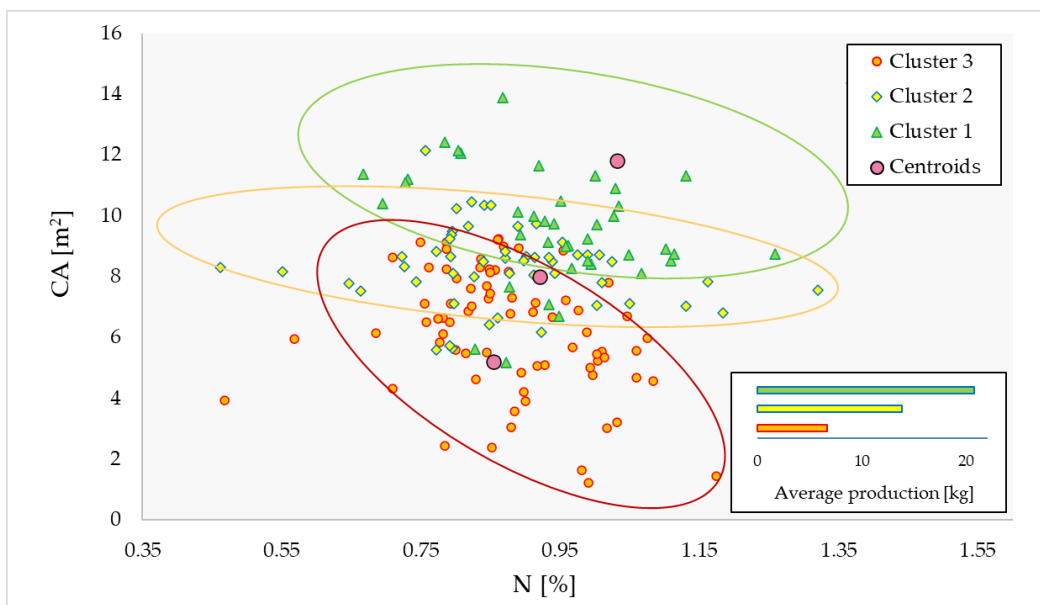
Figure 89. Cluster analysis of the three vigour groups (C1, C2, C3) according to total nitrogen content and CA and ANOVA test results for the production.

From the results previous shown, it appears that vegetative and nutritional conditions played a decisive factor in yield. Olive production and canopy area based on NDVI were overlapped in Figure 90, also showing a certain variability in olive yield.
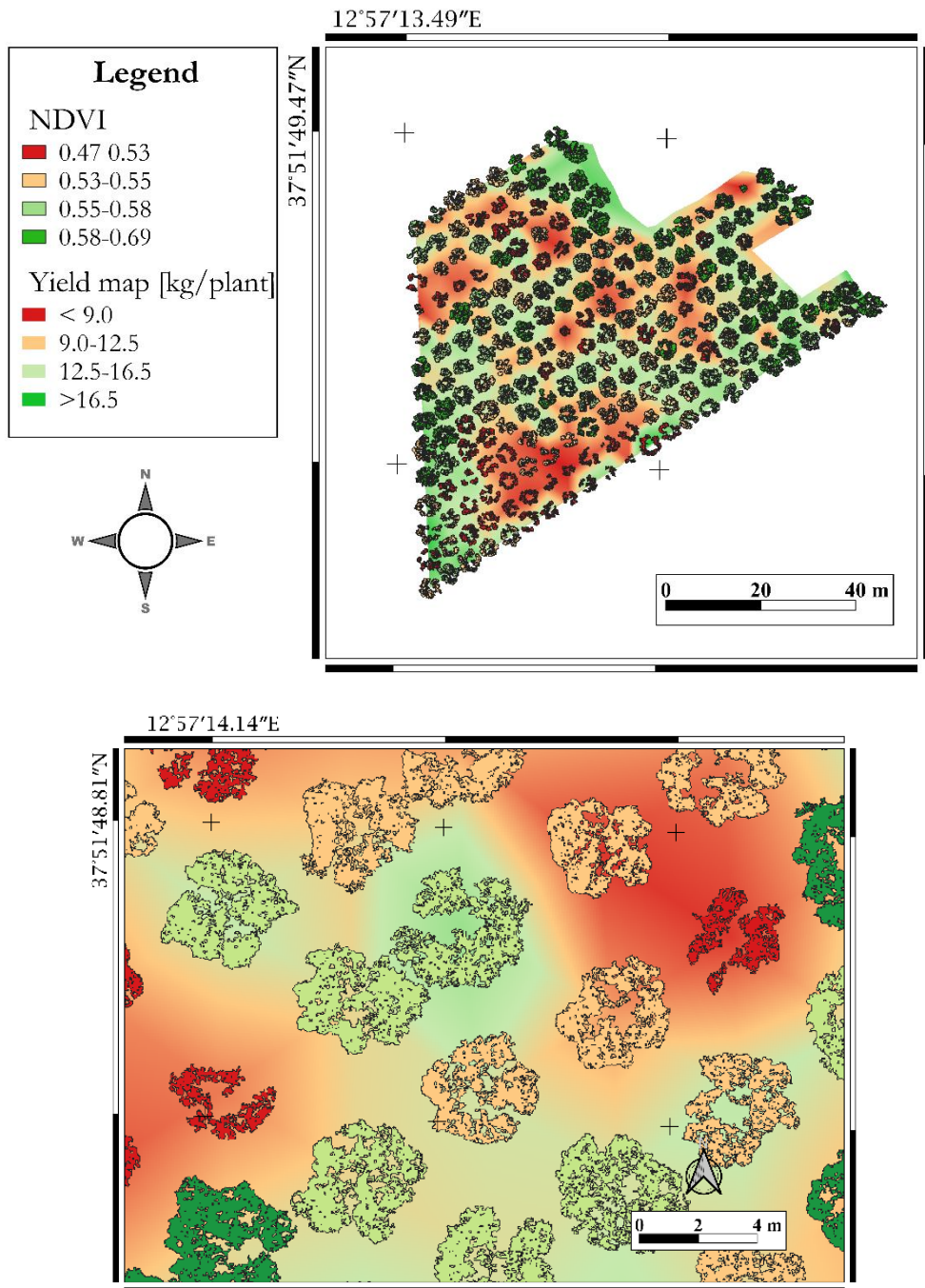
Figure 90. (Image above) Overlay of the yield map (red-green scale) and individual tree NDVI values; (Image below) particular of the image.

In the third year of experimentation, from the pruning and production survey it was possible to obtain the data of all the plants and make a prediction through the

multivariate analysis. In this way the map of the amount of nitrogen removed from the crop according to equation 12 was obtained (Figure 91).
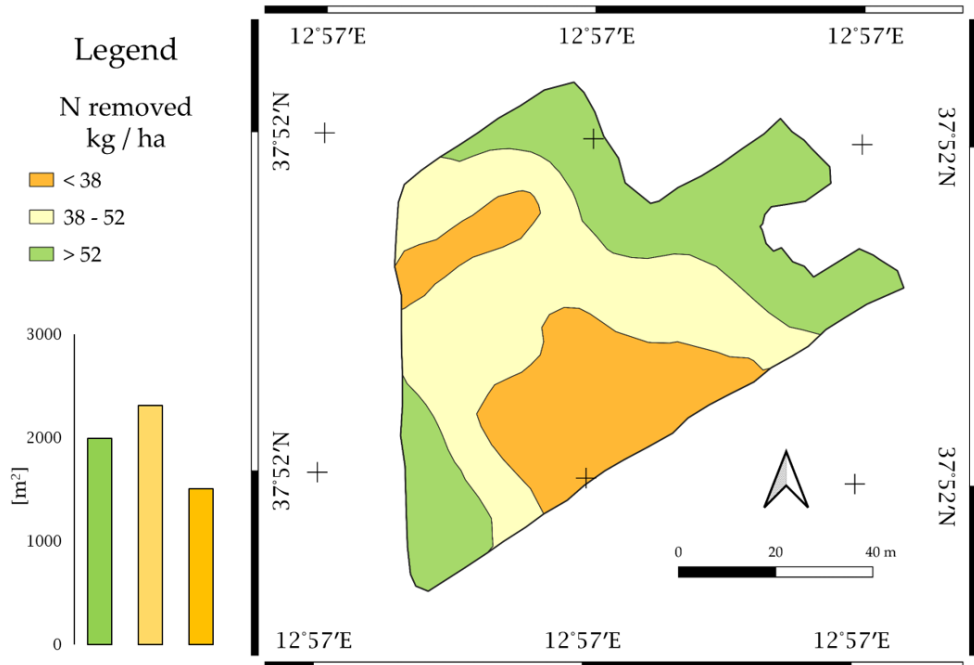
Figure 91. Nr map according to the equation12 divided for homogeneous classes. The bar graph indicates the extension of the different homogeneous areas.

The map above has a resolution of 1 m^2 (1 pixel) containing, as a digital number (DN), the amount of Nr distributed per square meter The quantity of Nr varied from 30 kg/ha to 60 kg/ha as shown in figure 45 and three homogeneous areas were distinguished.

4. DISCUSSION

The Mediterranean climate condition, being characterized by excessive temperatures during the summer period as well as low rainfall in the spring and summer seasons. This climate conditions do not allow many crops to grow properly. The olive tree, being a xerophytic plant, is able to withstand such conditions. In addition, the olive tree generally has a high alternation of production, so acting on the most important agronomic practices that can reduce it can lead to higher profitability. A precision management of water resources or fertilizers and of the main cultivation operations can play a key role in reaping economic and environmental benefits. The climatic trend over the three years has been typical for the Mediterranean area. Nevertheless, clear differences in temperature and rainfall were observed across the years. Temperatures showed a steady increase in average temperatures gradually from 2020 to 2022. This effect is probably related to global warming, which is putting a strain on world agriculture. In the experiment conducted, climatic conditions strongly influenced olive tree growth, looking at the NDVI trend calculated from the sentinel2A and UAV images. However, plant productivity was not affected by rainfall. In the years 2020 and 2021, approximately the same production was obtained with similar rainfall, while no production was obtained in the year 2021. This is related to the intensive pruning carried out at the end of 2020.

The economic benefits of site-specific nutrient management are likely to come from the more efficient use of fertilizers and from increases in crop yield. Soil sampling density depends on the variability of the field being tested. As sampling density increases, so do the costs of soil sampling, soil testing, etc. In general, site-specific management can be carried out at different scales of detail. The scale of detail that can be adopted depends on a number of factors, but mainly depends on the internal degree of variability of each area that we are able to achieve in order to homogeneously manage the sub-areas. In countries where the average farm area is very large, site-specific management is concentrated in the identification of homogeneous management areas (Zone management, ZM) that are more or less large. In the Mediterranean area, the oliviculture is characterized by several small fields with high inside variability. However, the site-specific application at the farmer's plot level has not been carried out in Sicily due to limitations in the development and adoption of agricultural science and technology. Therefore, it is important to verify that the main data acquisition platforms used in precision agriculture are able to allow variable rate management of an olive orchard in Mediterranean conditions.

Geostatistical analysis of the maps enabled us to trace the spatial variability of the main soil variables such as texture, pH, EC, TOC and TN. The possible spatial structure of the different soil properties was identified by calculating the semivariograms and the best model describing these spatial structures was found. The best fit model was applied to each parameter, the accuracy of soil property

values was estimated by kriging (using parameters of the modelled semivariogram) also at unsampled locations. Parameters used to apply the best model included nugget effect (Co), sill (Co + C), and influence range for each terrain. Furthermore, the degree of autocorrelation between sampling points was found to be related to the spatial dependence (nugget: sill ratio) and expressed as a percentage. Spatial variables were classified as randomly to strongly dependent by the ratio (nugget : sill, Clark, 1979; Trangmar et al., 1986). Various models are used for semivariogram analysis such as linear and spherical. The electrical conductivity values of soil samples show a strong spatial dependency and an opposite trend like TOC. As the electrical conductivity of soils varies depending on the amount of moisture held by soil particles, thus its variability is distinct throughout the sampling area. The map of TOC shows that whole study area has a TOC content of less than 1%, which is the critical limit for organic carbon in most agricultural soils. The semivariograms and kriging interpolation map of TOC show a parallel (strong) spatial pattern trend as soil CE and TN (Buttafuoco et al., 2017), this results were confirmed in the correlation matrix in table 6. Indeed, it shows that there was good correlation between TOC and TN with EC. Their higher level was mainly observed in the eastern part of the study area, while in the middle and north zone the concentrations were low. This effect can be partially explained because the TOC directly influenced the water source and CE is strongly related to it. The main factors for the low TOC concentration in the study area could be long-term soil tillage, low water content and high soil temperature induced by climatic conditions. Similarly, this variability may be based on landscape attributes, including slope and altitude although they are not very pronounced in our field as represented in the figure 36 (Rezaei and Gilkes, 2005). In the whole experimental area, the concentration of TOC, as well as TN, was low, probably due to concomitant factors: i) excessive mineralization of organic matter and ii) the lack of organic matter supply.

The determination of the different base maps subsequently allowed co-kriging for the identification of the MZs, after defining a spatial dependence model. The MZ maps made it possible to define 3 zones with statistically different soil characteristics. The map of homogeneous soil zones seems to be perfectly in line with the distribution of TOC and TN while it does not seem to follow the values of texture as found in other studies (Buttafuoco et al., 2017; López-Granados et al., 2004). The productive results recorded in the different areas emphasise that knowledge of soil variability is of central importance for site-specific management. Indeed, the production of olive trees was influenced by soil fertility, particularly the amount of TN and TOC as found in similar studies (e.g. Fountas et al., 2015). Soil parameters showed a good correlation with plant nutrition and vegetative status. The low amount of foliar nitrogen, thus, may be explained by the low concentration of soil nitrogen. Indeed, the foliar N concentration values were lower than the threshold in the 76% of the area, although in line with previous studies (López-Granados et al., 2004; Maran and Fernandez-Escobar, 1996). TOC was correlated with vegetative activity (NDVI and canopy area) and

production while TN was correlated only with production. Probably, TN did not correlate closely with vegetative parameters because these are influenced by many variables such as pruning, agronomic management, etc. and not only by nitrogen availability, which fluctuates over the years. Another important result was the influence of the amount of TC with the concentration of certain metals in the leaves. Indeed, TC positively influenced the concentration of K, Ca and Mn. This effect is related to the increased availability in the soil caused by TC itself. Mn was found to be highly correlated with N in leaves, as widely accepted in the literature, as its concentration influences the formation of lignin and is part of some enzymes for cell division, metabolism and photosynthesis. Similar results were observed with the elements K and Ca showing high correlations with the amount of nitrogen in the leaves. Many agronomic techniques such as fertilization and irrigation are strongly dependent on soil conditions. In particular, for fertilization, distinguishing the areas that require intervention from those that are in suitable TOC can greatly reduce the amount to be distributed. Therefore, precision agriculture should make use of the study of soil variability to increase agroecosystem efficiency.

The experiment showed that the majority plot area had nitrogen deficiency, as all samples had N concentration below the optimal threshold of 1.2%. No values below the threshold were observed for any of the other elements based on (Maran and Fernandez-Escobar, 1996). For this reason it was not possible to exclude zones of the plot from N fertilization (Aggelopoulou et al., 2011; López-Granados et al., 2004; Noori and Panda, 2016). However, several studies recommend that the best strategy to optimise nitrogen fertilization in olive orchards is to apply nitrogen fertilizers only when the leaf analysis of the previous season shows values below the deficiency threshold. The deficiency threshold for olive trees has been set at 1.5% leaf dry weight for July samples (Beutel et al., 1983). However, other studies have shown that there is no reduction in yield or growth in trees with a leaf nitrogen concentration below the threshold, suggesting that the deficiency threshold in olive trees must be lower (Fernández-Escobar et al., 2009b; Molina-Soria and Fernández-Escobar, 2010). Based on these reports, it becomes necessary to establish a nitrogen balance in orchards that takes into account the spatial variability of all parameters that may influence vegetative growth and productive activity of plants. Indeed, the nutritional condition for each plant was not correlated well with the vegetative parameters. However, this deficiency was one of the determining factors for plant production, as obtained from the PCA that supported the grouping of plants into three groups (Figure 89). In our study, foliar nitrogen levels were probably not well correlated because the plants had different accumulated resources. However, nitrogen deficit status was the main limiting factor for plant growth in the plot considered, as found in another study (Fountas et al., 2015). The low NDVI values found (López-Granados et al., 2004; Noori and Panda, 2016) and the entire vegetative heterogeneity detected could be explained by the deficient nutritional status of the plants, whose production was highly correlated to the vegetative parameters.

Therefore, using foliar nitrogen concentration threshold of 1.2, a new fertilization map was created. This, highlights the areas that actually need fertilization and coincides well with the areas of low productivity. Thus, the vigour map made on the basis of CA also shows important similarities. In this case the percentage of the total area that need the fertilization is 76%. Therefore, the amount of fertilizer actually saved per hectare compared to normal distributions is 24%. The fertilization prescription map applied at the beginning of 2021 enabled good plant growth conditions to be restored. This map appears to be similar to the previous maps obtained from the soil. It confirms that knowledge of the soil, plants and their interactions is an important management tool. A careful survey of the surrounding area showed that the dose of nitrogen commonly used is about 150 kg ha^{-1}, which corresponds to 88 kg in our plot. Using the fertilization map showed in the figure 44, the quantity to be actually distributed was 114 kg ha^{-1}; consequently, a final fertilizer saving is 36 kg ha^{-1}. This amount saving is in accordance to previous studies (Aggelopoulou et al., 2011; Van Evert et al., 2017).

The construction of the prescription map starting from nitrogen deficiencies represents an effective method that can be easily adopted by companies. However, looking at figure 45 it can be seen that the fertilizer savings can be greater. This map is obtained from all the variables that mainly contribute to the nitrogen balance. Furthermore, it is easy to apply since once the MZ zones have been outlined, the determination of the fertilizer dose to be distributed is weighted on the actual minimum and maximum quantities that are distributed in the zone (Roma et al., 2023). Using the map in figure 45, a saving of 66% was achieved. This result, although it may seem high, is in agreement with the literature which in various articles confirms that it does not seem necessary to resort to annual fertilization in olive groves(Fernández-Escobar, 2011; Fernández-Escobar et al., 2012; López-Granados et al., 2004). Furthermore, excessive amounts of fertilizers can cause low quality olive oil. (Fernández-Escobar et al., 2006). Map 45 seems to be in line with the map in figures 66 and 40 from which it was obtained. Therefore, this result also confirms that the examination of soil and crop variability and their interpolation through correct management techniques can significantly help to reduce resources and increase the efficiency of the entire olive grove. Due to the pandemic and the energy crisis, all countries including Italy are witnessing a sudden increase in fertilizer prices. Therefore, the correct use of fertilizer can also be a determining factor in the success of the crop economically(Koch et al., 2004). Our study shows that saving an important amount of nitrogen fertilizer corresponds to a saving more of 100 euros for hectare. The detail that can be obtained for the creation of fertilization maps can be different. In our study we focused on the identification of MZ zones (Casa et al., 2011). However, given the new technological developments, a different dose can be applied to each individual plant. Figure 91 highlights that it is possible to calculate the actual quantities of nitrogen removed per plant (Cointault et al., 2003; Ehlert et al., 2004). By applying the different GIS methodologies, it is

possible to extend this result also to the pedological parameters. This way you will get a true balance of fertilization per plant.

The technologies available today in precision agriculture are able to describe and determine the health status of the olive orchard. As observed in this study, variability must be observed in soil, climate and vegetation, as all three variables can be managed at variable rates and lead to increased resource use efficiency. However, as shown in other studies (Caruso et al., 2019; Zarco-Tejada and Sepulcre-Cantó, 2007) the investigation of crop variability is the main factor for the best precision agriculture applications. Direct size assessment of certain geometric features of olive trees, such as CA, HC the perimeter and CV, is now possible through the combined use of UAV imagery and advanced image processing and analysis procedures. This technology opens up new opportunities for monitoring the condition and progress of trees on a field scale, as an efficient, objective and accurate alternative to laborious and often inconsistent manual measurements on the ground (Rosell and Sanz, 2012). By estimating vegetative conditions well, they can be used as important predictors for the classification of vigour classes, homogeneous zones or for estimating biomass and carbon stocks using allometric functions (Asari et al., 2013). Geometrical canopy characteristics are also important in order to optimize the spray volume in pesticides application (Miranda-Fuentes et al., 2015). To calculate the optimal amount of pesticide to be applied, several dosing models have been proposed, including the canopy height model (CHT model), the surface orchard model (SO model) and the tree row volume model (TRV model) (Rüegg et al., 2001). Therefore, the ability of UAVs to easily provide these characteristics of the olive canopy and interconnect them with other types of information could positively contribute to reducing the environmental impact of pesticide applications. In the present work, crop variability was assessed in several ways. Precisely, the vegetative, spectral and nutritional conditions of individual trees were investigated. The condition of the plants was the most important factor in determining production. As confirmed by several studies, accuracy in data acquisition is important and can be improved by knowing which variables may affect it. (J. A. Berni et al., 2009; Caruso et al., 2019; Fountas et al., 2011).

Canopy area and NDVI reflect the real vegetative status of the plants at the moment in which they are determined. Since they are significantly correlated with TCSA, this finding suggests the good ability of the remote sensing platform (UAV) to detect and investigate the variability of vigour in the olive grove (Noori and Panda, 2016; Roma and Catania, 2022), thus minimising field sampling (Fulton and Port, 2018; Shafi et al., 2019). Furthermore, the vegetative characteristics had a significant and robust correlation with production. It rather confirms that production was strongly influenced by the biometric characteristics of the crop and their correct management can improve the quality and the quantity of the products (Fernandez-Escobar et al., 2008). Therefore, by having a broad knowledge of the field conditions, it is also possible to trace the production as other studies proved (Stateras and Kalivas, 2020).

To express the vegetative variable, i.e., vigour, it was decided to use the TCSA, HC, CA and CV. All these characteristics express a condition of vegetative vigour, they showed statistically significant relationships with each other.

TCSA was only measured during the year 2020 but showed good correlations with the CA of the following years estimated by image analysis. This means that the two vegetative parameters are able to express plant vigour conditions well. This, however, is a measurement that is often affected by much error, since in some plants, the presence of trunk hyperplasia prevents it from being measured correctly. TCSA is a condition formed over the years of cultivation and it cannot describe the annual condition of the plant, while the area of the canopy certainly expresses a precise condition at an exact moment. Probably, for this reason the canopy area was indeed more correlated with plant production and NDVI (Figure 81). The reduction in the correlation between TCSA and CA over the years is linked to the directly proportional development of canopy depending on plant vigour. Observing the HC values before and after pruning, the height interval between the various vigour classes is 1.08m, while afterwards it is reduced to only 30 cm. This means that the pruning intervention resulted in a substantial reduction in plant heights in the entire plot. In general, the height of the canopy was reduced by 20% with different weights depending on the vigour class, in order to homogenize the vegetative condition of the plants.

A very interesting result that has so far not been investigated in the literature is the perimeter differences found at different heights. Indeed, in scattered canopies such as those surveyed with flight 3, the different heights were able to identify the different holes in the canopy. Whereas these differences were not found in denser canopies because these may be covered by lower canopy layers. This survey system can also be conducted on a few plants to effectively determine the penetrability of light in the canopy considering its importance for canopy efficiency. Although no measurements were made regarding the actual canopy density, this result lays the foundation for future investigations that could improve the use of UAV platforms for the determination of parameters related to this aspect such as LAI.

The UAV equipped with multispectral and RGB camera showed a good capacity to extract the vegetative information using the orthomosaic and SfM products to obtain the spectral and biometric data (Catania et al., 2023). They were able to predict the production and consequently to better manage variability with significant environmental, agronomic and economic benefits (Aggelopoulou et al., 2011; Van Evert et al., 2017). Geometric reconstruction showed interesting results. The high value of RMSE obtained between observed and estimated data were found in previous studies (Anifantis et al., 2019; Torres-Sánchez et al., 2015b). These volume differences were caused by ground measurements applying the geometric equation as explained in Figure 59 (Torres-Sánchez et al., 2015b; West, 2009). Indeed, similar magnitudes were observed between the two approaches; in fact, the largest and smallest trees on the ground remained the same in the geometric reconstruction. Therefore, if one assumes that data from 3D

reconstruction are able to determine a better estimate of CV, it is possible to better balance and manage certain agronomic practices such as variable-rate treatments, resulting in significant product savings. Such savings consequently translate into greater environmental and economic sustainability. CV showed a strong relationship with CA and TCSA, pointing out that vigour conditions are interconnected. From the cluster analysis, the vigour conditions were able to differentiate the real health status of each tree expressed by its production. Getting accurate data on plant vigour is an important condition to obtain the best growth pattern of the olive tree and to better manage the orchard (Stateras and Kalivas, 2020). However, during the first few years of the experiment, it was not always possible to use the DEM data because the pruning that was initially carried out resulted in too sparse canopies that did not allow for an accurate reconstruction, as has also been observed in other studies (Kattenborn et al., 2014; Torres-Sánchez et al., 2015b).

For the investigation of the above parameters, a UAV equipped with a multispectral and RGB camera was used as a platform. One of the aims of the thesis experiment was to understand how varying the direction of flight according to plants can alter and cause different results. The experiment showed that in the plot in all path configurations there was a difference in the multispectral and geometric results of the individual plants. In geometric terms, plant height was better estimated by the diagonal configuration, whereas the other configurations tended to overestimate values. This was characterised by a greater extension of high vigour areas than the sloping plot. However, the NS configuration was better at estimating CA values than the other configurations even though there were no statically significant differences with the EO configuration. The correct estimation of CA is crucial for correctly predicting yield, as it is the parameter most closely correlated with it. The effect of flight paths on the 3D geometric reconstruction of plants raises important questions about which method is actually better. Diagonal flight showed the best results as it had the highest correlations with the ground. However, as shown in the figure59, the measurements on the ground tend to strongly overestimate the CV especially if sparse. In fact, the CV measurements made by the NS and EO flight directions had much lower values, suggesting that diagonal flight overestimates the CV values.

Another important effect evaluated in this thesis work was the influence of flight altitude on the geometric and spectral reconstruction of plants. The results showed that the flight performed at 70m slightly underestimated the CV measurements compared to the flight performed at 30m as showed in (Johansen et al., 2018). However, a closer look at the figure 65 shows that the plants that caused the most problems were those with very high CV. This difference was not observed for CA between the flight performed at different heights. There was no statically significant difference and the correlation between the two datasets was very close. Considering the entire workflow from flight operations to feature extraction, the time required to monitor one hectare of field area varied by several minutes in our plot. However, when referring to larger areas, the time consumed can have a very

important influence. Most of the time was spent on mosaicking and analysing the images, which is mainly influenced by the spatial resolution of the images. The time required between RGB and multispectral images was slightly less in RGB images. However, the opposite was observed in other studies. Probably due to the higher resolution of the RGB sensor Consequently, an agreement between the accuracy of the results and the duration of flight and calculation operations is necessary. In quantifying the time taken for image processing, the use of computers with high computing power is of crucial importance. This trade-off can be improved by choosing a good sensor and the correct flight configuration. In our investigation, the results obtained at lower altitudes did not always show the best results and image processing took much longer. From a practical point of view, imaging at an altitude of 70 m is recommended to increase the area of terrain covered in each flight and, consequently, to reduce both mission duration and the size of the image set. However, the potential accuracy expected from each flight altitude must be considered according to the starting conditions of the plants, as low or high canopy density conditions can greatly influence the final result.

The impact of the pruning operation was found in previous study (Caruso et al., 2021; Jiménez-Brenes et al., 2017) The pruning operation had a considerable effect in changing the vegetative condition of the entire plot. The CV was notably reduced, resulting in no statistical difference between the medium and high vigour classes. Most of the removal was carried out in the high vigour plants in terms of pruning as shown in the graph 91 Observing the correlations between the biomass removed and the initial volume of the plants, it is observed that this relationship is closer in low vigour plants than in medium and high vigour plants. This may be due to the greater cutting possibilities that can be performed in a high CV plant. The type of cutting that is carried out is also different. In fact, as is shown in the graph 63. the density of the pruning material was different. The high and medium volume plants had a higher weight because the percentage of wood in relation to the daughters was higher. In contrast, less light material was removed in the low vigour plants. However, a higher correlation is observed in the selected plants as more targeted pruning was carried out on plants with similar vegetative conditions.

Multispectral and hyperspectral images are an important tool for understanding the real condition of plants. it is known in the literature that their applications are very much for olive orchard management. In this thesis work, an attempt was made to highlight the potential of using such information sources to predict the main vigour parameters and productivity. The crop spectral conditions were investigated by calculating NDVI that describes the general vegetative and nutritional conditions of each plant because the bands used for its calculation (NIR and red) are strongly related with them (Liang, 2004; Xie et al., 2014).

The NDVI calculated from the Sentinel2 images had peaks during the autumn-winter periods. This phenomenon is linked to the development of weeds. The increased availability of water during the winter period resulted in the development of weeds that masked the spectral response of the olive tree from the

Sentinel2 data. During the growing season, NDVI values do not seem to have a typical trend as monitored by UAV. This may be related to continuous changes in the optical properties of the soil. Indeed, even when the weeds have been controlled, either chemically or by tillage, the spectral response of the soil is highly dependent on its water conditions. In fact, during the dry season, from June to August, a slight increase in NDVI can be appreciated. The trends in this period compared with drone images from the same years are not discordant. However, the inability to discriminate vegetation and strong soil influence due to the low ground cover coefficient, such images cannot be applied as well as UAVs for investigating the spectral conditions of individual plants.

Using the UAV images, during the season 2021, the NDVI showed low values, especially where conditions of low vigour and low nitrogen concentration in the leaves were found. As also shown in other studies (Caruso et al., 2019; Gómez et al., 2011) the NDVI has a good relation with the vegetative status (81, 83, 84). As found in Caruso et al., (2021) the NDVI was more correlated with the TCSA and its increment, suggesting the great importance of this indices to predict, from remote platform, this data. The NDVI was found to be more correlated with the prior year's TCSA value, as was the CA. This means that there has been vegetative growth which should be monitored every year for site specific management of the olive orchard. Moreover, when it correlates with the CA, it was able to discern the plants with high or low productivity with a high level of precision (84). When it was correlated with production, it was able to underline the plant with high vigour (precisely with high canopy area; 83). The correlation between NDVI and CA is a most import result. In fact, knowing what the average NDVI is per plant and the relationship that exists, makes it possible to obtain excellent information for the prediction of the production. NDVI showed better correlations with canopy area than the vigour parameters because the multispectral bands used in the calculation are sensitive to both effects: leaf efficiency (red band) and canopy structural conditions (NIR band) (Liang, 2004). Since production was mainly linked to the availability of plant resources and therefore to CA, NDVI always proved to be a good indicator and predictor of production even in non-optimal nutritional conditions. These results emphasize that NDVI is more able to determine the vegetative parameters than production. Therefore, by having precise multispectral and RGB images of the entire olive orchard, it is possible to use this information to obtain crop status data that can be used in development models or DSS for the optimization of agronomic management.

The hyperspectral data are consistent with those generally found in the literature. Rubio-Delgado et al. (2021) have also attempted to describe and identify the spectral signature of olive trees, given the wealth of information on their health status that can be obtained. They obtained in the NIR region a slightly different curve than the one described in this study that can be explained by the different point of view (POV) of the sensor compared to the crop (Ye et al., 2008). The difference in the reflectance of the hyperspectral curve in the four exposures marked the results of the entire experiment. The normalization of the spectral data,

and therefore of the calculation of the different indices, allowed a better understanding of the crop's status. The hyperspectral VI values showed a close dependence on the acquisition exposure. Nevertheless, their correlation with the multispectral data was found to be statistically significant regardless of the type of VI and exposure.

In a traditional breeding system like the one used in the experiment, the different growth conditions in the four exposures influenced the relative spectral characteristics. This effect is related to the different angle of the rows, which influences the interception of photosynthetically active radiation (PAR) (Campos et al., 2017). Indeed, as observed by Campos et al., (2017) with the rows in the NE-SW direction, the part with the highest light interception in a latitude close to 40° are the South and West zones. In our experiment, the hyperspectral VI showed a clear dependence on exposure, as found in another study with hyper and/or multispectral side-view cameras (Saiz-Rubio et al., 2021). The differences found are probably due to different cultivation conditions such as climate (solar radiation, wind direction, etc..) and agronomic characteristics such as volume of the canopy, number of foliar, LAI. However, also to the different mode of acquisition and operation of the sensor have influenced the reconstruction of the image. By grouping the hyperspectral data from the South and West exposures and comparing them with the North and East data, it is evident that the South-West exposure resulted in statistically higher NDVI, MSAVI and NDRE values. The higher values found in the South and West exposures can be explained by the better growing conditions of the crop due to the higher luminosity (Campos et al., 2017). These different growth conditions, although not supported by the differences in volume between the two sides, are shown in productive terms. In fact, as shown in Figure85 the NDVI values of the South exposure for the plants selected in the 2022 were well correlated with production levels. Probably, these production differences are linked to a different amount of irradiance available for the two sides, as can be seen in figure 78. The result obtained in the South and West exposures is also supported by the very high and statistically significant r^2 values found between the hyperspectral and multispectral VIs. It remains to be investigated how the different regions of the spectrum change and under which conditions it is correct to use one region rather than another when using side-view spectroradiometers. In fact, different studies investigated the crop status using the entire spectral signature but with more problems with the data management.

The multispectral images were able to determine for each plant the crown area and the multispectral information with high precision, as obtained in previous studies (Anifantis et al., 2019; Deng et al., 2018; Stateras and Kalivas, 2020). The multispectral images were thus able to appreciate the spectral condition of each plant. A good linearity of the extrapolated data was obtained from the multispectral VI analysis. In fact, no statistically significant differences were observed for the same indices among the various exposures, in all three indices. However, statistically significant differences were found among all the indices,

probably related to the different bands used for the calculation, thus providing different spectral information (Gómez et al., 2011; Modica et al., 2020).

From the comparison between multi and hyperspectral images, it can be deduced that the different VIs do not associate the same value to the same level of crop stress. In general, MSAVI gave higher values, followed by NDVI and then by NDRE both from multispectral and hyperspectral data.

The use of the multi and hyperspectral sensors, despite the different viewpoint of the object, was able to describe the health status of the plants as found in Vanegas et al., (2018). Data coming from the hyperspectral camera with a side view of the object correlated well with the aerial multispectral images from drone, paying attention to the exposure. Therefore, hyperspectral information is more accurate, but at the same time more affected and/or at risk of error than multispectral information. This effect is explained by the variation in the data and the lower correlation value between the hyperspectral data in the four exposures. The exposures that showed the best correlation among the VIs calculated from the two datasets were the S and W. This is probably related to the better growth conditions of the two canopy portions, confirmed by the higher values appreciable in the hyperspectral dataset, as found in (Marshall and Thenkabail, 2015).

Crossing the spectral, biometric, productive and nutritional characteristics of each plant by means of cluster analysis yields very interesting results that confirm the effectiveness of the entire experiment. The three statistically different clusters (C1, C2, C3) were identified by cluster analysis according to vigour and nutritional characteristics (Figures 89). The production of the three clusters showed statistically significant differences. C1 was the most productive and vigorous, while C3 was the lowest (Figure 89). This condition is also confirmed by Figure 82 where it can be observed that CA, CV and NDVI increase with increasing vigour class. These results are also supported by other studies conducted on olive orchards with traditional systems. However, in super-intensive olive groves, there is an increasing attempt to intensify the planting density. In this case, the increase in AC and relative CV may not lead to an increase in productivity. The results obtained with the PCA confirm that plant productivity is positively correlated with canopy development and secondarily with nutritional conditions, since high productivity was observed even in plants with a very vigorous canopy and moderate foliar nitrogen concentrations. As described above, this condition can be explained by the different resources immobilised in the wood, when there are no other limiting factors.

5. Research activity carried out at Valencia Polytechnic University

The aim of the study conducted during the research period abroad was to evaluate the GNSS positioning system and the CWSI calculation to be implemented in an intelligent handheld system. The CWSI was calculated in the empirical and analytical form to assess the water stress conditions in olive orchard. The smart handheld instrument was also equipped with other sensors that could provide an accurate detection of the stress plant conditions.

5.1. Materials and Methods

5.1.1. Study area

The experimentation was carried out in an experimental field located in the Valencia Polytechnic University, Spain (39°28'59.24"N, 0°20'15.01"W; WGS84). The surface of the plot is about 2000m^2 and a regular orography and predominantly flat. The climate of the area is Mediterranean with an average annual rainfall lower than 500 mm, concentrated from autumn to spring. According to the Koppen–Geiger's classification, the climate of the area is classified as Mediterranean hot summer (Kottek et al., 2006). The soil moisture regime is xeric, border with the aridic one, and the temperature regime is thermic. The main characteristics of the soil of the studied area according to the ISSS (International Society of Soil Science) classification system of soil particles, soil texture was sandy clay (Hillel, 2013). The trial was carried out in an olive orchard (*Olea europaea* subsp *europaea*) during the season 2022. The cultivation system was traditional and the total number of the plants was 20. Layout was rectangular with planting distances of 4.5 x 4 in the inter-row and intra-row respectively, in a NE–SO direction. At the time of the trial, the plants were in full productivity, in good vigor condition and the crop height varied between 3 m and 5 m.

5.1.2. Experimental design

The experiment involved two different irrigation treatments: a full irrigation (FI) according to the evapotranspiration calculated with the Penman-Monteith and a deficit irrigation (DF) treatment where the only irrigation input was rainfall. The data were collected during the season considering all twenty-one olive trees for the experimentation. Trees were irrigated (FI) using a surface drip irrigation system, placed before the experimentation, with a distance of 0.75 m apart on a single drip line, discharging 8 L for h^{-1}. In the FI plants the irrigation volumes will be calculated on the basis of to replace crop evapotranspiration (ET$_c$) as follows:

$$ET_c = ET_0 * K_c * K_r \qquad (29)$$

the coefficient used was: the reference evapotranspiration crop (ET_0), crop coefficient (K_c) of 0.55 and a coefficient of ground cover (K_r) of 0.46. Reference evapotranspiration, ET_0 will be calculate using the FAO-Penman-Monteith method (Allen et al., 1998). Once the evapotranspiration was calculated, the hydrological balance was used to schedule irrigation. Of the twenty or so plants, nine will be subjected to full irrigation treatment (FI) and the remaining eleven to no treatment. The layout of the drip system used for the experiment is shown in Figure 92.

Figure 92. Experimentation site location and irrigation design. Blue lines represent the drip irrigation system used to apply the full irrigation (FI) treatment.

5.1.3. Handheld System

The handheld system was created in the "Departamento de Ingenieria Rural y Agroalimentararia de Valencia" of the Valencia Polytechnic University. It was equipped of several sensors to investigate the main parameter to identify the health condition of the plants and of growth. Exactly there are sensors for measure the environmental condition (relative humidity, temperature of air), multispectral data (NDVI) and thermal crop condition (Temperature of the canopy). In addition, there is a Global Navigation Satellite System (GNSS) for storing the position of measurements and a system to visualize the parameter directly. GNSS is able to transport the data in a whatever Geographic Information System (GIS) to spatialize and manage the data. However, as the instrumentation is under patent, it cannot be shown and the individual components cannot be described in detail.

5.1.4. Experimental surveys

Before the experimentation, the plants were georeferenced using a GNSS instrument already used in other study and described in the section 2.5.1. During the experimentation has been taken all sampling and measurement at midday (from 12:00 to 14:00) as expected to determine the LWP and the CWSI. The thermal and hydraulic status (LWP) were taken in the bright zone of the canopy from the medium part, in several trees per treatments; because the plants have one sunny and one shady area of the canopy. LWP during the dry season was measured in three leaf samples per area to make the measure water status. Leaf water potential was measured by taking the leaf directly and inserting it into the Scholander chamber (PWSC Model 3000, Soil moisture equipment Corp., California, USA) following the procedure described in (Moriana et al., 2012; Guadalupe Sepulcre-Cantó et al., 2006b). The thermal measure (Temperature of the canopy, Tc) was taken near the sample to LWP. The acquisition angle was 60° from zenith axis, to eliminate the soil influence, and 1 meter of distance from the plant. If Tc is measured from a (near-) nadir position, it is the temperature of the outer canopy layer, which tends to be larger than T_0 because of the direct sunlight received (Chehbouni et al., 2001; Jones et al., 2003). At larger angle, the measured Tc incorporates the temperature of deeper canopy layers and is closer to T_0. In theory, an optimum angle is between 50 and 70 ° from nadir (Huband and Monteith, 1986). To calculate the CWSI with analytic method need of external measurements from the handheld system such as wind speed and net radiation. Therefore, simultaneously the water status and thermal measure we measured the NDVI and weather condition with the handheld system and environmental instrumentation. To measure the net radiation was used a pyranometer. To measure the wind speed, we used a Kestrel 5400 datalogger positioned at 2m above the ground.

5.1.5. Validation of GNSS receiver

The handheld system was equipped with instrumentation capable of detecting geographical position. The positioning accuracy was evaluated by testing the differences in positions measured by the S7 Stonex instrument and the handheld system. The acquisitions were carried out simultaneously in three different areas of Spain. Specifically, the sites were located two in Requena (Valencia; Lat: 39°32'11.82" N and Long:1° 9'33.34" W in the first site and Lat:39°27'55.88" N and Long: 1° 8'40.59" W in the second site) and one in Turis (Valencia, Lat: 39°23'41.10" N and Long: 0°41'58.96" W). Furthermore, these three sites had different climatic conditions. It was therefore possible to test the accuracy of the positioning system even under different climatic conditions.

5.1.6. CWSI equations

For the experimentation were evaluated the two main methods to obtain the CWSI, analytic and empirical. Precisely, for the analytic equation has been used two different equation such as: Jackson's formula (-) and the reformulation (-). While, empirical equations used was obtained starting from the data measured in the plot; because the two equation presented in the literature from J. Berni et al., (2009) and Egea et al., (2017) showed negative results. Below are explained the different equations and parameters used to obtain the CWSIa (in two main equation) and CWSIe.

5.1.6.1. Analytic CWSI

In this method the Tc (Temperature of the canopy) measurements are combined with meteorological data to compute CWSI. The utilization of the analytical approach requires measurement of incoming solar radiation, air temperature, relative humidity, and wind speed. These measurements are available from any meteorological station, and can be representative for an entire field or orchard; but there is some uncertainty in the estimation of the resistances, which induces a level of uncertainty to this approach as well (Jackson et al., 1981). Thus, △Tdry only requires Rn and raH for its estimation and is often assumed constant. The estimation of △Tpot bears more uncertainty. Originally, (Jackson et al., 1981) proposed to calculate only with meteorological parameters the Tdry and Twet. From Jackson, Twet can be calculated using the equation 30, as:

$$T_{pot} = T_{air} + \frac{r_a * Rn}{\rho C_p} * \frac{\gamma_1}{\Delta + \gamma_1} - \frac{VPD}{\Delta + \gamma_1} \qquad (30)$$

Where Rn is the net radiative flux density (W m^{-2}), ρ the air density (kg m^{-3}), Cp the specific heat at constant pressure (J kg^{-1} °C^{-1}), γ the psychrometric constant (Pa ∘C^{-1}), Δ the slope of the saturated vapor pressure vs. temperature curve (Pa °C^{-1}), ra the aerodynamic resistance (s m^{-1}), and γ_1 is calculated as (equation 31):

$$\gamma_1 = \gamma * (1 + \frac{r_{cp}}{r_a}) \qquad (31)$$

Where γ the psychrometric constant (Pa ∘C^{-1}), ra the aerodynamic resistance (s m^{-1}), and rcp the canopy resistance at potential transpiration (s m^{-1}). Furthermore, there are the possibility of subtract the soil heat flux density or the energy flux density leaving the lower canopy layer (W m^{-2}; G) at the Rn because generally is hypnotize equal zero.

Another method to calculate Twet, used in different study, it becomes straightforward to rearrange the basic energy balance equation to estimate the canopy resistance to water vapour transfer directly (Jones, 1999b, p. 1; Möller et al., 2007). The theoretical values for leaf or reference surface temperatures can be calculated using a standard rearrangement of the leaf energy balance (equation 32).

$$T_{wet} = T_{air} - \frac{r_{RH}\, r_v\, \gamma}{\rho C_p (s\, r_{RH} + r_v\, \gamma)}\, Rn_i + \frac{r_{RH}}{s\, r_{RH} + r_v\, \gamma}\, VPD \qquad (32)$$

where Rni is the isothermal net radiative flux density (W m^{-2}), *VPD* the vapor pressure deficit (kPa), *s* (the same with Δ in the equation before) the slope of saturated water vapor pressure versus temperature curve (kPa °C^{-1}), γ the psychrometric constant (kPa K^{-1}), ρ the air density (kg m^{-3}), *Cp* the specific heat at constant pressure (J kg^{-1} °C^{-1}), rV or rW the total resistance to vapour transports (s m^{-1}), rHR is the resistance to heat and radiative transport (Jones, 1992, 1999a). The rHR is composed from other two parameters as: resistance to sensible heat transfer and leaf resistance to radiative heat loss. The leaf boundary layer resistance to heat transfer (raH or rH) can be estimate using the following equation 33 (Guilioni et al., 2008):

$$r_h = 100 \sqrt{\frac{d}{u}} \qquad (33)$$

where d (m) is a characteristic dimension of the leaf (the length in the direction of the wind) and u (m s^{-1}) is the wind speed at the height of the leaf, usually estimated from a wind profile. rR is the leaf resistance to radiative transfer rewritten as (Guilioni et al., 2008; equation 34):

$$r_R = \frac{\rho C_p}{(8\, \varepsilon_l\, \sigma\, T_a^3)} \qquad (34)$$

The total resistance to heat and radiative transfer given by equation 35:

$$r_{H,R} = \frac{r_H\, r_R}{(r_H + r_R)} \qquad (35)$$

A leaf exchanges heat and water vapour with the surrounding air from its two sides. Leaf resistance to water vapour transfer rV (rW) can be calculated from leaf temperature T_L and environmental variables on the basis of a linearized form of the energy balance equation written showed in several studies (Guilioni et al., 2008; Hamlyn G.. Jones, 1992). But for the olive tree, where the transpiration is in the lower side of the leaf (hypostomatous leaves), we used another method. In this case, the rW was calculated as (equation 36):

$$r_W = r_{S2} + r_{aWl} \qquad (36)$$

Where the rs2 is the stomal resistance only in the lower side. The boundary layer resistance to water vapour transport (raWl) is slightly lower than the one for sensible heat, as explained by (Hamlyn G.. Jones, 1992) as: rW = 0.92 rH. The stomal resistance was assumed as the resistance of the canopy and was calculated as (equation 37):

$$r_c = \frac{r_a(e_c^* - e_a)}{\gamma \left(\frac{r_a Rn}{\rho C_p} - (T_c - T_a) \right)} - r_a \qquad (37)$$

Where ra the aerodynamic resistance. In our study the effective aerodynamic resistance (rae) because it showed good results in several previous studies. This semi-empirical equation includes the influence of buoyancy on aerodynamic resistance and was calculated with the (Thom and Oliver, 1977) empirical method, as:

$$r_{ae} = 4.72 \frac{[\ln(\frac{z_u - d}{z_{0M}})]^2}{(1 + 0.54u)} \qquad (38)$$

Where zu are the heights at which u (wind speed) was measured, d is the zero-displacement height, z0M the roughness length of momentum. Because we used the rV parameter to calculate the Tpot, we hypothesised to calculate rs2 no as rc but as rcp (potential resistance of canopy). In this case, rcp was calculate with the follow equation derivate from (O'Toole and Real, 1986). Where the α and β coefficient are determine from (J. Berni et al., 2009; Egea et al., 2017) and the environmental was calculated always in the field.

When the leaf does not transpire and all the available energies dissipate into sensible heat Tdry given by (equation 39):

$$T_{dry} = T_{air} + \frac{Rn_i \, r_{HR}}{\rho C_p} \qquad (39)$$

For both equations used to obtain the CWSI analytic the Tdry was obtain using the equation above. Therefore, only the calculation of the leaf temperature at potential transpiration was recalculated according to the two methods expressed before.

4.1.6.2. Empirical CWSI

The empirical method was created by Idso, (1982). The data input is limited to Ta, VPD and Tc. The approach was inspired by the observation that △T (Tc- Ta)

decreases linearly with VPD. Idso, (1982) demonstrated that the lower limit of the CWSI is a linear function of VPD for a number of crops and locations. In this method, the equation to calculate the CWSIe is (equation 40):

$$CWSI = \frac{(T_c - T_a) - (T_c - T_a)_{LL}}{(T_c - T_a)_{UL} - (T_c - T_a)_{LL}} \qquad (40)$$

where Tc-Ta denotes the measured canopy-air temperature difference; $(T_c\text{-}T_a)_{LL}$ is the lower limit of (Tc-Ta) for a given vapor pressure deficit (VPD) which is equivalent to a canopy transpiring at the potential rate; and $(T_c\text{-}T_a)_{UL}$ is the maximum (Tc-Ta), which corresponds to a non-transpiring canopy. $(T_c\text{-}T_a)_{LL}$ is a linear function of VPD (non-water-stressed baseline, NWSB) that, once empirically obtained, $(T_c\text{-}T_a)_{LL}$ is calculated by solving the baseline equation for the actual VPD. Therefore in this equation there are two limits (Hamlyn G.. Jones, 1992). The calculation of CWSI relies on two baselines: the NWSB, which represents a fully watered crop (lower limits), and the maximum stressed baseline, which corresponds to a non-transpiring crop (upper limits, stomata fully closed); these limits can be calculated from the equations 41 and 42:

$$\Delta T_l = \alpha + \beta * VPD \qquad (41)$$

$$\Delta T_u = \alpha + \beta(VP_{sat}(T_a) - VP_{sat}(T + \alpha)) \qquad (42)$$

where VP_{sat} (Ta) is the saturation vapor pressure at air temperature Ta and VP_{sat} (Ta+a) is the saturation vapor pressure at air temperature plus the intercept value as for the crop of interest. Slope b and intercept a have been determined for a number of crops but for the olive orchard there are only two study calculated that coefficient (J. Berni et al., 2009; Egea et al., 2017; Roma and Catania, 2022). The basic assumption of the method is that α pot and β pot are constant and crop specific, at least for a given location and for a certain growth stage. To calculate the DT_{pot}, in our experimentation, we decided to obtain an own equation calibrated using the experimentation condition. The Tdry calculation was implemented with two equations. One is the analytic method previous represented while the second method widely used in the literature involves to add + 5°C at the temperature of the air (T_{air}). However, no statistical differences were shown between the two calculation methods, but the analytical method yielded the best results. Therefore, in the results that will be shown, the calculation of Tdry was obtained analytically.

5.2. Results

The experiment evaluated the accuracy of the receiver positioning in different sites and weather conditions. The low-cost system was able to maintain a positioning error of less than 2m even in harsh weather conditions (Figure 93). Indeed, there were no statically significant differences between the measured positioning accuracies using the ANOVA test.
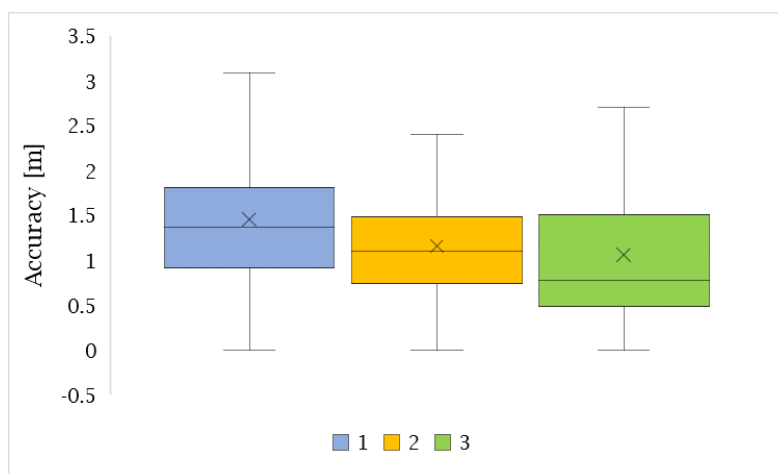
Figure 93. Different position accuracy tested in three different zone and weather condition. Zone1-2 (Requena), zone3 (Turis).

Aside from evaluating the accuracy of the positioning system, the experimentation focused on validating the instrument's ability to effectively determine the spectral and water conditions of crops. In each method used to determine the hydrological status, a response with similar tendencies and behaviour was shown, confirming that there is a soil-plant-environment continuum. The climatological trend in the plot was in line with seasonal averages. The average temperatures observed were 31.8 °C, while the canopy temperature varied depending on irrigation. Average values of 2m/s, 980 W/ m^2 and 50% were measured for wind speed, net radiation and relative humidity respectively. The multispectral data collected from two sides showed a different value. Indeed, the leaves in bright side has higher value of NDVI than the shadow side with difference statically significant ($p_{value} > 0.001$; Figure 94). The average NDVI in the bright side was 0.82 ± 0.06 while in the shadow side was 0.68 ± 0.05.
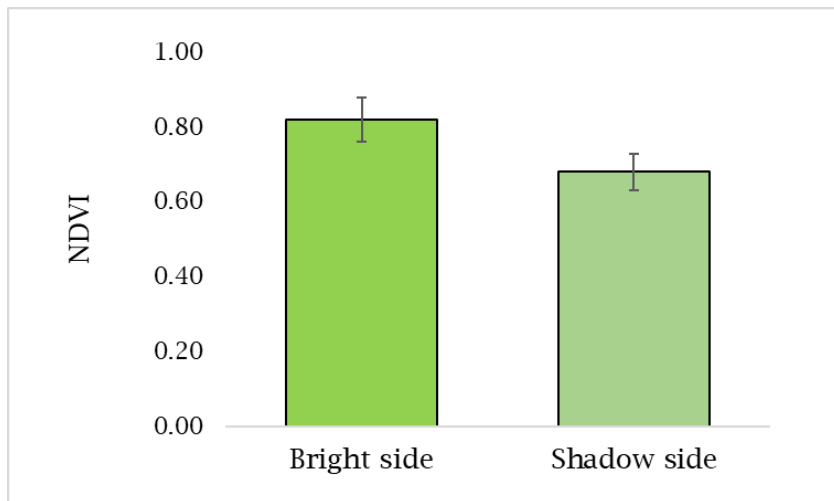
Figure 94. Average NDVI values of the canopy from the leaves on the bright side and the shaded side (Bar errors represent the $\pm$ st.dev).

The canopy temperature (Tc) of each tree was closely related to the air temperature (Ta) and other parameters such as irrigation status. However, different lighting conditions did not influence always the canopy temperature. There were no statistically significant differences between the canopy temperature in the FI treatment. Instead, a statistical difference in canopy temperatures was found between the two side of the DI treatments. The higher values of canopy temperature were found in the deficit system for both sides. (Figure 95).
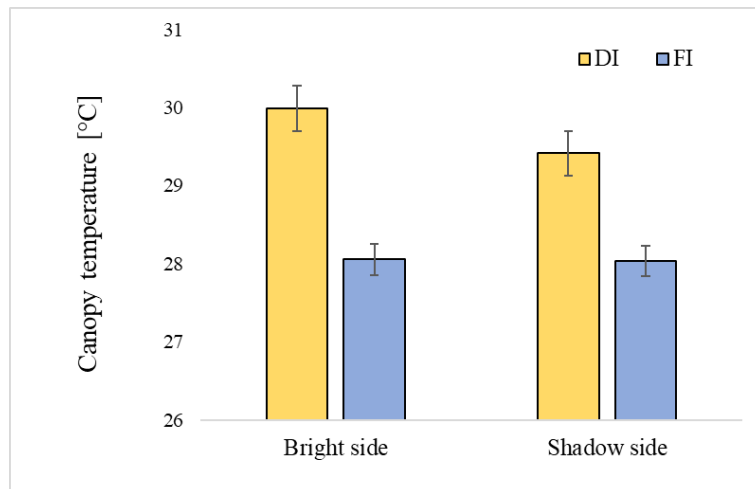
Figure 95. Canopy temperature for the two different irrigation treatments and canopy side acquisition.

From the difference in the transpiration rate of leaves, plants can vary in temperature. In general, the temperature difference (T) in leaves in good condition

is more negative, whereas plants in a stressed condition tend to have a higher value. The ANOVA test showed a statically significant difference between the two treatments ($p_{value} < 0.001$; Figure 96).
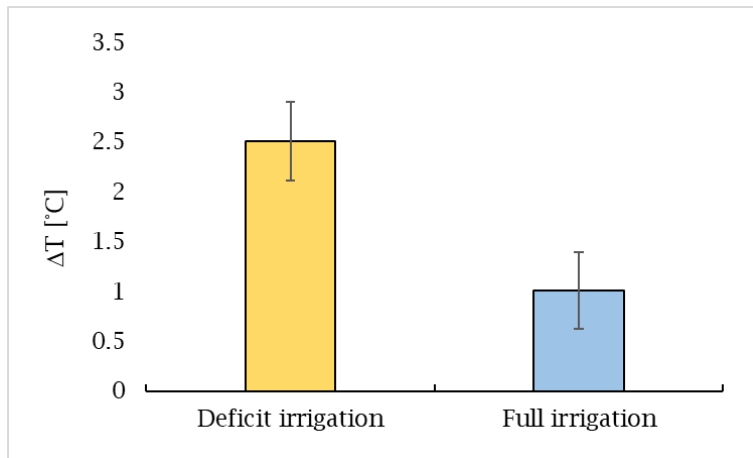
Figure 96. Average ΔT for each irrigation treatment.

The plants transpiration showed strong relation with the VPD condition of the atmosphere as reimported from the NWBL. The CWSIe showed a strong linear relationship with more parameters mainly DT and CWSI. The NWBL obtained is represented below and showed one high value of R^2 with the VPD (Figure 97).
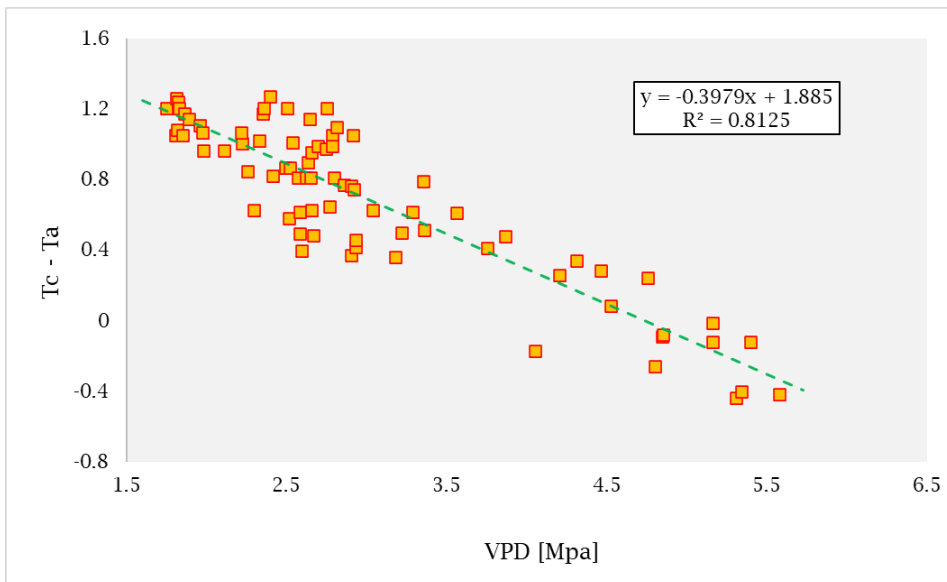
Figure 97. representation of the NWSB ($\Delta T = a + b \cdot VPD$) obtained in experimental site.

The experimentation was able to define the hydrologic status of the plants differencing the two irrigation treatments. Below, the response of the olive trees

to irrigation treatments detected by various CWSI are presented by the average value for each treatment (Figure 98).

All the main indicators strictly relate with the water stress, showed an important trend during the experimentation season (Figure 98). The LWP measured in the DI showed a growing trend more pronounced of the experimentation than the LWP measured in the FI, though in the last time of the experimentation when the irrigation was stopped and there was not rain both increased.
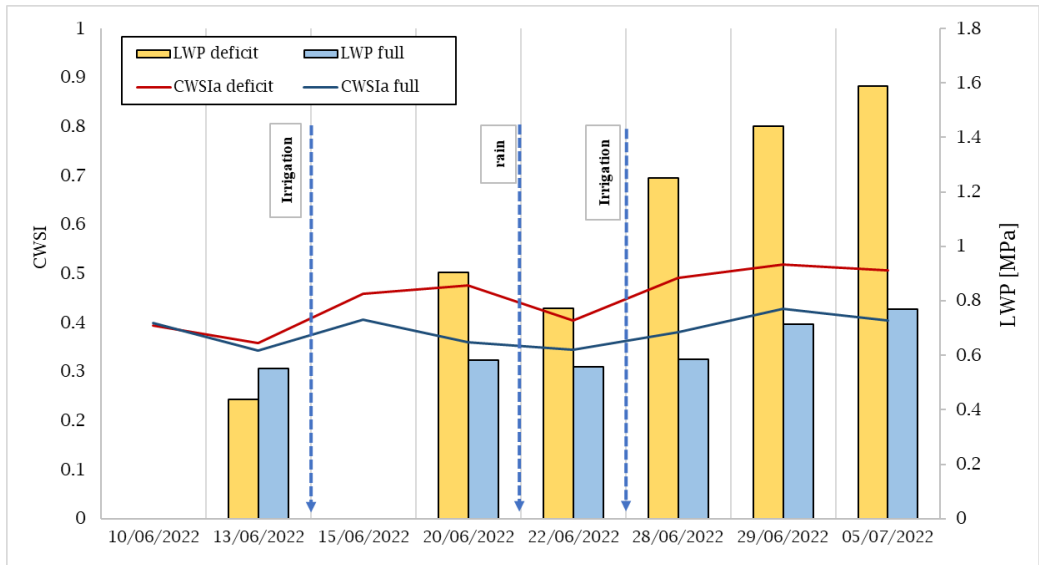
Figure 98. Trend representation of the main parameters such as: LWP, CWSIj and CWSIa during the experimentation season under the different irrigation treatments.

LWP values were different for the two-irrigation schedule. However, they were lower than 2 MPa. The LWP value was found in the DF system with an average of 1.2 ± 0.46 MPa, while in the FI system it was average 0.63 ± 0.2. LWP was strong related with the difference of the temperature with a R^2 of 0.71*** (Figure 99).
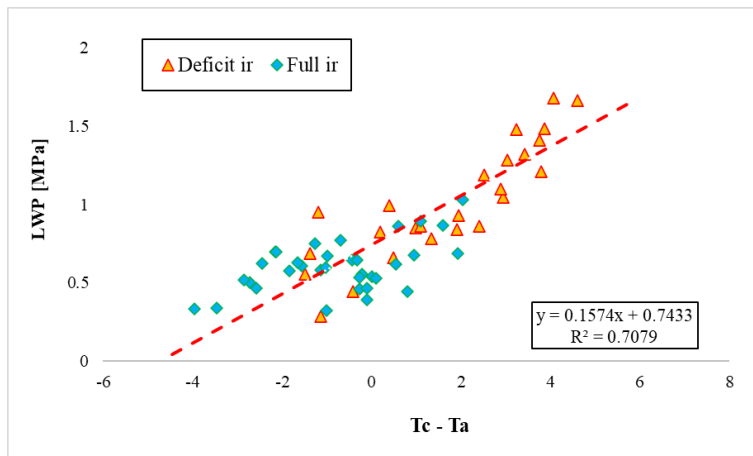
Figure 99. Relationship among the Leaf Water Potential and the Difference of Temperature (DT) obtained for the two irrigation treatments.

The CSWI analytics showed strong relationship statically significance with the LWP, as R^2 of 0.62*** and 0.57*** for CWSIj and CWSIa respectively (Figure 100). Both CWSI also showed best correlation with a DT, with a R^2 of 0.91*** and 0.88*** for CWSIj and CWSIa respectively (Figure 99).
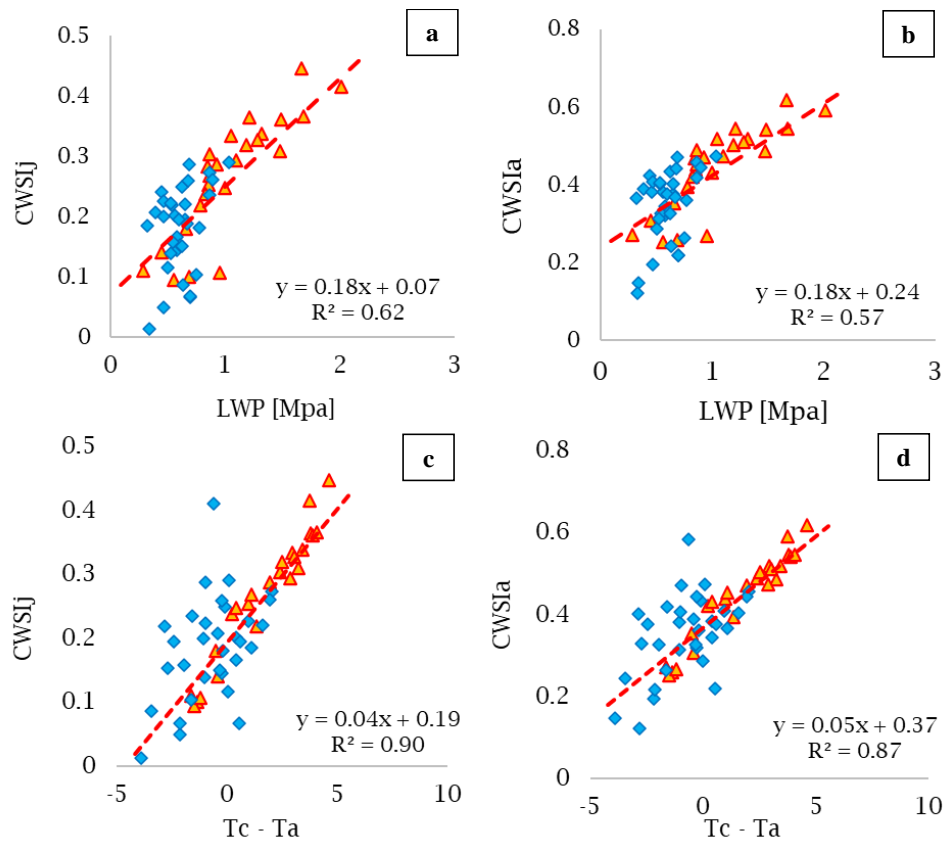
Figure 100. (**a**) Correlation relationship between the CWSIj and LWP; (**b**) correlation relationship between the CWSIa and the LWP; (**c**) correlation relationship between the CWSIj and the ΔT; (**d**) correlation relationship between the CWSIa and the DT. $p_{value} <$ 0.001 (***).

5.3. Discussion

The results obtained on the accuracy of the global positioning system confirm that the handheld system was able to acquire vegetative and weather geo-referenced data with excellent accuracy. These results emphasise how the increased deployment of low-cost positioning systems can help the spread and use of smart technologies in the service of agriculture. The results of the evaluation carried out by Jackson et al., (2018) with reference to the GNSS receiver Navcom SF-3050 showed that the low-cost receivers do not achieve the same positioning accuracy as the survey-grade ones. All low-cost receivers during static applications, could achieve centimetre-level accuracy in rural environments and perform better when using high quality versus a low-quality antenna. Indeed, the tropospheric error can be affected a low percentage of the accuracy depending on the weather condition (Karaim et al., 2018).

The results regarding the NDVI differences found per canopy side confirm the results regarding the spectral investigation assessed in Italy. Optimising the quantity and quality of olive oil requires finely tuned water management, since

143

increased irrigation, up to a certain level, increases yield, but a certain degree of stress improves oil quality. It would therefore be useful to have monitoring tools that provide accurate information on the water status of the orchard. Of the various existing methods, those with high resolution, both temporal (i.e. continuous) and spatial, have the greatest potential for adoption. One of the commonly used spatial methods is the Crop Water Stress Index (CWSI). The use of handheld systems allows the influence of external parameters to be reduced to zero. Indeed, Sepulcre-Cantó et al., (2007, 2006) observed a better relationship between DT and stomatal resistance early in the morning and a deterioration in the relationship towards noon. Their explanation of these findings was that during the early morning hours the soil temperature is lower, and thus has a smaller influence on the measurements.

The objective of this research was to test the ability of the CWSI to characterise the dynamics of the water status of olive trees in order to implement it in a handheld system. The CWSI was tested in empirical form and in two analytical configurations. The empirical and analytical CWSI was calculated based on the canopy temperature extracted from thermal images. The CWSI has already shown its high ability to determine water status, although with some differences between authors. The Jackson method has not been applied much in the literature (Jackson et al., 1981; Yuan et al., 2004); however, it has proven to be the most accurate. The other method that seems to have given very good results was that of (Hamlyn G.. Jones, 1992; Jones, 1999b). Both allowed a distinction to be made between well-watered trees, however, the analytical method using Jackson's formula showed the best results. However, the analytical forms of CWSI still require improvement as they required several parameters such as wind speed and net radiation that were not easily detectable without the help of a weather station. Thus, the analytical formulas need further testing before they can be used as a tool for monitoring the water status of olive orchards. The empirical CWSI seems to be promising, despite its limitations. In our experiment, the NWBL was derived for the measured conditions. This seems to be slightly different from the one proposed by (J. Berni et al., 2009; Egea et al., 2017). Probably due to their different climatic and cultivation conditions. Specifically, the formula found was NWBL = 1.88 + [(-0.398) * VPD]. This seems to be slightly different in the β parameter compared to the other equation. However, the NWSB obtained in our experiment, as well as in Berni et al., (2009) and Egea et al., (2017), showed a wide dispersion and a very small slope compared to the baselines reported by other authors. This means that for large variations in VPD, $T_c - T_a$ varies less than 1.5 K, a very small difference when compared to the NWSB for herbaceous crops, but also for some tree species such as pistachios (Testi et al., 2008). This is a consequence of the small leaves of the olive tree being highly coupled to the atmosphere (Villalobos et al., 2006), and also because, even for well-watered trees, some stomatal closure occurs when evaporative demand increases. A consequence of this very small slope is that the CWSI for olive trees is very sensitive to errors in estimating T_c and measuring T_a.

6. CONCLUSIONS

The growing population and the need to consume more sustainable agricultural products have set new goals for the agri-food sector, which will have to move towards a more efficient use of resources. This new form of agricultural management, also known as precision agriculture, is now widely used in many countries characterized by extensive and highly productive agriculture, which needs this change.

Today, the olive sector is characterized by a wide variability, due to the different forms of farm management. The new forms of breeding and cultivation (hedgerow olive groves) have undeniable productive, qualitative, and environmental advantages, but they pose new problems in their management (Marino et al., 2019). Therefore, scientific research is working to better control the vegetative-productive activity of the various cultivation systems, in different areas and under different agronomic (management and soil and climate) conditions. In this context, precision olive cultivation is in line with the needs of the olive sector as it is able to maximize production and quality, with the least use of input (fertilizers, water, fuel, etc.), safeguarding biodiversity and enhancing environmental sustainability.

The precision oliviculture manage all the information that we are currently able to obtain with the various devices, in order to carry out site-specific management with the smallest margin of error. The limits of precision olive-growing are represented by an overview of the agricultural variables (soil, climate, and cultivation) that is still not completely unambiguous and closely linked to the various experimental sites.

This thesis work sought to provide a clear picture of the possibilities and applications of different technologies and analysis methodologies in an olive orchard. Precisely, this thesis was focused on evaluation how proximal and remote sensing technologies equipped with different sensors can be applied to provide advantages in the olive oil sector. Specifically, the main results that this thesis work showed were:

i)   Potential application of the remote and proximal sensing platforms in the olive orchard to obtain georeferenced information and spatial variability;
ii)   Development of a GEOBIA methodology to extract information from orthomosaic and DEM images;
iii)   Effect of the altitudes and flight paths in the final photogrammetric reconstruction in dense or sparse canopy conditions;
iv)   Evaluation of biometric and vigour conditions of plants measured and predicted remotely;
v)   Evaluation of the information extracted from RGB, multispectral images and hyperspectral data to predict the production and other parameters useful for the management of each individual tree;

vi)   Assessment of the multispectral data to quantify the pruning operation impact;

vii)   Survey on nutritional status to establish the best nitrogen fertilization according to soil and crop conditions;

viii) Comparison of multispectral and hyperspectral data provided by different platforms with two different canopy viewpoints;

ix)   Evaluation of an intelligent handheld system to evaluate the water stress and vegetative condition;

x)   Evaluation of the ability of the CWSI calculated using the analytical and empirical equations to evaluate the hydrological status.

Mediterranean agricultural areas are characterised by heterogeneous orography and crop characteristics. Investigating the spatial and temporal variability of the olive orchard is a key step in site-specific management. This thesis work was able to provide clear results on the potential of UAV and proximal platform sensing in detecting and predicting the real conditions of each plant. The UAV data acquisition platform was able to investigate entire agricultural areas with high accuracy in rapid succession, achieving concrete time savings in the identification of variability. However, some mainly legislative limitations will have to be improved to allow a more radical diffusion in the area. Instead, the proximal systems had the advantage of being able to provide very precise data and through the different geostatistical techniques to also provide a description of the variability. However, they are often very laborious techniques and therefore require the automation of acquisition on mobile platforms to be more widely used in olive growing.

This thesis work was able to develop a GEOBIA methodology to extract information from the two main photogrammetric products, DEM and orthomosaic multiband. They were elaborated to obtain several information on the crop conditions allowing create new layers on GIS. For example, starting from the DEM it was possible to obtain both the DTM and the CSM and from their elaboration the geometric canopy information. The GEOBIA approach was particularly useful for delineating individual tree canopies and for deriving object shape, geometric and spectral conditions. It has also been verified that in conditions of sparse or dense foliage or the weed presence, the GEOBIA techniques must be suitably modified. In fact, the canopy was well identified using the different combinations of spectral bands of the orthomosaic which had a low presence of background spontaneous plants. Instead, during the winter period, when there was a high presence of spontaneous plants, the best segmentation of the canopy was obtained using the DEM. Mapping tree structure and pruning effects may therefore require specialized approaches to be applied to different tree crops. GEOBIA processing step that showed the greatest complexity turned out to be the segmentation itself, for this reason different algorithms were tested such as: K means, principal component analysis, neighbouring or thresholding.

Certainly, the GEOBIA analysis worked on two images deriving from the photogrammetric reconstruction. However, the different flight settings and acquisition mode of RGB and multispectral images can determine different results. The present thesis works also had the objective of evaluating these effects, focusing on the height and direction of flight in sparse or dense canopy conditions. From the results of this work, we can conclude that the canopy can be well studied starting from the RGB and multispectral images following their accurate GIS and photogrammetric analysis. The geometric parameters which were best estimated were: CA, CV, canopy perimeter and Hc. The canopy perimeter was mapped more accurately at a flight height of 30 m in sparse canopy conditions, while in dense canopy conditions there were no statistically significant differences. In the case of sparse canopies, it was possible to determine the percentage of empty spaces, a parameter not shown in the literature but which can provide important information. Nevertheless, the flight height at 70m in dense canopy conditions showed very good correlations between calculated and estimated CA. In the case of CV, these results were less accurate due to the lower estimation accuracy of the ground values. Flight altitude also had an important effect in modifying the NDVI in dense canopy whereas in the case of sparse canopy the effect was less. The flight paths that provided the best results was North-South for the estimation of Hc, Ca, and CV values. Unlike what was shown for the geometrical characteristics of the canopy, the flight paths did not give any statistically significant difference in the spectral condition. Therefore, the results shown in this thesis could be used to improve the flight settings in order to obtain the best compromise between data accuracy and cost. However, further investigations are needed to evaluate other flight parameters that can influence the final quality of the images, such as: overlap, focal length and others.

Multispectral and RGB images, were found to be able to accurately assess tree canopy biometric condition, including CA, CV, perimeter, and Hc. They were compared with the respective measurements on the ground. In all cases, excellent estimation accuracies were obtained. The parameter that was best estimated was the projection of the CA in all path configurations. An important result was instead observed in the CV estimation. Indeed, it was emphasised that ground-based measurement is coarser and overestimated than remotely estimated measurements. In the cases in which distinct results were obtained for vigor classes, the biometric data obtained from UAV images showed an excellent correspondence underlining their potential in being able to discriminate plants.

Data from several sensors has been merged to predict and highlight yield and crop conditions. The spectral conditions showed excellent correlations with the vegetative and productive parameters during the three years of experimentation. NDVI has been shown to be very sensitive to changes in leaf layers and an excellent predictor of vegetative conditions, especially for CA. These two parameters, NDVI and CA, were the best predictors of the yield and can be used to improve the new DSSs.

Canopy management is one of the key points in managing tree vigour. In the olive tree, canopy management is one of the most important techniques capable of modifying growth and yield. In this thesis work we have tried to outline what the, often expensive, impact of pruning operation was, using an innovative approach that exploits multispectral UAV images to measure the structural and spectral differences of trees. Indeed, from the UAV platform it was possible to observe with good accuracy the changes in terms of volume and spectral response of the canopy. Therefore, from this work, new ideas can be taken to understand how to use this agronomic technique in order to manage the canopy at a variable rate, also considering its influence on production. Indeed, SHD olive groves pruning is fully mechanized and such results could be very useful. Certainly, it will be necessary to investigate the real potential that this practice has on vegetative and productive activity.

Another important plants characteristic to determine the yield and the vegetative growth is the nutritional status. Therefore, the management of fertilization, especially the nitrogenous one in the case of Mediterranean environments, represents an important aspect for greater agronomic efficiency. A methodology was proposed in this study to create a prescription map for fertilizers to be applied in olive orchards, taking into account the actual agronomic and soil conditions of the agro-ecosystem. Nutritional status and pedological condition offer important information to create a prescription map to balance the crop status during the first and second years. Productivity, biometric, nutritional and spectral data of the olive trees provided important information for deriving the correct crop nitrogen requirements for each individual plant. In particular, for the application of precision nitrogen fertilization, productivity, amount of biomass produced and relative nitrogen concentration were needed. By integrating the different information, an even more accurate estimate of nitrogen requirements was obtained, taking into account the crop and the current agronomic conditions. A 24% and 66% fertilizer savings were obtained, with economic, agronomic and environmental benefits. This method determined a reduction in fertilizers distribution, lowering total costs and reaching greater sustainability. However, this particular topic will need to be better investigated in order to better understand how this agronomic practice can affect growth rates. The fertilisation maps obtained show various differences in the amount of application, so in future studies it will be important to understand which of the maps can provide the best results.

The multispectral images obtained from remote sensing by drone can be compared with the hyperspectral images from proximal systems as they correlate well. This is especially the case when the proper wavelengths are used from the hyperspectral data and the acquisitions made in the South and West exposures of olive trees. The data obtained from the remote platform showed very good correlation and data matching over the whole plot and allow it to be accurately investigated. However, the possibility of obtaining spectral information from the crop, the development of new acquisition platforms from proximal sensing such

as Unmanned Ground Vehicles (UGV) and the continuous improvement of technology, make the use of hyperspectral sensors in precision farming increasingly interesting. This study has shown that hyperspectral data acquired from proximal platform with a different viewpoint can more accurately describe the crop spectral status, despite the limited diffusion of proximal sensing platforms for investigating the entire variability of the plot and the high variability of the data, depending on crop conditions such as exposure and brightness. This study was able to discriminate the potential of hyperspectral and multispectral data also considering their simultaneous use. Anyway, some characteristics of the two different platforms, such as application time and data management, should be evaluated in depth for future applications.

The experiment conducted in Valencia Polytechnic University (Spain) confirmed that the CWSI calculated using different methodologies can be a valid tool for detecting water stress in the field as it is closely related to LWP. The CWSI value that provided the best results was found to be that of Jackson et al. (1981), but the limitations imposed by the amount of data required does not allow its easy implementation in handheld instruments. Indeed, the analytic and empirical CWSI showed good results; however calculation of CWSIa based on Jackson's (Jackson et al., 1981) definition needs more environmental variables than CWSIe based on the Idso's (Idso, 1982). The empirical CWSI for water stress detection is a valid substitute for the CWSIj by making the necessary calibrations. Indeed, the CWSIe proved to be a good predictor of hydraulic stress and from the experiments conducted in this thesis two new parameters were calculated which could be used in other studies. The handheld system created has proven to be a valid tool for the detection of water but also the crop conditions. In fact, it was possible to evaluate the different spectral condition of the two sides of the canopy, confirming what was observed previously. Furthermore, the two sides, in addition to having differences in terms of NDVI, had different temperatures. These results underline how important it is to know canopy development in order to better manage water stress conditions. The positioning system used also provided excellent results even in unfavourable climatic conditions, making this instrument easily applicable and integrable in the various precision oliviculture applications. In conclusion, this thesis was able to assess how the main growth parameters measured via a high-resolution remote and proximal platform equipped with several sensors such as spectral, thermal and RGB sensors processed on various GIS platforms can express the real field and plant conditions. It was possible to verify that the new technologies available in precision agriculture allow to obtain various information on the crop status of each olive trees. Precisely, the UAV platform equipped with multispectral and RGB cameras was able to determine, through the GIS analysis, the main vegetative characteristics such as: various VI, Hc, CA and CV. They can be modified with the different agronomic practices to improve crop efficiency. UAV technology has demonstrated an excellent ability to efficiently produce spectral and geometric data of hundreds of agricultural trees at field level in a timely and accurate manner, offering a viable alternative to hard

and inefficient field work by investigating the entire spatial variability of the orchard within minutes. In addition, the GIS platforms used were able to spatialize the collected point samples data, such as the nutritional ones. All geo-referenced information allows the creation of maps of orchard heterogeneity and the identification of incorrect growing conditions. This heterogeneity was expressed as spatial variability of different growth and production parameters. Knowing this variability is the key point for the creation of specific maps that allow the construction and use of accurate DSS systems for olive orchard management optimization. In this way, a site-specific management strategy can be applied to increase profitability by improving input utilization (fertilizers, pesticides, water, etc.) and field operations (pruning, spray application, irrigation, harvesting). The results obtained in this paper derive from the first study carried out in Sicily, a region of Italy that produces quality extra virgin olive oils. Although this thesis work has been able to provide a broad overview of the real potential of the UAV platform and handheld system in detecting the different crop parameters, further experiments will also be needed in other pedoclimatic contexts to validate these results.

REFERENCES

Agam, N., Cohen, Y., Berni, J., Alchanatis, V., Kool, D., Dag, A., Yermiyahu, U., Ben-Gal, A., 2013. An insight to the performance of crop water stress index for olive trees. Agricultural Water Management 118, 79–86.

Agam, N., Segal, E., Peeters, A., Levi, A., Dag, A., Yermiyahu, U., Ben-Gal, A., 2014. Spatial distribution of water status in irrigated olive orchards by thermal imaging. Precision agriculture 15, 346–359.

Aggelopoulou, K., Pateras, D., Fountas, S., Gemtos, T., Nanos, G., 2011. Soil spatial variability and site-specific fertilization maps in an apple orchard. Precision Agriculture 12, 118–129.

Agüera-Vega, J., Blanco, G., Castillo, F., Castro-Garcia, S., Gil-Ribes, J., Perez-Ruiz, M., 2013. Determination of field capacity and yield mapping in olive harvesting using remote data acquisition, in: Precision Agriculture'13. Springer, pp. 691–696.

Akdemir, B., Saglam, C., Belliturk, K., Makaraci, A., Urusan, A., Atar, E., 2018. Effect of spatial variability on fertiliser requirement of olive orchard cultivated for oil production. Journal of Environmental Protection and Ecology 19, 319–329.

Alahmadi, A., Alwajeeh, T., Mohanan, V., Budiarto, R., 2018. Wireless sensor network with always best connection for internet of farming, in: Powering the Internet of Things with 5G Networks. IGI Global, pp. 176–201.

Álamo, S., Ramos, M., Feito, F., Cañas, A., 2012. Precision techniques for improving the management of the olive groves of southern Spain. Spanish Journal of agricultural research 583–595.

Alcalá Jiménez, A., Álamo Romero, S., 1998. Using GPS for yield mapping in olive orchards. Presented at the First Internacional Conference on Geospatial Information in Agriculture and Forestry.

Ali, M., Al-Ani, A., Eamus, D., Tan, D.K., 2017. Leaf nitrogen determination using non-destructive techniques–A review. Journal of Plant Nutrition 40, 928–953.

Alkassem, M., Buis, S., Coulouma, G., Jacob, F., Lagacherie, P., Prévot, L., 2022. Estimating soil available water capacity within a Mediterranean vineyard watershed using satellite imagery and crop model inversion. Geoderma 425, 116081.

Allen, R.G., Pereira, L.S., Raes, D., Smith, M., 1998. Crop evapotranspiration-Guidelines for computing crop water requirements-FAO Irrigation and drainage paper 56. Fao, Rome 300, D05109.

Anifantis, A.S., Camposeo, S., Vivaldi, G.A., Santoro, F., Pascuzzi, S., 2019. Comparison of UAV photogrammetry and 3D modeling techniques with other currently used methods for estimation of the tree row volume of a super-high-density olive orchard. Agriculture 9, 233.

Apan, A., Young, F.R., Phinn, S., Held, A., Favier, J., 2004. Mapping olive varieties and within-field spatial variability using high resolution

QuickBird imagery. Presented at the Proceedings of the 12th Australasian Remote Sensing and Photogrammetry Conference, Spatial Sciences Institute.

Asari, N., Suratman, M.N., Jaafar, J., Khalid, M.M., 2013. Estimation of aboveground biomass for oil palm plantations using allometric equations. Presented at the 4th Int. Conf. on Biology, Environment and Chemistry.

Baiamonte, G., Minacapilli, M., Novara, A., Gristina, L., 2019. Time scale effects and interactions of rainfall erosivity and cover management factors on vineyard soil loss erosion in the semi-arid area of southern Sicily. Water 11, 978.

Baldoni, L., Belaj, A., 2009. Olive, in: Oil Crops. Springer, pp. 397–421.

Barranco-Navero, D., FERNANDEZ ESCOBAR, R., RALLO ROMERO, L., 2017. El cultivo del olivo 7ª ed. Mundi-Prensa Libros.

Bastiaanssen, W.G., Menenti, M., Feddes, R., Holtslag, A., 1998. A remote sensing surface energy balance algorithm for land (SEBAL). 1. Formulation. Journal of hydrology 212, 198–212.

Bellvert, J., Marsal, J., Girona, J., Gonzalez-Dugo, V., Fereres, E., Ustin, S.L., Zarco-Tejada, P.J., 2016. Airborne thermal imagery to detect the seasonal evolution of crop water status in peach, nectarine and Saturn peach orchards. Remote Sensing 8, 39.

Ben-Gal, A., Agam, N., Alchanatis, V., Cohen, Y., Yermiyahu, U., Zipori, I., Presnov, E., Sprintsin, M., Dag, A., 2009. Evaluating water stress in irrigated olives: correlation of soil water status, tree water status, and thermal imagery. Irrigation Science 27, 367–376.

Berni, J., Zarco-Tejada, P., Sepulcre-Cantó, G., Fereres, E., Villalobos, F., 2009. Mapping canopy conductance and CWSI in olive orchards using high resolution thermal remote sensing imagery. Remote Sensing of Environment 113, 2380–2388.

Berni, J.A., Zarco-Tejada, P.J., Suárez, L., Fereres, E., 2009. Thermal and narrowband multispectral remote sensing for vegetation monitoring from an unmanned aerial vehicle. IEEE Transactions on geoscience and Remote Sensing 47, 722–738.

Bianco, S., Ciocca, G., Marelli, D., 2018. Evaluating the performance of structure from motion pipelines. Journal of Imaging 4, 98.

Blackmore, S., 2003. The role of yield maps in precision farming.

Blaschke, T., 2010. Object based image analysis for remote sensing. ISPRS journal of photogrammetry and remote sensing 65, 2–16.

Blaschke, T., Hay, G.J., Kelly, M., Lang, S., Hofmann, P., Addink, E., Feitosa, R.Q., Van der Meer, F., Van der Werff, H., Van Coillie, F., 2014. Geographic object-based image analysis–towards a new paradigm. ISPRS journal of photogrammetry and remote sensing 87, 180–191.

Bongers, F., 2001. Methods to assess tropical rain forest canopy structure: an overview. Tropical Forest Canopies: Ecology and Management 263–277.

Bouhafa, K., Moughli, L., Bouchoufi, K., Douaik, A., Daoui, K., 2014. Nitrogen fertilization of olive orchards under rainfed Mediterranean conditions. American Journal of Experimental Agriculture 4, 890.

Boussadia, O., Steppe, K., Zgallai, H., El Hadj, S.B., Braham, M., Lemeur, R., Van Labeke, M.-C., 2010. Effects of nitrogen deficiency on leaf photosynthesis, carbohydrate status and biomass production in two olive cultivars 'Meski'and 'Koroneiki.' Scientia Horticulturae 123, 336–342.

Buttafuoco, G., Castrignanò, A., Cucci, G., Lacolla, G., Lucà, F., 2017. Geostatistical modelling of within-field soil and yield variability for management zones delineation: a case study in a durum wheat field. Precision Agriculture 18, 37–58.

Campos, I., Neale, C.M., Calera, A., 2017. Is row orientation a determinant factor for radiation interception in row vineyards? Australian Journal of Grape and Wine Research 23, 77–86.

Caruso, G., Gucci, R., Urbani, S., Esposto, S., Taticchi, A., Di Maio, I., Selvaggini, R., Servili, M., 2014. Effect of different irrigation volumes during fruit development on quality of virgin olive oil of cv. Frantoio. Agricultural water management 134, 94–103.

Caruso, G., Palai, G., Marra, F.P., Caruso, T., 2021. High-resolution UAV imagery for field olive (Olea europaea L.) phenotyping. Horticulturae 7, 258.

Caruso, G., Zarco-Tejada, P.J., González-Dugo, V., Moriondo, M., Tozzini, L., Palai, G., Rallo, G., Hornero, A., Primicerio, J., Gucci, R., 2019. High-resolution imagery acquired from an unmanned platform to estimate biophysical and geometrical parameters of olive trees under different irrigation regimes. PloS one 14, e0210804.

Casa, R., Cavalieri, A., Cascio, B.L., 2011. Nitrogen fertilisation management in precision agriculture: a preliminary application example on maize. Italian Journal of Agronomy 6, e5–e5.

Castillo-Ruiz, F.J., Castro-Garcia, S., Blanco-Roldan, G.L., Sola-Guirado, R.R., Gil-Ribes, J.A., 2016. Olive crown porosity measurement based on radiation transmittance: an assessment of pruning effect. Sensors 16, 723.

Castillo-Ruiz, F.J., Pérez-Ruiz, M., Blanco-Roldán, G.L., Gil-Ribes, J.A., Agüera, J., 2015. Development of a telemetry and yield-mapping system of olive harvester. Sensors 15, 4001–4018.

Catania, P., Comparetti, A., Febo, P., Morello, G., Orlando, S., Roma, E., Vallone, M., 2020. Positioning accuracy comparison of GNSS receivers used for mapping and guidance of agricultural machines. Agronomy 10, 924.

Catania, P., Orlando, S., Roma, E., Vallone, M., 2019. Vineyard design supported by GPS application, in: International Symposium. pp. 227–233. https://doi.org/10.17660/ActaHortic.2021.1314.29

Catania, P., Roma, E., Orlando, S., Vallone, M., 2023. Evaluation of Multispectral Data Acquired from UAV Platform in Olive Orchard. Horticulturae 9, 133.

Chehbouni, A., Nouvellon, Y., Lhomme, J.-P., Watts, C., Boulet, G., Kerr, Y., Moran, M.S., Goodrich, D., 2001. Estimation of surface sensible heat flux using dual angle observations of radiative surface temperature. Agricultural and Forest Meteorology 108, 55–65.

Cheng, H.-D., Jiang, X.H., Sun, Y., Wang, J., 2001. Color image segmentation: advances and prospects. Pattern recognition 34, 2259–2281.

Cheng, T., Ji, X., Yang, G., Zheng, H., Ma, J., Yao, X., Zhu, Y., Cao, W., 2020. DESTIN: A new method for delineating the boundaries of crop fields by fusing spatial and temporal information from WorldView and Planet satellite imagery. Computers and Electronics in Agriculture 178, 105787.

Chiles, J.-P., Delfiner, P., 2009. Geostatistics: modeling spatial uncertainty. John Wiley & Sons.

Clark, I., 1979. Practical geostatistics. Applied Science Publishers London.

Cohen, Y., Alchanatis, V., Meron, M., Saranga, Y., Tsipris, J., 2005. Estimation of leaf water potential by thermal imagery and spatial analysis. Journal of experimental botany 56, 1843–1852.

Cointault, F., Sarrazin, P., Paindavoine, M., 2003. Measurement of the motion of fertilizer particles leaving a centrifugal spreader using a fast imaging system. Precision agriculture 4, 279–295.

Cressie, N., 2015. Statistics for spatial data. John Wiley & Sons.

Cruz-Ramírez, M., Hervás-Martínez, C., Jurado-Expósito, M., López-Granados, F., 2012. A multi-objective neural network based method for cover crop identification from remote sensed data. Expert Systems with Applications 39, 10038–10048.

Dag, A., Ben-David, E., Kerem, Z., Ben-Gal, A., Erel, R., Basheer, L., Yermiyahu, U., 2009. Olive oil composition as a function of nitrogen, phosphorus and potassium plant nutrition. Journal of the Science of Food and Agriculture 89, 1871–1878.

De Gennaro, B., Notarnicola, B., Roselli, L., Tassielli, G., 2012. Innovative olive-growing models: an environmental and economic assessment. Journal of cleaner production 28, 70–80.

Deng, L., Mao, Z., Li, X., Hu, Z., Duan, F., Yan, Y., 2018. UAV-based multispectral remote sensing for precision agriculture: A comparison between different cameras. ISPRS journal of photogrammetry and remote sensing 146, 124–136.

Díaz-Varela, R.A., De la Rosa, R., León, L., Zarco-Tejada, P.J., 2015. High-resolution airborne UAV imagery to assess olive tree crown parameters using 3D photo reconstruction: application in breeding trials. Remote Sensing 7, 4213–4232.

Egea, G., Padilla-Díaz, C.M., Martinez-Guanter, J., Fernández, J.E., Pérez-Ruiz, M., 2017. Assessing a crop water stress index derived from aerial thermal imaging and infrared thermometry in super-high density olive orchards. Agricultural Water Management 187, 210–221.

Ehlert, D., Schmerler, J., Voelker, U., 2004. Variable rate nitrogen fertilisation of winter wheat based on a crop density sensor. Precision Agriculture 5, 263–273.

Elsayed, S., Mistele, B., Schmidhalter, U., 2011. Can changes in leaf water potential be assessed spectrally? Functional Plant Biology 38, 523–533.

European Agriculture Machinery Association, 2017. Digital Farming: what does it really mean. Position Paper, CEMA.

FAOSTAT, F., n.d. Statistics, Food and Agriculture Organization of the United Nations, Rome. 2020.

Fernández, J.E., 2017. Plant-based methods for irrigation scheduling of woody crops. Horticulturae 3, 35.

Fernández, J.E., Diaz-Espejo, A., Romero, R., Hernandez-Santana, V., García, J.M., Padilla-Díaz, C.M., Cuevas, M.V., 2018. Precision irrigation in olive (Olea europaea L.) tree orchards, in: Water Scarcity and Sustainable Agriculture in Semiarid Environment. Elsevier, pp. 179–217.

Fernández-Escobar, R., 2011. Use and abuse of nitrogen in olive fertilization. Acta Hortic 888, 249–257.

Fernández-Escobar, R., Beltrán, G., Sánchez-Zamora, M., García-Novelo, J., Aguilera, M., Uceda, M., 2006. Olive oil quality decreases with nitrogen over-fertilization. HortScience 41, 215–219.

Fernández-Escobar, R., García Novelo, J., Sánchez Zamora, M., Uceda, M., Beltrán, G., Aguilera, M., 2002. Efecto del abonado nitrogenado en la producción y la calidad del aceite de oliva. Dirección General de Investigación y Formación Agraria y Pesquera (Ed.), Jornadas de Investigación y Transferencia de Tecnología al Sector Oleícola, Córdoba (Spain) 299–302.

Fernández-Escobar, R., García-Novelo, J., Molina-Soria, C., Parra, M., 2012. An approach to nitrogen balance in olive orchards. Scientia horticulturae 135, 219–226.

Fernández-Escobar, R., Marín, L., 1997. Nitrogen fertilization in olive orchards. Presented at the III International Symposium on Olive Growing 474, pp. 333–336.

Fernandez-Escobar, R., Ortiz-Urquiza, A., Prado, M., Rapoport, H.F., 2008. Nitrogen status influence on olive tree flower quality and ovule longevity. Environmental and experimental Botany 64, 113–119.

Fernández-Escobar, R., Sánchez-Zamora, M.A., Garcia-Novelo, J.M., Molina-Soria, C., 2015. Nutrient removal from olive trees by fruit yield and pruning. HortScience 50, 474–478.

Ferwerda, J.G., Skidmore, A.K., 2007. Can nutrient status of four woody plant species be predicted using field spectrometry? ISPRS Journal of Photogrammetry and Remote Sensing 62, 406–414.

Fountas, S., Aggelopoulou, K., Bouloulis, C., Nanos, G., Wulfsohn, D., Gemtos, T., Paraskevopoulos, A., Galanis, M., 2011. Site-specific management in an olive tree plantation. Precision agriculture 12, 179–195.

Fountas, S., Aggelopoulou, K., Gemtos, T.A., 2015. Precision agriculture: crop management for improved productivity and reduced environmental impact or improved sustainability. Supply chain management for sustainable food networks 41–65.

Fuentes-Peñailillo, F., Ortega-Farías, S., Acevedo-Opazo, C., Fonseca-Luengo, D., 2018. Implementation of a two-source model for estimating the spatial variability of olive evapotranspiration using satellite images and ground-based climate data. Water 10, 339.

Fulton, J.P., Port, K., 2018. Precision agriculture data management. Precision agriculture basics 169–187.

Furferi, R., Governi, L., Volpe, Y., 2010. ANN-based method for olive Ripening Index automatic prediction. Journal of Food Engineering 101, 318–328.

Gamarra-Diezma, J.L., Miranda-Fuentes, A., Llorens, J., Cuenca, A., Blanco-Roldán, G.L., Rodríguez-Lizana, A., 2015. Testing accuracy of long-range ultrasonic sensors for olive tree canopy measurements. Sensors 15, 2902–2919.

Gargouri, K., Sarbeji, M., Barone, E., 2006. Assessment of soil fertility variation in an olive orchard and its influence on olive tree nutrition. Presented at the Second International Seminar on Biotechnology and Quality of Olive Tree Products Around the Mediterranean Basin, pp. 5–10.

Gee, G.W., Or, D., 2002. 2.4 Particle-size analysis. Methods of soil analysis: Part 4 physical methods 5, 255–293.

Ghahremani, M., Williams, K., Corke, F., Tiddeman, B., Liu, Y., Wang, X., Doonan, J.H., 2021. Direct and accurate feature extraction from 3D point clouds of plants using RANSAC. Computers and Electronics in Agriculture 187, 106240.

Gil, E., Arnó, J., Llorens, J., Sanz, R., Llop, J., Rosell-Polo, J.R., Gallart, M., 2014. Advanced technologies for the improvement of spray application techniques in Spanish viticulture: An overview. Sensors 14, 691–708.

Giovos, R., Tassopoulos, D., Kalivas, D., Lougkos, N., Priovolou, A., 2021. Remote sensing vegetation indices in viticulture: A critical review. Agriculture 11, 457.

Giuliani, R., Magnanini, E., Fragassa, C., Nerozzi, F., 2000. Ground monitoring the light–shadow windows of a tree canopy to yield canopy light interception and morphological traits. Plant, Cell & Environment 23, 783–796.

Godfray, H.C.J., Beddington, J.R., Crute, I.R., Haddad, L., Lawrence, D., Muir, J.F., Pretty, J., Robinson, S., Thomas, S.M., Toulmin, C., 2010. Food security: the challenge of feeding 9 billion people. science 327, 812–818.

Gómez, J., Zarco-Tejada, P., García-Morillo, J., Gama, J., Soriano, M., 2011. Determining Biophysical Parameters for Olive Trees Using CASI-Airborne and Quickbird-Satellite Imagery. Agronomy journal 103, 644–654.

Gómez-Casero, M.T., López-Granados, F., Pena-Barragán, J.M., Jurado-Expósito, M., García-Torres, L., Fernández-Escobar, R., 2007. Assessing nitrogen and potassium deficiencies in olive orchards through discriminant analysis of hyperspectral data. Journal of the American Society for Horticultural Science 132, 611–618.

Guilioni, L., Jones, H., Leinonen, I., Lhomme, J.-P., 2008. On the relationships between stomatal resistance and leaf temperatures in thermography. Agricultural and Forest Meteorology 148, 1908–1912.

Ha, W., Gowda, P.H., Howell, T.A., 2013. A review of downscaling methods for remote sensing-based irrigation management: Part I. Irrigation Science 31, 831–850.

Hamlyn G.. Jones, 1992. Plants and microclimate: a quantitative approach to environmental plant physiology. Cambridge University Press.

Hansen, P., Schjoerring, J., 2003. Reflectance measurement of canopy biomass and nitrogen status in wheat crops using normalized difference vegetation indices and partial least squares regression. Remote sensing of environment 86, 542–553.

Hernández-Clemente, R., Navarro-Cerrillo, R.M., Ramírez, F.J.R., Hornero, A., Zarco-Tejada, P.J., 2014. A novel methodology to estimate single-tree biophysical parameters from 3D digital imagery compared to aerial laser scanner data. Remote Sensing 6, 11627–11648.

Hillel, D., 2013. Fundamentals of soil physics. Academic press.

Hossain, M.D., Chen, D., 2019. Segmentation for Object-Based Image Analysis (OBIA): A review of algorithms and challenges from remote sensing perspective. ISPRS Journal of Photogrammetry and Remote Sensing 150, 115–134.

Huang, S.-W., Jin, J.-Y., Yang, L.-P., Bai, Y.-L., 2006. Spatial variability of soil nutrients and influencing factors in a vegetable production area of Hebei Province in China. Nutrient Cycling in Agroecosystems 75, 201–212.

Huband, N., Monteith, J., 1986. Radiative surface temperature and energy balance of a wheat canopy. Boundary-Layer Meteorology 36, 1–17.

Hui, F., Zhu, J., Hu, P., Meng, L., Zhu, B., Guo, Y., Li, B., Ma, Y., 2018. Image-based dynamic quantification and high-accuracy 3D evaluation of canopy structure of plant populations. Annals of Botany 121, 1079–1088.

Idso, S., Jackson, R., Pinter Jr, P., Reginato, R., Hatfield, J., 1981. Normalizing the stress-degree-day parameter for environmental variability. Agricultural meteorology 24, 45–55.

Idso, S.B., 1982. Non-water-stressed baselines: a key to measuring and interpreting plant water stress. Agricultural Meteorology 27, 59–70.

Irmak, S., Haman, D.Z., Bastug, R., 2000. Determination of crop water stress index for irrigation timing and yield estimation of corn. Agronomy Journal 92, 1221–1227.

Jackson, J., Saborio, R., Ghazanfar, S.A., Gebre-Egziabher, D., Davis, B., 2018. Evaluation of low-cost, centimeter-level accuracy OEM GNSS receivers.

Jackson, R.D., Idso, S., Reginato, R., Pinter Jr, P., 1981. Canopy temperature as a crop water stress indicator. Water resources research 17, 1133–1138.

Jackson, R.D., Kustas, W.P., Choudhury, B.J., 1988. A reexamination of the crop water stress index. Irrigation science 9, 309–317.

Jay, S., Rabatel, G., Hadoux, X., Moura, D., Gorretta, N., 2015. In-field crop row phenotyping from 3D modeling performed using Structure from Motion. Computers and Electronics in Agriculture 110, 70–77.

Jha, K., Doshi, A., Patel, P., Shah, M., 2019. A comprehensive review on automation in agriculture using artificial intelligence. Artificial Intelligence in Agriculture 2, 1–12.

Jiménez-Brenes, F.M., López-Granados, F., De Castro, A., Torres-Sánchez, J., Serrano, N., Peña, J., 2017. Quantifying pruning impacts on olive tree architecture and annual canopy growth by using UAV-based 3D modelling. Plant Methods 13, 1–15.

Johansen, K., Raharjo, T., McCabe, M.F., 2018. Using multi-spectral UAV imagery to extract tree crop structural properties and assess pruning effects. Remote Sensing 10, 854.

Jonckheere, I., Fleck, S., Nackaerts, K., Muys, B., Coppin, P., Weiss, M., Baret, F., 2004. Review of methods for in situ leaf area index determination: Part I. Theories, sensors and hemispherical photography. Agricultural and forest meteorology 121, 19–35.

Jones, H.G., 1999a. Use of infrared thermometry for estimation of stomatal conductance as a possible aid to irrigation scheduling. Agricultural and forest meteorology 95, 139–149.

Jones, H.G., 1999b. Use of infrared thermometry for estimation of stomatal conductance as a possible aid to irrigation scheduling. Agricultural and forest meteorology 95, 139–149.

Jones, H.G., Archer, N., Rotenberg, E., Casa, R., 2003. Radiation measurement for plant ecophysiology. Journal of Experimental Botany 54, 879–889.

Jorge, J., Vallbé, M., Soler, J.A., 2019. Detection of irrigation inhomogeneities in an olive grove using the NDRE vegetation index obtained from UAV images. European Journal of Remote Sensing 52, 169–177.

Jurado, J.M., Ortega, L., Cubillas, J.J., Feito, F., 2020. Multispectral mapping on 3D models and multi-temporal monitoring for individual characterization of olive trees. Remote Sensing 12, 1106.

Karaim, M., Elsheikh, M., Noureldin, A., Rustamov, R., 2018. GNSS error sources. Multifunctional Operation and Application of GPS 69–85.

Karydas, C., Gewehr, S., Iatrou, M., Iatrou, G., Mourelatos, S., 2017. Olive plantation mapping on a sub-tree scale with object-based image analysis of multispectral UAV data; Operational potential in tree stress monitoring. Journal of Imaging 3, 57.

Kattenborn, T., Sperlich, M., Bataua, K., Koch, B., 2014. Automatic single tree detection in plantations using UAV-based photogrammetric point clouds.

The International Archives of Photogrammetry, Remote Sensing and Spatial Information Sciences 40, 139.

Khan, M., Islam, M., Salam, A.B.A., Ray, T., 2021. Spatial variability and geostatistical analysis of soil properties in the diversified cropping regions of Bangladesh using geographic information system techniques. Applied and Environmental Soil Science 2021.

Koch, B., Khosla, R., Frasier, W., Westfall, D., Inman, D., 2004. Economic feasibility of variable-rate nitrogen application utilizing site-specific management zones. Agronomy Journal 96, 1572–1580.

Kottek, M., Grieser, J., Beck, C., Rudolf, B., Rubel, F., 2006. World map of the Köppen-Geiger climate classification updated.

Küng, O., Strecha, C., Beyeler, A., Zufferey, J.-C., Floreano, D., Fua, P., Gervaix, F., 2011. The accuracy of automatic photogrammetric techniques on ultra-light UAV imagery.

Lal, R., 2015. 16 Challenges and Opportunities in Precision Agriculture. Soil-Specific Farming: Precision Agriculture 22, 391.

Lee, W.-S., Alchanatis, V., Yang, C., Hirafuji, M., Moshou, D., Li, C., 2010. Sensing technologies for precision specialty crop production. Computers and electronics in agriculture 74, 2–33.

Liang, S., 2005. Quantitative remote sensing of land surfaces. John Wiley & Sons.

Liang, S., 2004. Quantitative remote sensing of land surfaces, Wiley series in remote sensing. Wiley-Interscience, Hoboken, N.J.

López-Granados, F., Jurado-Expósito, M., Alamo, S., Garcıa-Torres, L., 2004. Leaf nutrient spatial variability and site-specific fertilization maps within olive (Olea europaea L.) orchards. European Journal of Agronomy 21, 209–222.

Maccioni, A., Agati, G., Mazzinghi, P., 2001. New vegetation indices for remote measurement of chlorophylls based on leaf directional reflectance spectra. Journal of Photochemistry and Photobiology B: Biology 61, 52–61.

Makhloufi, A., Kallel, A., Chaker, R., Gastellu-Etchegorry, J.-P., 2021. Retrieval of olive tree biophysical properties from Sentinel-2 time series based on physical modelling and machine learning technique. International Journal of Remote Sensing 42, 8542–8571.

Manzo, M., 2020. Attributed relational sift-based regions graph: Concepts and applications. Machine Learning and Knowledge Extraction 2, 233–255.

Maran, L., Fernandez-Escobar, R., 1996. Optimization of nitrogen fertilization in olive orchards. Presented at the III International Symposium on Mineral Nutrition of Deciduous Fruit Trees 448, pp. 411–414.

Marino, G., Macaluso, L., Grilo, F., Marra, F.P., Caruso, T., 2019. Toward the valorization of olive (Olea europaea var. europaea L.) biodiversity: Horticultural performance of seven Sicilian cultivars in a hedgerow planting system. Scientia Horticulturae 256, 108583.

Marshall, M., Thenkabail, P., 2015. Advantage of hyperspectral EO-1 Hyperion over multispectral IKONOS, GeoEye-1, WorldView-2, Landsat ETM+,

and MODIS vegetation indices in crop biomass estimation. ISPRS Journal of Photogrammetry and Remote Sensing 108, 205–218.

Martínez-Casasnovas, J.A., Rufat, J., Arnó, J., Arbonés, A., Sebé, F., Pascual, M., Gregorio, E., Rosell-Polo, J.R., 2017. Mobile terrestrial laser scanner applications in precision fruticulture/horticulture and tools to extract information from canopy point clouds. Precision Agriculture 18, 111–132.

Martinez-Guanter, J., Agüera, P., Agüera, J., Pérez-Ruiz, M., 2020. Spray and economics assessment of a UAV-based ultra-low-volume application in olive and citrus orchards. Precision Agriculture 21, 226–243.

Matese, A., Di Gennaro, S.F., 2015. Technology in precision viticulture: A state of the art review. International journal of wine research 7, 69–81.

Meron, M., Tsipris, J., Charitt, D., 2003. Remote mapping of crop water status to assess spatial variability of crop stress. Presented at the Precision agriculture. Proceedings of the fourth European conference on precision agriculture. Academic Publishers, Berlin, pp. 405–410.

Miranda-Fuentes, A., Llorens, J., Gamarra-Diezma, J.L., Gil-Ribes, J.A., Gil, E., 2015. Towards an optimized method of olive tree crown volume measurement. Sensors 15, 3671–3687.

Modica, G., Messina, G., De Luca, G., Fiozzo, V., Praticò, S., 2020. Monitoring the vegetation vigor in heterogeneous citrus and olive orchards. A multiscale object-based approach to extract trees' crowns from UAV multispectral imagery. Computers and Electronics in Agriculture 175, 105500.

Möller, M., Alchanatis, V., Cohen, Y., Meron, M., Tsipris, J., Naor, A., Ostrovsky, V., Sprintsin, M., Cohen, S., 2007. Use of thermal and visible imagery for estimating crop water status of irrigated grapevine. Journal of experimental botany 58, 827–838.

Moorthy, I., Miller, J.R., Berni, J.A.J., Zarco-Tejada, P., Hu, B., Chen, J., 2011. Field characterization of olive (Olea europaea L.) tree crown architecture using terrestrial laser scanning data. Agricultural and Forest Meteorology 151, 204–214.

Moorthy, I., Miller, J.R., Hu, B., Chen, J., Li, Q., 2008. Retrieving crown leaf area index from an individual tree using ground-based lidar data. Canadian Journal of Remote Sensing 34, 320–332.

Morales, A., Guerra, R., Horstrand, P., Diaz, M., Jimenez, A., Melian, J., Lopez, S., Lopez, J.F., 2020. A Multispectral Camera Development: From the Prototype Assembly until Its Use in a UAV System. Sensors 20, 6129.

Moriana, A., Pérez-López, D., Prieto, M., Ramírez-Santa-Pau, M., Pérez-Rodriguez, J., 2012. Midday stem water potential as a useful tool for estimating irrigation requirements in olive trees. Agricultural Water Management 112, 43–54.

Moriana, A., Villalobos, F., Fereres, E., 2002. Stomatal and photosynthetic responses of olive (Olea europaea L.) leaves to water deficits. Plant, Cell & Environment 25, 395–405.

Moriondo, M., Leolini, L., Brilli, L., Dibari, C., Tognetti, R., Giovannelli, A., Rapi, B., Battista, P., Caruso, G., Gucci, R., 2019. A simple model simulating development and growth of an olive grove. European Journal of Agronomy 105, 129–145.

Mountrakis, G., Im, J., Ogole, C., 2011. Support vector machines in remote sensing: A review. ISPRS Journal of Photogrammetry and Remote Sensing 66, 247–259.

Noguera, M., Millán, B., Pérez-Paredes, J.J., Ponce, J.M., Aquino, A., Andújar, J.M., 2020. A new low-cost device based on thermal infrared sensors for olive tree canopy temperature measurement and water status monitoring. Remote Sensing 12, 723.

Noori, O., Panda, S.S., 2016. Site-specific management of common olive: Remote sensing, geospatial, and advanced image processing applications. Computers and Electronics in Agriculture 127, 680–689.

O'Toole, J., Real, J., 1986. Estimation of Aerodynamic and Crop Resistances from Canopy Temperature 1. Agronomy journal 78, 305–310.

Pallottino, F., Antonucci, F., Costa, C., Bisaglia, C., Figorilli, S., Menesatti, P., 2019. Optoelectronic proximal sensing vehicle-mounted technologies in precision agriculture: A review. Computers and Electronics in Agriculture 162, 859–873.

Pastor Muñoz-Cobo, M., 2005. Cultivo del olivo con riego localizado. Junta de Andalucía, Consejería de Agricultura y Pesca.

Patel, R., 2013. The long green revolution. The Journal of Peasant Studies 40, 1–63.

Peña-Barragán, J., Jurado-Expósito, M., López-Granados, F., Atenciano, S., Sánchez-De la Orden, M., Garcıa-Ferrer, A., Garcıa-Torres, L., 2004. Assessing land-use in olive groves from aerial photographs. Agriculture, ecosystems & environment 103, 117–122.

Popescu, D., Stoican, F., Stamatescu, G., Ichim, L., Dragana, C., 2020. Advanced UAV–WSN system for intelligent monitoring in precision agriculture. Sensors 20, 817.

Pouliot, D., King, D., Bell, F., Pitt, D., 2002. Automated tree crown detection and delineation in high-resolution digital camera imagery of coniferous forest regeneration. Remote sensing of environment 82, 322–334.

QGIS.org, 2022. QGIS Geographic Information System. QGIS Association., n.d.

Qi, J., Chehbouni, A., Huete, A.R., Kerr, Y.H., Sorooshian, S., 1994. A modified soil adjusted vegetation index. Remote sensing of environment 48, 119–126.

Rallo, G., Minacapilli, M., Ciraolo, G., Provenzano, G., 2014. Detecting crop water status in mature olive groves using vegetation spectral measurements. biosystems engineering 128, 52–68.

Rallo, L., 2006. The olive industry in Spain. Proc. Olivebioteq 5–10.

Rezaei, S.A., Gilkes, R.J., 2005. The effects of landscape attributes and plant community on soil chemical properties in rangelands. Geoderma 125, 167–176.

Roma, E., Catania, P., 2022. Precision Oliviculture: Research Topics, Challenges, and Opportunities—A Review. Remote Sensing 14, 1668.

Roma, E., Laudicina, V.A., Vallone, M., Catania, P., 2023. Application of Precision Agriculture for the Sustainable Management of Fertilization in Olive Groves. Agronomy 13, 324.

Rosati, A., Caporali, S., Paoletti, A., 2015. Fertilization with N and K increases oil and water content in olive (Olea europaea L.) fruit via increased proportion of pulp. Scientia Horticulturae 192, 381–386.

Rosell, J., Sanz, R., 2012. A review of methods and applications of the geometric characterization of tree crops in agricultural activities. Computers and electronics in agriculture 81, 124–141.

Rosell, J.R., Llorens, J., Sanz, R., Arno, J., Ribes-Dasi, M., Masip, J., Escolà, A., Camp, F., Solanelles, F., Gràcia, F., 2009. Obtaining the three-dimensional structure of tree orchards from remote 2D terrestrial LIDAR scanning. Agricultural and Forest Meteorology 149, 1505–1515.

Rotbart, N., Schmilovitch, Z., Cohen, Y., Alchanatis, V., Erel, R., Ignat, T., Shenderey, C., Dag, A., Yermiyahu, U., 2013. Estimating olive leaf nitrogen concentration using visible and near-infrared spectral reflectance. Biosystems engineering 114, 426–434.

Rotundo, A., Lombardo, N., Marone, E., Fiorino, P., 2003. La nutrizione minerale e le concimazioni.

Rouse, J.W., Haas, R.H., Schell, J.A., Deering, D.W., Harlan, J.C., 1974. Monitoring the vernal advancement and retrogradation (green wave effect) of natural vegetation. NASA/GSFC Type III Final Report, Greenbelt, Md 371.

Rovira-Más, F., Zhang, Q., Reid, J., 2005. Creation of three-dimensional crop maps based on aerial stereoimages. Biosystems Engineering 90, 251–259.

RStudio Team. (2015). RStudio: Integrated Development Environment for R. Boston, MA., n.d. . RStudio: Integrated Development for R. RStudio, PBC, Boston, MA.

Rubio-Delgado, J., Pérez, C.J., Vega-Rodríguez, M.A., 2021. Predicting leaf nitrogen content in olive trees using hyperspectral data for precision agriculture. Precision Agriculture 22, 1–21.

Rüegg, J., Siegfried, W., Raisigl, U., Viret, O., Steffek, R., Reisenzein, H., Persen, U., 2001. Registration of plant protection products in EPPO countries: current status and possible approaches to harmonization. EPPO Bulletin 31, 143–152.

Rufat, J., Romero-Aroca, A.J., Arbonés, A., Villar, J.M., Hermoso, J.F., Pascual, M., 2018. Mechanical Harvesting and Irrigation Strategy Responses on 'Arbequina'Olive Oil Quality. HortTechnology 28, 607–614.

162

Saiz-Rubio, V., Rovira-Más, F., Cuenca-Cuenca, A., Alves, F., 2021. Robotics-based vineyard water potential monitoring at high resolution. Computers and Electronics in Agriculture 187, 106311.

Santesteban, L.G., 2019. Precision viticulture and advanced analytics. A short review. Food chemistry 279, 58–62.

Schrijver, R., Poppe, K., Daheim, C., 2016. Precision agriculture and the future of farming in Europe. Science and Technology Options Assessment. Brussels. http://www. ep. europa. eu/stoa.

Senay, G.B., Ward, A.D., Lyon, J.G., Fausey, N.R., Nokes, S.E., 1998. Manipulation of high spatial resolution aircraft remote sensing data for use in site-specific farming. Transactions of the ASAE 41, 489.

Sepulcre-Cantó, G, Zarco-Tejada, P., Jiménez-Muñoz, J., Sobrino, J., de Miguel, E., Villalobos, F., 2006. Within-field thermal variability detection as function of water stress in Olea europaea L. orchards with high spatial remote sensing imagery. Agricultural and Forest Meteorology 136, 31–44.

Sepulcre-Cantó, G., Zarco-Tejada, P., Sobrino, J., Jiménez-Muñoz, J., Villalobos, F., 2005. Spatial variability of crop water stress in an olive grove with high-spatial thermal remote sensing imagery. Proc. Precision Agric 267–272.

Sepulcre-Cantó, Guadalupe, Zarco-Tejada, P.J., Jiménez-Muñoz, J., Sobrino, J., De Miguel, E., Villalobos, F.J., 2006a. Detection of water stress in an olive orchard with thermal remote sensing imagery. Agricultural and Forest meteorology 136, 31–44.

Sepulcre-Cantó, Guadalupe, Zarco-Tejada, P.J., Jiménez-Muñoz, J., Sobrino, J., De Miguel, E., Villalobos, F.J., 2006b. Detection of water stress in an olive orchard with thermal remote sensing imagery. Agricultural and Forest meteorology 136, 31–44.

Sepulcre-Cantó, G., Zarco-Tejada, P.J., Jiménez-Muñoz, J., Sobrino, J., Soriano, M., Fereres, E., Vega, V., Pastor, M., 2007. Monitoring yield and fruit quality parameters in open-canopy tree crops under water stress. Implications for ASTER. Remote Sensing of Environment 107, 455–470.

Shafi, U., Mumtaz, R., García-Nieto, J., Hassan, S.A., Zaidi, S.A.R., Iqbal, N., 2019. Precision agriculture techniques and practices: From considerations to applications. Sensors 19, 3796.

Shuttleworth, W.J., Wallace, J., 1985. Evaporation from sparse crops-an energy combination theory. Quarterly Journal of the Royal Meteorological Society 111, 839–855.

Silvero, N.E.Q., Di Raimo, L.A.D.L., Pereira, G.S., De Magalhães, L.P., da Silva Terra, F., Dassan, M.A.A., Salazar, D.F.U., Demattê, J.A., 2020. Effects of water, organic matter, and iron forms in mid-IR spectra of soils: Assessments from laboratory to satellite-simulated data. Geoderma 375, 114480.

Sims, D.A., Gamon, J.A., 2002. Relationships between leaf pigment content and spectral reflectance across a wide range of species, leaf structures and developmental stages. Remote sensing of environment 81, 337–354.

Sishodia, R.P., Ray, R.L., Singh, S.K., 2020. Applications of remote sensing in precision agriculture: A review. Remote Sensing 12, 3136.

Sola-Guirado, R.R., Bayano-Tejero, S., Rodríguez-Lizana, A., Gil-Ribes, J.A., Miranda-Fuentes, A., 2018. Assessment of the accuracy of a multi-beam LED scanner sensor for measuring olive canopies. Sensors 18, 4406.

Sola-Guirado, R.R., Castillo-Ruiz, F.J., Jiménez-Jiménez, F., Blanco-Roldan, G.L., Castro-Garcia, S., Gil-Ribes, J.A., 2017. Olive actual "on year" yield forecast tool based on the tree canopy geometry using UAS imagery. Sensors 17, 1743.

Solanelles, F., Planas, S., 2005. An electronic control system for proportional pesticide application to the canopy volume in tree crops. Presented at the EFITA/WCCA Joint Congress on IT in Agriculture, pp. 25–28.

Solano, F., Di Fazio, S., Modica, G., 2019. A methodology based on GEOBIA and WorldView-3 imagery to derive vegetation indices at tree crown detail in olive orchards. International Journal of Applied Earth Observation and Geoinformation 83, 101912.

Stateras, D., Kalivas, D., 2020. Assessment of Olive Tree Canopy Characteristics and Yield Forecast Model Using High Resolution UAV Imagery. Agriculture 10, 385.

Stoll, E., Konstanski, H., Anderson, C., Douglass, K., Oxfort, M., 2012. The RapidEye constellation and its data products. Presented at the 2012 IEEE Aerospace Conference, IEEE, pp. 1–9.

Stuppy, W.H., Maisano, J.A., Colbert, M.W., Rudall, P.J., Rowe, T.B., 2003. Three-dimensional analysis of plant structure using high-resolution X-ray computed tomography. Trends in plant science 8, 2–6.

Sundmaeker, H., Verdouw, C., Wolfert, J., Freire, L.P., 2016. Internet of food and farm 2020, in: Digitising the Industry. River Publishers, pp. 129–150.

Tang, T., Radomski, M., Stefan, M., Perrelli, M., Fan, H., 2020. UAV-based high spatial and temporal resolution monitoring and mapping of surface moisture status in a vineyard. Papers in Applied Geography 6, 402–415.

Tanriverdi, C., 2006. A review of remote sensing and vegetation indices in precision farming. J. Sci. Eng 9, 69–76.

Testi, L., Goldhamer, D., Iniesta, F., Salinas, M., 2008. Crop water stress index is a sensitive water stress indicator in pistachio trees. Irrigation Science 26, 395–405.

Testi, L., Orgaz, F., Villalobos, F.J., 2006. Variations in bulk canopy conductance of an irrigated olive (Olea europaea L.) orchard. Environmental and Experimental Botany 55, 15–28.

Thom, A., Oliver, H.R., 1977. On Penman's equation for estimating regional evaporation. Quarterly Journal of the Royal Meteorological Society 103, 345–357.

Tilman, D., Balzer, C., Hill, J., Befort, B.L., 2011. Global food demand and the sustainable intensification of agriculture. Proceedings of the national academy of sciences 108, 20260–20264.

Tognetti, R., d'Andria, R., Lavini, A., Morelli, G., 2006. The effect of deficit irrigation on crop yield and vegetative development of Olea europaea L.(cvs. Frantoio and Leccino). European journal of agronomy 25, 356–364.

Tognetti, R., Giovannelli, A., Lavini, A., Morelli, G., Fragnito, F., d'Andria, R., 2009. Assessing environmental controls over conductances through the soil–plant–atmosphere continuum in an experimental olive tree plantation of southern Italy. Agricultural and Forest Meteorology 149, 1229–1243.

Tognetti, R., Morales-Sillero, A., d'Andria, R., Fernandez, J., Lavini, A., Sebastiani, L., Troncoso, A., 2008. Deficit irrigation and fertigation practices in olive growing: convergences and divergences in two case studies. Plant Biosystems 142, 138–148.

Torres-Sánchez, J., López-Granados, F., Serrano, N., Arquero, O., Peña, J.M., 2015a. High-throughput 3-D monitoring of agricultural-tree plantations with unmanned aerial vehicle (UAV) technology. PloS one 10, e0130479.

Torres-Sánchez, J., López-Granados, F., Serrano, N., Arquero, O., Peña, J.M., 2015b. High-throughput 3-D monitoring of agricultural-tree plantations with unmanned aerial vehicle (UAV) technology. PloS one 10, e0130479.

Tous, J., Romero, A., Hermoso, J., 2007. The hedgerow system for olive growing. Olea (FAO Olive Network) 26, 20–26.

Trangmar, B.B., Yost, R.S., Uehara, G., 1986. Application of geostatistics to spatial studies of soil properties. Advances in agronomy 38, 45–94.

Tumbo, S., Salyani, M., Whitney, J.D., Wheaton, T., Miller, W., 2002. Investigation of laser and ultrasonic ranging sensors for measurements of citrus canopy volume. Applied Engineering in Agriculture 18, 367.

Van Evert, F.K., Gaitán-Cremaschi, D., Fountas, S., Kempenaar, C., 2017. Can precision agriculture increase the profitability and sustainability of the production of potatoes and olives? Sustainability 9, 1863.

Vanegas, F., Bratanov, D., Powell, K., Weiss, J., Gonzalez, F., 2018. A novel methodology for improving plant pest surveillance in vineyards and crops using UAV-based hyperspectral and spatial data. Sensors 18, 260.

Varghese, D., Radulović, M., Stojković, S., Crnojević, V., 2021. Reviewing the potential of sentinel-2 in assessing the drought. Remote sensing 13, 3355.

Veysi, S., Naseri, A.A., Hamzeh, S., Bartholomeus, H., 2017. A satellite based crop water stress index for irrigation scheduling in sugarcane fields. Agricultural water management 189, 70–86.

Vieri, M., Sarri, D., Rimediotti, M., Perria, R., Storchi, P., 2012. The new architecture in the vineyard system management for variable rate technologies and traceability. Presented at the I International Workshop on Vineyard Mechanization and Grape and Wine Quality 978, pp. 47–53.

Villa-Henriksen, A., Edwards, G.T., Pesonen, L.A., Green, O., Sørensen, C.A.G., 2020. Internet of Things in arable farming: Implementation, applications, challenges and potential. Biosystems Engineering 191, 60–84.

Villalobos, F., Testi, L., Hidalgo, J., Pastor, M., Orgaz, F., 2006. Modelling potential growth and yield of olive (Olea europaea L.) canopies. European Journal of Agronomy 24, 296–303.

Virnodkar, S.S., Pachghare, V.K., Patil, V., Jha, S.K., 2020. Remote sensing and machine learning for crop water stress determination in various crops: a critical review. Precision Agriculture 21, 1121–1155.

Webster, R., Oliver, M.A., 2007a. Geostatistics for environmental scientists. John Wiley & Sons.

Webster, R., Oliver, M.A., 2007b. Geostatistics for environmental scientists. John Wiley & Sons.

West, P.W., 2009. Measurements, in: Tree and Forest Measurement. Springer, pp. 5–10.

Williams, D., 1949. A rapid manometric method for the determination of carbonate in soils. Soil Science Society of America Journal 13, 127–129.

Xie, Q., Huang, W., Liang, D., Chen, P., Wu, C., Yang, G., Zhang, J., Huang, L., Zhang, D., 2014. Leaf area index estimation using vegetation indices derived from airborne hyperspectral images in winter wheat. IEEE Journal of Selected Topics in Applied Earth Observations and Remote Sensing 7, 3586–3594.

Xue, J., Su, B., 2017. Significant remote sensing vegetation indices: A review of developments and applications. Journal of sensors 2017.

Yang, C., 2018. High resolution satellite imaging sensors for precision agriculture. Frontiers of Agricultural Science and Engineering 5, 393–405.

Ye, X., Sakai, K., Okamoto, H., Garciano, L.O., 2008. A ground-based hyperspectral imaging system for characterizing vegetation spectral features. Computers and electronics in Agriculture 63, 13–21.

Yuan, G., Luo, Y., Sun, X., Tang, D., 2004. Evaluation of a crop water stress index for detecting water stress in winter wheat in the North China Plain. Agricultural Water Management 64, 29–40.

Yuan, G., Wang, Y., Zhao, F., Wang, T., Zhang, L., Hao, M., Yan, S., Dang, L., Peng, B., 2021. Accuracy assessment and scale effect investigation of UAV thermography for underground coal fire surface temperature monitoring. International Journal of Applied Earth Observation and Geoinformation 102, 102426.

Zaman, Q., Schumann, A.W., 2005. Performance of an ultrasonic tree volume measurement system in commercial citrus groves. Precision Agriculture 6, 467–480.

Zarco-Tejada, P., Sepulcre-Cantó, G., 2007. Remote sensing of vegetation biophysical parameters for detecting stress condition and land cover changes. Estudios de la Zona no Saturada del Suelo Vol. VIII 37–44.

Zarco-Tejada, P.J., Diaz-Varela, R., Angileri, V., Loudjani, P., 2014a. Tree height quantification using very high resolution imagery acquired from an unmanned aerial vehicle (UAV) and automatic 3D photo-reconstruction methods. European journal of agronomy 55, 89–99.

Zarco-Tejada, P.J., Diaz-Varela, R., Angileri, V., Loudjani, P., 2014b. Tree height quantification using very high resolution imagery acquired from an unmanned aerial vehicle (UAV) and automatic 3D photo-reconstruction methods. European journal of agronomy 55, 89–99.

Zarco-Tejada, P.J., Miller, J.R., Morales, A., Berjón, A., Agüera, J., 2004. Hyperspectral indices and model simulation for chlorophyll estimation in open-canopy tree crops. Remote sensing of environment 90, 463–476.

Zhai, A.F., Cheng, B.M., Zhang, C.L., Ding, D.T., Liu, E.Y., 2017. Optimization of agricultural production control based on data processing technology of agricultural internet of things. Italian Journal of Pure and Applied Mathematics 38, e252.

Zhang, C., Kovacs, J.M., 2012. The application of small unmanned aerial systems for precision agriculture: a review. Precision agriculture 13, 693–712.

Zhang, N., Wang, M., Wang, N., 2002. Precision agriculture—a worldwide overview. Computers and electronics in agriculture 36, 113–132.

Zhao, L., Li, Q., Zhang, Y., Wang, H., Du, X., 2019. Integrating the continuous Wavelet transform and a convolutional neural network to identify Vineyard Using Time series satellite images. Remote Sensing 11, 2641.

Zipori, I., Erel, R., Yermiyahu, U., Ben-Gal, A., Dag, A., 2020. Sustainable management of olive orchard nutrition: A review. Agriculture 10, 11.

Zou, Y., Quan, L., 2017. A new service-oriented grid-based method for AIoT application and implementation. Modern Physics Letters B 31, 1740064.